Unconventional fabrication of 2D nanostructures and graphene edges

Bellunato, A.

Citation

Bellunato, A. (2018, December 11). *Unconventional fabrication of 2D nanostructures and graphene edges*. Retrieved from https://hdl.handle.net/1887/67524

Cover Page

Universiteit Leiden

The handle http://hdl.handle.net/1887/67524 holds various files of this Leiden University dissertation.

Author: Bellunato, A.
Title: Unconventional fabrication of 2D nanostructures and graphene edges
Issue Date: 2018-12-11

Unconventional Fabrication of 2D Nanostructures and Graphene Edges

Proefschrift

Ter verkrijging van
de graad van Doctor aan de Universiteit Leiden,
op gezag van Rector Magnificus prof. mr. C. J. J. M. Stolker
volgens besluit van het College voor Promoties
te verdedigen op 11 December 2018
klokke 10:00 uur

Door

Amedeo Bellunato

Geboren te Turijn, Italië
in 1987

Promotiecommissie

Promotor: Prof. Dr. A. Kros

Copromotor: Dr. G. F. Schneider

Overige Leden: Prof. Dr. H.S. Overkleeft, LIC (voorzitter)

Prof. Dr. J. Brouwer, LIC (secretaris)

Prof. Dr. J.M. van Ruitenbeek, LION

Prof. Dr. P. Rudolf, University of Groningen

Prof. Dr. G.M. Whitesides, Harvard University, USA

To Lia Lima: my partner in crime.

Table of Contents

CHAPTER 1

Introduction

Graphene is a bi-dimensional allotrope of carbon arranged in a monoatomic layer of sp^2 hybridized carbon atoms packed in a honeycomb lattice. The hexagonal pattern of unsaturated atoms yields an extended aromaticity through the lattice formed by the p_z electrons responsible of the π bonds among the carbon atoms. As in conjugated organic semiconductors, the extended conjugation of half-filled p_z orbitals forms π valence and conductance bands. As opposed to σ orbitals, responsible for deep valence bands behind the rigid structure of graphene, π bands present a linear electronic dispersion where the valence and conduction bands meet at the Fermi level[1,2] (Figure 1.1a). π bands are responsible for the intrinsic conductivity of graphene, where electrons promoted to the conduction band by thermal energy or doping can move as massless fermions through the lattice of graphene, at speed up to only 300 times slower than light[3].
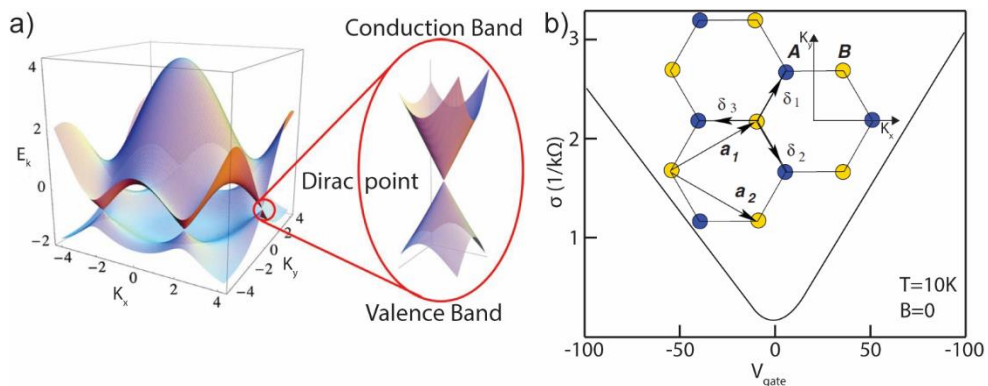
Figure 1.1. Hexagonal honeycomb lattice of graphene. a) Electronic dispersion in the graphene reciprocal lattice. Inset: magnification on the cone structure at the Dirac point. The two bands meet at the Fermi Level[1]. b) I-V$_{gate}$ characteristic of graphene. Inset: graphene lattice and reciprocal lattice defined by the K vectors[1].

The linear dispersion of the band structure has an immediate effect on the conductivity of graphene[4]. External electric fields modulate the electrons population of the conduction band, yielding a gate effect. In practice, the external field promotes electrons from the conduction to the valence band modifying the amount of charge carriers in graphene. Sweeping the gate field from lower potential to higher potential yields an increment of electrons in the conduction band. The conductivity curve of graphene assumes a semi-parabolic shape with a minimum of conductivity at the Dirac point, where the promotion of electrons

2

caused by the gate field balances the amount of holes at the - so called - charge neutrality point. By increasing further the potential, the promoted electrons overcome the amount of holes, restoring a higher conductivity (Figure 1.1b). In proximity of the charge neutrality point, the conductivity of graphene varies exponentially with the electric field, becoming extremely sensitive to field variations (while assuming a linear behaviour far apart of the charge neutrality point).

Similar to a gate field, the interaction between molecules and the surface of graphene results in a direct perturbation of the electronic band structure of graphene. Thus, thanks to the 2D nature of graphene, short-range interactions induced by charges such as dipoles or ions change the electronic band structure of graphene, therefore modulating the electron density populating the valence and conduction bands of graphene[5]. As a result, the conductivity of graphene is modified by the proximity of external perturbations such as adsorbed molecules. Similarly, the chemical functionalization of graphene locally alters the honeycomb lattice of sp^2 hybridized carbon atoms. The introduction of sp^3 defects corresponds to the addition of scattering centres perturbing the motion of the electrons, permanently altering the electronic structure of graphene, changing its conductivity and its entire band-structure. Nonetheless, the widespread sp^2 conjugation results in a relative chemical stability of the carbon atoms composing the lattice of graphene, yielding sensors of high sensitivity, but extremely poor selectivity.

Carbon atoms on the edge of graphene represent a singularity. In fact, these atoms are already located on ruptures of the lattice of graphene, introducing scattering and perturbations in the band structure of graphene. The chemistry at the edges alters the composition of such carbon atoms via functionalization and elemental substitution. Nonetheless, these modifications influence sp^3 carbons intrinsically present in the graphene, without additional damage on the basal plane. Ideally, selectivity can then be achieved without perturbing the physical properties of the basal plane (i.e. sensitivity). At the nanoscale, also, the increased ratio of edge atoms over basal plane atoms leads to a confinement of the aromatic structure of graphene[6]. Edge defects and their chemistry become predominant in the electrodynamics of graphene, modulating directly chemical and physical properties[7–16], such as chemical reactivity and electronic band structure.

The electrical responsiveness of graphene permits its integration as an active element within sensing devices. The atomic thickness and the relative chemical stability, also, offer further advantages in the design of sensors working at the molecular scale, ranging from DNA sequencers[17] to ultra-fast transistors for consumable electronics[4,18]. These, particularly, require the sculpting of graphene into complex architecture with nanometric and sub nanometric precision. Nanoribbons, nanopores and nanogaps form (bio)-sensing platforms relying on precisely patterned graphene nanostructures. The scalable nanoengineering of graphene, though, remains among the biggest challenges of graphene nanotechnology. Conventionally, the controlled sculpting of graphene distinguishes between bottom-up or top-down approaches.

The former assembles graphene nanostructures via the polymerization of polycyclic aromatic hydrocarbons[19]. Particularly, bottom-up techniques grow atomically tailored graphene nanostructures as narrow as a few carbon atoms with chemically designed edges, as explained in more details in Chapter 2. Nevertheless, bottom-up solution synthesis face solubility constrains, with severe issues toward device integration, which limit both the achievable size of the graphene samples and their application[20]. From the aspect of the chemical functionalization of graphene edges, chemical synthesis allows the control of crystallinity, purity, molecular structure and chemical functionality of the edge. Notably, some reports attempted the selective synthesis over pre-patterned substrates[21,22], allowing a precise alignment of the nanostructures over the substrate, but still requiring complex lithographic pre-treatments severely affecting its applicability.

Alternatively, top-down approaches narrow large area graphene films into nanostructures via selective etching of graphene protected underneath a mask. Electron beam lithography[23], either in the form of patterning through a resist or resist-free lithography via transmission electron microscopy, remains the method of choice for the top-down sculpting of graphene nanoarchitectures. Conventionally, electron beam lithography writes a pattern into a polymeric resist coating the graphene[23]. Chain scission occurs in the exposed regions of the *positive* resist yielding a significant change of its solubility into selected solvents, or developer. After the dissolution of the exposed resist, the remaining pattern acts as a mask over the surface of the graphene, while the unprotected graphene areas are further etched in harsh chemical environments such as reactive ion etching,

RIE. At last, the protecting resist is dissolved uncovering the graphene nanostructure. Beam lithography is used for the patterning of graphene nanoribbons as thin as ~10 nm[24]. Furthermore, it is used for the design of nanoconstrictions successively converted into nanogaps[25] for instance via electroburning[26]. Importantly, polymeric resists, organic solvents and harsh ion etching contribute to the contamination of the graphene nanostructures, and affect the composition and the topography of the edges in an uncontrolled manner[27]. Alternatively, transmission electron microscopes, TEM, can generate highly focused electron/ion beams capable of directly patterning graphene without any resist. The particle beam knocks out carbon atoms from the lattice by energetic exchange with graphene[28,29] , yielding for instance nanoribbons[30] and nanopores in free-standing graphene[31,32–35] and other two-dimensional materials[36,37], with superior control over the crystallinity and chemical composition of the edges. Conveniently, the final pattern is characterized in situ using the imaging mode of the electron/ion microscopes[38,31]. Despite the great step-forward performed by lithographic systems in the field of graphene nano-patterning, beam lithography remains a time consuming technique, requiring high vacuum and unable of parallel processing.

Aiming to overcome the main limitations of conventional bottom-up and top-down nanofabrications, in this thesis we showcase different powerful approaches for the simple and flexible design of nanopores, nanogaps and nanoribbons architectures and for the selective chemical functionalization of graphene edges, as illustrated in Chapter 3, Chapter 4 and Chapter 5. Furthermore, we employed such approaches to form metallic nanogaps and polymeric nanofluidic channels as presented respectively in Chapter 6 and Chapter 7. We used microtomy to precisely prepare metallic nanorods embedded in polymeric supports which we assembled into nanopores and nanogaps or used as inert mask for the top-down sculpting of graphene nanoribbons, without employing any conventional lithographic step nor clean room facilities.

Whitesides and co-workers were the first to introduce the microtomy of metallic thin films as an alternative route to fabricate and pattern metallic nanostructures[39,40]. Specifically, metallic thin films are grown via evaporation or atomic layer deposition onto flat substrates and further embedded in polymer, generally epoxy resins[41]. The resulting sample is a composite material constituted

of a metallic thin film surrounded by a polymeric matrix. A sharp diamond knife sections the polymer with nanometric precision, below 30 nm, yielding thin polymeric slabs embedding metallic nanostructures, Figure 1.2a. Practically, the knife works as a wedge at the interface with the polymer matrix, initiating a crack through the brittle polymer matrix[41]. The crack controllably propagates few nm ahead of the knife, extending in proportion to the radius of curvature of the knife. The knife slices through the polymer pushing forward the crack propagation, and yielding a thin section of polymer. The polymer operates as a mechanical support for the metallic filler, allowing the precise transfer and manipulation of the slab. The composite sample slides over the knife, which position is controlled by high-precision piezo-actuators. The diamond knife is atomically sharp with a radius of few nanometres (5 nm to 6 nm), yielding highly precise nanometric polymeric slabs.
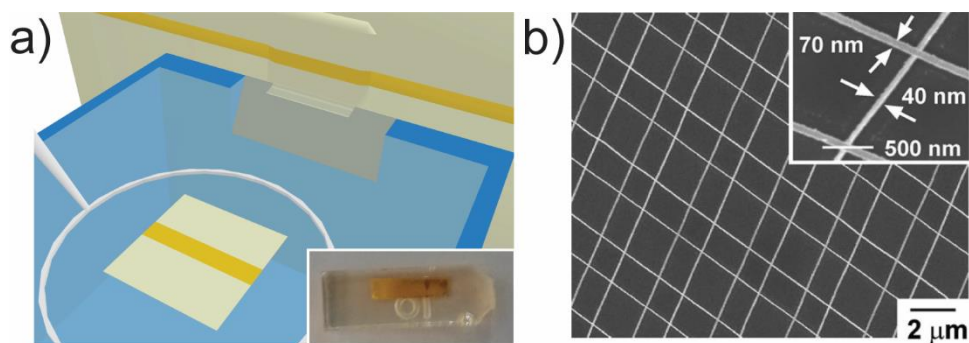
Figure 1.2. Microtomy of nanostructures. a) A diamond knife slices the metallic thin film embedded into the polymer matrix yielding polymeric slabs bearing the metallic nanostructure. Inset: the composite sample formed by a metallic thin film embedded in the polymer matrix. b) Metallic nanorods prepared via microtomy and assembled in complex nano-architectures[39].

The supporting polymer allows the manipulation of the samples and their assembly into suspended and overlapped architectures, Figure 1.2b. Afterwards, the polymer can be removed, leaving in place only the embedding, such as a metallic nanostructure. Alternatively, the metallic embedding can be etched or dissolved, leaving slits into thin polymeric slabs, which can be assembled into nanopores[42], for instance.

In this work, we illustrate the application of microtomy for the sculpting of complex nanostructures with innovative designs. We used microtomy to prepare edges in graphene, first demonstrating their selective chemical functionalization via bulk methods such as electrografting, as illustrated in Chapter 3. Furthermore, the removal of the supporting polymer slab or the metallic embedding resulted in edge tailored graphene nanoribbons with controlled edge chemistry, Chapter 5. By overlapping the slits within two polymeric slabs, we obtained highly precise and mechanically stable zero-depth nanopores, capable of reaching the performances of graphene nanopores, while demonstrating reduced noise, Chapter 7.

1.1 Graphene (bio-)nano-sensors

Graphene showed outstanding initial results in the field of molecular sensing, particularly toward DNA sequencing[33] and single molecule detection[43]. There are several sensing platforms based on graphene[44,45], which rely on multiple working mechanisms, exploiting features such as atomic thickness, mechanical stability and modulated electrical conductivity. These can be divided into three major classes based on diversified working designs and classified as graphene nanopores, graphene field effect transistors (GFET) and nanogaps. Particularly, atomically thin, bidimensional graphene nanopores, ideally, can perform real time DNA sequencing with single nucleotide resolution[46], promoting graphene and bidimensional materials as ideal candidates for the next generation sequencing devices. In the upcoming sections, we will introduce these technologies, their working mechanism, and major challenges, explaining their relevance in the sensing community and shedding a light over the significance of our work.

1.1.1 Graphene nanopores

A nanopore is a nanometric hole drilled in a thin membrane. Molecular sensing in nanopores proceeds by occlusion of the nanopore channel across the membrane[47], Figure 1.3a. In fact, by applying a transmembrane potential within an electrolytic solution, ions move across the hole, yielding a characteristic nanopore conductance G (1):

$$(1) \quad G = \sigma \left[\frac{4L}{\pi d^2} + \frac{1}{d} \right]^{-1}$$

Where σ is the conductivity of the electrolytic solution, L is the length of the nanopore channel and d is the diameter of the pore. Upon molecular translocation, the effective volume of the nanopore decreases, lowering the conductance of the pore. Consequently, despite of a constant transmembrane potential V_{tm}, the electrolytic current intensity across the pore I_p reduces, according to the Ohm's law (2):

$$(2)\ \ I_p = V_{tm}G$$

Thus, the overall reduction of the electrolytic current is directly modulated by the size of the translocating molecule[48,49]. The electrolytic current modulation becomes a fingerprint toward molecular recognition and sequencing of DNA strands, particularly single strands, and proteins driven through the pore by the transmembrane potential. In fact, negatively charged single strand DNA molecules are driven through the thread of the pore under the electrostatic force of the same transmembrane potential. Each single nucleotide occludes the pore in an ordered sequence, yielding characteristic dips in the electrolytic current intensity. Afterwards, the sequencing is performed by the analysis of the current dips induced by the molecular translocation[49].
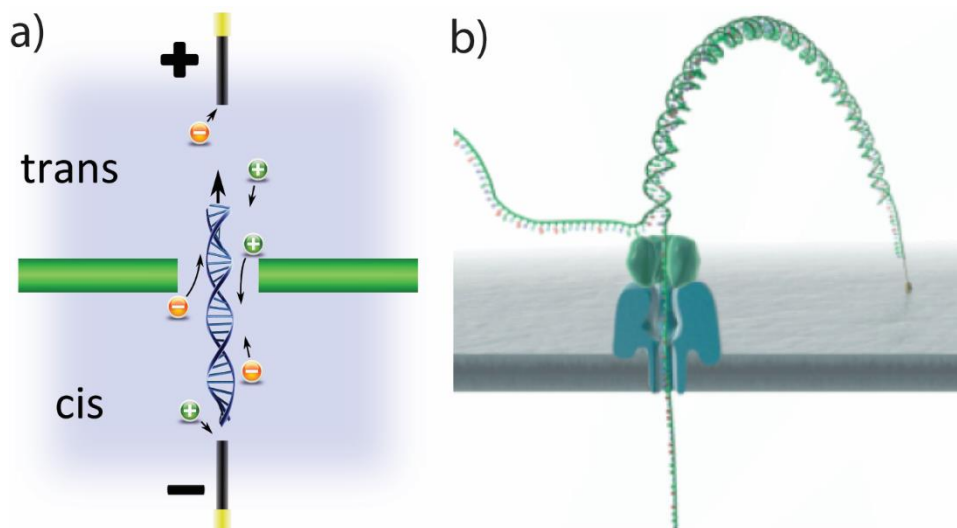

Figure 1.3. Nanopore bio-nanosensors. a) Nanopore working mechanism. A transmembrane voltage (+/-) drives the electrolytes and the analytes through the

pore[50]. b) Schematics of a biological nanopore embedded in a lipidic membrane with an enzyme motor on at its inlet.

The most recent nanopore devices achieved accurate read of long-length DNA single-strands, above 10^3 base pairs. Among these, so called biological nanopores demonstrated outstanding results. Biological nanopores incorporate protein channels such as α-hemolysin into a lipid or polymeric membrane. DNA sequencing happens by translocating the biopolymer through the pore of the protein channel, Figure 1.3b. Biological nanopores can modulate the translocation speed of the DNA single-strands toward a step-like nucleotide translocation which ideally permits single nucleotide resolution with high fidelity. The most effective mechanism to reduce the translocation speed relies on the functionalization of the pore with an enzyme[51], for instance using an enzyme motor such as a DNA polymerase[52–54]. Functionalized biological nanopores modulate the translocation of a single strand DNA, which is driven through the pore by a transmembrane potential. The nanopore modified with an enzyme is now a cheap, portable single strand DNA sequencer currently on the market: the MinION®. It is composed of an array of biological nanopores and is capable of ultra-long reads (> 100 kbp). Interestingly, the enzyme coupled technology allowed the sequencing of 85% of the human genome, corresponding to $2.867 \, 10^6$ nucleotides reaching a final read-out accuracy exceeding 99.8%[55]. Importantly, the accuracy achieved via nanopores technologies such as MinION® would have been unreachable without the increasing resolving ability of computational methods, capable of browsing through a dataset composed of around 10^7 bytes of data representative of more than $2 \, 10^6$ bases[55]. In fact, while the physical nanopore read-out is still affected by a remarkable mistake (above around 40% on its release in 2014 and reduced below 15% in 2018[56]), the multi-reading process and the analysis algorithm entitle this device of an outstanding reliability[57]. Despite the current commercial success and the dominance of biological nanopores in the landscape of nanopore based DNA sequencers, biological nanopores encounter some limitations. Among these, mechanical fluctuations of the biological membranes majorly affect the performances of such pores. Most importantly, the single nucleotide resolution depends on complex interpretation algorithms, capable of extrapolating sequencing information from the ionic current readings of multiple nucleotides clogging the pore at the same time. In fact, at the thinnest constriction, the pore is around 1,4 nm wide and capable of hosting up to 10 nucleotides in the β-barrel at

the same time, severely modulating the intensity of the ionic current[58]. At last, current technology is single-read, which means that each device can be used once, and needs to be replaced after each read-out.

Alternatively to the current technology, 2D (two-dimensional) materials such as graphene attracted increasing interest for their use in nanopore sequencers. In fact, graphene forms nanopores which channels are atomically thin[31,34] allowing the passage of a single nucleotide per time (Figure 1.4a). Specifically, atomically thin membranes form nanopores which length dimension L is at least one order of magnitude smaller than the diameter d, increasing the overall conductivity of the pore, that becomes $G \propto d$[33]. The ability of a graphene nanopore to detect the passage of a DNA molecule was first demonstrated experimentally in 2010 using a nanopore drilled in a transmission electron microscope, TEM, through a suspended graphene membrane over a SiN support[31]. Figure 1.4b shows the electrolytic current dips relative to translocation events caused by the passage of double stranded DNA through a 22nm wide pore. The sensitivity of the graphene is high enough to distinguish among three different folding configurations of a 16µm long DNA molecule. Ever since, nanopores in graphene have been widely tested and implemented.
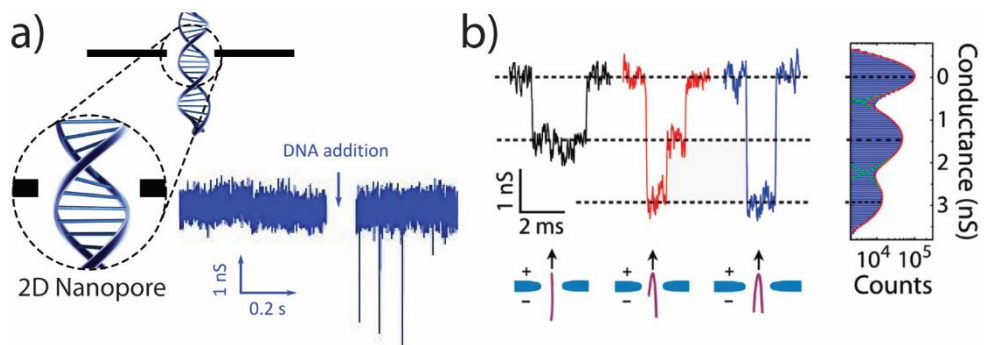

Figure 1.4. Graphene nanopores. a) Top: graphene nanopores translocating a single DNA molecule. Bottom: electrolytic current through a nanopore. The passage of biomolecules such as DNA strands clogs the pore reducing the conductance[31]. b) Differentiation between translocation events in folded and unfolded DNA strands.

Despite the great sensitivity to molecular translocation, graphene based nanopores sequencers are not available yet. The most relevant challenges relate both to the dynamic of translocation, such as the translocation speed, and the intrinsic characteristics of the nanopore, such as the mechanical stability, the hydrophobicity and the - so called - access resistance. The translocation speed is among the most severe limitations[59]. In the case of single stranded lambda DNA, each nucleotide translocates at a rate around 20 ns/nucleotide[31,50], under a transmembrane potential in the order of 100 mV. Consequently, such a translocation speed demands for an acquisition speed above 1 MHz to resolve between the current dips due to the passage of each nucleotide. Additionally, the ions surrounding the membrane form a capacitive coupling with high frequency noise, usually filtered at 10 kHz via a band-pass filter during the current recording[60].

Graphene nanopores (more generally 2D nanopores) have also a low frequency (f) noise[61] that modulates as 1/f and its origin is not yet fully understood, negatively affecting the resolution of the pore. Mechanical fluctuations of the suspended membrane are a possible cause of the 1/f noise. It has been demonstrated experimentally that the noise reduces proportionally to the thickness of the membrane[62], as a consequence of the higher membrane stiffness. Alternatively, shrinking the suspended area of the membrane appears to increase the signal to noise ratio[50].

The transmigration of ions through the pore, also, gives rise to the so called access resistance[63]. When considering the elements composing the conductivity of a nanopore as expressed in equation 1, two components are involved: the channel resistance and the access resistance. The channel resistance stems from the physical passage of ions through the channel composing the pore. The access resistance, on the other hand, relates to a hemisphere around both sides of the mouth of the pore where the concentration of ions increases at the inlet/outlet of the pore. When considering 2D membranes, the channel resistance converges to null. Thus, the access resistance becomes predominant, and the hemispherical volume of ions condensation around the pore represents a so called effective volume of the pore and is directly proportional to the pore diameter, extending over the same nanometer scale. In fact, the condensation of the ions flow already modulates the ionic transport, thus the electrolytic current. Consequently, the hemispheric volume around the mouth of the pore represents an area of reduced

sensitivity of the pore, which loses its ability of distinguishing between different nucleotides within the volume of access resistance, thus losing single nucleotide resolution.

Furthermore, the interaction of molecules such as DNA with the hydrophobic graphene membrane might perturb the translocation through the nanopores[64]. In fact, graphene tends to adsorb irreversibly molecules such as single DNA strands on its surface, hindering the molecular flow. Interestingly, such a drawback is considered often as a starting point to controllably modulate the translocation speed[65]. For instance, exposed graphene nanopores stacked in between two nanopores drilled in aluminium oxide (Al_2O_3) membranes might locally interact with the DNA strand slowing the passage of the strand through the nanopore[66]. Also, the chemical functionalization of the graphene surface might allow a trap-release mechanism, which influences the rate of nucleotides crossing the pore. Nonetheless, while hydrophilic coatings appeared effective in preventing the adsorption of hydrophobic molecules on graphene[67], they also increase the overall thickness of the membrane, thus affecting its resolution abilities.

In conclusion, it is still a technological challenge to achieve molecular sensors, particularly sequencers, based on graphene nanopores or other 2D materials. The advantages introduced by the monoatomic thickness are counterbalanced by obstacles preventing single nucleotide resolution, such as access resistance or translocation speed. Aiming to overcome some of the limitations affecting graphene nanopores, an alternative strategy to assemble subatomic thin nanopores: zero-depth nanopores capillaries, is presented in Chapter 7. These form at the intersection of two slits carved into polymeric thin films prepared via microtomy, showing reduced noise and modulated hydrophobicity and capable of slowing the passage of DNA strands through the pore.

The most important limitation of nanopores remains the indirect detection system. In fact, nanopores do not directly probe molecules. Instead, nanopores extrapolate information from fluctuations in the ionic solution surrounding and interacting with the transmigrating molecule. Indirect characterization has several inherent drawbacks caused directly by the nanopore architecture, for instance mechanical instability or irreversible molecular adsorption.

1.1.2   Graphene field effect transistors

Field effect transistors exploit the modular electronic properties of graphene upon interaction with external stimuli such as molecular adsorption[43,68].

The extended conjugation network of graphene forms a diffused electron distribution that entitles this material of an extremely high charge carrier mobility[69] up to 10^5 cm^2 V^{-1} s^{-1}. The highly regular lattice of carbon atoms and the absence of a layered structure, ideally, yields massless fermion-like electrons moving unscattered over the surface of graphene, and arranged within a conical semi-metallic band structure with 0 eV bandgap[70,71]. These mobile electrons can be perturbed under the effect of an external field, modulating the conductivity of the film.

In a transistor configuration, graphene is connected via a source and a drain electrode, while an external field is applied in the form of a gate voltage, either through an electrolytic solution, for instance KCl, or through a capacitive substrate such as SiO$_2$[72]. Sweeping the gate voltage returns a cone-shaped conductance characteristic of graphene and with a minimum of conductance at the so called Dirac point, or charge neutrality point, Figure 1.5a. The cone-shaped conductance curve offers interesting features for sensing applications. In fact, the interaction between graphene and molecules locally perturbs the electronic band structure of graphene, operating a shift of its Dirac point. Covalent bonds[73–75] and non-covalent interactions[76–78] such as van der Waals, dipoles and π-π stacking modulate the conductivity of graphene, shifting the position of its Dirac point and the amplitude of the cone-shaped conductance curve. The induced variation in conductance works as the sensing fingerprint. Importantly, the cone-shaped conductance curve is steep around the Dirac-point where it follows a parabolic trend. Thus, sensing at the Dirac point returns highly responsive sensors, where small perturbations have a significant impact on the overall conductivity of graphene. This yielded sensors capable of detecting molecules dispersed in extremely low concentrations[72], up to a single molecule physisorbed on the surface of a graphene transistor[43,79].
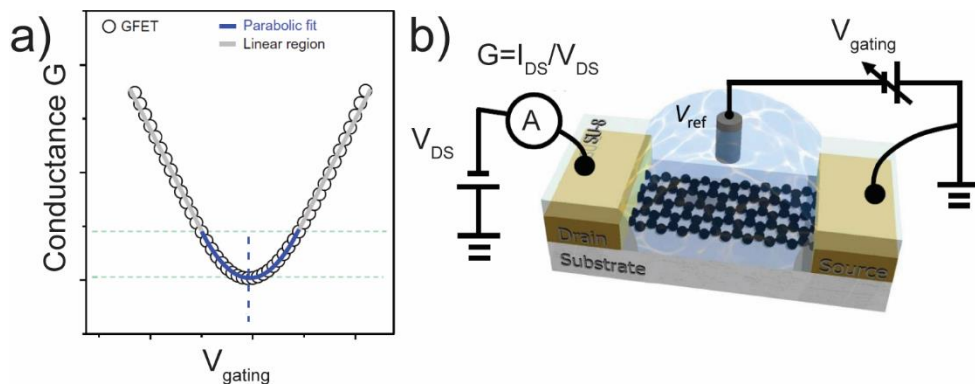
Figure 1.5. Graphene field effect transistor. a) Conductivity curve of graphene under the effect of an external electric field: the gate voltage modulates the conductance of graphene with a minimum of conductance at the Dirac point. b) Liquid gated GFET. A potential is applied between the source and drain electrode of graphene, while the gate potential is applied through an electrolytic solution (blue droplet), modulating the conductance of graphene[80].

Similarly, a gate potential can be applied by means of a reference electrode immersed in an electrolytic solution[81], a process so called liquid gating. Ideally, the electrolyte works as a dielectric causing the potential fall between the electrode and the graphene, Figure 1.5b. The ions of the electrolyte move both toward the surface of the electrode and the surface of graphene. The local charging of the graphene surface attracts immediately oppositely charged ions which counterbalance the potential fall across the solution via the formation of an electrical insulating double layer[82,83]. The field developing across the double layer, then, works as the gating source of the graphene. Liquid gating is an interesting feature of graphene for molecular sensing, as it allows to integrate graphene transistors within fluidic channels and to dissolve analytes into the electrolytic solution. Sensing is based on the local charge perturbation induced by the interaction between the graphene and the molecule. This causes a shift of the Dirac point position resulting in a change in conductance of the liquid gated graphene transistor[82].

Graphene transistors are primarily responsive to charge distributions carried by the molecules. Complex analytes composed of several molecular species might induce non-selective sensing responses. Accordingly, the selectivity of the

14

transistor can be increased by chemical functionalization of the graphene[82]. Covalent functionalization introduces target receptors chemically bound to the honeycomb lattice of graphene. The resulting chemical bond in graphene induces a sp^2 to sp^3 re-hybridization of the carbon atoms composing the lattice of graphene[84]. This introduces defects in the conjugation network of the honeycomb lattice of graphene, yielding local scattering centres affecting the conductivity of graphene[85]. The overall effect is a reduction of the conductivity and flattening of the Dirac cone, leading to a higher selectivity at the cost of a lower sensitivity.

Alternatively, non-covalent functionalization absorbs selective receptors on the surface of graphene via short range interactions, such as π-π stacking, van der Waals and electrostatic forces[86–88]. For instance, single stranded DNA was immobilized on graphene field effect transistors via non covalent adsorption of biotinylated bovine serum albumin[89] which immobilize DNA via biotin–streptavidin-binding. These were then capable of detecting the immobilization and hybridization of complementary DNA with concentration as low as 100 fM. Interestingly, it was also demonstrated the ability of a graphene field effect transistor, GFET, to distinguish between the adsorption of the four different nucleotides[90].

Particularly, GFET composed of graphene nanoribbons have shown promising theoretical results toward DNA sequencing. Graphene nanoribbons, nanometric thin strips of graphene, compose GFETs embedded within nanofluidic channels capable of stretching DNA strands for sequencing. In a first attempt, a nanopore was drilled through a nanoribbon[35,91], Figure 1.6a. During the translocation of each nucleotide through the pore, the local charge density fluctuation provokes a shift in the conductivity of the ribbon, which is recorded along with the electrolytic current. Theoretical calculations demonstrated that the specific conformation of DNA nucleotides lead to specific charge fluctuations and were proposed for sequencing applications. As an alternative configuration, a GFET composed of a nanoribbon over a nanofluidic channel[92], Figure 1.6b, was also proposed for DNA sequencing. Here, the DNA temporarily adsorbs onto the graphene via π-π stacking modulating the conductance of graphene. In the meantime, a trans-channel potential pushes further the DNA strand. Accordingly to the molecular dynamics, MD, simulations the conductivity of graphene varies as a function of the gate potential as $G(V_g)$[92]:

$$(3) \quad G\left(V_g\right) = \frac{2e^2}{h} T(\mu)$$

Where h is the Planck's constant, e the elementary charge and T the transmission curve of the graphene nanoribbon as a function of the chemical potential $\mu(V_g)=E_F$ - V_g, with E_F that is the Fermi Level of the graphene ribbon, thus (3) becomes:

$$(4) \quad G\left(V_g\right) = \frac{2e^2}{h} T\left(E_F - V_g\right)$$

In order to retain the most detailed sequencing information the model demands for a scan over the gating potential to characterize the conductance curve during the interaction of graphene with each nucleotide. These requirements showcase once more the problem related to the translocations speed, which also in case of sweeping frequency in the order of 10 Mhz, would still impose a flow rate of the DNA strand in the order of 0.1 µs per nucleotide.
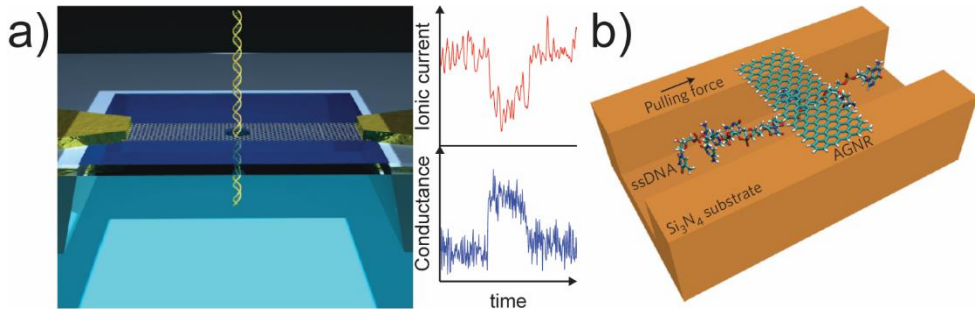

Figure 1.6. Graphene field effect transistors, GFETS, DNA sequencers. a) Left: schematics of a DNA molecule translocating through a nanopore drilled through a GFET nanoribbon. Right: upon the passage of a DNA strand, the ionic current through the nanopore reduces, while the electronic perturbation of the graphene rises its conductance[35]. b) A GFET nanoribbon bridging a nanochannel. The pulling force is the electric field leading the DNA molecule through the channel[92].

Practically, the extremely fast passage of DNA strands allows to identify the resistive variation of the graphene ribbon, nonetheless without achieving single nucleotide resolution. An ideal solution would be the chemical design of highly selective graphene transistors capable of modulating the interaction with DNA strands, but without affecting the electrical properties of graphene. As a result, there is an increasing interest in the chemical functionalization of the edges of

graphene. It is expected that highly reactive edges can precisely modulate the functionality of graphene without lowering the conjugation degree of the honeycomb lattice thus the electronic properties of graphene.

Notably, important steps forward were made recently. Particularly, Heerema et al.[93] successfully drilled a nanopore through a nanoribbon, and managed to design an electronic acquisition system capable of detecting the resistive response of graphene upon interaction with DNA molecules. Even if the carefully designed electronics manages to drastically reduce many capacity elements detrimental for the measurement, the approach remains too challenging. Indeed, they reported the severe unreliability of the device, due to the complex, multistep nanofabrications with a high failure rate, stressing the need of alternative fabrication methods than conventional lithography. Accordingly, Chapter 5 describes the single step fabrication of high aspect ratio graphene nanoribbons, using inert metallic masks fabricated via microtomy instead of lithographically designed polymeric masks.

1.1.3 Graphene nanogaps

Graphene nanogaps comprise two graphene electrodes interfaced at nanometric distance[94,95]. Under the application of a bias potential, a tunnelling current flows between the edges of the contactless electrodes, which intensity decays exponentially with the size of the gap. The gap between the edges of two graphene layers yields a nanogap composed of atomically thin electrodes. Therefore, graphene nanogaps exploit both the atomic thickness and the electrical properties of graphene.

Ideally, molecular sensing with nanogaps employs transverse tunnelling currents transmitted through the molecule crossing the gap[96–99], Figure 1.7a. The atomic thickness of the electrode ensures the single molecule resolution of the sensing nanogap. In 2010 Postma proposed a theoretical model for DNA sequencing across a graphene nanogap[100]. In principle, fixing the gap size, the transmission probability of each nucleotide yields a tunnelling current used as a sequencing fingerprint. The current varies according to equation (5):

$$(5) \ \ I(V, x_0) = \sum_{i=1}^{N} I_0^{B_i}(V) e^{-2k\sqrt{d^2 + (x_i - x_0)^2}}$$

Where I_0^{Bi} transverse tunnelling current for the nucleotide "I" along the backbone, V is the bias voltage across the gap, k is the decay constant of the tunnelling current across the gap and function of the gap size, d is the gap size and x_i is the position of the crossing nucleotide with respect the intersecting plane of the gap.

Even though each nucleotide, due to its chemical and structural unicity, is expected to deliver an individual tunnelling intensity, conformational modifications in terms of orientation and distance from the gap electrodes might affect the electron transmission probability, thus the current intensity. Different orientations within the gap broaden the tunnelling current associated to each nucleotide[101]. As a result, it is possible to distinguish between two classes of nucleotides such as purines (G, A) and pyrimidines (C, T), based on their size. Theoretically, a more in-depth resolution can be obtained by sweeping the bias voltage across the gap, allowing sequencing resolution. Experimentally[102], the identification of at least three nucleotides was accomplished in a gold nanogap of about 1nm, respectively resolving between thymidine monophosphate TMP, guanosine monophosphate GMP and cytidine monophosphate CMP, Figure 1.7b.
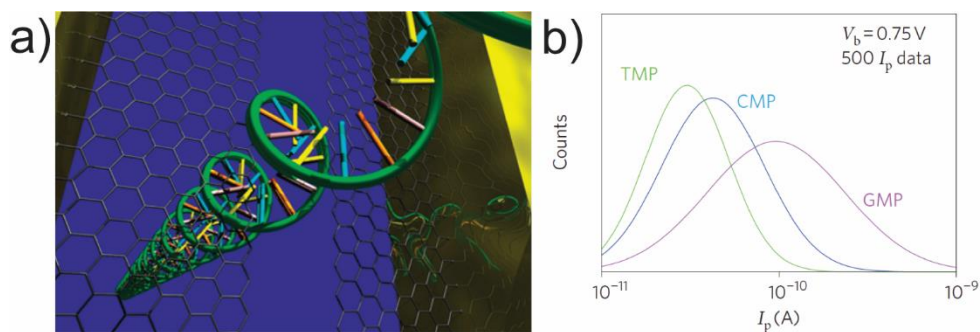
Figure 1.7. DNA sequencing with tunnelling nanogaps. a) Schematics of the sensing mechanisms: a biopolymer passes through the electrodes across the nanogap between the edges of two graphene layers. A bias voltage imposes a tunnelling current which intensity is modulated by the translocating nucleotide[103]. b) Current distributions of TMP, CMP and GMP nucleotides in a gold nanogap of 1nm at V_{bias} = 0.75V[102].

Furthermore, the chemical functionalization of the edges of the graphene electrodes improves the sensing performances of the gap[104]. In fact, theoretical models presented the advantages of hydrogen functionalities on gold electrodes,

18

promoting the stability of the conduction channels through the nucleotides based on hydrogen-hydrogen interaction[105]. Additionally, the weak bond slows the translocation of the DNA strands through the gap. A similar approach is proposed in graphene, where the controlled chemistry of the edges would stabilize the interactions dynamics between the molecule and the nanogap.

Nonetheless, there is no experimental evidence of DNA sequencing using nanogaps. First, the only current technology available for nanogap sequencing is based on molecular break junctions forming gold atomic contacts[103,106,107]. The resulting gold electrodes lack the atomic thickness of graphene and introduce multiple binding sites for DNA strands, preventing the correct single nucleotide analysis, as explained in Chapter 4. Additionally, the state of the art is the use of supported graphene nanogap, which lack a fluidic system capable of transporting the analytes, introducing a hindering factor for molecular characterization, particularly for sequencing applications.

In Chapter 4, the first dynamic tunnelling junction between independently supported graphene edge electrodes is presented. The formation of a gap between independently supported graphene films interfaced with sub nanometric precision is the first step toward the integration of graphene nanogaps into fluidic systems capable of driving molecules to be directly probed by tunnelling currents. The aim of these experiments is the assessment of a sensing platform able to probe directly the molecules transmigrating through the pore, rather than their influence on the surroundings (as it is in conventional nanopore experimental design). Our results also represent a promising proof of concept for the design of graphene nanogaps integrated into supportive nanopores/nanofluidics architectures. The layered structure of the zero-depth nanopore capillaries (Chapter 7) allows the embodiment of graphene films further converted into independent electrodes reciprocally interfaced across the rim of a pore.

1.2   Aim and outline

In this thesis, we demonstrate unconventional fabrication protocols which differentiate from conventional techniques such as lithography. Particularly, Chapter 2 reports a thorough literature study concerning the state of the art in graphene fabrications toward the selective chemical functionalization of graphene edges. Starting from the literature results, we explored a wide series of

experimental approaches toward the fabrication of graphene bio-sensors with chemically controlled edges, comprising nanopores, nanoribbons and nanogaps architectures. In fact, at the present stage, most of the difficulties relate to extremely complicated fabrication approaches, often based on high resolution electron microscopy or lithography, which severely limits the wide spread of graphene based devices, and the control of the (edge) chemistry.

Accordingly, we investigated the fabrication of edges in graphene, their chemical functionalization and their use as active components at the atomic scale for sensing applications. Particularly, in Chapter 3, microtomy was employed to prepare edges in a graphene transistor embedded in a polymer scaffold, first demonstrating their selective chemical functionalization via bulk methods such as electrografting. In Chapter 4, the first dynamic tunnelling junction between two single carbon atoms at the edge of graphene was prepared via reactive ion etching of a suspended graphene sheet. In Chapter 5, graphene nanoribbons with selectively functionalized edges were formed under the shadowing of a metallic nanorod obtained via microtomy – so called inert mask lithography.

Flexible, unconventional fabrications were employed also in metallic and polymeric materials. Particularly, in Chapter 6 multilayered polyelectrolytes were deposited via Layer-by-Layer deposition between two large area gold films further processed via microtomy into transverse nanogaps between nanorod electrodes. Furthermore, in Chapter 7, we propose a platform that will allow for the first time the integration of graphene electrodes directly within a nanopore, here a nanopore of zero-depth.

Importantly, in our research we tried to preserve the physical integrity of graphene while controlling the chemistry at its edges, with the goal of fabricating reproducible and selective sensors. In this quest, we achieved for the first time the electrochemical functionalization of the edge of a large area graphene monolayer. We overcome the requirements of atomic scale characterizations, clean rooms, and complex designs, targeting a single line of carbon atoms performing experiments at the macroscopic scale and with simple tools available in almost any chemical laboratory.

1.3   References

(1)   Castro Neto, a. H.; Peres, N. M. R.; Novoselov, K. S.; Geim, a. K. *Rev. Mod. Phys.* **2009**, *81* (1), 109–162.

(2)   Georgakilas, V.; Otyepka, M.; Bourlinos, A. B.; Chandra, V.; Kim, N.; Kemp, K. C.; Hobza, P.; Zboril, R.; Kim, K. S. *Chem. Rev.* **2012**, *112* (11), 6156–6214.

(3)   Enoki, T.; Andō, T. *Physics and chemistry of graphene : graphene to nanographene, CRC Press,* **2013**.

(4)   Schwierz, F. *Nat. Nanotechnol.* **2010**, *5* (7), 487.

(5)   Jiang, D.; Chen, Z. *Graphene Chemistry: Theoretical Perspectives*; Wiley, **2013**.

(6)   Baldoni, M.; Sgamellotti, A.; Mercuri, F. *Chem. Phys. Lett.* **2008**, *464* (4–6), 202–207.

(7)   Lu, Y. H.; Wu, R. Q.; Shen, L.; Yang, M.; Sha, Z. D.; Cai, Y. Q.; He, P. M.; Feng, Y. P. *Appl. Phys. Lett.* **2009**, *94* (12), 122111.

(8)   Simbeck, A. J.; Gu, D.; Kharche, N.; Satyam, P. V.; Avouris, P.; Nayak, S. K. *Phys. Rev. B* **2013**, *88* (3), 35413.

(9)   Ohtsuka, M.; Fujii, S.; Kiguchi, M.; Enoki, T. *ACS Nano* **2013**, *7* (8), 6868–6874.

(10)   Cervantes-Sodi, F.; Csányi, G.; Piscanec, S.; Ferrari, A. *Phys. Rev. B* **2008**, *77* (16), 165427.

(11)   Lee, G.; Cho, K. *Phys. Rev. B* **2009**, *79* (16), 165440.

(12)   Hod, O.; Barone, V.; Peralta, J. E.; Scuseria, G. E. *Nano Lett.* **2007**, *7* (8), 2295–2299.

(13)   Radovic, L. R.; Bockrath, B. *J. Am. Chem. Soc.* **2005**, *127* (16), 5917–5927.

(14)   Seitsonen, A. P.; Saitta, a. M.; Wassmann, T.; Lazzeri, M.; Mauri, F. *Phys. Rev. B* **2010**, *82* (11), 115425.

(15)   Jiang, D.; Sumpter, B. G.; Dai, S. *J. Chem. Phys.* **2007**, *126* (13), 134701.

(16)   Qi, Z. J.; Rodríguez-Manzo, J. A.; Botello-Méndez, A. R.; Hong, S. J.; Stach, E.

A.; Park, Y. W.; Charlier, J.-C.; Drndić, M.; Johnson, A. T. C. *Nano Lett.* **2014**, *14* (8), 4238–4244.

(17)   Heerema, S. J.; Dekker, C. *Nat. Nanotechnol.* **2016**, *11* (2), 127–136.

(18)   Zhan, B.; Li, C.; Yang, J.; Jenkins, G.; Huang, W.; Dong, X. *Small* **2014**, *10* (20).

(19)   Cai, J.; Ruffieux, P.; Jaafar, R.; Bieri, M.; Braun, T.; Blankenburg, S.; Fasel, R.; Muoth, M.; Seitsonen, A. P.; Saleh, M.; Feng, X.; Mu, K.; Müllen, K. *Nature* **2010**, *466* (7305), 470–473.

(20)   Xu, W.; Lee, T.-W. *Mater. Horizons* **2016**, *3* (3), 186–207.

(21)   Yu, W. J.; Chae, S. H.; Perello, D.; Lee, S. Y.; Han, G. H.; Yun, M.; Lee, Y. H. *ACS Nano* **2010**, *4* (9), 5480–5486.

(22)   Kato, T.; Hatakeyama, R. *Nat. Nanotechnol.* **2012**, *7* (10), 651–656.

(23)   Zhang, Y.; Kim, P.; Han, M. Y.; Barbaros, O.; Özyilmaz, B.; Zhang, Y.; Kim, P. *Phys. Rev. Lett.* **2007**, *98* (20), 206805.

(24)   Zhang, Y.; Tan, Y.-W.; Stormer, H. L.; Kim, P. *Nature* **2005**, *438* (7065), 201–204.

(25)   Wang, H. M.; Zheng, Z.; Wang, Y. Y.; Qiu, J. J.; Guo, Z. B.; Shen, Z. X.; Yu, T. *Appl. Phys. Lett.* **2010**, *96* (2), 23106.

(26)   Ullmann, K.; Coto, P. B.; Leitherer, S.; Molina-Ontoria, A.; MartIn, N.; Thoss, M.; Weber, H. B. *Nano Lett.* **2015**, *15* (5), 3512–3518.

(27)   Bellunato, A.; Arjmandi Tash, H.; Cesa, Y.; Schneider, G. F. *ChemPhysChem* **2016**, *17* (6), 785–801.

(28)   Smith, B. W.; Luzzi, D. E. *J. Appl. Phys.* **2001**, *90* (7), 3509.

(29)   Girit, C. O.; Meyer, J. C.; Erni, R.; Rossell, M. D.; Kisielowski, C.; Yang, L.; Park, C.-H.; Crommie, M. F.; Cohen, M. L.; Louie, S. G.; Zettl, A. *Science.* **2009**, *323* (5922), 1705–1708.

(30)   Qi, Z. J.; Rodríguez-Manzo, J. a; Botello-Méndez, A. R.; Hong, S. J.; Stach, E. a; Park, Y. W.; Charlier, J.-C.; Drndić, M.; Johnson, a T. C. *Nano Lett.* **2014**.

(31)   Schneider, G. F.; Kowalczyk, S. W.; Calado, V. E.; Pandraud, G.; Zandbergen, H. W.; Vandersypen, L. M. K.; Dekker, C. *Nano Lett.* **2010**, *10* (8), 3163–3167.

(32)   Fischbein, M. D.; Drndić, M. *Appl. Phys. Lett.* **2008**, *93* (11), 113107.

(33)   Merchant, C. A.; Healy, K.; Wanunu, M.; Ray, V.; Peterman, N.; Bartel, J.; Fischbein, M. D.; Venta, K.; Luo, Z.; Johnson, A. T. C.; Drndić, M.; et al. *Nano Lett.* **2010**, *10* (8), 2915–2921.

(34)   Garaj, S.; Hubbard, W.; Reina, A.; Kong, J.; Branton, D.; Golovchenko, J. a. *Nature* **2010**, *467* (7312), 190–193.

(35)   Traversi, F.; Raillon, C.; Benameur, S. M.; Liu, K.; Khlybov, S.; Tosun, M.; Krasnozhon, D.; Kis, A.; Radenovic, A. *Nat. Nanotechnol.* **2013**, *8* (12), 939–945.

(36)   Liu, K.; Feng, J.; Kis, A.; Radenovic, A. *ACS Nano* **2014**, *8* (3), 2504–2511.

(37)   Liu, S.; Lu, B.; Zhao, Q.; Li, J.; Gao, T.; Chen, Y.; Zhang, Y.; Liu, Z.; Fan, Z.; Yang, F.; You, L.; Yu, D. *Adv. Mater.* **2013**, *25*, 4549–4554.

(38)   Schneider, F.; Houben, L.; Malladi, S. K.; Dekker, C.; Xu, Q.; Wu, M.-Y.; Schneider, G. F.; Houben, L.; Malladi, S. K.; Dekker, C.; Yucelen, E.; Dunin-Borkowski, R. E.; Zandbergen, H. W. *ACS Nano* **2013**, *7* (2), 1566–1572.

(39)   Xu, Q.; Rioux, R. M.; Dickey, M. D.; Whitesides, G. M. *Acc. Chem. Res.* **2008**, *41* (12), 1566–1577.

(40)   Oomen, P. E.; Zhang, Y.; Chiechi, R. C.; Verpoorte, E.; Mathwig, K. *Lab Chip* **2018**.

(41)   Lipomi, D. J.; Martinez, R. V; Rioux, R. M.; Cademartiri, L.; Reus, W. F.; Whitesides, G. M. *ACS Appl. Mater. Interfaces* **2010**, *2* (9), 2503–2514.

(42)   Arjmandi-Tash, H.; Bellunato, A.; Wen, C.; Olsthoorn, R. C.; Scheicher, R. H.; Zhang, S.-L.; Schneider, G. F. *Adv. Mater.* **2017**, 1703602.

(43)   Schedin, F.; Geim, a K.; Morozov, S. V; Hill, E. W.; Blake, P.; Katsnelson, M. I.; Novoselov, K. S.; F. Schedin A.K. Geim, S. V. M. E. W. H. P. B. M. I. K. & K. S. N. *Nat. Mater.* **2007**, *6* (9), 652–655.

(44)   Liu, Y.; Dong, X.; Chen, P. *Chem. Soc. Rev.* **2012**, *41* (6), 2283–2307.

(45)   Morales-Narváez, E.; Baptista-Pires, L.; Zamora-Gálvez, A.; Merkoçi, A. *Adv. Mater.* **2017**, *29* (7), 1604905.

(46)   Drndić, M. *Nat. Nanotechnol.* **2014**, *9* (10), 743.

(47)   Edel, J. B.; Albrecht, T. *Engineered Nanopores for Bioanalytical Applications*;
          William Andrew, 2013.

(48)   Deamer, D. W.; Akeson, M. *Trends Biotechnol.* **2000**, *18* (4), 147–151.

(49)   Schneider, G. F.; Dekker, C. *Nat. Biotechnol.* **2012**, *30* (4), 326–328.

(50)   Garaj, S.; Liu, S.; Golovchenko, J. A.; Branton, D. *Proc. Natl. Acad. Sci. U. S.
          A.* **2013**, *110* (30), 12192–12196.

(51)   Deamer, D. *Annu. Rev. Biophys.* **2010**, *39* (1), 79–90.

(52)   Lieberman, K. R.; Cherf, G. M.; Doody, M. J.; Olasagasti, F.; Kolodji, Y.;
          Akeson, M. *J. Am. Chem. Soc.* **2010**, *132* (50), 17961–17972.

(53)   Cockroft, S. L.; Chu, J.; Amorin, M.; Ghadiri, M. R. *J. Am. Chem. Soc.* **2008**,
          130 (3), 818–820.

(54)   Sánchez-Quesada, J.; Saghatelian, A.; Cheley, S.; Bayley, H.; Ghadiri, M. R.
          Angew. Chemie Int. Ed. **2004**, *43* (23), 3063–3067.

(55)   Jain, M.; Koren, S.; Miga, K. H.; Quick, J.; Rand, A. C.; Sasani, T. A.; Tyson, J.
          R.; Beggs, A. D.; Dilthey, A. T.; Fiddes, I. T.; Malla, S.; Marriott, H.; Nieto, T.;
          O'Grady, J.; Olsen, H. E.; Pedersen, B. S.; Rhie, A.; Richardson, H.; Quinlan,
          A. R.; Snutch, T. P.; Tee, L.; Paten, B.; Phillippy, A. M.; Simpson, J. T.; Loman,
          N. J.; Loose, M. *Nat. Biotechnol.* **2018**, *36* (4), 338–345.

(56)   Rang, F. J.; Kloosterman, W. P.; de Ridder, J. *Genome Biol.* **2018**, *19* (1), 90.

(57)   Jansen, H. J.; Liem, M.; Jong-Raadsen, S. A.; Dufour, S.; Weltzien, F.-A.;
          Swinkels, W.; Koelewijn, A.; Palstra, A. P.; Pelster, B.; Spaink, H. P.; den
          Thillart, G. E.; Dirks, R. P.; Henkel, C. V. *bioRxiv* **2017**.

(58)   Venkatesan, B. M.; Bashir, R. *Nat. Nanotechnol.* **2011**, *6* (10), 615–624.

(59)   Arjmandi-Tash, H.; Belyaeva, L. A.; Schneider, G. F. *Chem. Soc. Rev.* **2015**, *45*
          (3), 476–493.

(60)   Wanunu, M. *Phys. Life Rev.* **2012**, *9* (2), 125–158.

(61)   Heerema, S. J.; Schneider, G. F.; Rozemuller, M.; Vicarelli, L.; Zandbergen,
          H. W.; Dekker, C. *Nanotechnology* **2015**, *26* (7), 74001.

(62)   Kumar, A.; Park, K.-B.; Kim, H.-M.; Kim, K.-B. *Nanotechnology* **2013**, *24* (49),

495503.

(63)   Hall, J. R. *J. Gen. Physiol.* **1975**, *66* (2), 531–532.

(64)   Wells, D. B.; Belkin, M.; Comer, J.; Aksimentiev, A. *Nano Lett.* **2012**, *12* (8), 4117–4123.

(65)   Sathe, C.; Zou, X.; Leburton, J.-P.; Schulten, K. *ACS Nano* **2011**, *5* (11), 8842–8851.

(66)   Kowalczyk, S. W.; Wells, D. B.; Aksimentiev, A.; Dekker, C. *Nano Lett.* **2012**, *12* (2), 1038–1044.

(67)   Schneider, G. F.; Xu, Q.; Hage, S.; Luik, S.; Spoor, J. N. H.; Malladi, S.; Zandbergen, H.; Dekker, C. *Nat. Commun.* **2013**, *4*, 2619.

(68)   He, Q.; Wu, S.; Yin, Z.; Zhang, H. *Chem. Sci.* **2012**, *3* (6), 1764.

(69)   Novoselov, K. S.; Geim, A. K.; Morozov, S. V; Jiang, D.; Zhang, Y.; Dubonos, S. V; Grigorieva, I. V; Firsov, A. A. *Science* **2004**, *306* (5696), 666–669.

(70)   Geim, A. K.; Novoselov, K. S. *Nat. Mater.* **2007**, *6*, 183.

(71)   Das Sarma, S.; Adam, S.; Hwang, E. H.; Rossi, E. *Rev. Mod. Phys.* **2011**, *83* (2), 407–470.

(72)   Fu, W.; Jiang, L.; van Geest, E. P.; Lima, L. M. C.; Schneider, G. F. *Adv. Mater.* **2017**, *29* (6), 1603610.

(73)   Bekyarova, E.; Itkis, M. E.; Ramesh, P.; Berger, C.; Sprinkle, M.; de Heer, W. A.; Haddon, R. C. *J. Am. Chem. Soc.* **2009**, *131* (4), 1336–1337.

(74)   Koehler, F. M.; Luechinger, N. A.; Ziegler, D.; Athanassiou, E. K.; Grass, R. N.; Rossi, A.; Hierold, C.; Stemmer, A.; Stark, W. J. *Angew. Chemie Int. Ed.* **2009**, *48* (1), 224–227.

(75)   Fu, W.; Nef, C.; Knopfmacher, O.; Tarasov, A.; Weiss, M.; Calame, M.; Schönenberger, C.; Schönenberger, C. *Nano Lett.* **2011**, *11* (9), 3597–3600.

(76)   Zhang, Z.; Huang, H.; Yang, X.; Zang, L. *J. Phys. Chem. Lett.* **2011**, *2* (22), 2897–2905.

(77)   Katoch, J.; Kim, S. N.; Kuang, Z.; Farmer, B. L.; Naik, R. R.; Tatulian, S. A.; Ishigami, M. *Nano Lett.* **2012**, *12* (5), 2342–2346.

(78) Cui, Y.; Kim, S. N.; Jones, S. E.; Wissler, L. L.; Naik, R. R.; McAlpine, M. C. *Nano Lett.* **2010**, *10* (11), 4559–4565.

(79) Sun, J.; Muruganathan, M.; Mizuta, H. *Sci. Adv.* **2016**, *2* (4), e1501518–e1501518.

(80) Fu, W.; Feng, L.; Panaitov, G.; Kireev, D.; Mayer, D.; Offenhäusser, A.; Krause, H. J. *Sci. Adv.* **2017**, *3* (10), e1701247.

(81) Fu, W.; Nef, C.; Knopfmacher, O.; Tarasov, A.; Weiss, M.; Calame, M.; Schönenberger, C. *Nano Lett.* **2011**, *11* (9), 3597–3600.

(82) Aguilella, V. M.; Pellicer, J.; Aguilella-Arzo, M. *Langmuir* **1999**, *15* (19), 6156–6162.

(83) Bockris, J. O.; Gileadi, E.; Müller, K. *J. Chem. Phys.* **1966**, *44* (4), 1445–1456.

(84) Sinitskii, A.; Dimiev, A.; Corley, D. A.; Fursina, A. A.; Kosynkin, D. V; Tour, J. M. *ACS Nano* **2010**, *4* (4), 1949–1954.

(85) Niyogi, S.; Bekyarova, E.; Itkis, M. E.; Zhang, H.; Shepperd, K.; Hicks, J.; Sprinkle, M.; Berger, C.; Lau, C. N.; deHeer, W. A.; Conrad, E. H.; Haddon, R. C. *Nano Lett.* **2010**, *10* (10), 4061–4066.

(86) Yan, F.; Zhang, M.; Li, J. *Adv. Healthc. Mater.* **2014**, *3* (3), 313–331.

(87) Dong, X.; Shi, Y.; Huang, W.; Chen, P.; Li, L.-J. *Adv. Mater.* **2010**, *22* (14), 1649–1653.

(88) Mohanty, N.; Berry, V. *Nano Lett.* **2008**, *8* (12), 4469–4476.

(89) Xu, G.; Abbott, J.; Qin, L.; Yeung, K. Y. M.; Song, Y.; Yoon, H.; Kong, J.; Ham, D. *Nat. Commun.* **2014**, *5*, 4866.

(90) Dontschuk, N.; Stacey, A.; Tadich, A.; Rietwyk, K. J.; Schenk, A.; Edmonds, M. T.; Shimoni, O.; Pakes, C. I.; Prawer, S.; Cervenka, J. *Nat. Commun.* **2015**, *6*, 6563.

(91) Paulechka, E.; Wassenaar, T. A.; Kroenlein, K.; Kazakov, A.; Smolyanitsky, A. *Nanoscale* **2016**, *8* (4), 1861–1867.

(92) Min, S. K.; Kim, W. Y.; Cho, Y.; Kim, K. S. *Nat. Nanotechnol.* **2011**, *6* (3), 162–165.

26

(93)   Heerema, S. J.; Vicarelli, L.; Pud, S.; Schouten, R. N.; Zandbergen, H. W.; Dekker, C. *ACS Nano* **2018**, *12* (3), acsnano.7b08635.

(94)   Zhang, P. *Sci. Rep.* **2015**, *5* (1), 9826.

(95)   Reed, M. A. *Science* **1997**, *278* (5336), 252–254.

(96)   Girdhar, A.; Sathe, C.; Schulten, K.; Leburton, J.-P. *Proc. Natl. Acad. Sci. U. S. A.* **2013**, *110* (42), 16748–16753.

(97)   Isaeva, O. G.; Katkov, V. L.; Osipov, V. A. *Eur. Phys. J. B* **2014**, *87* (11), 272.

(98)   Liang, X.; Chou, S. Y. *Nano Lett.* **2008**, *8* (5), 1472–1476.

(99)   Porath, D.; Bezryadin, A.; de Vries, S.; Dekker, C. *Nature* **2000**, *403* (6770), 635–638.

(100) Postma, H. W. C. *Nano Lett.* **2010**, *10* (2), 420–425.

(101) J. Prasongkit, A. Grigoriev, B. Pathak, R. Ahuja and R. H. Scheicher *Nano Lett.*, **2011**, 11(5), 1941–1945.

(102) Tsutsui, M.; Taniguchi, M.; Yokota, K.; Kawai, T. *Nat. Nanotechnol.* **2010**, *5* (4), 286–290.

(103) Ohshiro, T.; Tsutsui, M.; Yokota, K.; Furuhashi, M.; Taniguchi, M.; Kawai, T. *Nat. Nanotechnol.* **2014**, *9* (10), 835–840.

(104) He, Y.; Scheicher, R. H.; Grigoriev, A.; Ahuja, R.; Long, S.; Huo, Z.; Liu, M. *Adv. Funct. Mater.* **2011**, *21* (14), 2674–2679.

(105) He, H.; Scheicher, R. H.; Pandey, R.; Rocha, A. R.; Sanvito, S.; Grigoriev, A.; Ahuja, R.; Kama, S. P. *J. Phys. Chem. C* **2008**, *112* (10), 3456–3459.

(106) Tsutsui, M.; Taniguchi, M.; Kawai, T. *Appl. Phys. Lett.* **2008**, *93* (16), 163115.

(107) Huang, S.; He, J.; Chang, S.; Zhang, P.; Liang, F.; Li, S.; Tuchband, M.; Fuhrmann, A.; Ros, R.; Lindsay, S. *Nat. Nanotechnol.* **2010**, *5* (12), 868–873.

CHAPTER 2

Chemistry at the Edge of Graphene

The selective functionalization of graphene edges is driven by the chemical reactivity of its carbon atoms. The chemical reactivity of an edge, as an interruption of the honeycomb lattice of graphene, differs from the relative inertness of the basal plane. In fact, the unsaturation of the p_z orbitals and the break of the π conjugation on an edge increase the energy of the electrons at the edge sites, leading to specific chemical reactivity and electronic properties. Given the relevance of the chemistry at the edges on many aspects of graphene, the present review investigates the processes and mechanisms that drive the chemical functionalization of graphene at the edges. Focus is given to the selective chemical functionalization of graphene edges from theoretical and experimental perspectives, with a particular focus on the characterization tools available to characterize graphene edge chemistry.

2.1   Introduction

Graphene is an allotrope of carbon with a two-dimensional, atomically thin, honeycomb structure[1]. The 2s, $2p_x$ and $2p_y$ orbitals from each carbon atom in the graphene lattice hybridize into three sp^2 orbitals, each developing a σ bond with an adjacent carbon atom. The remaining un-hybridized p_z orbitals – perpendicular to the graphene lattice – form a conjugated π bond network in which the delocalized electrons are responsible for the electronic properties of graphene, such as a transport velocity only three hundred times lower than the speed of light[2] and the extraordinary high charge carrier mobility[3].

Breaking the aromaticity of the honeycomb lattice – for example by creating edges – alters the properties of graphene[4] and, depending on the crystallographic orientation of the lattice, two types of edges are observed: zig-zag and armchair edges[5], each characterized by specific chemical reactivity and electronic properties.

The chemical reactivity of the carbon atoms localized on a graphene edge differs from the relative inertness of the basal plane[6]. Broken σ bonds at the edges develop radical groups with accessible and highly active electrons. The conjugation system is different on a zig-zag edge compared to an armchair edge, yielding significant discrepancies in reactivity[7,8].

Furthermore, depending on the chemical properties of the group grafted on the edge, *p* or *n* doping can be promoted, leading to the modulation of the electrical conductivity of graphene. Local defects in the graphene lattice (such as dislocations or imperfections) can also be considered as edges as they define a termination of the conjugated honeycomb network[7,9,10].

Edges form during the exfoliation of graphene from graphite[11] as well as during the chemical growth of graphene sheets[12], or as a result of mechanical and chemical processes such as ionic bombardment, and reactive etching of the basal plane, to name a few[13]. Forming a crystalline edge with a predefined orientation (i.e., zig-zag or armchair) is particularly important in order to specifically address the chemical reactivity of graphene. Thus, the ability to distinguish the edge from the basal plane is crucial to characterize the edge. Several techniques are employed to

do so, for example scanning tunnelling microscopy[4,14], Raman spectroscopy[10,15,16] and high resolution electron microscopy[17–19].

The presence of edges and defects in graphene promote new possibilities to tailor the chemistry of graphene with additional implications on the physical and electrical properties of graphene. Considering the rapidly growing interests in the field, this review aims to provide an overview over the most appealing topics concerning the edges of graphene and their chemistry.

2.2 Chemical reactivity of graphene edges

An edge in graphene forms following the breaking of σ bonds between adjacent carbon atoms and of the π conjugation network. Depending on the orientation of the edge along the honeycomb structure, two configurations arise: namely the zig-zag and the armchair edges (Figure 2.1a). An edge, however, typically does not develop along a unique crystallographic direction and leads to more complex geometries often with alternated zig-zag and armchair segments known as "chiral edge"[20].

In absence of reactants (i.e. in ideal vacuum), the atoms on the edges are di-radicals observed as metastable σ and π dangling bonds[8,21–23] with unsaturated sp^2 and p_z orbitals[24]. Dangling bonds can develop during the edge formation. They are unstable and difficult to observe. In fact, for instance, the electrons of an armchair edge could reduce their energy by establishing a triple bond between the outer carbon atoms[24]. On a zig-zag edge, instead, the p_z electrons are confined on each outer carbon atom and maintain a radical singlet configuration responsible of the so called "edge state"[25–28], Figure 2.1a. Consequently, zig-zag edges are very energetic and the planar reconstruction of six-fold benzene rings to pentagonal or heptagonal structures often occurs to lower their energy[28]. The atomic structure of the edges determines the presence of specific electronic distributions that affect the energy states of the atoms on the edges and, consequently, their chemistry.

Graphene can be represented as a polycyclic aromatic hydrocarbon (PAH) built by translation of a hexagonal unit cell of benzene (C_6H_6). Interestingly, the chemical reactivity of graphene can be expressed from the aromaticity of its PAH representation. For a cyclic hydrocarbon such as benzene, a ring deriving from the overlap of the resonant structures of the molecule and representing the

delocalization of the π electrons between the unsaturated sp^2 carbon atoms best represents the aromaticity. The most stable structure of a PAH molecule is the one maximizing the number of aromatic rings among its unit cells (known as Clar's structure).
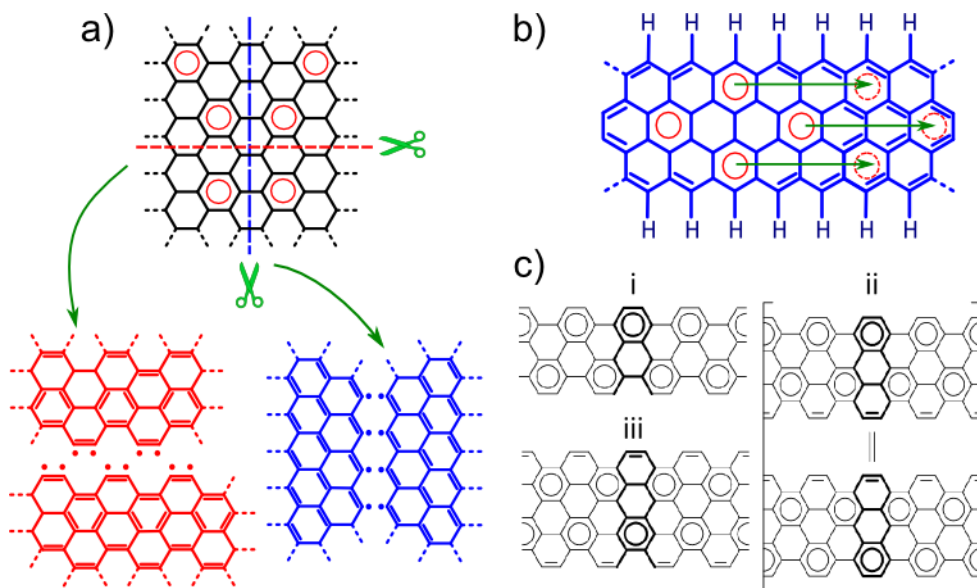

Figure 2.1. The edges of graphene. a) Formation of edges in graphene by cutting along the two crystallographic directions: blue) zig-zag edges and the singlet radical bond; red) armchair edges and rearrangement of radicals into triple bonds. b) Chemical structure of a graphene nanoribbon with zig-zag edges. The green arrows depict the isomeric structures obtained by sliding the position of the aromatic rings across the ribbon[29]. c) Armchair graphene ribbons. The number of isomeric structures and the presence of localized double bonds depend on the width n of the graphene. (i) has a unique isomeric structure, while (iii) has a unique isomeric structure with double bonds localized at the edges. (ii) has localized double bonds on the edges and more than one resonant structure[30].

Similarly, the aromaticity of the graphene[31], and particularly its reactivity at the edge can also be defined by the overlap of the different isomeric Clar's structures. Importantly, the edge geometry influences the aromaticity of graphene as shown in Figure 2.1b-c. For a semi-infinite zig-zag ribbon three hexagons wide (Figure 2.1b), the zig-zag geometry promotes infinite isomeric Clar structures, primarily because aromatic rings can slide along the length of the ribbons, highlighting the intrinsic reactivity of the molecule[32]. Independently from their width, zig-zag graphene ribbon can not be represented with a fully benzenoid structure. Thus,

the graphene aromaticity is in balance between the aromatic ring along its lattice and the highly reactive localized double bonds present on the edge. A semi-infinite armchair graphene ribbon, however, shows a limited number of Clar's formulas independently of the width of the structure indicating a lower chemical reactivity (Figure 2.1c). In fact, the width of the ribbon also influences the overall aromaticity of the graphene molecule and therefore its subsequent chemical reactivity. For example, PAH (i) and (iii) have a unique resonant structure regardless of the different width, but while (i) is fully benzenoid with no localized double bonds, (iii) is defined as a Kekule molecule, without a fully benzenoid structure and with reactive double bonds localized on the edges. The molecule (ii), however, can be divided in a fully benzenoid molecule connected to a strip of non-aromatic hexagons with double bonds localized on the edges. The two resonant structures imply two configurations with the double bonds localized on the opposite sides of the molecule (Figure 2.1c, (ii)), revealing a chemical reactivity comprised between a benzenoid system and localized double bonds[30]. In conclusion, the chemical reactivity of the edges of (ii) is expected to be lower than (iii), even in presence of multiple resonant structures. In fact, the edges of (iii) present reactive localized double bonds, while the reactivity of the edges of (ii) is modulated by a resonant structure with an aromaticity extended up to the edges.

The difference between zig-zag and armchair graphene nanostructures is therefore that zig-zag edged molecules are incompatible with a fully benzenoid graphene molecule and are expected to present localized double bonds. For armchair graphene molecules, however, the reactivity is modulated by the probability of having either an aromatic ring or localized double bonds on its edges.

The Clar's representation of graphene is therefore a simple and effective method to link the edge configuration with the reactivity of a particular graphene molecule. The specific reactivity of the edges is modulated by the probability of finding a localized double bond at the edge.

In most PAH representations, molecules are mono-hydrogenated at the edge. To what extend does the aromaticity and/or the edge structure impact the reactivity of that particular C-H is still poorly understood for graphene. Thermodynamics say that the conversion of C-H into a functional group is determined by the variation of the free energy of the system upon functionalization, which requires to consider

external factors such as the chemical activity of the functional group and the specific chemistry of the carbon atoms in proximity[33]. So, in chemically complex environments it is difficult to foresee the specific chemical functionalization of the edges at the atomic scale, because of the many possible combinations that can satisfy the thermodynamic criteria of the functionalization[34]. Nevertheless, simple systems like graphene exposed to H_2 have been modelled. Thermodynamically, the hydrogenation of the edges is driven by the chemical potential of the molecular hydrogen, μ_{H2} and the energy of the system tends to decrease with a higher density of hydrogen functionalities on the edges. Consequently, at standard conditions of pressure and temperature, zig-zag graphene tends to acquire a particular configuration known as ZZ(211), Figure 2.2a. Practically, it leads to a semi-benzenoid configuration which limits the amount of double bonds on the edges, according to the corresponding Clar representation[29].

In conclusion, Clar's structures represent well the break of the lattice symmetry induced by an edge according to the probability of finding a localized double bond. Tuning precisely the geometry and the specific chemistry of an edge in formation is, however, still a difficult exercise in practice.
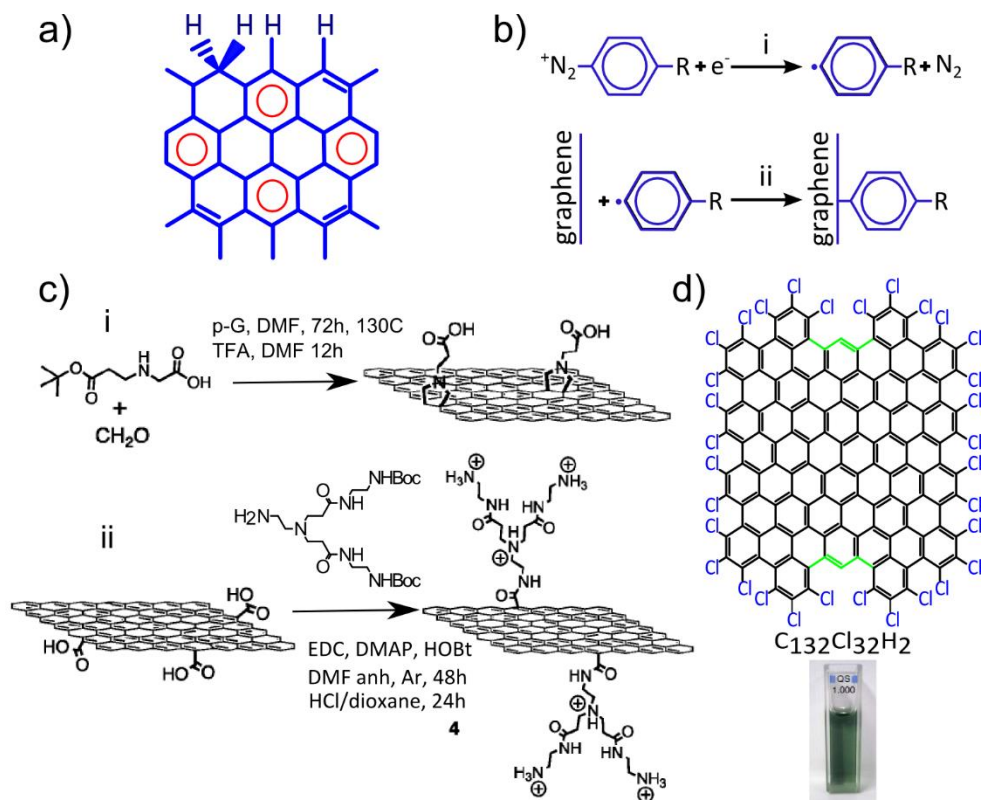
Figure 2.2. Functionalized edges. a) zz(2,1,1) edge configuration of a zig-zag edge. b) Chemical reaction scheme of an aryl-diazonium salt onto graphene[35]. The reaction proceeds in two steps: the electrophilic salt dissociates to form N_2 and an aryl radical (i). The reactive aryl radical binds the nucleophilic graphene (ii). c) (i) Scheme of cycloaddition on exfoliated graphene (p-G) of a molecule of paraformaldehyde conjugated with a modified alpha amino acid. (ii) Direct condensation of the dendron on the carboxyl functionalities on the edge of the pristine exfoliated graphene[36]. d) Top, Edge chlorination of nanographene (PAH systems). The functionalization is influenced by the topography of the molecule, gulf regions are not functionalized because of steric hindrance effects[37]. Bottom, edge chlorinated graphene dispersion in toluene.

2.3   Chemical functionalization of graphene edges

Organic chemistry allows the design of peculiar edge terminations that are known to modulate the physical properties of graphene without severely altering the aromatic structure of the basal plane[38]. While edge functionalization has primarily been investigated in liquid-based exfoliation procedures, recent electron beam

methods yielding crystalline graphene edges suggest new research routes to selectively functionalize graphene edges.

2.3.1 Liquid-based functionalization of graphene edges

Two main approaches were proposed to achieve the selective functionalization of graphene edges in solution. In a first approach, edge functionalized graphene flakes were fabricated by exfoliating graphite using organic reactions such as diazonium electrografting, 1-3 dipolar cyclo-addition and Friedel-Crafts acylation, which are well known organic reactions used to functionalize graphene[39]. For example, the acylation of graphite using poly (phosphoric acid) (PPA) and phosphorous pentoxide (P_2O_5) in presence of 4-aminobenzoic acid resulted in 4-amino-benzoyl-functionalized graphite[40]. The acylation typically proceeds through electrophilic substitution at the sp^2 C-H atoms located mainly at the edges[41]. The acylation mechanism was modelled using a pyrene molecule treated in PPA/P_2O_5 with 4-(2,4,6-trimethylphenyloxy)benzamide (TMPBA). The yield of reaction and the amount of edge functionalization was determined by the number of sp^2 C-H sites available for the chemical reaction, and was further improved by the formation/activation of new edges by, for example, ball milling[42] (i.e. the bombardment of graphite with steel balls). Ball milling mechanically breaks C-C bonds within graphite layers, producing unsaturated graphene flakes with highly reactive edges[43]. By subsequently exposing the just formed edges to several reactive gas yielded various functionalizations of the edges. Hydrogen, sulphur, carboxylic acid and other functionalities have therefore been conjugated to the graphene edges, particularly to promote a better solubility of graphene flakes in organic solvents[43,44].

Similarly, diazonium chemistry on the edges of graphite was performed in order to produce highly soluble graphene dispersions[45], Figure 2.2b. The functionalization was obtained by the in-situ reaction of graphite with 4-bromophenyl radicals deriving from the dissociation of the diazonium salt in solution. The selective edge functionalization is ensured by the molecular size of the functional groups grafted at the edges. In fact, 4-bromophenyl is a bulky molecule that hardly intercalates in between graphitic layers. The functionalized graphite was then sonicated in order to exfoliate edge functionalized graphene flakes and to form a stable dispersion in DMF, achieving a solubility in the order of 10-20 µg/mL, with 70% of the flakes

thinner than five layers[45]. The diazo-chemistry has also been widely used to functionalize various other carbon allotropes such as glassy carbon[46] and highly oriented pyrolytic graphite.[47] Additionally, the reactivity of graphene edges with diazonium compounds has been probed and demonstrated to be higher than the one of the basal plane. In fact, the aryl functionalization by diazonium-salt reaction is based on the electron exchange reaction between the nucleophilic graphene and the electrophilic aryl radical forming upon N_2 dissociation. The reaction leads to the covalent functionalization and rehybridization of the edge carbon atoms from sp^2 to sp^3. In principle the reaction occurs when the density of states of the graphene overlaps the unoccupied electronic states of the aryl radical. Edges are therefore prone to be more reactive than the basal plane. Experimentally, the larger reactivity of the edges vs the basal plane towards diazonium salts has been proven by Raman spectroscopy and transport measurements[48,49].

A second approach involves the chemical functionalization of graphene flakes already exfoliated in solution. For example, 1,3 dipolar-cycloaddition in combination with amide-bond condensation was carried in order to probe whether edges are more sensitive to functionalization[36]. Two reaction schemes were proposed. First, paraformaldehyde conjugated with a modified alpha amino acid undergoes a cycloaddition reaction with graphene. The functionalized graphene was then subjected to a condensation reaction with an aminated dendron such as the one shown in Figure 2.2c (i). In a second case, pristine graphene was directly subjected to a condensation reaction with the dendron (Figure 2.2c (ii)), directly reacting with the carboxylic acid functionalities on the edges formed during the exfoliation process[50]. It has been reported that the condensation after cycloaddition yielded a functionalization degree five times higher than the direct condensation on the carboxylic groups. In fact, the cycloaddition lacks the edge selectivity and offers docking sites for the condensation reaction to happen on the edges and on the basal plane. The direct condensation on the carboxylic groups, instead, is constrained on the edges, since the carboxylic functionality develops only (almost) on the edges during the exfoliation[50].

Selective edge functionalization was also carried on chemically synthetized nano-graphene flakes[51]. PAH systems of different size and topography were chlorinated in CCl_4 at 80 °C with $AlCl_3$ as a catalyst[37]. The edge selectivity was obtained using

electrophilic substitution reactions only occurring with sp^2 C-H which are only present on the edges. Interestingly, the reaction yield is largely influenced by gulf regions which cannot be functionalized because of steric hindrance effects (Figure 2.2d, in green).

2.3.2 Direct beam lithography: chemical perspectives

Direct beam lithography uses highly focused electrons (above 80 keV) or ions (typically helium or gallium above 30 keV) to form edges by knocking out carbon atoms from the lattice or by breaking C-C bonds[52,53]. The absence of lithographic resists preserves the edges from contaminations, making direct beam lithography particularly suitable to control the chemical structure of the edges and their post functionalization[54,55].

So far, research focused on forming graphene nanoribbons primarily with the goal of opening a band-gap. Importantly, the control over the crystallinity of the resulting edges (i.e., zig-zag vs. armchair), showed a large impact on the electrical properties of ribbons, e.g. from being semi-conducting to metallic[56,57]. Adding electron donating or withdrawing group at the edge result in different doping levels[58].

Graphene edges are typically fabricated by lithography, using transmission electron microscopes (TEM) or focused ions beams (FIB)[55,59–65]. TEM sculpting at temperature up to 700°C yields graphene nanostructures which remain crystalline up to the edges, also preserving the graphene from contaminations and amorphization[66]. The absence of amorphization and defects at high temperatures suggests the presence of a self-repair mechanism, where the carbon ad-atoms (either knocked out from the lattice or originating from carbon-rich contaminations) migrate on the surface and heal the defect sites in the graphene crystal, Figure 2.3a.

The technique was further improved in the scanning transmission electron microscopy (STEM) mode of the TEM[54], where the beam of electrons is focused onto a sharp spot (d ~ 1 Å, less than an atom size) whose position is controlled with sub-nanometric precision, Figure 2.3b. High-temperature STEM is a very unique technique for sculpting graphene, atom-by-atom, and to customize the orientation of edges into zig-zag or armchair configurations.
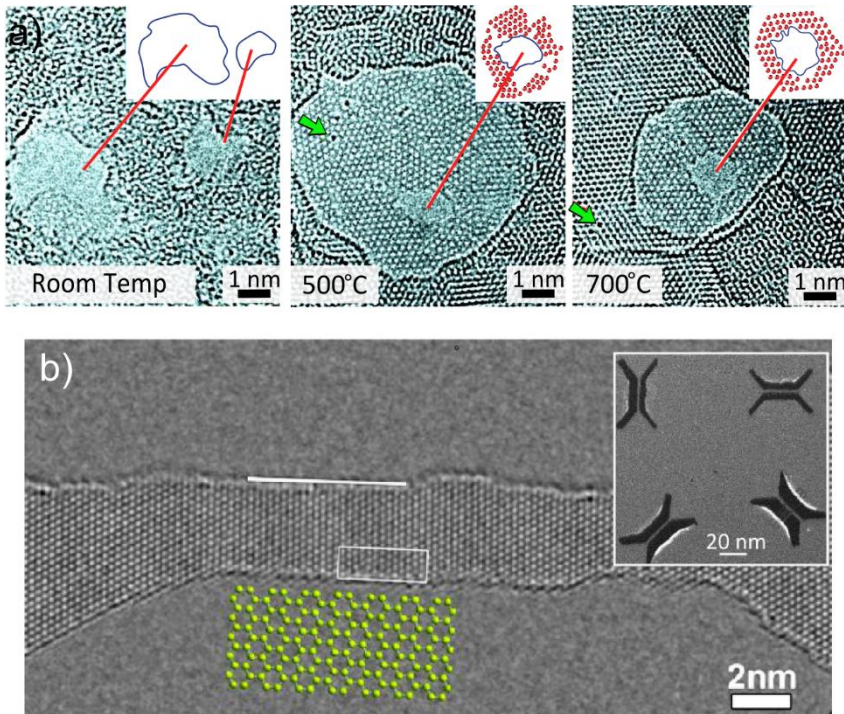
Figure 2.3. Direct beam lithography of graphene edges. a) High resolution transmission electron micrographs of few-layer graphene sculpted in the bright-field mode of a transmission electron microscope (TEM) at different specimen temperatures[66]. The estimated positions of the identifiable hexagons and location of the carbon atoms at the edge are represented by red dots and blue lines respectively (insets). The green arrows point out carbon ad-atoms trapped at defect sites. b) High resolution TEM micrographs of graphene nanoribbons sculpted by scanning transmission electron microscopy (STEM) at 600°C under a 300 kV electron beam (inset) and imaged at 80 kV[54]. Inset: sculpting of very narrow and similar rotated nanoribbons (inset) highlights the reproducibility of the high temperature STEM sculpting process.

Similarly to electrons, helium ions were also used to create edges in graphene[67]. The minor interaction of helium ions with graphene allowed the reduction of the beam size down to ~2.5 Å[68], a value comparable – but still larger – than the STEM sculpting technique[54].

2.3.3   Reactive plasma etching

Lithographic techniques are typically used in combination with reactive plasma to pattern edge-like structures in graphene[13]. The highly energetic ions and radicals

inside a plasma can interact mechanically and/or chemically with graphene. Plasma etching is a chemical reaction between the species in the plasma and the carbon atoms of the graphene, which preferentially starts from the chemically active sites on graphene, such as edges and defects[69,70].

Etching of graphene in presence of a H_2 plasma showed that the hydrogenation of the graphene preferentially occurs at the edges forming mono-hydrogenated and di-hydrogenated edges[71,72], while developing volatile CH_4 and preserving the integrity of the basal plane[69]. The thermodynamic stability of mono-hydrogenated and di-hydrogenated edges depends on the chemical activity of hydrogen. The chemical potential μ_{CH} and μ_{CH2} varies with temperature and pressure: mono-hydrogenated edges preferably form at standard conditions of T=300 K and low H_2 pressure (e.g. in air with a H_2 partial pressure in the order of 10^{-4} mbar)[73,74], while di-hydrogenation occurs at higher H_2 pressure and results in a sp^3 re-hybridization fully saturating the carbon orbitals and requiring the arrangement of the hydrogen functionalities out of the graphene plane, increasing the CH_2 configuration energy[75]. The amount of mono-hydrogenated *vs.* di-hydrogenated edges varies and is proportional to the thermodynamic stability of graphene in presence of H_2, and depends on the activity of the gas (i.e. the partial pressure of the gas and the temperature). Consequently, it was shown that the amount of CH_2 terminated edges rises proportionally with the hydrogen partial pressure at a given temperature[74].

Similarly, in presence of O_2, graphene edges get oxidized. Theory predicts that ketones and ethers are the most stable configurations[56]. The principal difference between ketones and ethers lays in the bond structure with the carbon atoms. The ketones maintain the sp^2 hybridization of the carbon atoms. The ether groups, instead, bind two carbon atoms and develop a planar configuration on both the armchair and zig-zag edges[56,76]. Similarly to the case of hydrogenation, the oxidation is driven by the chemical activity of the O_2 and the structural configuration of zig-zag or armchair edges[34]. The oxidation of the edges appears to lower the free energy of the system by maximizing the density of oxygen groups per carbon atoms, yielding to CO_2 formation, Figure 2.4a (i). Oxygenated edges most likely assume two configurations known as arm-chair O(11) and zig-zag O(11), Figure 2.4a (ii) and (iii), where each carbon atom on the edge. Zig-zag edges are prone to form cyclic ester at the edges by esterification of carboxylic groups. The

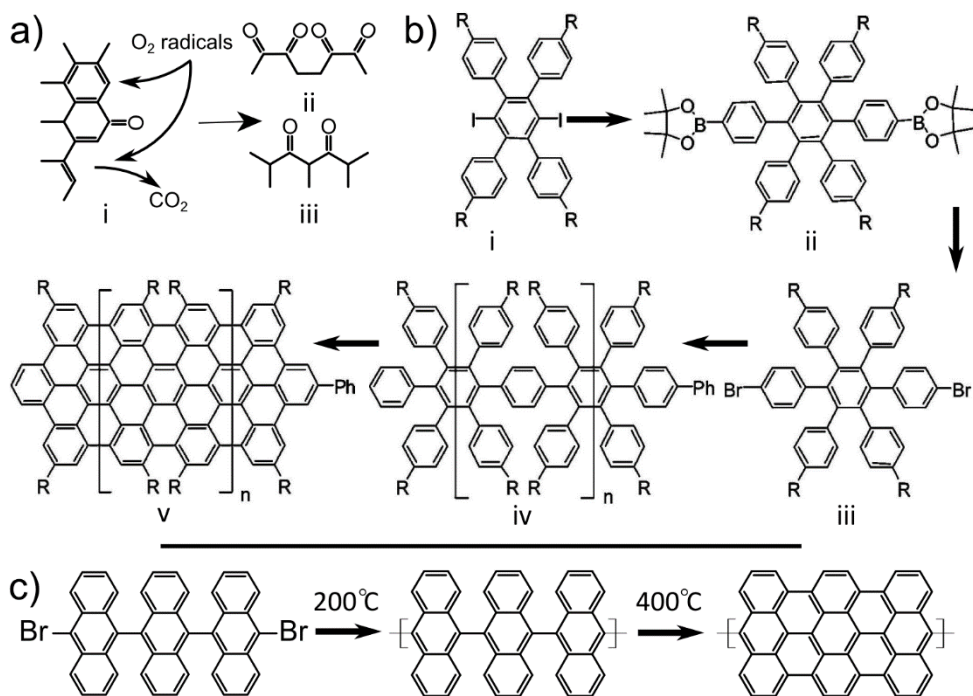process has a negative energy of formation and has been used to electrochemically functionalize edges[34,77,78].

Figure 2.4. Design and functionalization of graphene edges. a) (i) Etching and functionalization of graphene in O_2 plasma. (ii) and (iii) are the preferential functionalization configurations in presence of O_2 at equilibrium with the formation of CO_2[34]. b) Solution synthesis of graphene nanoribbons from a 1,4 tetraphenylbenzene precursor in solution[79]. c) Surface assisted synthesis of graphene nanoribbons from a bianthryl monomeric precursor[80].

Among the factors that influence the functionalization mechanisms, the steric hindrance of the functional groups or the development of a mechanical stress state can influence the functionalization. For example, theoretical models foresee hydroxyl functionality to be even more stable than oxidized or hydrogenated edges[78], even if –OH groups develop out of plane functionalities, which could lead to stress states on the graphene.

Another important edge passivation mechanism is the amination. The nitrogen chemistry is particularly interesting in some research fields such as molecular sensing[81]. Under standard conditions it is difficult to predict the most stable

configuration. In the simplest model, aromatic zig-zag edges exposed to ammonia tend to acquire specific configurations, consisting of an NH group every two mono-hydrogenated carbons. Armchair edges, instead, most likely alternate mono-hydrogenated carbons and NH_2 functionalities[34]. Thermodynamically, these configurations are the most stable, but the break of the NH_3 molecules in plasma can lead to the formation of other energetic radicals competing with the NH_2 functionalization (i.e., N˚, NH˚, and H˚ radicals). It is thus complicated to assume a unique functionalization of the edges with a single species in presence of an ammonia plasma[81–83]. Experimentally, the application of a mild NH_3 plasma yielded the functionalization of graphene edges with nitrogen atoms. With a 25 W NH_3 plasma, chemical reactions were also specifically promoted at the edge preserving the basal plane[83]. Additionally, the reactivity of the edges with ammonia, has been studied following the *n*-doping of graphene nanoribbons in presence of a NH_3 plasma[81]. Amination has been also achieved in presence of NH_3 exploiting the self-heating of graphene upon electron beam irradiation. The self-heating excites the graphene atoms and provides the energy for the functionalization reactions[82].

Reactions of graphene edges in plasmas are governed by several parameters such as the gas mixture, the partial pressure and the temperature[69], which tune the reactivity of both the plasma species and the graphene. For example, low temperature stimulates the recombination of the reactive species into molecules before reaching the graphene surface, reducing the supply of reactants. Elevated temperatures, instead, provoke a strong increase of the basal plane reactivity, yielding more uncontrollable reaction rates and the loss of the edge selectivity[69]. Similarly, the pressure as well as the power of the plasma influence the energy of the ions and radicals reaching the graphene, promoting or limiting the reaction rate and the edge selectivity.

2.3.4 Organic synthesis of functional graphene edges

The chemical synthesis (also known as "bottom-up") of nanographene via the polymerization of molecular building blocks of aromatic molecules is among the most powerful methodologies to fabricate functional graphene edges[79]. Graphene ribbons with length up to 12 nm (Figure 2.4b) were synthetized using this method, particularly using the reaction of 1,4 tetraphenylbenzene **(i)** with bromophenylboronic acid yielding a hexaphenylbenzene derivative **(ii)**. In a second

step, **(ii)** reacts with n-butyllithium and 2-isopropoxy-4,4,5,5-tetramethyl-[1,3,2]dioxaborolane to form compound **(iii)** that subsequently polymerizes producing polyphenylene **(iv)**[79]. The resulting polyphenylene undergoes a graphenization reaction[51] through de-hydrogenation, forming compound **(v)**, which is a precursor of graphene. Several routes exist to strip off the hydrogens from the precursor. One approach is the $FeCl_3$-Scholl mediated reaction[51,79] which yields graphene nanoribbons of up to 100 nm in length[84]. The functional groups R used on the outer phenyls are generally alkyl chains. In fact, long aliphatic chains reduce the aggregation tendency of the polymer (i.e. the polymerized ribbon) by preventing intermolecular π-stacking, promoting its solubility. The molecular size of the graphene precursor is crucial, as larger precursors tend be less soluble, yielding aggregation and precipitation even before the polymerization starts[51,79,84].

To overcome the aggregation tendency of the graphene in solution, surface thermal assisted polymerization has been developed[80]. The synthesis involves the adsorption of a bianthryl monomeric precursor on a metallic surface, usually Au(111), which topography and grain boundaries determine the size of the obtained graphene ribbons[51,80]. Next, a thermal annealing induces the di-radicalization of the monomer and provides the driving force for the surface diffusion of precursors leading to the polymerization. After this step, the polymer is still hydrogenated, hence the requirement for a further thermal annealing step which activates the intra-molecular cyclo-dehydrogenation and the planarization of the molecule into sp^2-bonded nanographene (Figure 2.4c). The drawback, however, is that the surface-assisted synthesis is dependent on the quality of its processing environment: it requires ultra-high vacuum (UHV) to avoid any contamination that could prominently react with the graphene in formation, hence also degrading its edges[80].

Using bottom-up approaches, the topology of the synthetic graphene is fully governed by the chemical structure of its precursor, allowing the synthesis of atomically precise graphene structures, more particularly graphene with tunable edge chemistry and geometry, which is a unique feature of the bottom-up chemical synthesis. The chemical synthesis of graphene also faces the important issue concerning the achievable size of graphene which do not yet reach the dimension obtained by mechanical exfoliation[1] or chemical vapor deposition[85].

2.3.5 Functionalization of graphene edges by anodic oxidation

Scanning tunnelling microscopy (STM) and atomic force microscopy (AFM) are the typical scanning probe microscopes employed in anodic oxidative lithography [86].

The probe (or tip) is driven over graphene in proximity of its surface. The adsorbates on the surface build a meniscus that connects the surface to the tip, providing the reactants for the anodic oxidation. The potential difference applied between the surface and the tip ignites the reaction, etching the carbon atoms of graphene and producing functional edges and volatile compounds such as CO and CO_2[87–90].

The anodic oxidation is electrochemically driven and depends on the applied bias voltage, the tip velocity, the distance between the tip and the graphene and the relative humidity in the air[91]. More precisely, STM lithography operates via tunnelling current. On a flat surface such as graphene, the tunnelling current selectively flows through the atomic features at the very top of the probe, constraining the oxidation into a narrow conductive channel on the surface of graphene and promoting the nanometric resolution[86].

AFM lithography, instead, operates without tunnelling current: the applied bias distributes from the tip to the graphene through the meniscus[92,93]. The size of the conductive channel is comparable to the size of the meniscus on the tip. As a result, AFM lithography typically achieves edges with a resolution in the order of 10-15 nm[94].

From a chemical point of view the control over the chemistry of the edge is rather complex. There is a lack of literature about the chemical composition of fresh cut edges. Incomplete oxidation processes yield graphene oxides on both the surface and the edges of graphene, particularly if the field intensity is weaker than the threshold required for the complete carbon oxidation [95].

Anodic oxidation of graphene develops carbon oxides on the patterned edges, which is generally considered as a drawback of this technique, while it can be a valuable tool to control the chemistry of the edges, especially in the perspective of post-functionalization.

2.4　Electrochemistry of graphene edges

The perturbation of the conjugation system increases the local density of states at the edges and at defects sites[96,97]. Thus, the electrochemical activity of an graphene edge is expected to be higher than the basal plane[8]. In fact, cyclic voltammograms of graphene edges show an electron transfer current up to four orders of magnitude higher than the basal plane (Figure 2.5 a,b). The square shape of the curves highlights the capacitive behaviour of graphene, with a capacitance at the edges estimated to be around $10^5 \mu F/cm^2$ in a 100 mM phosphate buffer supplemented with 100 mM KCl, and reaching a static current density around 0.1 A/cm^2 in presence of 5 mM $K_3Fe(CN)_6$ as an electrochemical probe[98]. The stronger electrochemical activity of graphene edges has also been reported in a nanopore device. For that, the graphene sheet was embedded between two insulating Al_2O_3 layers[99], Figure 2.5c. The contour length of the rim of a 5 nm diameter pore (i.e. around 30 nm) yielded an electrochemical current density higher than 12000 A/cm^2 in 1M KCl, a value more than four orders of magnitude higher than the previous experiment[98]. This has been attributed to a higher concentration of electrolyte in the solution, in combination with a more prominent convergent diffusion regime promoted by the smaller edge electrode surface[98,99]. In fact, large area electrodes (such as the surface of the graphene) operate in a regime of linear diffusion: the electrolyte approaches the electrode following a linear distribution of the molecules. Contrarily, the convergent diffusion regime strongly depends on the size of the electrode (i.e. the length of the edge), increasing the density of the electrolyte and rising the current density[98–100].

The higher electrochemical activity of graphene edges with respect to the basal plane has been the starting point for the development of a new class of redox electrodes alternative to the more conventional glassy carbon or graphite electrodes[100,101]. For example, the growth of multilayer graphene platelets lead to the formation of graphene nano-walls with preferential vertical orientation of the platelets, therefore presenting edges facing out perpendicularly to the substrate[102], and promoting electrochemical reactions specifically at the edges.

As graphene edges yield a more intense electrochemical current, they were used to oxidize dopamine, uric acid and ascorbic acid with a sensitivity sufficient to resolve, by means of CV curves, the separate oxidation peaks of the three

molecules, even when mixed together in a ternary mixture (i.e. 1 mM ascorbic acid, 0.1 mM dopamine and 0.1 mM uric acid, Figure 2.5d)[102].
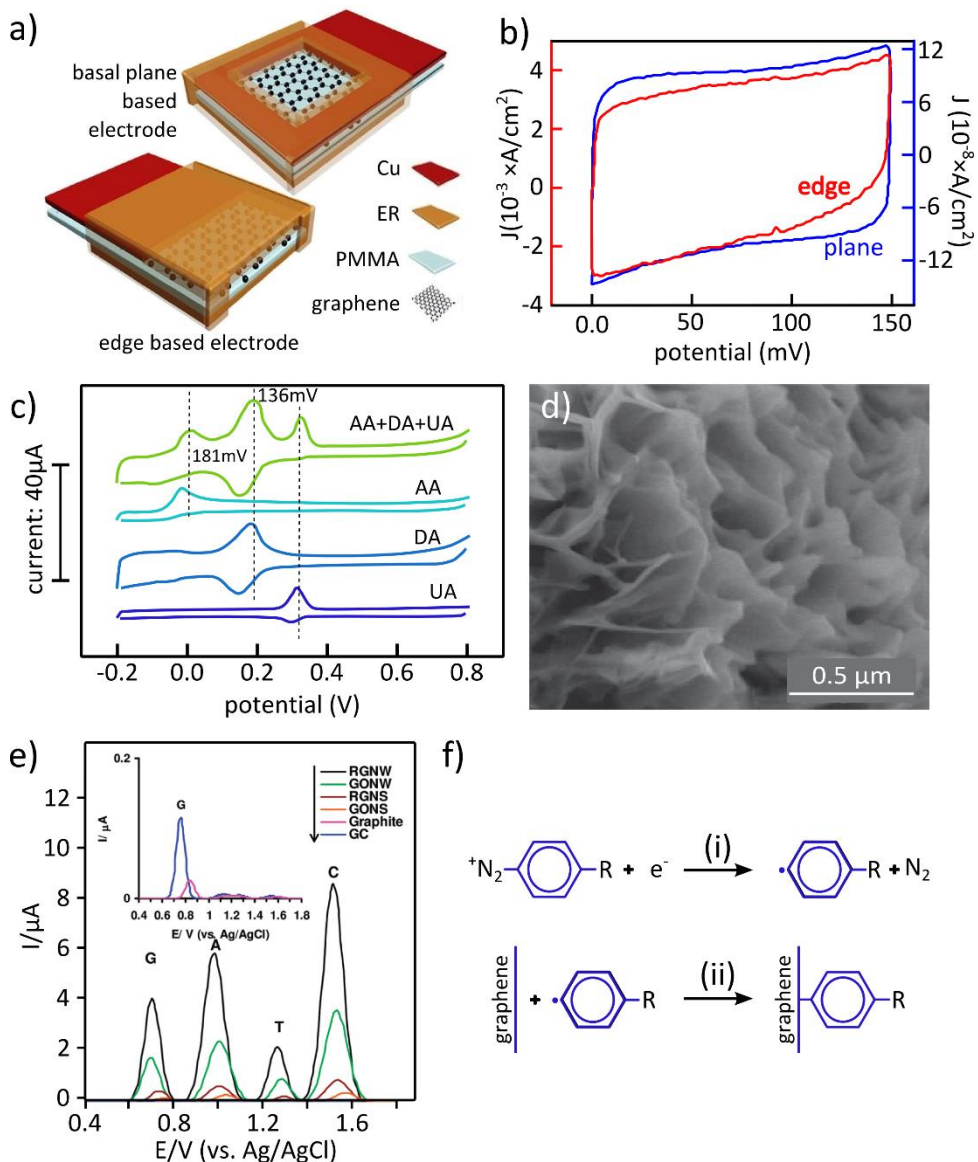

Figure 2.5. Electrochemistry of graphene edges. a) Illustration of two graphene electrodes employing respectively the basal plane (top) and the edge (bottom) of graphene. The basal plane electrode has been prepared by embedding the graphene inside a polymeric matrix

and by further etching the coating to solely expose the basal plane. The edge electrode has been prepared by mechanical cutting of the polymeric matrix embedding the graphene leaving only the edge exposed at the cut[98]. b) Cyclic voltammograms (CV) of the basal plane (blue) and of a graphene edge (red) in an aqueous solution of phosphate buffer saline[98]. c) Graphene edge electrode in a nanopore. The graphene is embedded between two Al_2O_3 insulating layers in order to inhibit the electrochemistry at the basal plane[99]. d) Cyclic voltammograms (CV) of graphene nanowalls (GNW). From top to bottom: solution of ascorbic acid (AA), dopamine (DA) and uric acid (UA). The upper curve is the CV of mixed solution of AA, DA and UA[102]. e) SEM picture of reduced graphene oxide nanowalls (RGNW) electrophoretically deposited on a graphite electrode[103]. f) Comparison between the sensitivity of electrodes made from reduced graphene oxide nanowalls (RGNW), graphene oxide nanowalls (GONW), reduced graphene nanosheets (RGNS), graphene oxide nanosheets (GONS), graphite and glassy carbon (GC) in the detection of the oxidation potentials of the four DNA nucleotides guanine, adenine, thymine, and cytosine (0.1 µM in 0.1 M of PBS, pH=7). The inset is a magnification of the peaks detected by graphite and glassy carbon electrodes which have a much lower detection limit than graphene-based electrodes [103].

Furthermore, the adoption of alternative production techniques of graphene, such as the reduction of graphene oxide, promoted the rise of defects and residual functionalities[104], which reduces the quality of the graphene with respect to chemical vapor deposition or exfoliated graphene, but inherently increasing the local electrochemical activity of graphene. Recently, reduced graphene oxide nano-walls electrodes (Figure 2.5e) have been fabricated through the electrophoretic deposition of graphene oxide on top of a graphitic substrate. Its chemical reduction in hydrazine showed that the edges and the surface defects of reduced graphene oxide allowed to detect both single-stranded and double stranded DNA molecules with an improved sensitivity compared to more conventional carbon electrodes such as graphite and glassy carbon[103]. The results, when compared to graphene oxide electrodes (i.e. before the reduction), highlighted the efficiency of the reduction step in increasing the sensitivity towards resolving between the four nucleotides (Figure 2.5f). The higher sensitivity (at least with respect to graphene oxide) has been ascribed to the higher availability of electrochemically active sites on the reduced graphene oxide, consequence of the presence of graphene edges whose aromaticity is shared with the conducting basal plane of graphene (note that graphene oxide is an insulating material). Interestingly, it was observed that the signal resulting from single stranded DNA is higher than for double stranded DNA, explained by the fact that double stranded

DNA has a higher resistance toward oxidation[103,105], perhaps thanks to the fact that in double-stranded DNA nucleotides are buried within the interior of the α-helix.

The concentration of analyte can be a limit in the sensing performance of a graphene edge. Nevertheless, in the case of DNA nucleotides, the strong electrochemical behaviour of reduced graphene oxide exploits the high sensitivity of the graphene edges to push the detection limits to concentrations down to 0.1 fM. The upper limit instead was confirmed to be below 10 mM, as a result of the aggregation tendency of the DNA molecules on the graphene surface, which decreases the electrodes activity[103,105].

2.5   Characterizing the chemical functionality of a graphene edge.

Several techniques have been employed to characterize the structure, topography, chemical functionalities, and electronic properties of graphene. Nevertheless, it is still a challenge to distinguish the chemical composition and the atomic structure of the edges with respect to the basal plane, primarily because the number of carbon atoms located on the edges only represents a small fraction of the total carbon atoms constituting graphene. Just a few methods allow such differentiation being even sensitive to the chemical functionality of the edge.

2.5.1   Scanning tunnelling microscopy, STM

Scanning tunnelling microscopy (STM) can effectively resolve between the edge and the basal plane of graphene, providing atomic resolution imaging of the edges.

Under an applied bias voltage, the electrons tunnel between the STM tip and the surface of graphene, Figure 2.6a. The distance between the tip and the surface of graphene, the applied bias voltage, as well as the intensity of the tunnelling current, are used to extract information about the surface of the sample (e.g. topography, defects and density of charge carriers). Remarkably, the localization of the p_z electrons on the zig-zag edges of graphene (the "edge state") locally increases the tunnelling current: the zig-zag edges are visible as brighter spots in STM micrographs, Figure 2.6b (top). These edge states can be further investigated in the scanning tunnelling spectroscopy (STS) mode of the STM. STS measures the first derivative of the tunnelling current with respect to voltage, i.e. dI/dV,

revealing the density of the charge carriers at a specific point[4,106,107], Figure 2.6b (bottom).
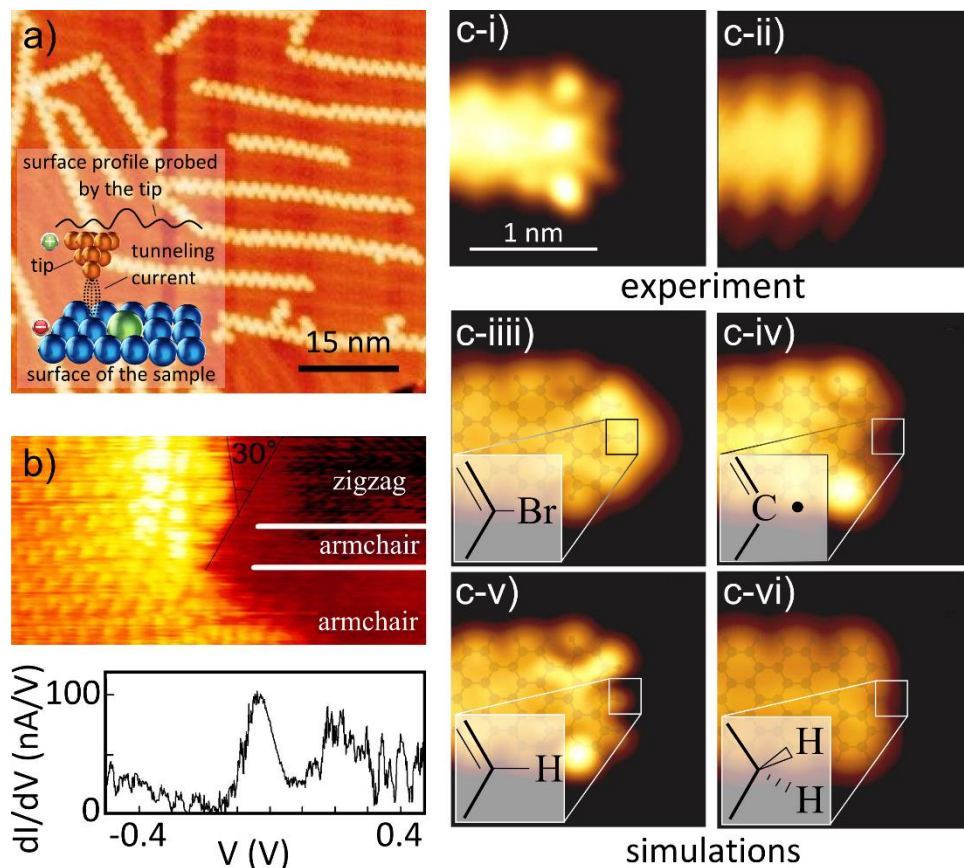

Figure 2.6. Scanning tunnelling microscopy of graphene. a) Scanning tunnelling microscopy (STM) imaging of graphene nanoribbons produced by surface assisted chemical synthesis of graphene on a gold substrate[80]. The inset illustrates the working principles of a STM. b) Top: STM mapping of an edge presenting zig-zag and armchair segments, the brighter spots correspond to the higher local charge carrier density of the zig-zag segment, which is absent along armchair sections. Bottom: plot of the tunnelling current derivative against the tip voltage (i.e. dI/dV). The more intense peak corresponds to one of the brighter zig-zag edges imaged in the mapping on top[72]. c) Impact of the edge chemical functionality on STM micrographs. (i) and (ii) experimental STM micrographs of chemically synthetized graphene nanoribbons with two presumably unknown termini. (iii) to (vi): density functional theory (DFT) simulations of the STM images for graphene nanoribbons terminated with four different functional groups (The inset represents the chemical structure of the graphene termini)[14].

STM measurements combined with theoretical calculations allowed to identify the chemical composition of the graphene edges[17]. STM imaging (Figure 2.6c (i-ii)) of chemically synthesized graphene nanoribbons with unknown chemical terminations were compared to the simulated electronic structures of four ribbons with different chemical termini: Br, mono- and di-hydrogenated as well as radical carbon terminations (Figure 2.6c (iii-iv)). Hydrogen passivated carbons show the best matching, highlighting that mono- and di-hydrogenated edges are the most notable termini (Figure 2.6c (v and vi). Remarkably, most of the ribbons measured experimentally in this work (85% of the total) showed mono-hydrogenated terminations[14].

To further investigate the effect of the edge hydrogenation on the electronic structure of graphene, nanoholes with predominantly zig-zag hydrogenated edges were fabricated using low energy argon ion bombardment of a graphitic surface, immediately followed by hydrogen plasma etching[73]. The STM micrographs, when compared to simulations, showed that hydrogenating the zig-zag edges distorted the distribution of the electronic structure: while for mono-hydrogenated carbon edges the local charge densities were stretched towards the centre: they were parallel to the edges if di-hydrogenation occurs. In other studies, surprisingly, zig-zag terminated graphene did not show the existence of the localized edge states (i.e. absence of bright spots in the STM images). Density functional theory (DFT) calculation and thermodynamic stability analysis showed that the absence of the edge state occurs when every third edge sites (not all of the carbon atoms) are di-hydrogenated (Figure 2.7d)[73]. The presence of localized edge states on zig-zag edges (Figure 2.7 a,c), which are absent on armchair edges, are the most appealing distinctions between zig-zag and armchair edges in STM. Additionally, in a particular configuration zig-zag edges do not show the edge state (Figure 2.7 b and d), appearing similarly as an armchair edge, because of subtle differences in chemical functionality (i.e. mono- vs di-hydrogenation)[73].
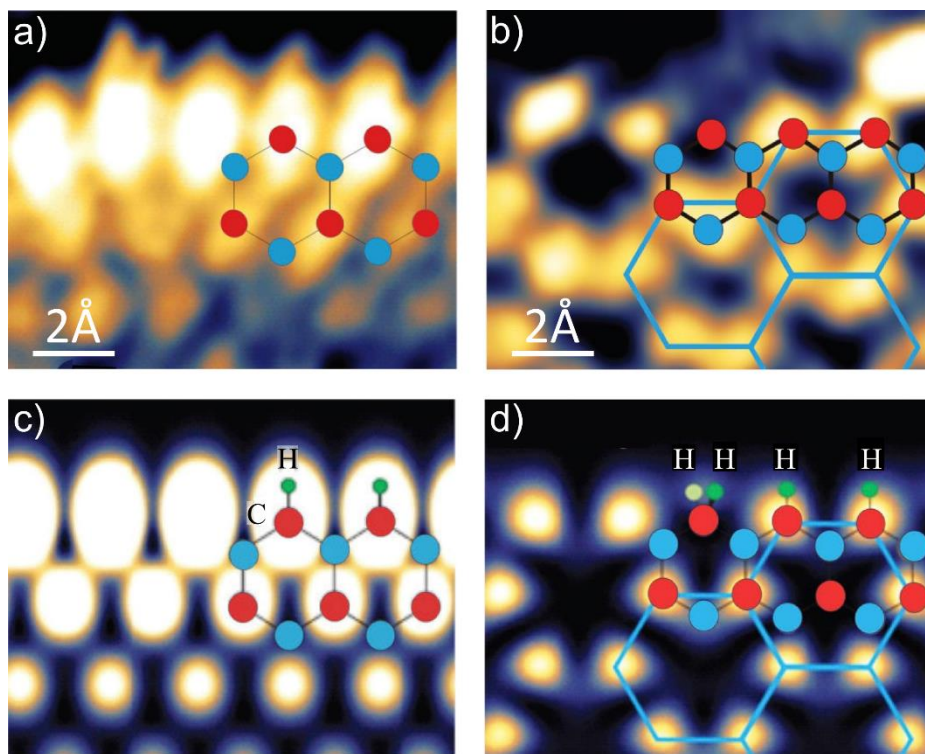
Figure 2.7. STM micrograph of mono and di-hydrogenated graphene edges. a) Experimental and b) simulated STM mapping of a zig-zag edge terminated with mono-hydrogenated carbon atoms. c) Experimental and d) simulated STM mapping of a zig-zag edge presenting mixed mono and di-hydrogenated carbon atoms. The small hexagonal unit cells represent the structure of graphene, while the large ones indicate the superlattice due to the underlying graphitic substrate. The presence of a di-hydrogenated carbon atom on the edge can locally destroy the edge state typical of a zig-zag edge configuration, resulting in a dark spot on the STM micrograph[73].

Not only the geometrical shape of graphene edges tunes the electronic characteristics of graphene edges, but also the finest chemistry of the edges, which can be probed by means of STM imaging, at the cost of systematic DFT calculations.

2.5.2   X-ray photoelectron spectroscopy, XPS

X-ray photoelectron spectroscopy (XPS), also referred as ESCA (electron spectroscopy for chemical analysis), is widely used to study the chemical composition of surfaces[108]. An X-ray beam irradiates the surface of the sample and the photons exchange their energy with the electrons of the atoms in proximity of

the surface. The electrons get excited, overwhelming the atomic binding energy and escaping the sample surface. Starting from the kinetic energy of the emitted electrons, it is possible, in principle, to resolve all the elements of the periodic table. Additionally, chemical reactions univocally shift the energy levels of the atoms involved (chemical shifts). Thus, the XPS is suited to read, not only the chemical composition, but even the chemical functionalization of the sample[109].

Consequently, for each emitted electron, the XPS records an intensity peak at a specific binding energy (E_B) which characterizes the elemental composition of the sample. Usually, the X-ray photon source lacks of atomic resolution and the irradiation area can reach several micrometres. Nevertheless, the intensity of the peaks and their shifts, as well as their broadening, can be deconvoluted in order to estimate the relative amount of chemical species on a surface[110].

Indeed, the peaks deconvolution has been applied to probe the chemical functionalization of graphene edges. Chemically synthesized graphene nanoribbons, which edges were chlorinated, have been analysed by XPS. The chemical synthesis was employed in order to ensure the selective functionalization of the graphene edges. As a result, the C1s peak of the carbon highlights two components: the C=C bond at high intensity, which rises due to the honeycomb lattice of graphene, and a second component induced by the chlorination, Figure 2.8a. Symmetrically, the Cl 2p peak is fully influenced by the bonding with the edge carbon atoms[37].
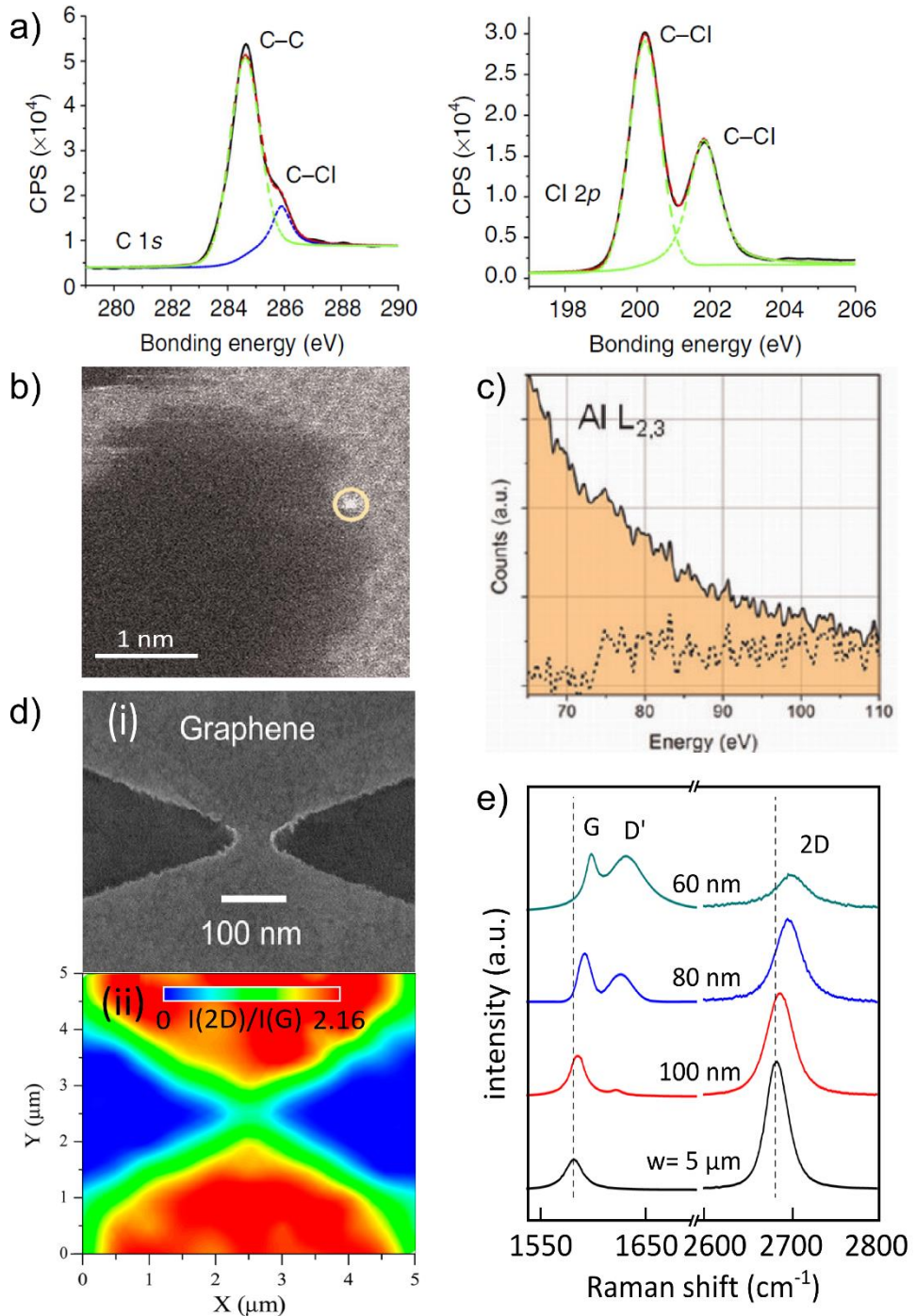
a)

b)

c)

d) (i) Graphene

(ii)

e)

Figure 2.8. Spectroscopic characterization of graphene edges. a) X-ray photoelectron spectroscopy of a chlorinated graphene nanoribbon. The C-Cl bond shifts the energy of the C 1s orbital and symmetrically of the Cl 2p energetic levels[37]. b) z-contrast TEM (a mode sensitive to atomic number) image of a sheet of graphene with a large hole. The bright spot marked by the circle corresponds to a single aluminium adatom[18]. c) EELS spectra on the bright spot in b). The dotted line is obtained after filtering and reveals the presence of aluminium[18]. d) Effect of the oxygen plasma etching on the oxidation state of a graphene nanoconstriction. The basal plane of graphene was covered with poly (methyl methacrylate) allowing the etching from the edges. (i) SEM image of the nanoconstriction with a width of 60 nm. (ii) The corresponding I(2D)/I(G) Raman map differentiates the edges from the basal plane, highlighting the oxidation of the edges[10]. e) Raman blue shift of graphene nanoconstriction as a function of the width. The blue-shift is a consequence of the edge oxidation and becomes more prominent in Raman for narrower nanoconstrictions[10].

Similarly, bromo-phenyl functionalities have been added to the graphene edge using diazonium chemistry. The edge selectivity of the process was demonstrated by the weaker intensity of the C-Br peak of the bromo-phenyl functionalized graphene[45] compared to another graphene sample which surface was chemically modified with the diazonium compound. In fact, the selective edge functionalization offers few binding sites, reducing the intensity of the spectroscopic fingerprint of the functional groups.

2.5.3 Electron energy loss spectroscopy, EELS

Electron energy loss spectroscopy (EELS) measures the variation of the kinetic energy of an electron beam once it interacts with the material, probing its chemical composition[111]. Having atomic level resolution, EELS is capable to determine the chemical composition in a specific region of the sample[112], such as the functionalization of graphene edges.

EELS measurements are performed in a transmission electron microscope, in conjunction with different imaging modes of this instrument. The technique is typically performed on suspended samples in order to avoid the influence of the substrate, even more particularly for graphene, which thickness is order of magnitude shorter than the penetration distances of the electrons.

Experimentally, EELS allows differentiating single atom substitution on graphene. For example, the inelastic scattering induced by the interaction between the electron beam and the graphene highlighted a reduction of the π* peak energy

passing from the lattice of graphene to the armchair edges and finally to the zig-zag edges[19].

Additionally, EELS resolved the residual oxidation in multilayer graphene and graphite, where the oxidation of the carbon atoms is tracked by the rise of the k-oxygen peak. The relevance of multilayer systems is correlated to the relaxation mechanisms of the edges in multilayer graphene films. The study underlined the tendency of the edges to close on themselves, limiting the amount of functionalized and reconstructed edges[113].

Furthermore, EELS resolution is high enough to detect the specific chemistry of unbound impurities such as adatoms (i.e. atoms adsorbed on the graphene surface), if their atomic mass is higher than carbon. Figure 2.8b shows the edge of a graphene sheet close to a large hole obtained by metal mediated etching[18]. The spot marked by the yellow circle appears brighter than the other atoms. This element can be identified in the complementary EELS measurement shown in Figure 2.8c. The presence of a peak around 75 eV in the EELS spectrum is a fingerprint of aluminium (i.e., the metal used for etching the hole in graphene, which got conjugated at the edges of the hole).

2.5.4   Edge functionality probed by Raman spectroscopy

Raman spectroscopy is widely used to characterize both the atomic structure and the electronic properties of graphene[114–116]. Raman resolves the number of graphene layers in few-layers systems[117,118], and is sensitive to defects and to the presence of edges, more particularly to the atomic arrangement at the edge (i.e. the zig-zag and armchair configuration[119–122]). Raman spectroscopy has also been used to monitor edge disorder, graphene quality, doping and strain[123–127], as well as to study the chemical functionality of an edge[83].

The Raman spectrum of graphene shows few characteristic peaks, each corresponding to an inelastic scattering event of the incident light by the lattice of graphene. At an excitation wavelength of 514 nm, the D, G, D' and 2D (also known as G') peaks respectively positioned at ~1350 cm^{-1}, ~1580 cm^{-1}, 1620 cm^{-1}, ~2700 cm^{-1}, represent the signature of graphene in a Raman spectrum[117,128]. A defect site or an edge breaks the symmetry of the honeycomb lattice and influences the

vibrational modes of the graphene: yielding usually to the rise of the D and D' peaks in the Raman spectrum of graphene[114,115].

In principle, zig-zag edges inactivate these defect-related peaks[115,118]. Hence, the presence of a D peak can respectively be due to the presence of either zig-zag or armchair edges[119,121]. Nevertheless, the polarization of the incident light, the microscopic disorder of the edges and the size of the illuminated spot area can induce the appearance of a D peak in proximity of a zig-zag edge, limiting the reliability of this particular approach[120].

The chemical reactivity of graphene can be probed by Raman when the functionalization changes the hybridization of the carbon atoms from sp^2 to sp^3[48]. Before the functionalization, the D peak of graphene presents a strong dependence on the polarization of the incident light, consistent with previous observations and theories[120]. After the functionalization, the polarization dependency is lost. In fact, the re-hybridization introduced by the chemical functionality becomes the main contribution to the D peak. Interestingly, in the case of aryl functionalization of graphene by diazonium chemistry, the ratio I(D)/I(G) is about two times larger at the edge (I(D)/I(G) ~ 0.8) compared to the basal plane (I(D)/I(G) ~ 0.4), confirming the higher edge reactivity of graphene[48].

Another important property of the Raman spectrum of graphene, when studying its functionalization, is the sensitivity of G and 2D peaks to doping (e.g. via oxidation or amination with NH_3[10,83]). A blue and a red shift of the G and 2D peaks occur upon *p* and *n* type doping respectively (i.e. oxidation and amination). Additionally, the doping leads to a reduction of the intensity of the 2D peak[129].

Recently, the influence of edge oxidation on the doping of graphene has been studied on nanoconstrictions produced by e-beam lithography and oxygen plasma etching (Figure 2.8d)[10]. The nanoconstriction was fabricated covering the basal plane of graphene with PMMA, while the etching was carried from the edges. The I(2D)/I(G) mapping of the nanoconstriction (Figure 2.8d (ii)) highlights the decrease of the 2D peak intensity moving from the centre to the edges. Additionally, by reducing the width of nanoconstrictions from 5 μm to 60 nm, prominent blue shifts of the G and 2D peaks as well as a strong reduction of the 2D intensity were observed (Figure 2.8e).

The amination of graphene in presence of NH_3 was followed by mapping the intensity of the D peak and the blue-shift of the G peak[83]. The presence of the D peak reveals that the functionalization under NH_3 mild plasma conditions occurs preferentially at the edges. This result is consistent with an increased reactivity of the edges compared to the basal plane. Additionally, the chemical doping was further confirmed by the red shift (*n*-type doping) of the G peak.

The Raman technique efficiently provides information about the type of defects formed upon graphene functionalization, but is not capable to identify directly the composition of the chemical groups attached to the reactive sites. Nevertheless, the local variation of the position and intensity of the peaks provides relevant information about, for example, the doping induced by the chemical functionalization of graphene edges.

2.6   Summary and outlook

The chemical reactivity of graphene is inherently influenced by its edges. Zig-zag and armchair configurations locally determine the distribution of electrons, and therefore the chemical reactivity of the carbon atoms at the edge sites.

In this context, zig-zag and armchair configurations largely influence the reactivity of the edges towards cycloaddition, condensation, and electrophilic substitution reactions.

Important improvements are required to selectively promote an organic reaction at the edges: at the atomic scale each carbon atom behaves as a reaction site. Each atom is influenced both by its specific properties, such as its chemical functionality, and by the nearby carbon atoms composing the edge. The configuration of the edge (zig-zag or armchair), its position on the edge and the aromaticity of the graphene molecule, all concomitantly determine the reactivity of that particular carbon atom. Consequently, the chemistry of a single carbon atom has hardly been foreseen in the context of further chemical functionalization.

Additionally, STM is very suited to characterize the specific chemistry of a carbon atom on the edge, particularly if combined with DFT calculations. The STM scans the graphene atom by atom acquiring the specific features of the edges, such as

the electron density of states. Alternatively, other characterization methods, such as Raman spectroscopy and XPS are used, although they lack the atomic resolution.

So far, only organic chemistry is capable of offering perfectly tailored graphene edges with a full control over the geometry and the chemistry of the graphene edge. The atomic characterizations of graphene edges, however, remain challenging for many graphene materials systems, where the lack of well suited analytic tools is the obstacle.

2.7   References

(1)   Geim, A. K.; Novoselov, K. S. *Nat. Mater.* **2007**, *6*, 183.

(2)   Katsnelson, M. I. *Mater. Today* **2007**, *10* (1), 20–27.

(3)   Wang, L.; Meric, I.; Huang, P. Y.; Gao, Q.; Gao, Y.; Tran, H.; Taniguchi, T.; Watanabe, K.; Campos, L. M.; Muller, D. a; Guo, J.; Kim, P.; Hone, J.; Shepard, K. L.; Dean, C. R. *Science* **2013**, *342* (6158), 614–617.

(4)   Kobayashi, Y.; Fukui, K.; Enoki, T. *Phys. Rev. B* **2006**, *73* (12), 125415.

(5)   Enoki, T.; Fujii, S.; Takai, K. *Carbon* **2012**, *50* (9), 3141–3145.

(6)   Sun, Z.; James, D. K.; Tour, J. M. *J. Phys. Chem. Lett.* **2011**, *2* (19), 2425–2432.

(7)   Gunlycke, D.; Li, J.; Mintmire, J. W.; White, C. T. *Appl. Phys. Lett.* **2007**, *91* (11), 112108.

(8)   Jiang, D.; Sumpter, B. G.; Dai, S. *J. Chem. Phys.* **2007**, *126* (13), 134701.

(9)   Castro Neto, a. H.; Peres, N. M. R.; Novoselov, K. S.; Geim, A. K. *Rev. Mod. Phys.* **2009**, *81* (1), 109–162.

(10)   Iqbal, M. W.; Iqbal, M. Z.; Jin, X.; Hwang, C.; Eom, J. *ACS Appl. Mater. Interfaces* **2014**, *6*, 4207.

(11)   Novoselov, K. S.; Geim, A. K.; Morozov, S. V; Jiang, D.; Zhang, Y.; Dubonos, S. V; Grigorieva, I. V; Firsov, A. A. *Science* **2004**, *306* (5696), 666–669.

(12)   De Arco, L. G.; Zhang, Y.; Kumar, A.; Zhou, C. *IEEE Trans. Nanotechnol.* **2009**, *8* (2), 135–138.

(13)   Böttcher, A.; Heil, M.; Stürzl, N.; Jester, S. S.; Malik, S.; Pérez-Willard, F.; Brenner, P.; Gerthsen, D.; Kappes, M. M. *Nanotechnology* **2006**, *17* (23), 5889–5894.

(14)   Talirz, L.; Söde, H.; Cai, J.; Ruffieux, P.; Blankenburg, S.; Jafaar, R.; Berger, R.; Feng, X.; Müllen, K.; Passerone, D.; Fasel, R.; Pignedoli, C. a; De, H. S.; Ru, P.; Mu, K. *J. Am. Chem. Soc.* **2013**, *135* (6), 2060–2063.

(15)   Eckmann, A.; Felten, A.; Mishchenko, A.; Britnell, L.; Krupke, R.; Novoselov, K. S.; Casiraghi, C. *Nano Lett.* **2012**, *12* (8), 3925–3930.

(16)   Lucchese, M. M.; Stavale, F.; Ferreira, E. H. M.; Vilani, C.; Moutinho, M. V. O.; Capaz, R. B.; Achete, C. a.; Jorio, a. *Carbon* **2010**, *48* (5), 1592–1597.

(17)   Zhang, X.; Yazyev, O. V; Feng, J.; Xie, L.; Tao, C.; Chen, Y.-C.; Jiao, L.; Pedramrazi, Z.; Zettl, A.; Louie, S. G.; Dai, H.; Crommie, M. F. *ACS Nano* **2013**, *7* (1), 198–202.

(18)   Ramasse, Q. Q. M.; Zan, R.; Bangert, U.; Boukhvalov, D. W.; Son, Y.; Novoselov, K. S. *ACS Nano* **2012**, *6* (5), 4063–4071.

(19)   Suenaga, K.; Koshino, M. *Nature* **2010**, *468* (7327), 1088–1090.

(20)   Yazyev, O. V; Capaz, R. B.; Louie, S. G. *J. Phys. Conf. Ser.* **2011**, *302* (1), 012016.

(21)   Sheka, E. F.; Chernozatonskii, L. A. *Int. J. Quantum Chem.* **2009**, 110(10), 1938-1946.

(22)   Cervantes-Sodi, F.; Csányi, G.; Piscanec, S.; Ferrari, A. C. *Phys. Rev. B* **2008**, *77* (16), 165427.

(23)   Yan, L.; Zheng, Y. B.; Zhao, F.; Li, S.; Gao, X.; Xu, B.; Weiss, P. S.; Zhao, Y. *Chem. Soc. Rev.* **2012**, *41* (1), 97–114.

(24)   He, K.; Lee, G.-D.; Robertson, A. W.; Yoon, E.; Warner, J. H. *Nat. Commun.* **2014**, *5*, 3040.

(25)   Nakada, K.; Fujita, M.; Dresselhaus, G.; Dresselhaus, M. S. M. M. *Phys. Rev. B. Condens. Matter* **1996**, *54* (24), 17954–17961.

(26)   Son, Y.-W.; Cohen, M. L.; Louie, S. G. *Phys. Rev. Lett.* **2006**, *97* (21), 216803.

(27)   Acik, M.; Ã, Y. J. C.; Chabal, Y. J. *Jpn. J. Appl. Phys.* **2011**, *50* (7), 070101.

(28)   Koskinen, P.; Malola, S.; Häkkinen, H. *Phys. Rev. B* **2009**, *80* (7), 073401.

(29)   Wassmann, T.; Seitsonen, A. P.; Saitta, A. M.; Lazzeri, M.; Mauri, F. *J. Am. Chem. Soc.* **2010**, *132* (10), 3440–3451.

(30)   Baldoni, M.; Sgamellotti, A.; Mercuri, F. *Chem. Phys. Lett.* **2008**, *464* (4–6), 202–207.

(31)   Fujii, S.; Enoki, T. *Acc. Chem. Res.* **2013**, *46* (10), 2202–2210.

(32)   Jiang, D.; Chen, Z. *Graphene Chemistry: Theoretical Perspectives*; Wiley,

2013.

(33) Wassmann, T.; Seitsonen, A.; Saitta, a.; Lazzeri, M.; Mauri, F. *Phys. Rev. Lett.* **2008**, *101* (9), 096402.

(34) Seitsonen, A. P.; Saitta, a. M.; Wassmann, T.; Lazzeri, M.; Mauri, F. *Phys. Rev. B* **2010**, *82* (11), 115425.

(35) Kariuki, J. K.; McDermott, M. T. *Langmuir* **1999**, *15* (19), 6534–6540.

(36) Quintana, M.; Montellano, A.; del Rio Castillo, A. E.; Van Tendeloo, G.; Bittencourt, C.; Prato, M. *Chem. Commun.* **2011**, *47* (33), 9330–9332.

(37) Tan, Y.-Z.; Yang, B.; Parvez, K.; Narita, A.; Osella, S.; Beljonne, D.; Feng, X.; Müllen, K. *Nat. Commun.* **2013**, *4*, 2646.

(38) Lu, Y.; Lerner, M. B.; John Qi, Z.; Mitala, J. J.; Hsien Lim, J.; Discher, B. M.; Charlie Johnson, A. T. *Appl. Phys. Lett.* **2012**, *100* (3), 033110.

(39) Chua, C. K.; Pumera, M. *Chem. Soc. Rev.* **2013**, *42* (8), 3222–3233.

(40) Liu, K.; Chen, S.; Luo, Y.; Jia, D.; Gao, H.; Hu, G.; Liu, L. *Compos. Sci. Technol.* **2013**, *88*, 84–91.

(41) Jeon, I.-Y.; Choi, E.-K.; Bae, S.-Y.; Baek, J.-B. *Nanoscale Res. Lett.* **2010**, *5* (10), 1686–1691.

(42) Zhao, W.; Fang, M.; Wu, F.; Wu, H.; Wang, L.; Chen, G. *J. Mater. Chem.* **2010**, *20* (28), 5817.

(43) Jeon, I.-Y.; Choi, H.-J.; Jung, S.-M.; Seo, J.-M.; Kim, M.-J.; Dai, L.; Baek, J.-B. *J. Am. Chem. Soc.* **2013**, *135* (4), 1386–1393.

(44) Xu, J.; Shui, J.; Wang, J.; Wang, M.; Liu, H.-K.; Dou, S. X.; Jeon, I.-Y.; Seo, J.-M.; Baek, J.-B.; Dai, L. *ACS Nano* **2014**, *8* (10), 10920–10930.

(45) Sun, Z.; Kohama, S.; Zhang, Z.; Lomeda, J. R.; Tour, J. M. *Nano Res.* **2010**, *3* (2), 117–125.

(46) Kariuki, J. K.; McDermott, M. T. *Langmuir* **2001**, *17* (19), 5947–5951.

(47) Park, J.; Yan, M. *Acc. Chem. Res.* **2012**, *46* (1), 181–189.

(48) Sharma, R.; Baik, J. H.; Perera, C. J.; Strano, M. S. *Nano Lett.* **2010**, *10* (2), 398–405.

(49)   Paulus, G. L. C.; Wang, Q. H.; Strano, M. S. *Acc. Chem. Res.* **2013**, *46* (1), 160–170.

(50)   Jeon, I.-Y.; Shin, Y.-R.; Sohn, G.-J.; Choi, H.-J.; Bae, S.-Y.; Mahmood, J.; Jung, S.-M.; Seo, J.-M.; Kim, M.-J.; Wook Chang, D.; Dai, L.; Baek, J.-B. *Proc. Natl. Acad. Sci. U. S. A.* **2012**, *109* (15), 5588–5593.

(51)   Chen, L.; Hernandez, Y.; Feng, X.; Müllen, K. *Angew. Chem. Int. Ed. Engl.* **2012**, *51* (31), 7640–7654.

(52)   Smith, B. W.; Luzzi, D. E. *J. Appl. Phys.* **2001**, *90* (7), 3509.

(53)   Girit, C. O.; Meyer, J. C.; Erni, R.; Rossell, M. D.; Kisielowski, C.; Yang, L.; Park, C.-H.; Crommie, M. F.; Cohen, M. L.; Louie, S. G.; Zettl, A. *Science.* **2009**, *323* (5922), 1705–1708.

(54)   Schneider, F.; Houben, L.; Malladi, S. K.; Dekker, C.; Xu, Q.; Wu, M.-Y.; Schneider, G. F.; Houben, L.; Malladi, S. K.; Dekker, C.; Yucelen, E.; Dunin-Borkowski, R. E.; Zandbergen, H. W. *ACS Nano* **2013**, *7* (2), 1566–1572.

(55)   Schneider, G. F.; Kowalczyk, S. W.; Calado, V. E.; Pandraud, G.; Zandbergen, H. W.; Vandersypen, L. M. K.; Dekker, C. *Nano Lett.* **2010**, *10* (8), 3163–3167.

(56)   Lee, G.; Cho, K. *Phys. Rev. B* **2009**, *79* (16), 165440.

(57)   Wang, Z.; Li, Q.; Zheng, H.; Ren, H.; Su, H.; Shi, Q.; Chen, J. *Phys. Rev. B* **2007**, *75* (11), 113406.

(58)   Terrones, H.; Lv, R.; Terrones, M.; Dresselhaus, M. S. *Rep. Prog. Phys.* **2012**, *75* (6), 062501.

(59)   Qi, Z. J.; Rodríguez-Manzo, J. a; Botello-Méndez, A. R.; Hong, S. J.; Stach, E. a; Park, Y. W.; Charlier, J.-C.; Drndić, M.; Johnson, a T. C. *Nano Lett., 2014, 14 (8), pp 4238–4244.*

(60)   Fischbein, M. D.; Drndić, M. *Appl. Phys. Lett.* **2008**, *93* (11), 113107.

(61)   Merchant, C. A.; Healy, K.; Wanunu, M.; Ray, V.; Peterman, N.; Bartel, J.; Fischbein, M. D.; Venta, K.; Luo, Z.; Johnson, A. T. C.; Drndić, M.; et al. *Nano Lett.* **2010**, *10* (8), 2915–2921.

(62)   Garaj, S.; Hubbard, W.; Reina, A.; Kong, J.; Branton, D.; Golovchenko, J. a. *Nature* **2010**, *467* (7312), 190–193.

62

(63) Traversi, F.; Raillon, C.; Benameur, S. M.; Liu, K.; Khlybov, S.; Tosun, M.; Krasnozhon, D.; Kis, A.; Radenovic, A. *Nat. Nanotechnol.* **2013**, *8* (12), 939–945.

(64) Liu, K.; Feng, J.; Kis, A.; Radenovic, A. *ACS Nano* **2014**, *8* (3), 2504–2511.

(65) Liu, S.; Lu, B.; Zhao, Q.; Li, J.; Gao, T.; Chen, Y.; Zhang, Y.; Liu, Z.; Fan, Z.; Yang, F.; You, L.; Yu, D. *Adv. Mater.* **2013**, *25*, 4549–4554.

(66) Song, B.; Schneider, G. F.; Xu, Q.; Pandraud, G.; Dekker, C.; Zandbergen, H. *Nano Lett.* **2011**, *11* (6), 2247–2250.

(67) Bell, D. C.; Lemme, M. C.; Stern, L. a; Williams, J. R.; Marcus, C. M. *Nanotechnology* **2009**, *20* (45), 455301.

(68) Ward, B. W.; Notte, J. a.; Economou, N. P. *J. Vac. Sci. Technol. B Microelectron. Nanom. Struct.* **2006**, *24* (6), 2871.

(69) Xie, L.; Jiao, L.; Dai, H. *J. Am. Chem. Soc.* **2010**, *132* (42), 14751–14753.

(70) Wang, X.; Dai, H. *Nat. Chem.* **2010**, *2* (8), 661–665.

(71) Jia, X.; Campos-Delgado, J.; Terrones, M.; Meunier, V.; Dresselhaus, M. S. *Nanoscale* **2011**, *3* (1), 86–95.

(72) Kobayashi, Y.; Fukui, K.; Enoki, T.; Kusakabe, K.; Kaburagi, Y. *Phys. Rev. B* **2005**, *71* (19), 193406.

(73) Ziatdinov, M.; Fujii, S.; Kusakabe, K.; Kiguchi, M.; Mori, T.; Enoki, T. *Phys. Rev. B* **2013**, *87* (11), 115427.

(74) Lu, Y. H.; Wu, R. Q.; Shen, L.; Yang, M.; Sha, Z. D.; Cai, Y. Q.; He, P. M.; Feng, Y. P. *Appl. Phys. Lett.* **2009**, *94* (12), 122111.

(75) Wagner, P.; Ivanovskaya, V. V.; Melle-Franco, M.; Humbert, B.; Adjizian, J.-J.; Briddon, P. R.; Ewels, C. P. *Phys. Rev. B* **2013**, *88* (9), 094106.

(76) Simbeck, A. J.; Gu, D.; Kharche, N.; Satyam, P. V.; Avouris, P.; Nayak, S. K. *Phys. Rev. B* **2013**, *88* (3), 035413.

(77) Ohtsuka, M.; Fujii, S.; Kiguchi, M.; Enoki, T. *ACS Nano* **2013**, *7* (8), 6868–6874.

(78) Hod, O.; Barone, V.; Peralta, J. E.; Scuseria, G. E. *Nano Lett.* **2007**, *7* (8),

2295–2299.

(79)   Yang, X.; Dou, X.; Rouhanipour, A.; Zhi, L.; Räder, H. J.; Müllen, K.; Ra, H. J.; Mu, K. *J. Am. Chem. Soc.* **2008**, *130* (13), 4216–4217.

(80)   Cai, J.; Ruffieux, P.; Jaafar, R.; Bieri, M.; Braun, T.; Blankenburg, S.; Fasel, R.; Muoth, M.; Seitsonen, A. P.; Saleh, M.; Feng, X.; Mu, K.; Müllen, K. *Nature* **2010**, *466* (7305), 470–473.

(81)   Baraket, M.; Stine, R.; Lee, W. K.; Robinson, J. T.; Tamanaha, C. R.; Sheehan, P. E.; Walton, S. G. *Appl. Phys. Lett.* **2012**, *100* (23), 233123.

(82)   Wang, X.; Li, X.; Zhang, L.; Yoon, Y.; Weber, P. K.; Wang, H.; Guo, J.; Dai, H. *Science* **2009**, *324* (5928), 768–771.

(83)   Kato, T.; Jiao, L.; Wang, X.; Wang, H.; Li, X.; Zhang, L.; Hatakeyama, R.; Dai, H. *Small* **2011**, *7* (5), 574–577.

(84)   Vo, T. H.; Shekhirev, M.; Kunkel, D. A.; Morton, M. D.; Berglund, E.; Kong, L.; Wilson, P. M.; Dowben, P. A.; Enders, A.; Sinitskii, A. *Nat. Commun.* **2014**, *5*, 3189.

(85)   Li, X.; Cai, W.; An, J.; Kim, S.; Nah, J.; Yang, D.; Piner, R.; Velamakanni, A.; Jung, I.; Tutuc, E.; Banerjee, S. K.; Colombo, L.; Ruoff, R. S. *Science.* **2009**, *324* (5932), 1312–1314.

(86)   Biró, L. P.; Lambin, P. *Carbon* **2010**, *48* (10), 2677–2689.

(87)   Puddy, R. K.; Scard, P. H.; Tyndall, D.; Connolly, M. R.; Smith, C. G.; Jones, G. A. C.; Lombardo, A.; Ferrari, A. C.; Buitelaar, M. R. *Appl. Phys. Lett.* **2011**, *98* (13), 133120.

(88)   Hiura, H. *Appl. Surf. Sci.* **2004**, *222* (1–4), 374–381.

(89)   Park, J.; Kim, K. B.; Park, J.-Y.; Choi, T.; Seo, Y. *Nanotechnology* **2011**, *22* (33), 335304.

(90)   Kondo, S.; Lutwyche, M.; Wada, Y. *Appl. Surf. Sci.* **1994**, *75* (1–4), 39–44.

(91)   Albrecht, T. R.; Dovek, M. M.; Kirk, M. D.; Lang, C. A.; Quate, C. F.; Smith, D. P. E. *Appl. Phys. Lett.* **1989**, *55* (17), 1727.

(92)   Kurra, N.; Prakash, G.; Basavaraja, S.; Fisher, T. S.; Kulkarni, G. U.; Reifenberger, R. G. *Nanotechnology* **2011**, *22* (24), 245302.

(93)   Masubuchi, S.; Ono, M.; Yoshida, K.; Hirakawa, K.; Machida, T. *Appl. Phys. Lett.* **2009**, *94* (8), 082107.

(94)   Nemes-Incze, P.; Tapasztó, L.; Magda, G. Z.; Osváth, Z.; Dobrik, G.; Jin, X.; Hwang, C.; Biró, L. P. *Appl. Surf. Sci.* **2014**, *291*, 48–52.

(95)   Weng, L.; Zhang, L.; Chen, Y. P.; Rokhinson, L. P. *Appl. Phys. Lett.* **2008**, *93* (9), 093107.

(96)   Pumera, M. *Chem. Soc. Rev.* **2010**, *39* (11), 4146.

(97)   Ambrosi, A.; Bonanni, A.; Pumera, M. *Nanoscale* **2011**, *3* (5), 2256–2260.

(98)   Yuan, W.; Zhou, Y.; Li, Y.; Li, C.; Peng, H.; Zhang, J.; Liu, Z.; Dai, L.; Shi, G. *Sci. Rep.* **2013**, *3* (1), 2248.

(99)   Banerjee, S.; Shim, Â. J.; Rivera, Â. J.; Jin, X.; Estrada, D.; Solovyeva, V.; Shim, J.; Rivera, J.; You, X.; Pak, J.; Pop, E.; Aluru, N.; Bashir, R. *ACS Nano* **2013**, *7* (1), 834–843.

(100)   Brownson, D. A. C.; Kampouris, D. K.; Banks, C. E. *Chem. Soc. Rev.* **2012**, *41* (21), 6944–6976.

(101)   McCreery, R. L.; McDermott, M. T. *Anal. Chem.* **2012**, *84* (5), 2602–2605.

(102)   Shang, N. G.; Papakonstantinou, P.; McMullan, M.; Chu, M.; Stamboulis, A.; Potenza, A.; Dhesi, S. S.; Marchetto, H. *Adv. Funct. Mater.* **2008**, *18* (21), 3506.

(103)   Akhavan, O.; Ghaderi, E.; Rahighi, R. *ACS Nano* **2012**, *6* (4), 2904–2916.

(104)   Ambrosi, A.; Bonanni, A.; Sofer, Z.; Cross, J. S.; Pumera, M. *Chemistry* **2011**, *17* (38), 10763–10770.

(105)   Zhou, M.; Zhai, Y.; Dong, S. *Anal. Chem.* **2009**, *81* (14), 5603.

(106)   Klusek, Z.; Waqar, Z.; Denisov, E. .; Kompaniets, T. .; Makarenko, I. .; Titkov, a. .; Bhatti, A. . *Appl. Surf. Sci.* **2000**, *161* (3–4), 508–514.

(107)   Tao, C.; Jiao, L.; Yazyev, O. V.; Chen, Y.-C.; Feng, J.; Zhang, X.; Capaz, R. B.; Tour, J. M.; Zettl, A.; Louie, S. G.; Dai, H.; Crommie, M. F. *Nat. Phys.* **2011**, *7* (8), 616–620.

(108)   Turner, N. H. *Anal. Chem.* **1988**, *60* (12), 377–387.

(109) Henning, B.; Holger, J. *Surface and Thin Film Analysis: A Compendium of Principles, Instrumentation, and Applications*; John Wiley & Sons, **2011**.

(110) Kuwana, T. *Physical Methods in Modern Chemical Analysis, Volume 2*; Elsevier Science, **2012**.

(111) Egerton, R. F. *Reports Prog. Phys.* **2009**, *72* (1), 016502.

(112) Suenaga, K.; Tence, M.; Mory, C.; Colliex, C.; Kato, H.; Okazaki, T.; Shinohara, H.; Hirahara, K.; Bandow, S.; Iijima, S. *Science* **2000**, *290* (5500), 2280–2282.

(113) Liu, Z.; Suenaga, K.; Harris, P.; Iijima, S. *Phys. Rev. Lett.* **2009**, *102* (1), 015501.

(114) Malard, L. M.; Pimenta, M. a.; Dresselhaus, G.; Dresselhaus, M. S. *Phys. Rep.* **2009**, *473* (5–6), 51–87.

(115) Ferrari, A. C.; Basko, D. M. *Nat. Nanotechnol.* **2013**, *8* (4), 235–246.

(116) Zhang, D.; Yang, J.; Li, Y. *Small* **2013**, *9* (8), 1284–1304.

(117) Ferrari, A. C.; Meyer, J. C.; Scardaci, V.; Casiraghi, C.; Lazzeri, M.; Mauri, F.; Piscanec, S.; Jiang, D.; Novoselov, K. S.; Roth, S.; Geim, A. K. *Phys. Rev. Lett.* **2006**, *97* (18), 187401.

(118) Cançado, L.; Reina, a.; Kong, J.; Dresselhaus, M. M.; Cancado, L. *Phys. Rev. B* **2008**, *77* (24), 245408.

(119) You, Y.; Ni, Z.; Yu, T.; Shen, Z. *Appl. Phys. Lett.* **2008**, *93* (16), 163112.

(120) Casiraghi, C.; Hartschuh, A.; Qian, H.; Piscanec, S.; Georgi, C.; Fasoli, A.; Novoselov, K. S.; Basko, D. M.; Ferrari, A. C. *Nano Lett.* **2009**, *9* (4), 1433–1441.

(121) Xu, Y. N.; Zhan, D.; Liu, L.; Suo, H.; Ni, Z. H.; Nguyen, T. T.; Zhao, C.; Shen, Z. X. *ACS Nano* **2011**, *5* (1), 147–152.

(122) Begliarbekov, M.; Sul, O.; Kalliakos, S.; Yang, E.-H.; Strauf, S. *Appl. Phys. Lett.* **2010**, *97* (3), 031908.

(123) Ferrari, A. C. *Solid State Commun.* **2007**, *143* (1–2), 47–57.

(124) Ferrari, A. C.; Robertson, J. *Phys. Rev. B* **2000**, *61* (20), 14095–14107.

(125) Venezuela, P.; Lazzeri, M.; Mauri, F. *Phys. Rev. B* **2011**, *84* (3), 035433.

(126) Stampfer, C.; Molitor, F.; Graf, D.; Ensslin, K.; Jungen, A.; Hierold, C.; Wirtz, L. *Appl. Phys. Lett.* **2007**, *91* (24), 241907.

(127) Xie, W.-G. W.; Lai, X.; Wang, X.-M. X.; Wan, X.; Yan, M.-L.; Mai, W.-J.; Liu, P.-Y.; Chen, J.; Xu, J. *Spectrosc. Lett.* **2014**, *47* (6), 465–470.

(128) Jorio, A. *ISRN Nanotechnol.* **2012**, *2012* (2), 1–16.

(129) Kalbac, M.; Reina-cecco, A.; Farhat, H.; Kong, J.; Kavan, L.; Dresselhaus, M. S. *ACS Nano* **2010**, *4* (10), 6055–6063.

CHAPTER 3

Electrophilic Radical Coupling at the Edge of Graphene

We report the selective functionalization of an edge of graphene via the electrografting of 4-nitrobenzene diazonium tetrafluoroborate. The edge – a single line of carbon atoms – forms during the process of cutting a graphene monolayer with an atomically sharp microtome knife. Embedded in a polymeric matrix, the just cut bare graphene edge efficiently transfers electrons to a ferricyanide probe in solution. By monitoring the electron exchange reactions of the edge upon functionalization, we observe an annihilation of the reduction and oxidation peaks of the ferricyanide probe, characteristic of the formation of a nitroaryl passivation layer on the edge of graphene. For the first time, the chemical state of a single line of carbon atoms is influenced and monitored using an electrochemical cell, therefore bypassing the usual requirements of atomic resolution characterization techniques, which often demand very clean graphene samples and vacuum processing.

3.1   Introduction

The selective functionalization of the edge of graphene aims to target the chemically active carbon atoms on the edge without interfering with the sp^2 honeycomb structure of the surface of graphene.[1,2] The abrupt interruption of the conjugated structure of graphene entails the edges with a higher chemical reactivity with respect to the basal plane,[3–11] a consequence of the rupture in symmetry of the lattice. The exclusive functionalization of the edges, however, has hardly been achieved, often relying on bulk methods such as ball-milling and plasma or by polymerizing edge functionalized polycyclic aromatic hydrocarbon monomers.[7,12,13] Here, we selectively functionalize the edge of a graphene monolayer by grafting electrophilic nitrobenzene-aryl radicals in acidic conditions.

The graphene edge is prepared by transverse sectioning of a polymeric block with an embedded graphene film[14,15] using a microtome[16] and an ultra-sharp diamond knife. The mechanical cut proceeds by breaking the lattice of graphene forming an edge. Experimentally, microtomy of graphene from highly oriented pyrolytic graphite (HOPG) yields edges in graphene composed of zig-zag and armchair segments alternated by reconstructed edges where the carbon atoms locally arrange into heptagons and pentagons[17]. Additionally, the cut is performed at the meniscus between water and air, leading to the passivation of the edges predominantly by hydrogenation and hydroxylation[18,19].

Prior to sectioning, chemical vapor deposition (CVD) graphene is transferred on top of an ultra-flat polymeric substrate containing a metallic gold contact and moulded as a replica of a polished Si/SiO₂ wafer (Figure 3.1a-i and ii). The flatness of the substrate preserves the electronic structure of the graphene layer, thereof preventing strains, curvatures or distortions.[20–23]

Next, the graphene layer covered with a film of poly (methyl methacrylate) (i.e., PMMA) is transferred on top of the polymeric substrate and electrically wired (Figure 3.1a-iii). Lastly, the PMMA/graphene/polymer stack is further re-embedded inside the polymer block (Figure 3.1a-iv). Upon cutting (Figure 3.1b), a single line of carbon atoms forms on the surface of the polymer and is constituted by the edge of graphene. Notably, the orthogonal orientation of the graphene with respect to the blade prevents the polymer to fall over and hinder the surface of the edge (Figure 3.1c), which is used as an active electrode for monitoring and

characterizing electrochemically the edge electrode upon functionalization. In fact, the variation of the electrochemical activity of a graphene edge electrode is proposed as an indirect characterization tool related to the chemical state of a single line of carbon atoms, without employing atomic resolution probe microscopy.[24–27] Specifically, the formation of a passivation layer composed of nitroaryl moieties decouples the edge electrode from the electrochemical probe, indicating the functionalization of the edge of graphene. The binding of a layer of aryl moieties is further characterized by Raman spectroscopy. In fact, the functionalization of the edges of graphene, and the nature of the functionalization (either covalent bonding or physisorption) can be addressed by studying the variation of the Raman signature of graphene.[28]
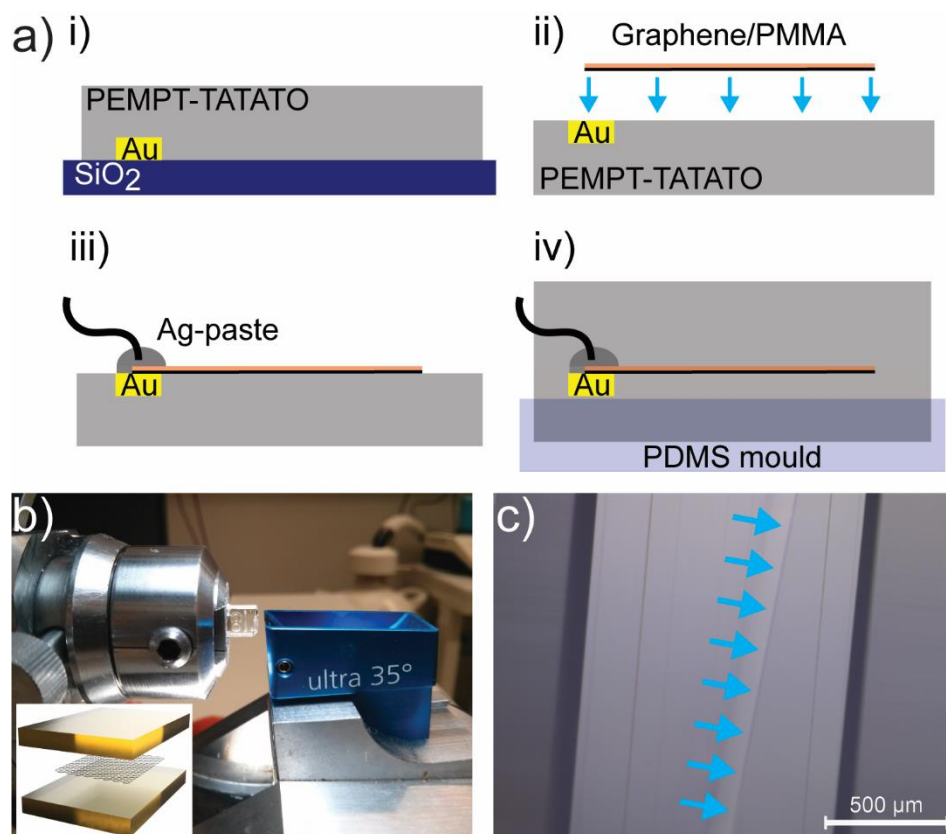
Figure 3.1. The graphene-edge electrode. a) (i) to (iv) embedding of a graphene monolayer within a polymer matrix. b) Transverse sectioning of the polymer/graphene/polymer block using microtomy. The inset illustrates the embodiment of the graphene inside the polymer. c) Optical micrograph of the trimmed surface of the polymer-graphene composite showing

the graphene edge electrode obtained after the microtomy process. The blue arrows indicate the interface between the polymer and the PMMA coated graphene.

3.2   Results and discussion

Conventional characterization tools such as scanning tunnelling microscopy (STM/AFM) or even highly sensitive elemental analysis like X-ray photoelectron spectroscopy (XPS), can hardly resolve the edge of graphene from the surrounding polymer, specifically because of the organic, insulating nature of the embedding material. The major advantage of graphene is that it is the solely conductive component of the composite sample, thus, as long as the line of carbon atoms is exposed through the trimmed surface of the block, it can be probed electrically and exposed to solvents.

While electrical measurements would require the precise deposition of metal contacts, such as chromium, on top of the trimmed polymer/graphene/polymer edge,[29] here we directly monitor the functionalization of the edge by electrochemistry. In fact, the edge of graphene is here the active electrode of an electrochemical cell. The addition of a redox probe such as ferricyanide $K_3Fe(CN)_6$ provides information on the starting electrochemical status of the edge by means of electron exchange reactions between the probe and the edge electrode. Consequently, the mass transport of ions inside the electrolytic solution together with the electron exchange reactions between the electrode and $K_3Fe(CN)_6$ are employed in order to interface the atomically thin graphene edge. This requires the edge electrode to be exposed through the surface of the polymer block. In fact, if the insulating polymer would cover the edge of graphene, a zero potential would develop across the edge electrode and the counter electrode, resulting in a zero-current flow through the cell.

Before electrochemically characterizing the edge, we first studied the quality of the graphene used to generate the edge electrode. As shown in the inset of Figure 3.2a, the Raman spectrum of graphene shows a negligible D peak (around 1340 cm^{-1}) and the intensity ratio I(2D)/I(G) between the 2D peak at 2700 cm^{-1} and the G peak at 1590 cm^{-1} is above one, characteristic of single layer graphene.

The electrochemical characterization of the graphene edge was then first carried in an aqueous solution containing 0.1 M KCl (Figure 3.2a) and in 0.1 M KCl

supplemented with 5 mM ferricyanide $K_3Fe(CN)_6$ (Figure 3.2b). In presence of ferricyanide probe, the cyclic voltammetry presents an oxidation and a reduction peak on the edge of graphene with a minimum and a maximum respectively at 0.23 V and 0.3 V, and with a peak separation of 77 mV at 50 mVs^{-1}. These oxidation and reduction peaks were not detected in KCl solutions without $K_3Fe(CN)_6$ (Figure 3.2a). The presence of such peaks suggests that the chemical state of the edge is deprived of any passivation layer that would otherwise hinder the reversible electron exchange reaction with the probe.
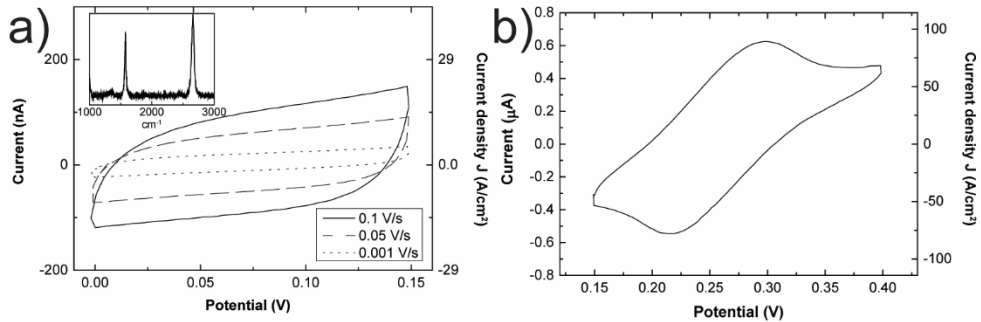
Figure 3.2. Characterization of a graphene edge by cyclic voltammetry. a) Cyclic voltammetry (CV) of a graphene edge electrode in 0.1M KCl at 0.1Vs^{-1} 0.05 Vs^{-1} and 0.01Vs^{-1}. Inset: Raman signature of a control sample of graphene on Si/SiO$_2$. b) CV of the as exposed graphene edge electrode at 0.05 Vs^{-1} in 0.1M KCl and 5mM $K_3Fe(CN)_6$.

As highlighted by Li et al.[15], at scan rates of 50 mVs^{-1} the cyclic voltammetry curve of a graphene edge electrode assumes a peak shape (Figure 3.2b), characteristic of a linear diffusion regime of the electrolytes towards the edge electrode. The associated wave current density, j_p, is described by equation (1):

$$j_p = \frac{i_p}{S} = 2.69 * 10^5 n^{3/2} C D^{1/2} v^{1/2} \quad (1)$$

Where S is the surface of the electrode, n equals to one and is the number of electrons exchanged in the redox reaction, C is the electrolyte concentration, D the diffusion constant of the electrolyte and v the scan rate. The expected theoretical current density with this model is around 10^{-3} A/cm^2 at 50 mVs^{-1}, orders of magnitude smaller than our measured peak current density (i.e. 85 A/cm^2, Figure 3.2b). Li[15], Yuan[14] and Banerjee[30] already noticed such a discrepancy in three different studies concerning graphene edge electrodes, where the current densities varied from 0.11 A/cm^2 up to 1.2 10^4 A/cm^2. Accordingly, Li and Yuan

observed a more prominent sigmoidal shape of the cyclic voltammetry curve at lower scan rates. Therefore, they proposed to apply a non-linear diffusion regime[31], described by equation (2):

$$j_s = 2\pi FDCL \left[\ln\left(4Dt\left(\frac{\pi}{w}\right)^2\right)\right]^{-1} (2)$$

where F is the Faraday constant, n the number of electrons involved in the redox reaction, C the electrolyte concentration, D the diffusion coefficient,[32] L and w the length and thickness of the graphene electrode, and t defined as t = RT/Fv where v is the scan rate. At scan rates of 50 mVs^{-1} applied to a graphene edge electrode extending over centimetres scale in length, Yuan also observed a peak shape cyclic voltammetry curve, suggesting the transition to a microscopic linear regime. Our measured steady current of 57 A/cm^2 (obtained at 50 mV s^{-1}) is therefore in agreement with the theoretical value of 100 A/cm^2 calculated with equation 2 and with an edge electrode extending over two millimetres in length. Thus, for a 2 mm long single atom thin electrode at a 50 mVs^{-1} scan rate, we assume a mixed diffusion regime characterized by both convergent and linear diffusion[33], and thus with higher measured current densities with respect to a purely linear regime.

Consequently, the convergent diffusion could alter the actual diffusion coefficient of the electrolyte, causing such a discrepancy from the theoretical peak current intensity. Other origins could be the quality of the graphene employed in previous studies, such as multilayer graphene,[15] and most importantly the preparation of the edge electrode. Particularly, we believe that a rough sectioning and processing of the graphene film have detrimental effects on the quality of the edge.

After the electrochemical characterization of the graphene edge electrode, we electro-grafted aryl radicals from a 1 mM solution of 4-nitrobenzene diazonium tetrafluoroborate (NBD; $BF_4N_2C_6H_4NO_2$) dissolved in an acidic solution of 0.1 M perchloric acid ($HClO_4$). In fact, in acidic environment N_2 is cleaved from the nitrobenzene diazonium NBD, forming an electrophilic nitro-aryl radical[34] with respect to the nucleophilic graphene. The application of a potential difference across the graphene and its counter electrode yields electrophilic reactions, where aryl radicals from NBD bind the edge of graphene (the potential difference increases the energy levels of the electron density of states of graphene overlapping the HOMO's of graphene with the LUMO's of the aryl radicals). [35]

For graphene flakes where both the basal plane and the edges are exposed, the grafting reaction most likely starts at the edge,[36] which are intrinsically more reactive because of the rupture of the sp^2 conjugation. Similarly, grain boundaries and defects have also a higher density of states, therefore competing with the aryl radical grafting reaction. In our work, the selectivity towards the edges of graphene is guaranteed by protecting the graphene basal plane with a polymeric matrix. The reduction of the current density at negative oxidative potentials among the cyclic voltammetry cycles (CV), especially between the first, second and third cycle (Figure 3.3a, black curves), is the first proof of the formation of a functional passivation layer on the edge of graphene, with chemical properties similar to those reported for the electrografting of nitrobenzene on the surface of graphene.[37] In fact, the NO_2 moieties from NBD constitute an insulating layer passivating the graphene electrode therefore preventing additional binding of nitro-aryl radicals, as confirmed by the stabilization of the CV curves after the first four cycles (Figure 3.3a red curves). As a confirmation, Figure 3.3b compares the cyclic voltammetry in presence of 5mM $K_3Fe(CN)_6$ in 0.1 M KCl performed before (black curve) and after (dashed curve) the electrografting of the nitrobenzene aryl-radicals. The formation of an insulating nitrobenzene passivation layer results in the suppression of the electron exchange with the redox-probe in the electrolyte (Figure 3.3b, dashed curve), as evidenced by the absence of the redox peaks present before the functionalization (Figure 3.3b, black curve).
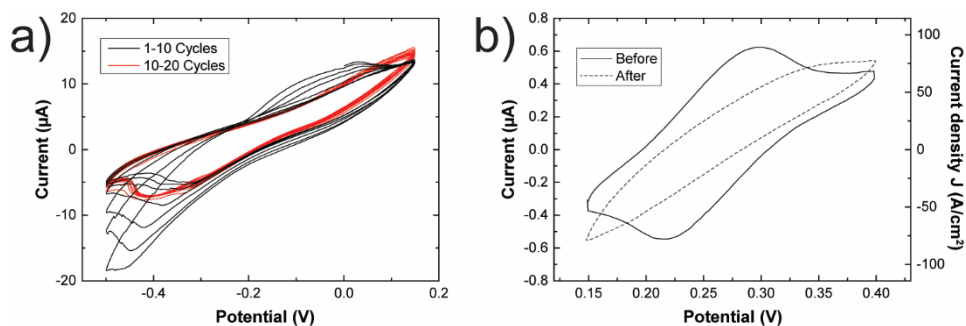

Figure 3.3. Functionalization of the edge of graphene. a) Current-voltage curves (CVs) of the graphene edge electrodes in 4-nitrobenzene diazonium in 0.1M $HClO_4$ at 0.05 Vs^{-1}. b) CVs at 0.05 Vs^{-1} CV in 0.1M KCl and 5mM $K_3Fe(CN)_6$ before (black curve), and after (dashed curve) the electrografting of the edge.

Subsequently, the functionalization of the edge electrode is investigated by Raman spectroscopy, using a low intensity power laser at 532 nm, shone directly over the polymer/graphene/polymer stack. The red and black crosses in Figure 3.4a highlight the location on the sample where the Raman was performed. The inset compares the Raman spectra of the polymer before (red line) and after (blue line) electrografting to exclude the adsorption of nitrobenzene on the polymeric surface. The Raman fingerprints of the polymer arise around 1300 cm^{-1}, 1450 cm^{-1}, 1600 cm^{-}1 and 2600 cm^{-1}, without overlapping with the D, G and 2D bands of graphene.
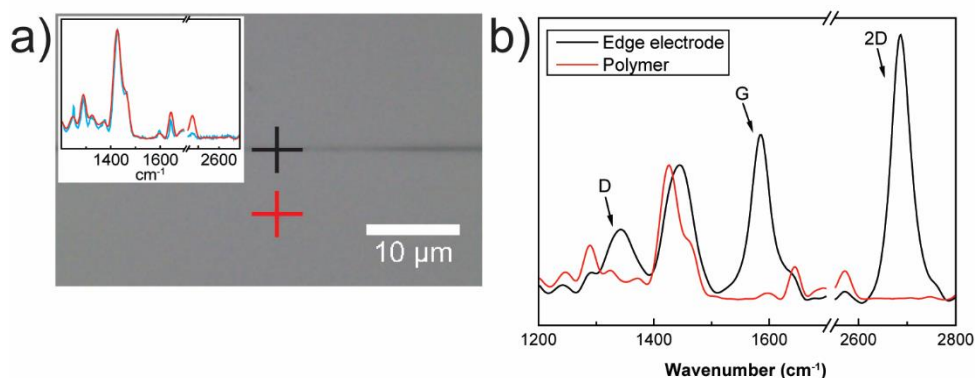
Figure 3.4. Raman spectroscopy of the edge of graphene. a) Optical micrograph of the edge electrode prepared via microtomy. Inset: comparison between the embedding polymer before (red) and after (blue) functionalization of the edge electrode and normalized over the peak around 1450 cm^{-1}. b) Comparison of the Raman signature of the graphene edge and of the polymer embedding only at the positions indicated by the black and red crosses in panel a).

Notably, the Raman signature of graphene (black curve in Figure 3.4b) differentiates from the polymer (red curve in Figure 3.4b) allowing the characterization of the graphene edge upon diazonium coupling. Particularly, we monitor the variation of the intensity I(D) of the D peak with respect the G peak. In fact, the covalent functionalization of graphene converts the carbons of the honeycomb lattice from sp^2 to sp^3, introducing breaks in the lattice symmetry of graphene and activating the Raman emission mode yielding the D peak. This mode is associated to the stretching of the carbon bonds and requires a defect to be activated.[38] The edges naturally break the periodic lattice of graphene and present an intrinsic D signature,[28,38] as observed by the Raman spectra of graphene in

Figure 3.4b. The G peak, instead, is an antisymmetric stretching of the carbon bonds within the hexagons of the lattice of graphene.[38] Upon chemical functionalization, the I(D)/I(G) ratio monitors the density and the modification of the sp^3 centres in the lattice of graphene, thus the proceeding of the reaction. At the edges particularly, the formation of bonds influences the vibrations modes activating the D band, modifying its intensity.

Accordingly, upon electrografting (Figure 3.5a), we observe the increase of the D peak intensity with respect to the intensity of the G peak, consequently to the covalent functionalization of the edge.[39,40] The Raman results are in agreement with the cyclic voltammetry study: in presence of nitrobenzene diazonium, the edge electrode shows an initial non reversible wave at negative potential (Figure 3.3a), which is attenuated in the following cycles. The negative wave rises from the reduction of diazonium moieties into radicals that attack the electrode forming a blockade layer physically hindering the electron exchange reaction from the edge electrode to the redox probe.[35,41]
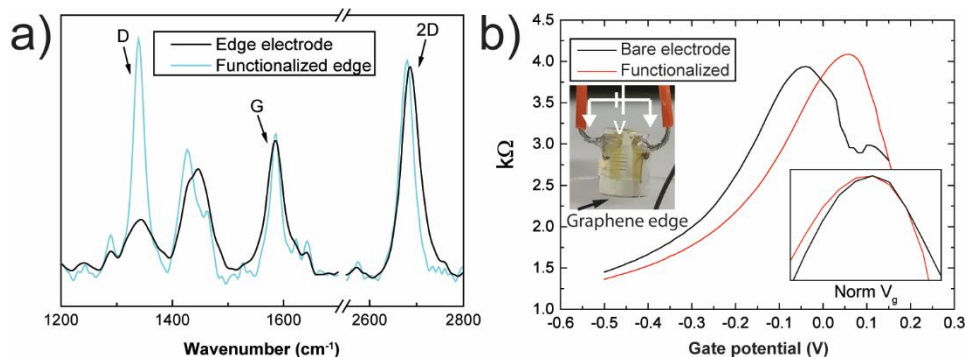

Figure 3.5. Graphene edge field effect transistor. a) Comparison between the Raman spectra of the edge of graphene before, and after electrografting of nitrobenzene. b) Gate dependent conductivity curves of bare (black curve) and functionalized graphene edge (red curve). Left inset: a graphene field-effect transistor embedded in the polymeric matrix and sectioned via microtomy. The white arrows indicate the Drain and the Source. The black arrow indicates the exposed graphene edge electrode. Right inset: conductivity curves around the Dirac point and normalized at the gate potential of the charge neutrality point.

Cyclic voltammetry in Fig. 3.2a and b, and the Raman in Fig 3.5a, therefore show the formation of a uniform passivation layer on the edge of graphene. In order to quantify the amount of atoms involved in the reaction, we can model a minimum amount of nitrobenzene grafted to the edge electrode. Referring to density

functional theory DFT calculations for the spontaneous grafting of aryl radicals on the edge of graphene, we can estimate that both zig-zag and armchair edges bind 50% of the carbon atoms composing the edge[42]. In a 2 mm long edge electrode there are around ~300 10^{-15} mol of carbon atoms, therefore resulting in the functionalization of 150 10^{-15} mol of carbon atoms at the edge.

At last, a graphene field effect transistor (GFET) was used to investigate the selectivity of the electrografting at the edges. For that, a graphene transistor is embedded within the polymer matrix, which edge is exposed via microtomy. The transistor (left inset in Figure 3.5b) is composed of a drain and a source embedded in the polymer (white arrows). The gate potential is applied to edge electrode via an electrolytic solution of 1 M KCl in ultra pure water.[43] By comparing the transistor characteristics of the graphene before and after the functionalization (respectively black line and red line in Figure 3.5b), shows that the conductivity of graphene is not affected by the electrografting. In fact, the two curves show the same conductivity values around the charge neutrality point, as well as far apart from the Dirac point. Particularly, the basal plane is chemically preserved during electrografting and only the edge is functionalized (the right inset in Figure 3.5b shows the normalized conductivity curves at the charge neutrality points, normalized also with respect to the gate voltage). These results indicate the preservation of the basal plane of graphene during electrografting and the selective functionalization of the edge. In fact, in the case of surface functionalization, the conversion from sp^2 to sp^3 of the carbon atoms composing the honeycomb lattice of graphene would affect its electrical properties, lowering its conductivity and modifying the shape of the resistivity curve close to the neutrality point.[44,45]

3.3   Conclusions

To conclude, the present chapter reports the selective functionalization of a graphene edge prepared by precise transverse microtomy of a PMMA coated graphene layer embedded inside a polymer matrix. Interestingly, the fine sectioning appears to offer important advantages in the preparation of the edge electrode, first re-conciliating theoretical models and experimental results for the convergent diffusion of electrolytes towards sub-nanometric electrodes.

The functionalization step is confirmed through the measurement of the passivation abilities of the nitro-functionalities ahead of the graphene edge against a ferricyanide probe. In fact, the formation of an electrically passivating layer, specifically the assembly of NO_2 functionalities, prevents the reduction of the ferricyanide ions at the graphene edge electrode.

The grafting of nitrobenzene at the edge of graphene was also characterized by Raman spectroscopy: the rise in intensity of the D band of the graphene edge confirms the covalent coupling of the nitroaryl radicals selectively on the edge electrode. Conductivity measurements, also, indicate the selective functionalization of the edges, while preserving the integrity of the basal plane. Furthermore, the possibility of a physisorbed layer can be neglected given the established high reactivity of nitrobenzene radicals in acidic conditions.[46]

Importantly, the choice of a NO_2 terminated functional group has the double advantage of being easily detected by means of a redox probe and can be used as a chemical precursor for further functionalization of the edges of graphene.

One of the most important challenges in the chemistry of graphene is to only functionalize the carbon atoms on the edges, for example in edge-based sensors such as nanopores or nanogaps[47] or in nanoribbons graphene field-effect transistors.[48] Thus, the controlled edge chemistry together with methods of characterization of the edge state will open new perspectives to tune the properties of graphene devices in applications ranging from molecular sensing to consumer electronics.

3.4   References

(1)   Girit, C. O.; Meyer, J. C.; Erni, R.; Rossell, M. D.; Kisielowski, C.; Yang, L.; Park, C.-H.; Crommie, M. F.; Cohen, M. L.; Louie, S. G.; Zettl, A. *Science* **2009**, *323* (5922), 1705–1708.

(2)   Bellunato, A.; Arjmandi Tash, H.; Cesa, Y.; Schneider, G. F. *ChemPhysChem* **2016**, *17* (6), 785–801.

(3)   Wang, X.; Dai, H. *Nat. Chem.* **2010**, *2* (8), 661–665.

(4)   Cervantes-Sodi, F.; Csányi, G.; Piscanec, S.; Ferrari, A. C. *Phys. Rev. B* **2008**, *77* (16), 165427.

(5)   Soldano, G. J.; Juarez, M. F.; Teo, B. W. T.; Santos, E. *Carbon* **2014**, *78*, 181–189.

(6)   Diankov, G.; Neumann, M.; Goldhaber-Gordon, D. *ACS Nano* **2013**, *7* (2), 1324–1332.

(7)   Kato, T.; Jiao, L.; Wang, X.; Wang, H.; Li, X.; Zhang, L.; Hatakeyama, R.; Dai, H. *Small* **2011**, *7* (5), 574–577.

(8)   Mooste, M.; Kibena, E.; Kozlova, J.; Marandi, M.; Matisen, L.; Niilisk, A.; Sammelselg, V.; Tammeveski, K. *Electrochim. Acta* **2015**, *161*, 195–204.

(9)   Kirkman, P. M.; Güell, A. G.; Cuharuc, A. S.; Unwin, P. R. *J. Am. Chem. Soc.* **2014**, *136* (1), 36–39.

(10)   Jiang, D. E.; Sumpter, B. G.; Dai, S. *J. Phys. Chem. B* **2006**, *110* (47), 23628–23632.

(11)   Greenwood, J.; Phan, T. H.; Fujita, Y.; Li, Z.; Ivasenko, O.; Vanderlinden, W.; Van Gorp, H.; Frederickx, W.; Lu, G.; Tahara, K.; Tobe, Y.; Uji-I, H.; Mertens, S. F. L.; De Feyter, S. *ACS Nano* **2015**, *9* (5), 5520–5535.

(12)   Hung, Y.-J.; Hofmann, M.; Cheng, Y.-C.; Huang, C.-W.; Chang, K.-W.; Lee, J.-Y. *RSC Adv.* **2016**, *6* (15), 12398–12401.

(13)   Jeon, I.-Y.; Shin, Y.-R.; Sohn, G.-J.; Choi, H.-J.; Bae, S.-Y.; Mahmood, J.; Jung, S.-M.; Seo, J.-M.; Kim, M.-J.; Wook Chang, D.; Dai, L.; Baek, J.-B. *Proc. Natl. Acad. Sci. U. S. A.* **2012**, *109* (15), 5588–5593.

(14)   Yuan, W.; Zhou, Y.; Li, Y.; Li, C.; Peng, H.; Zhang, J.; Liu, Z.; Dai, L.; Shi, G. *Sci.*

Rep. **2013**, *3* (1), 2248.

(15) Li, K.; Jiang, J.; Dong, Z.; Luo, H.; Qu, L. *Chem. Commun.* **2015**, *51* (42), 8765–8768.

(16) Xu, Q.; Rioux, R. M.; Dickey, M. D.; Whitesides, G. M. *Acc. Chem. Res.* **2008**, *41* (12), 1566–1577.

(17) Mohanty, N.; Moore, D.; Xu, Z.; Sreeprasad, T. S.; Nagaraja, A.; Rodriguez, A. A.; Berry, V. *Nat. Commun.* **2012**, *3*, 844.

(18) Jiang, L.; Wang, J.; Liu, P.; Song, W.; He, B. *RSC Adv.* **2018**, *8* (20), 11216–11221.

(19) Seitsonen, A. P.; Saitta, a. M.; Wassmann, T.; Lazzeri, M.; Mauri, F. *Phys. Rev. B* **2010**, *82* (11), 115425.

(20) Castro Neto, a. H.; Peres, N. M. R.; Novoselov, K. S.; Geim, A. K. *Rev. Mod. Phys.* **2009**, *81* (1), 109–162.

(21) Wu, Q.; Wu, Y.; Hao, Y.; Geng, J.; Charlton, M.; Chen, S.; Ren, Y.; Ji, H.; Li, H.; Boukhvalov, D. W.; Piner, R. D.; Bielawski, C. W.; Ruoff, R. S. *Chem. Commun.* **2013**, *49* (7), 677–679.

(22) Pereira, V. M.; Castro Neto, A. H. *Phys. Rev. Lett.* **2009**, *103* (4), 046801.

(23) Aslani, M.; Garner, C. M.; Kumar, S.; Nordlund, D.; Pianetta, P.; Nishi, Y. *Appl. Phys. Lett.* **2015**, *107* (18), 183507.

(24) Lin, Y.-C.; Lu, C.-C.; Yeh, C.-H.; Jin, C.; Suenaga, K.; Chiu, P.-W. *Nano Lett.* **2012**, *12* (1), 414–419.

(25) Liu, J.; Li, B.-W.; Tan, Y.; Giannakopoulos, A.; Sanchez-Sanchez, C.; Beljonne, D.; Ruffieux, P.; Fasel, R.; Feng, X.; Müllen, K. *J. Am. Chem. Soc.* **2015**, *137* (18), 6097–6103.

(26) Cai, J.; Ruffieux, P.; Jaafar, R.; Bieri, M.; Braun, T.; Blankenburg, S.; Fasel, R.; Muoth, M.; Seitsonen, A. P.; Saleh, M.; Feng, X.; Mu, K.; Müllen, K. *Nature* **2010**, *466* (7305), 470–473.

(27) Huang, H.; Wei, D.; Sun, J.; Wong, S. L.; Feng, Y. P.; Neto, a H. C.; Wee, A. T. S. *Sci. Rep.* **2012**, *2*, 983.

(28) Casiraghi, C.; Hartschuh, A.; Qian, H.; Piscanec, S.; Georgi, C.; Fasoli, A.;

Novoselov, K. S.; Basko, D. M.; Ferrari, A. C. *Nano Lett.* **2009**, *9* (4), 1433–1441.

(29)   Wang, L.; Meric, I.; Huang, P. Y.; Gao, Q.; Gao, Y.; Tran, H.; Taniguchi, T.; Watanabe, K.; Campos, L. M.; Muller, D. a; Guo, J.; Kim, P.; Hone, J.; Shepard, K. L.; Dean, C. R. *Science* **2013**, *342* (6158), 614–617.

(30)   Banerjee, S.; Shim, Â. J.; Rivera, Â. J.; Jin, X.; Estrada, D.; Solovyeva, V.; Shim, J.; Rivera, J.; You, X.; Pak, J.; Pop, E.; Aluru, N.; Bashir, R. *ACS Nano* **2013**, *7* (1), 834–843.

(31)   Brownson, D. A. C.; Kampouris, D. K.; Banks, C. E. *Chem. Soc. Rev.* **2012**, *41* (21), 6944–6976.

(32)   Konopka, S. J.; McDuffie, B. *Anal. Chem.* **1970**, *42* (14), 1741–1746.

(33)   Banks, C. E.; Davies, T. J.; Wildgoose, G. G.; Compton, R. G. *Chem. Commun.* **2005**, *0* (7), 829–841.

(34)   Le Floch, F.; Simonato, J.-P.; Bidan, G. *Electrochim. Acta* **2009**, *54* (11), 3078–3085.

(35)   Paulus, G. L. C.; Wang, Q. H.; Strano, M. S. *Acc. Chem. Res.* **2013**, *46* (1), 160–170.

(36)   Lim, H.; Lee, J. S.; Shin, H.-J.; Shin, H. S.; Choi, H. C. *Langmuir* **2010**, *26* (14), 12278–12284.

(37)   Greenwood, J.; Phan, T. H.; Fujita, Y.; Li, Z.; Ivasenko, O.; Vanderlinden, W.; Van Gorp, H.; Frederickx, W.; Lu, G.; Tahara, K.; Tobe, Y.; Uji-I, H.; Mertens, S. F. L.; De Feyter, S. *ACS Nano* **2015**, *9* (5), 5520–5535.

(38)   Ferrari, A. C.; Basko, D. M. *Nat. Nanotechnol.* **2013**, *8* (4), 235–246.

(39)   Sharma, R.; Baik, J. H.; Perera, C. J.; Strano, M. S. *Nano Lett.* **2010**, *10* (2), 398–405.

(40)   Wang, Q. H.; Jin, Z.; Kim, K. K.; Hilmer, A. J.; Paulus, G. L. C.; Shih, C.-J.; Ham, M.-H.; Sanchez-Yamagishi, J. D.; Watanabe, K.; Taniguchi, T.; Kong, J.; Jarillo-Herrero, P.; Strano, M. S. *Nat. Chem.* **2012**, *4* (9), 724–732.

(41)   Le Floch, F.; Simonato, J.-P.; Bidan, G. *Electrochim. Acta* **2009**, *54* (11), 3078–3085.

(42)   Jiang; D.; Sumpter, B. G.; Dai, S. *J. Phys. Chem. B* **2006**, *110* (47), 23628–23632.

(43)   He, R. X.; Lin, P.; Liu, Z. K.; Zhu, H. W.; Zhao, X. Z.; Chan, H. L. W.; Yan, F. *Nano Lett.* **2012**, *12* (3), 1404–1409.

(44)   Sinitskii, A.; Dimiev, A.; Corley, D. A.; Fursina, A. A.; Kosynkin, D. V; Tour, J. M. *ACS Nano* **2010**, *4* (4), 1949–1954.

(45)   Farmer, D. B.; Roksana, G. M.; Perebeinos, V.; Lin, Y. M.; Tuievski, G. S.; Tsang, J. C.; Avouris, P. *Nano Lett.* **2009**, *9* (1), 388–392.

(46)   Bélanger, D.; Pinson, J. *Chem. Soc. Rev.* **2011**, *40* (7), 3995.

(47)   Arjmandi-Tash, H.; Belyaeva, L. A.; Schneider, G. F. *Chem. Soc. Rev.* **2015**, *45* (3), 476–493.

(48)   Fu, W.; Jiang, L.; van Geest, E. P.; Lima, L. M. C.; Schneider, G. F. *Adv. Mater.* **2017**, *29* (6), 1603610.

CHAPTER 4

Dynamic tunnelling junctions at the atomic intersection of two twisted graphene edges

The investigation of the transport properties of single molecules by flowing tunnelling currents across extremely narrow gaps is relevant for challenges as diverse as the development of molecular electronics and sequencing of DNA. The achievement of well-defined electrode architectures remains a technical challenge, especially due to the necessity of high precision fabrication processes and the chemical instability of most bulk metals. Here, we illustrate a continuously adjustable tunnelling junction between the edges of two twisted graphene sheets. The unique property of the graphene electrodes is the fact that the sheets are rigidly supported all the way to the atomic edge. By analysing the tunnelling current characteristics, we also demonstrate that the spacing across the gap junction can be controllably adjusted. Finally, we demonstrate the transition from the tunnelling regime to contact and the formation of an atomic sized junction between the two edges of graphene.

4.1   Introduction

The great potential that graphene offers as an electrode material for addressing individual molecules has been widely recognized. This is of particular importance in the study of electron transport across individual molecules[1–3], in the development of molecular electronics[4,5], and for direct electron current readout in the quest of sequencing biopolymers[6,7]. In a typical essay in any of these fields of research, a voltage is applied across a nanoscale gap between two metallic electrodes where the measured current contains information on the nature of the molecule bridging this gap. In absence of molecules in the gap the current that flows is a pure tunnelling current, resulting from the finite overlap of the exponentially decaying electron wave functions on either side of the gap. Currently, nearly all experiments have been performed using some form of break junction devices with metallic electrodes, mostly gold[8]. Metallic electrodes pose serious limitations, associated with poor characterization and poor reproducibility of the molecule-electrode bonding configurations. The size and shapes of the metal electrodes are generally unknown, the shape and surface coverage are subject to rapid chemical and geometrical modifications, and the radius of curvature of the electrodes is much larger than the size of the molecules under study, notably in the case of the widely used gold electrodes at room temperature[9]. The large size and the poorly known shape of the electrodes limits accurate comparison with computational modelling[10]. Moreover, (gold) metal electrodes offer a wide variety of choice for the position of the molecules between the electrodes and for the bonding motifs, which lead to more unknowns in the analysis of the observations[11]. The size of the electrodes is of particular interest in developing direct current readout for sequencing of biopolymers, in which case the extent of the electrodes in the direction along the length of the biopolymer should ideally be smaller than the size of the individual building blocks forming the biopolymer.

For many of those concerns the use of graphene edge electrodes offers a promising approach. Graphene is a good conductor of electricity and the size of the layer in the direction perpendicular to its plane is given by the size of just a single carbon atom. Further benefits of the use of graphene include the stability of the covalently bonded lattice, the fact that image charges are nearly absent, which greatly simplifies the comparison with computational models, the fact that the

edges offer a limited range of bonding motifs, which can be further exploited by edge-specific chemical decorations. Graphene electrodes can be contacted via π-stacking[3,12] or through covalent bonds[13–15], introducing selective docking sites for molecular trapping and characterization[16,17].

Several approaches towards exploiting graphene electrodes for addressing individual molecules have already been reported, where the challenge is the required small size of the gap between the electrodes. By exploiting the surface tension of an evaporating solvent a freely suspended sheet of graphene can be torn into forming a tunnelling junction on a Si/SiO$_2$ substrate[18]. Alternatively, feedback-controlled electroburning can be used for fabricating graphene nanogaps[1–4,19], or high-resolution electron-beam patterning in combination with oxygen plasma etching[20] . These methods have in common that the size of the gap cannot be precisely and freely designed, and the resulting junctions are static: once created, the size of the nanogap cannot be adjusted. A drawback in the context of applications for sequencing is the fact that both the electrodes are sculpted on a common substrate that covers the gap between the electrodes, physically preventing the flow of molecules across the gap.

4.2   Results and discussion

In this chapter, the fabrication and characterization of two twisted graphene edge electrodes supported to the atomic edge is described, where electrons tunnel between the two carbon atoms facing each other. Using piezoelectric actuators of a modified scanning tunnelling device the two graphene edges are positioned relative to each other with sub-atomic precision, leaving an empty gap between the two facing carbon atoms that could be eventually used for the translocation of molecules (Figure 4.1).
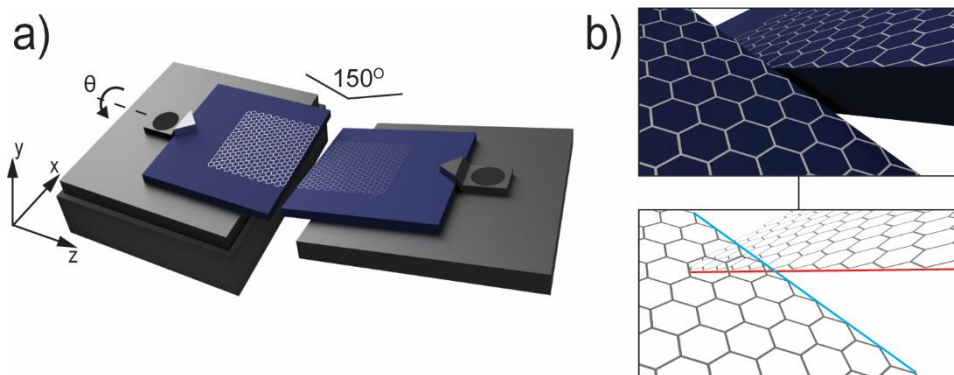
Figure 4.1. Schematic illustration of the method for producing a dynamically adjustable graphene-graphene junction. a) Two independent graphene electrodes, each supported to the atomic edge, can be approached edge-to-edge with sub-atomic precision, creating a junction between two single rows of carbon edge atoms. The electrodes are twisted and tilted in order to form a well-defined intersection point between the two electrodes, and for preventing mechanical contact of the supports. The twist angle Θ is between 10 and 45 degrees. b) Illustration of the carbon-carbon point contact formed at the intersection of two graphene sheet edges.

Two independent supports with atomically sharp edges were prepared by cleaving-off a polished Si/SiO_2 wafer, after introducing a notch on the surface at the edge of the wafer with a diamond knife. The notch initiates a crack that develops along a high-symmetry crystallographic direction of the silicon, yielding straight edge profiles. The supports are mounted over a slit in a holder, facing each other at a distance of about a millimetre (Figure 4.2a). A graphene sheet supported by a layer of polycarbonate[21] (PCA) is deposited on top of the two wafer halves, bridging the gap between them (Figure 4.2b). The graphene is obtained by chemical vapor deposition (CVD) on a copper film, followed by spin coating PCA to cover the graphene. The copper is etched in 0.5 M ammonium persulfate, while the polymer works as support. The film is rinsed three times with ultrapure water to remove residuals of ammonium persulfate, and transferred over the wafers. Subsequently, the holder with the wafers and the polymer-supported graphene are exposed from below to an isotropic H_2 plasma. The plasma removes the graphene suspended over the slit, while the polymer protects the parts that cover the SiO_2 supports.
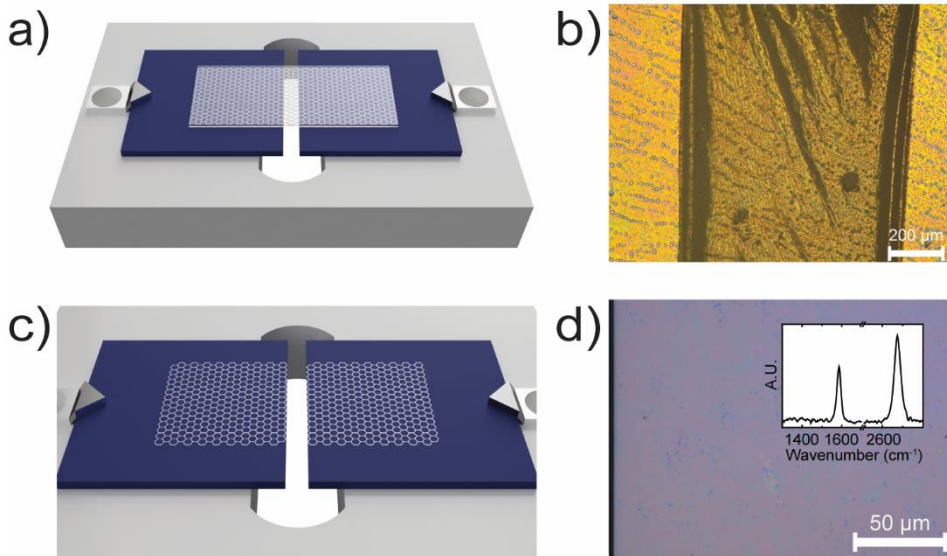
Figure 4.2. Fabrication of graphene edge electrodes. a) Schematic illustration of a graphene layer protected by a polymer coating (white shading covering the graphene) bridging the gap between two Si/SiO$_2$ wafer halves mounted over the slit of a holder. b) Optical microscopy image showing the two Si/SiO$_2$ wafer halves (yellow) bridged by the freestanding polymer-coated graphene (dark yellow). c) Schematic illustration of the setup after plasma etching and polymer removal. d) Optical microscopy image of the supported graphene edge (visible at the far left) after polymer removal. The inset shows a Raman spectrum of the graphene after plasma etching and polymer removal.

Next, the PCA coating is dissolved in chloroform, the assembly is rinsed in methanol, isopropanol and the resulting graphene edge electrodes are imaged using optical microscopy (Figure 4.2c, d). The protective role of the polymer towards the highly reactive hydrogen plasma is confirmed by the presence of a strong G peak[22] around 1590 cm^{-1} and a negligible D peak around 1340 cm^{-1}.

Prior to performing tunnelling measurements, we characterized the graphene edge electrodes using scanning Raman spectroscopy, scanning electron microscopy (SEM) and atomic force microscopy (AFM), see Figure 4.3. The mapping in Figure 4.3a overlaps Raman peak intensity distributions over the surface of the electrode near the edge, with the 2D band around 2700 cm^{-1} shown in green, the G band at 1590 cm^{-1} shown in blue, and the D band at 1340 cm^{-1} shown in red. The graphene extends uniformly all over the surface of the SiO$_2$ substrate, beyond which the mapping appears black (left side of the image). The uniformity of the

colour scale illustrates the quality of the graphene, and representative single-spot spectra acquired at the edge of the support are shown in Figure 4.3b. The ratio of the intensities of the 2D and the G peaks is in agreement with the ratio expected for monolayer graphene, while the onset of a D peak at the edge is characteristic of the breaking in the symmetry of the graphene lattice[23]. The relative intensity of the D band with respect to the G and 2D bands is an indicator of the uniformity of the graphene lattice[24]. The bright yellow spot at the right side of the image is attributed to a polymer residue. Such polymer residues could be removed by high-temperature annealing. However, the high temperatures required for cleaning the surface may induce ruptures of the graphene sheet, therefore displacing the graphene from the edge of the substrate due to differences in thermal expansion coefficients of graphene and Si/SiO_2. Accordingly, we avoid annealing and accept the presence of some polymer residues.
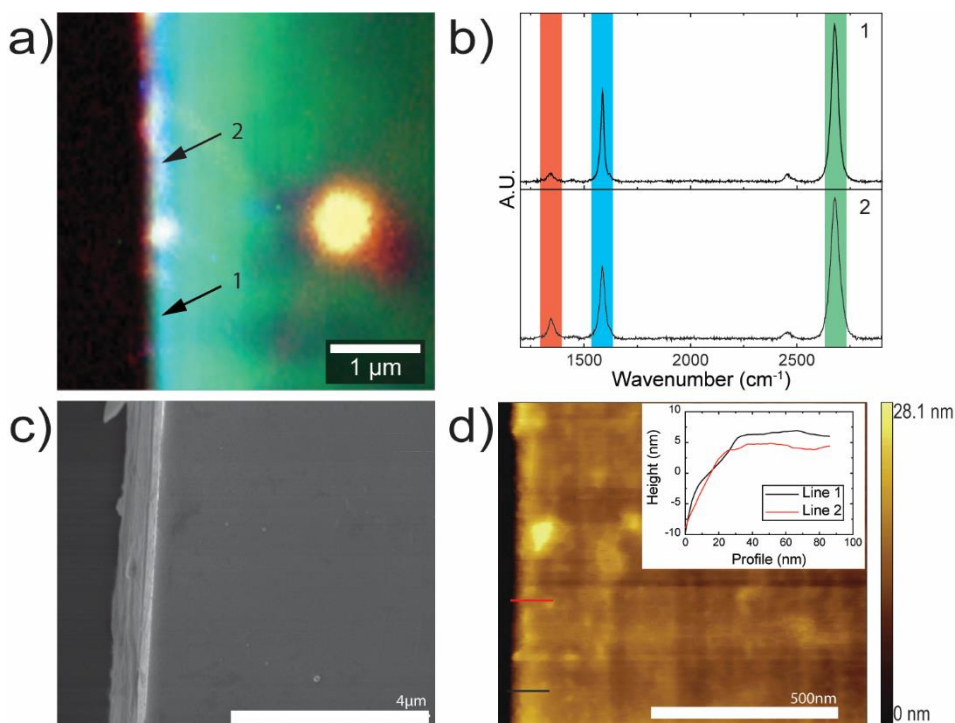

Figure 4.3. Characterization of the graphene edge. a) Overlay of the Raman mapping of the D band (1340 cm^{-1}, red tone), G band (1590 cm^{-1}, blue tone) and 2D band (2667 cm^{-1}, green tone). The large yellow island is due to a polymer residue. b) Raman spectra of two single points on the edge, as marked in panel a. c) SEM micrograph of the edge electrode. d) AFM

topography of a graphene edge electrode. Inset: AFM height profiles of the graphene extending to the edge of the support.

Figure 4.3c shows a SEM micrograph of a graphene edge electrode on Si/SiO$_2$ support. The small darker regions indicate the formation of local graphene bi-layer islands during the CVD growth[25]. Additionally, small white features are attributed to polymer residues. We observe no variations in the colour contrast of the graphene film on top of the SiO$_2$ in proximity of the edge, suggesting the continuous extension of the film.

Neither SEM nor Raman can resolve the extension of the graphene sheet to the edge of its substrate down to the nanometer scale. We refine the characterization towards higher resolution by performing atomic force microscopy (AFM). Special care was taken in choosing the appropriate scanning parameters in order to be able to image at the sharp edge. The line-scan direction was chosen perpendicular to the edge of the wafer and the feedback was set to a low value in order to prevent fast descent of the cantilever once beyond the edge, and subsequent crashing. Figure 4.3d shows a tapping mode AFM topography image of the surface of graphene up to the edge and beyond the wafer support (black area on the left in Figure 4.3d). The bright areas correspond to higher regions such as graphene bi-layer areas typical of CVD grown graphene, as well as polymer residues accumulated near the edges of the graphene film during the removal of the polymer. We observe uniformity of the colour contrast up to the edge of the wafer within the AFM resolution (~5 nm). The inset in Figure 4.3d shows two height profiles perpendicular to the edge electrode.

The final test of whether graphene extends to the edge is in the observation of a tunnelling current. Tunnelling currents decay exponentially with the distance between the electrodes. If the graphene would be displaced from the edge of the support by more than a few nanometres, no tunnelling current could be measured. Tunnel junctions between two graphene edges were formed by approaching a pair of edge electrodes using a modified piezo actuator of a scanning tunnelling microscope (STM), operating under ambient conditions. The piezo actuator permits the controlled approach into tunnelling distance of the graphene layers on the Si supports. The wafers are tilted downwards forming an angle of 15° in order to avoid the Si substrates hampering the approach of the electrodes. A twist of one of the supports around the Z-axis (see Figure 4.1) leads to the formation of a single

point of intersection between the two graphene edges. Ideally, two single carbon atoms meet at the intersection, constituting an atomic tunnelling junction. Piezo actuator controlled displacements in X and Y directions permit selecting fresh spots for tunnelling.

Figure 4.4 shows an example of the measured current-voltage (IV) dependence of a graphene-graphene tunnel junction, for a bias voltage sweep of $\pm$ 1.0 V. The sigmoidal shape of the curve is a distinctive feature of electron tunnelling through a potential barrier. Here, the barrier height is determined by the work function, and the width of the barrier is given by the distance between the graphene edges. We employ the Simmons model for tunnelling through symmetric barriers[26] to fit the size of the vacuum gap and the height of the work function (see supporting information). From this fit we obtain a distance of 1.3 nm (± 5%), and an effective work function Φ = 1.4 eV (± 8%). The work function is significantly lower than the values reported from Kelvin probe microscopy on the face of graphene sheets, which are in the range from 4.45 to 4.8 eV, depending on the doping.[27] Much lower work functions, ranging from 0.25 to 1.0 eV are typically found from Simmons fits and edge tunnelling, as reported for graphene nanogaps obtained from electroburning.[2,3,5] In our case, the chemistry of the edges under fabrication conditions influences the work function.[28–30] Since we etch the sample in H_2 plasma we assume most of the carbon dangling bonds to be hydrogenated, which reduces the work function below 4eV.[31] The presence of chemisorbed and physisorbed species at the edges of the electrodes under ambient conditions is expected to further reduce the work function.[3]
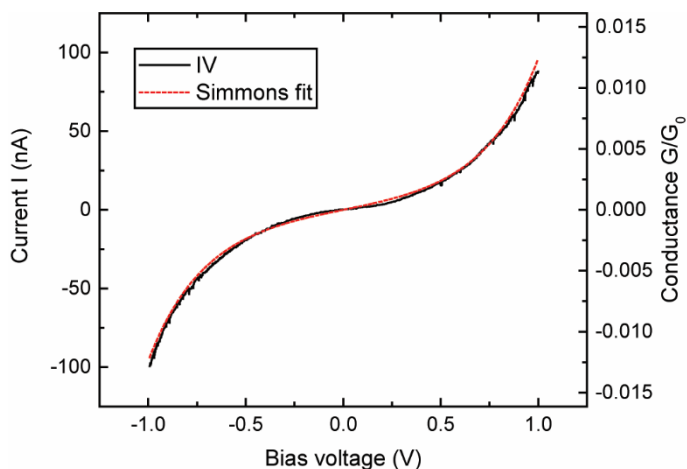
Figure 4.4. Current-voltage characteristics of the junction in the tunnelling regime. Black curve, experimental current-voltage characteristic. Red curve, fit to the Simmons model with a vacuum gap size of 1.3 nm, barrier height of 1.4 eV. The left axis shows the measured current, while the right axis shows the conductance proportional to the quantum of conductance G0 approximated to 77.5 µS.

The independent positioning of our edge electrodes allows fine adjustment of the gap. Figure 4.5 shows a current-distance curve, I(z), measured at a bias voltage of V = 0.1 V, black curve. We fit the measured I(z) curve with an exponential function (in red) using the effective work function Φ as obtained from the IV characteristic in Figure 4.4. Since the shape of the curve is fully determined and only the exponential pre-factor is freely adjustable, the fit provides strong confirmation of the vacuum tunnelling origin of the current. We are not aware of any previous methods for recording the tunnelling current between the edges of two graphene sheets as a function of their distance. Although the measured curve still has some irregularities due to vibrations and possibly due to fluctuations in adsorbents, the observed exponential dependence confirms that we are able to tune the gap of a tunnel junction with sub-nanometric precision.
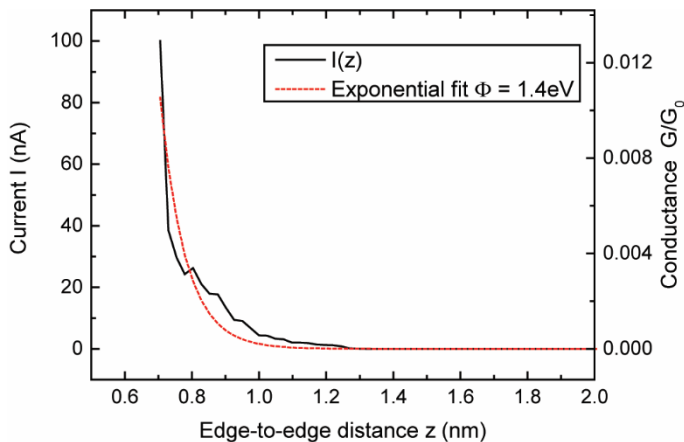

Figure 4.5. Electrical characterization of a dynamically adjustable graphene-graphene edge tunnelling junction under ambient conditions. Current-distance, I(z), characteristics of the tunnel junction (black line). Red curve, exponential fit for tunnelling against gap size, adopting the barrier height obtained from the fit in Figure 4.4. The left axis shows the measured current, while the right axis shows the conductance proportional to the quantum of conductance G_0 approximated to 77.5 µS.

Moving the graphene electrodes closer together the electron transport across the junction transforms from the tunnelling to the contact regime. The twisted configuration should lead to an initial point contact between single carbon atoms at the intersection of the two edges of the graphene electrodes. Figure 4.6a shows an I(z) curve for a junction across the transition from the tunnel regime to the point contact regime, at a bias voltage of 0.1 V, black curve. Following the exponential increase of the current in tunnel regime we observe a kink at about 3 µA, indicating a switch to contact. Pushing the electrodes further into contact yields the current to increase further, approximately linearly. The onset of the linear regime is found at a contact resistance of around 30 kΩ, which is of the order of the quantum of resistance expected for point contacts, $R_q = 12.9$ kΩ, equivalent to a quantum of conductance G_0 = 77.5 µS. Figure 4.6b shows a histogram of the current values observed at the kink, for 29 independent junctions formed. The histogram shows that, statistically, the onset of the linear resistance regime is found at 28 kΩ or 0.46 G_0. Note that this resistance is the actual contact quantum resistance, measured in series with the resistance of the graphene electrodes (see supporting information). The estimated quantum point contact resistance is 11±3 kΩ or 1.2±0.3 G_0, which is in good agreement with the value calculated for carbon-carbon atomic contacts at low strain[32], and with the quantum of resistance.

The linear trend to higher conductance after the kink suggests that the contact between the edges of graphene of the two graphene sheets can be increased by indentation. Note that we are only indenting the electrodes by a few atomic distances. The linear trend in conductance agrees with the two-dimensional geometry of the graphene sheets, and differs from the nearly quadratic growth of conductance for three-dimensional metallic contacts[9].
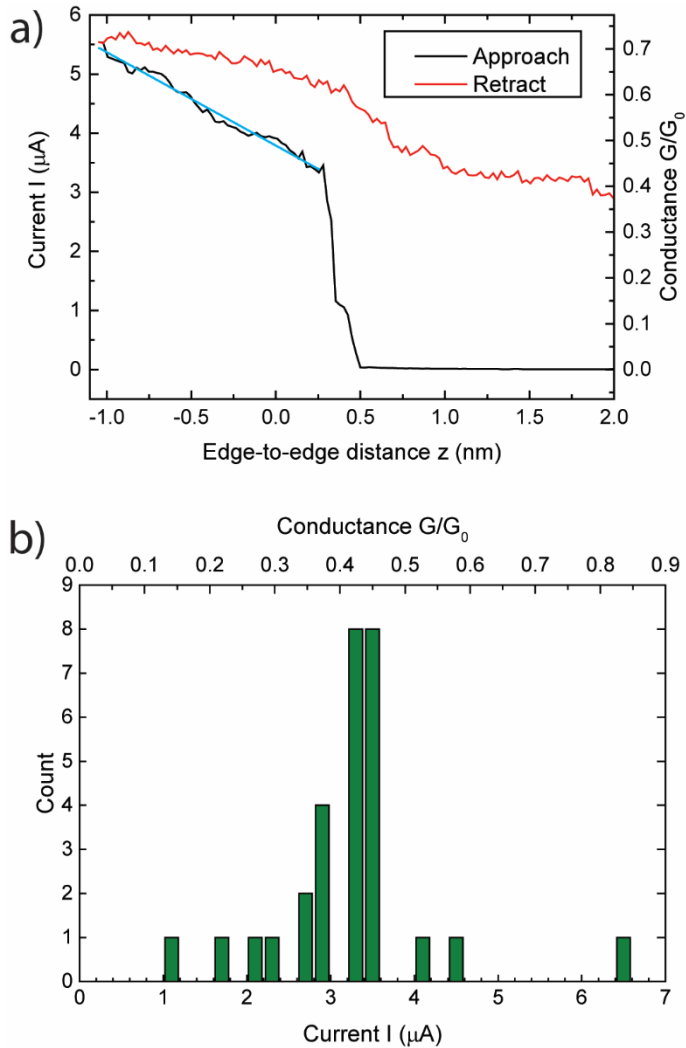
Figure 4.6. From tunnelling regime to point contact. a) Black: approach curve obtained for the 'closing-up' of the nanogap, showing a transition from the exponential tunnelling regime to a linear point contact regime (indicated by the blue line fit) at a bias voltage of 0.1 V. Red: retraction curve showing hysteresis that we attribute to bond formation. b) Green bars: histogram of the point contact formation (current at the kink in (a)) for 29 junctions, at a bias voltage of 0.1 V. The left and bottom scales in a) and b), respectively, show the measured current, while the scales at the opposite sides are converted to conductance in units of the quantum of conductance G_0. The measurements are performed under ambient conditions.

When we retract the electrodes after this indentation, in order to restore the vacuum gap, we observe hysteresis, as shown by the red curve in Figure 4.6a. During retraction, the conductance remains high, and after a small downward step near the point where the initial contact was formed, the contact is not broken even for further stretching of the junction over several nm. The persistence of high conductance suggests that strong bonds have been formed under the influence of the high mechanical pressure, possibly in combination with the potential of 0.1 V applied across the junction. We speculate that carbon-carbon bonds have been formed between the graphene sheets during indentation, despite the fact that all carbon bonds initially should be saturated. The long distance over which a high-conductance state survives (up to 3 nm or more) suggests that elongated atomic-chain like structures are formed in the retraction process, as has been observed previously in transmission electron microscope experiments[32–34], and in first-principles molecular dynamics.[35–37] Accordingly, we observed that after several hundred cycles of point contact formation and retraction at different spots along the edge, the damage to the electrodes hindered reaching the point contact regime and at times even obstructed an exponential increase of the current. Nonetheless, the validity of this speculation will need further experiments for detailed evaluation.

4.3   Conclusions

To conclude, we have presented a system consisting of dynamically adjustable graphene-graphene edge tunnelling junctions. The independently supported graphene electrodes uniquely allow the fine adjustment of the gap size. The tuneability of the gap is relevant for applications of such junctions, especially in the fields of single-molecule characterization, biosensing, and DNA sequencing. The junction can be adapted for sensing in liquid environments, required for the translocation of molecules such as DNA strands across the gap and recording their electric fingerprint.[38] In testing of the junctions we monitored the transition from the tunnel regime to atomic-size contact, and observed a preferred initial contact resistance value of 28 kΩ (0.46 G_0). The presence of hysteresis in the contact formation-and-breaking cycle suggests that bonds are formed between the graphene electrodes under influence of mechanical pressure. With further developments of this system under controlled atmosphere, in liquid environments and at cryogenic temperatures, we believe that our findings will advance molecular

electronics research, will open the way to research of atomic-size junctions in graphene, and will find applications in sensing and biopolymer sequencing.

4.4 References

(1) Prins, F.; Barreiro, A.; Ruitenberg, J. W.; Seldenthuis, J. S.; Aliaga-Alcalde, N.; Vandersypen, L. M. K.; van der Zant, H. S. J. *Nano Lett.* **2011**, *11* (11), 4607–4611.

(2) Nef, C.; Pósa, L.; Makk, P.; Fu, W.; Halbritter, A.; Schönenberger, C.; Calame, M. *Nanoscale* **2014**, *6* (13), 7249–7254.

(3) Ullmann, K.; Coto, P. B.; Leitherer, S.; Molina-Ontoria, A.; Martín, N.; Thoss, M.; Weber, H. B. *Nano Lett.* **2015**, *15* (5), 3512–3518.

(4) Wen, H.; Li, W.; Chen, J.; He, G.; Li, L.; Olson, M. A.; Sue, A. C.-H.; Stoddart, J. F.; Guo, X. *Sci. Adv.* **2016**, *2* (11), e1601113–e1601113.

(5) Lau, C. S.; Mol, J. A.; Warner, J. H.; Briggs, G. A. D. *Phys. Chem. Chem. Phys.* **2014**, *16* (38), 20398–20401.

(6) Lagerqvist, J.; Zwolak, M.; Di Ventra, M. *Nano Lett.* **2006**, *6* (4), 779–782.

(7) Arjmandi-Tash, H.; Belyaeva, L. A.; Schneider, G. F. *Chem. Soc. Rev.* **2016**, *45* (3), 476–493.

(8) Cuevas, J. C.; Scheer, E. *Molecular Electronics*; World Scientific, **2010**.

(9) Agraït, N.; Yeyati, L.; van Ruitenbeek, J. M. *Phys. Rep.* **2003**, *377* (2–3), 81–279.

(10) Perrin, M. L.; Verzijl, C. J. O.; Martin, C. A.; Shaikh, A. J.; Eelkema, R.; Van Esch, J. H.; Van Ruitenbeek, J. M.; Thijssen, J. M.; Van Der Zant, H. S. J.; Dulić, D. *Nat. Nanotechnol.* **2013**, *8* (4), 282–287.

(11) Paulsson, M.; Krag, C.; Frederiksen, T.; Brandbyge, M. *Nano Lett.* **2009**, *9* (1), 117–121.

(12) Fu, W.; Nef, C.; Tarasov, A.; Wipf, M.; Stoop, R.; Knopfmacher, O.; Weiss, M.; Calame, M.; Schönenberger, C. *Nanoscale* **2013**, *5* (24), 12104.

(13) Baraket, M.; Stine, R.; Lee, W. K.; Robinson, J. T.; Tamanaha, C. R.; Sheehan, P. E.; Walton, S. G. *Appl. Phys. Lett.* **2012**, *100* (23), 233123.

(14) Chua, C. K.; Pumera, M. *Chem. Soc. Rev.* **2013**, *42* (8), 3222.

(15) Liu, Y.; Dong, X.; Chen, P. *Chem. Soc. Rev.* **2012**, *41* (6), 2283–2307.

(16)   Zhang, B.; Cui, T. *Appl. Phys. Lett.* **2011**, *98* (7), 73116.

(17)   Xu, G.; Abbott, J.; Qin, L.; Yeung, K. Y. M.; Song, Y.; Yoon, H.; Kong, J.; Ham, D. *Nat. Commun.* **2014**, *5*, 4866.

(18)   Wang, H. M.; Zheng, Z.; Wang, Y. Y.; Qiu, J. J.; Guo, Z. B.; Shen, Z. X.; Yu, T. *Appl. Phys. Lett.* **2010**, *96* (2), 23106.

(19)   Sadeghi, H.; Mol, J.; Lau, C.; Briggs, A.; Warner, J.; Lambert, C. J. *Proc. Natl. Acad. Sci. U. S. A.* **2016**, *112* (9), 2658–2663.

(20)   Cao, Y.; Dong, S.; Liu, S.; He, L.; Gan, L.; Yu, X.; Steigerwald, M. L.; Wu, X.; Liu, Z.; Guo, X. *Angew. Chemie - Int. Ed.* **2012**, *51* (49), 12228–12232.

(21)   Wood, J. D.; Doidge, G. P.; Carrion, E. A.; Koepke, J. C.; Kaitz, J. A.; Datye, I.; Behnam, A.; Hewaparakrama, J.; Aruin, B.; Chen, Y.; Dong, H.; Haasch, R. T.; Lyding, J. W.; Pop, E. *Nanotechnology* **2015**, *26* (5), 55302.

(22)   Ferrari, A. C.; Meyer, J. C.; Scardaci, V.; Casiraghi, C.; Lazzeri, M.; Mauri, F.; Piscanec, S.; Jiang, D.; Novoselov, K. S.; Roth, S.; Geim, A. K. *Phys. Rev. Lett.* **2006**, *97* (18), 187401.

(23)   Casiraghi, C.; Hartschuh, A.; Qian, H.; Piscanec, S.; Georgi, C.; Fasoli, A.; Novoselov, K. S.; Basko, D. M.; Ferrari, A. C. *Nano Lett.* **2009**, *9* (4), 1433–1441.

(24)   Ferrari, A. C.; Basko, D. M. *Nat. Nanotechnol.* **2013**, *8* (4), 235–246.

(25)   Li, X.; Cai, W.; An, J.; Kim, S.; Nah, J.; Yang, D.; Piner, R.; Velamakanni, A.; Jung, I.; Tutuc, E.; Banerjee, S. K.; Colombo, L.; Ruoff, R. S. *Science.* **2009**, *324* (5932), 1312–1314.

(26)   Simmons, J. G. *J. Appl. Phys.* **1963**, *34* (6), 1793–1803.

(27)   Oshima, C.; Nagashima, A. *J. Phys. Condens. Matter* **1997**, *9* (1), 1–20.

(28)   Yuan, H.; Chang, S.; Bargatin, I.; Wang, N. C.; Riley, D. C.; Wang, H.; Schwede, J. W.; Provine, J.; Pop, E.; Shen, Z. X.; Pianetta, P. A.; Melosh, N. A.; Howe, R. T. *Nano Lett.* **2015**, *15* (10), 6475–6480.

(29)   Song, S. M.; Park, J. K.; Sul, O. J.; Cho, B. J. *Nano Lett.* **2012**, *12* (8), 3887–3892.

(30)   Shi, Y.; Kim, K. K.; Reina, A.; Hofmann, M.; Li, L.-J.; Kong, J. *ACS Nano* **2010**,

4 (5), 2689–2694.

(31)   Kvashnin, D. G.; Sorokin, P. B.; Brüning, J. W.; Chernozatonskii, L. A. *Appl. Phys. Lett.* **2013**, *102* (18), 183112.

(32)   Cretu, O.; Botello-Mendez, A. R.; Janowska, I.; Pham-Huu, C.; Charlier, J. C.; Banhart, F. *Nano Lett.* **2013**, *13* (8), 3487–3493.

(33)   Jin, C.; Lan, H.; Peng, L.; Suenaga, K.; Iijima, S. *Phys. Rev. Lett.* **2009**, *102* (20), 205501.

(34)   Chuvilin, A.; Meyer, J. C.; Algara-Siller, G.; Kaiser, U. *New J. Phys.* **2009**, *11* (8), 83019.

(35)   Erdogan, E.; Popov, I.; Rocha, C. G.; Cuniberti, G.; Roche, S.; Seifert, G. *Phys. Rev. B - Condens. Matter Mater. Phys.* **2011**, *83* (4), 41401.

(36)   Zhang, G. P.; Fang, X. W.; Yao, Y. X.; Wang, C. Z.; Ding, Z. J.; Ho, K. M. *J. Phys. Condens. Matter* **2011**, *23* (2), 25302.

(37)   Topsakal, M.; Ciraci, S. *Phys. Rev. B - Condens. Matter Mater. Phys.* **2010**, *81* (2), 24107.

(38)   Postma, H. W. C. *Nano Lett.* **2010**, *10* (2), 420–425.

CHAPTER 5

One-pot inert mask lithography of edge narrowed graphene nanoribbons directly contacted to metallic electrodes

Graphene nanoribbons, namely nanometric stripes of graphene constrained into a single dimension, are formed via inert mask lithography underneath metallic nanorods. The masks are prepared via the microtomy of metallic thin films embedded within polymeric scaffolds and precisely deposited on top of a graphene monolayer. The inertness of the metallic masks – here gold and aluminium –allows the precise narrowing of graphene into nanoribbons under different etching environments, thus also permitting the control over the edge chemistry of graphene, while protecting the basal plane. Remarkably, the nanoribbons can be electrically measured by converting the metallic mask into in-situ electrodes by local melting of the metal using a laser pulse. Our method proposes a simple, direct approach towards the design of chemically tailored, scalable, and electrically connected graphene nanoribbons.

5.1   Introduction

Remarkable step-forwards in graphene synthesis and clean transfer protocols prompted the expectations for future applications of graphene in numerous technological fields[1] such as energy storage[2], filtration[3], diagnostic[4] and even consumable electronics[5,6]. Thus, the growing demand of graphene also requires precisely patterned graphene films, particularly into miniaturized architectures such as quantum dots and nanoribbons[7–10]. For instance, precisely designed graphene nanoribbons, namely nanometric thin strips of graphene,[11] can widen the band-gap of graphene from 0 eV up to 10 eV, yielding graphene based transistors for logic operations[12,13], operating as gas sensors[14], thermosensors[15] or photodetectors[16].

In this chapter, graphene nanoribbons are fabricated using the shadowing of a metallic mask. Metallic masks are prepared by sectioning metallic thin films embedded in a polymer scaffold using microtomy[17], and converted into metallic nanorods. Next, the nanorods are aligned over the surface of graphene and are exposed to reactive ion etching. Upon etching, the nanorod covers the graphene underneath, yielding a graphene nanoribbon. The nanorod forms an inert interface with graphene, preserving the integrity and the chemical structure of the basal plane of graphene, as opposed to polymeric masks employed in conventional lithography of graphene[18]. In fact, polymeric masks generate residuals that uncontrollably contaminate the graphene, with detrimental consequences for the chemistry of graphene, both at the basal plane and at the edges[19,20].

The use of metallic masks allows the sculpting of graphene ribbons also in harsh and highly reactive environments, permitting the selective functionalization of graphene, otherwise not compatible with standard lithographic approaches. Metallic masks physically hinder the basal plane of the graphene underneath, forcing the etching to proceed via the edges. As a result, metallic masks permit the fabrication of graphene nanoribbons selectively functionalized at the edges in highly reactive environments such as reactive ion etching, organic solvents and under UV irradiation, thanks to the physical protection of a nanorod prepared via microtomy.

Importantly, microtomy allows the versatile fabrication of graphene nanoribbons, controllably yielding nanorods varying between few nanometres up to hundreds

of nanometres in width and extending over hundreds of micrometres in length. Additionally, we demonstrate the possibility of locally melting the mask by laser pulse irradiation, yielding in-situ controlled electrodes for the electrical characterization of the graphene nanoribbons, therefore achieving the single step fabrication of graphene nanoribbons and their electrodes.

5.2   Results and discussion

Metallic masks are prepared in the form of nanorods sectioned via microtomy starting from metallic thin films and deposited over supported graphene monolayers (Figure 5.1). Microtomy of metallic nanorods was first introduced by Whitesides and co-workers[17], who showcased that the slicing of metallic thin films using an ultra-sharp diamond knife[21] can be used as an unconventional approach to fabricate plasmonic resonators[22]. In Figure 5.1, a metallic film embedded within a polymer scaffold (Figure 5.1 a-i to a-iii) is sectioned with nanometric precision using a diamond knife (Figure 5.1 b-i). The cut yields polymeric slabs embedding metallic nanorods extending over several micrometres in length. The polymer/nanorod/polymer slab slides from the blade to float over a water reservoir at the back of the diamond knife. A perfect loop ring exploits the surface tension of the water to withdraw the slab from the reservoir. Subsequently, the ring is placed over a graphene substrate (Figure 5.1b-ii), while the water evaporates landing the slab on the graphene. In the meantime, a microneedle attached to a step-manipulator pins the slab during the water evaporation, allowing the proper alignment of the metallic mask over the surface of the graphene. This step, notably, permits the deposition of nanorods over pre-patterned electrodes for the electrical characterization of the nanoribbon.
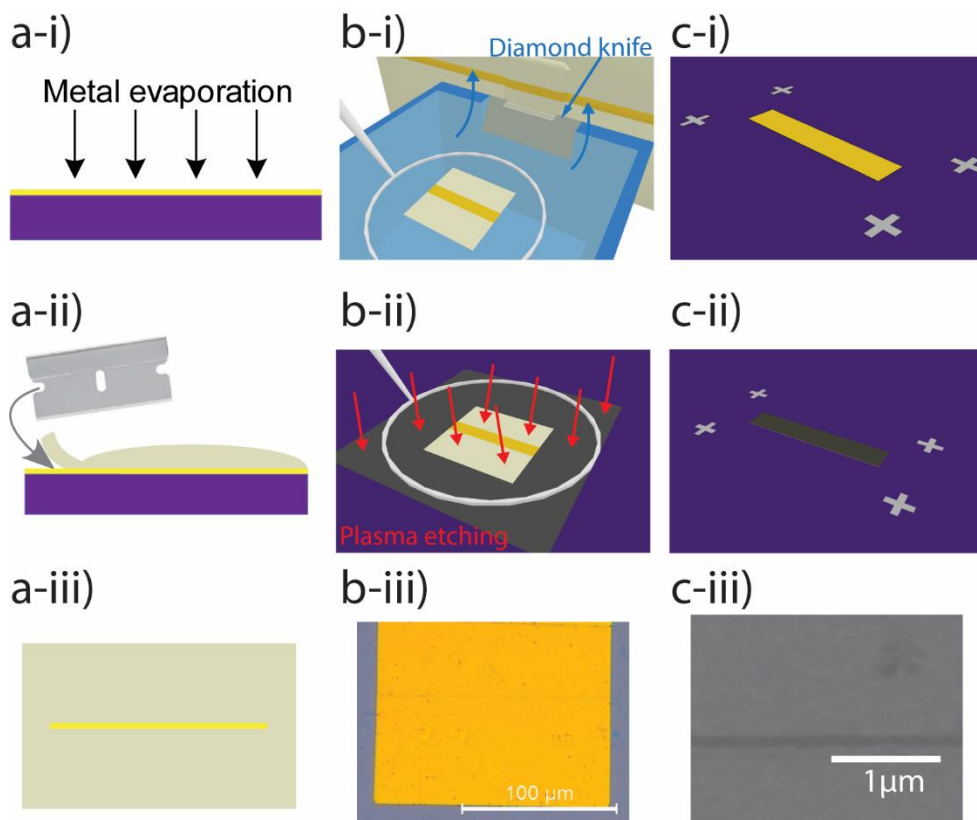
Figure 5.1. Fabrication of a graphene nanoribbon underneath a metallic nanorod prepared via microtomy. a-i) to a-iii) Embedding of the metallic thin film into the polymer scaffold. The metallic film is evaporated over a Si/SiO$_2$ wafer. A drop of polymer is casted and cured on the surface of the metal while a razor blade lifts the gold and the polymer from the substrate. At last, the gold is fully embedded in the polymer. b-i) Microtomy of metallic thin films into metallic inert masks. The polymer is sectioned by a diamond knife forming polymeric slabs supporting metallic nanorods. b-ii) Transfer of the polymer slab over the graphene film using a perfect loop. Plasma etching removes the polymer slab and the graphene surrounding the metallic mask. b-iii) Optical micrograph of a slab over the graphene film. c-i) and c-ii) The metallic mask is removed from the substrate via sonication or wet etching, uncovering the mask. c-iii) Scanning electron micrograph, SEM, of a graphene nanoribbon fabricated via inert mask lithography.

Reactive ion etching removes the polymer slab and the graphene surrounding the mask until the boundaries of the nanorod, Figure 5.1 c-i to c-iii. The mask covers and protects the basal plane of graphene, forcing the etching to proceed via the edges of graphene, thus promoting the control over the chemical composition of the edges while preserving the integrity of the basal plane. Lastly, the metallic inert

mask is either removed via sonication, or melted in the centre forming (in situ) electrodes for the characterization of the nanoribbons.

Accordingly, the edge narrowing via reactive ion etching yields nanoribbons narrower than the width of the covering mask, as shown by the scanning electron microscopy, SEM, micrograph of an 80 nm graphene nanoribbon (Figure 5.2a) formed in H_2 plasma (0.3mbar and 60W) underneath 300 nm wide aluminium mask (inset Figure 5.2a). Thus, while the metallic nanorod protects the surface of graphene, limited diffusion of reactive species proceeds underneath the mask through etching of the edges. As a result, the mask protects the basal plane of graphene yielding thin nanoribbons uniformly extending over several micrometres in length. The AFM topography image in Figure 5.2b shows the 80nm wide graphene nanoribbon (Figure 5.2c) uniformly extending over one micrometre in length without breakings. The nanoribbon presents some poly (methyl methacrylate), PMMA, residuals, result of the PMMA assisted deposition of the graphene monolayer on the Si/SiO_2 support. Finally, the Raman mapping of the nanoribbon shown in Figure 5.2d extends uniformly over a window of three micrometres, showing a Raman signature (inset) characteristic of a high quality, single layer graphene, as suggested also by a 2D band (at 2684 cm^{-1}) over G band (at 1590 cm^{-1}) ratio above one[23,24]. The ratio between the D peak (at 1341 cm^{-1}) and the G band is lower than one, indicating a high quality graphene[25], confirming the protective role of the metallic mask, and in agreement with both the scanning electron microscopy, SEM, and the atomic force microscopy, AFM, images.
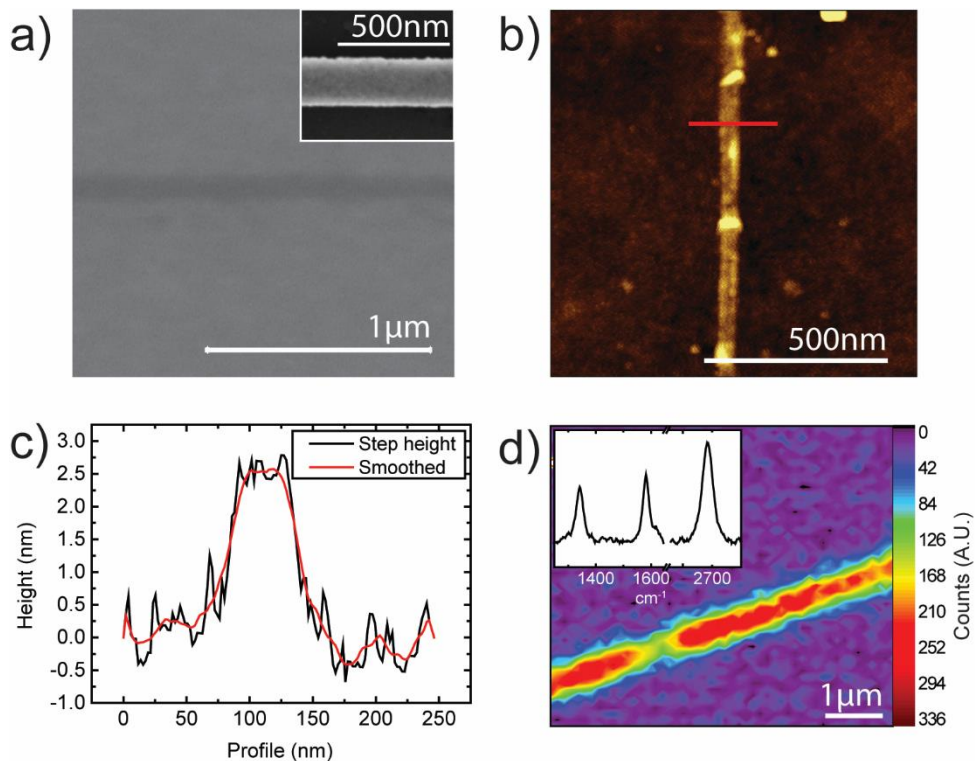
Figure 5.2. Characterization of a graphene nanoribbon formed from a 300nm wide aluminium mask. a) Scanning electron microscope, SEM, micrograph of a graphene nanoribbon on SiO_2 extending over 1 µm. Inset: SEM micrograph of the 300 nm aluminium nanorod prepared by microtomy and used as etching mask. b) and c) AFM intermittent contact mode image and step-height (red line in b)) of an 80 nm wide graphene nanoribbon. d) Raman mapping of the 2D band of the graphene nanoribbon at 2684 cm^{-1}. Inset: Raman signature of the nanoribbon.

At first, the metallic mask is supported by a polymer slab, which allows the precise transfer and alignment of the nanorod from the microtome knife to the surface of the graphene. A microneedle connected to a microstep manipulator pins the slab, securing its position over the surface of graphene during the transfer. Figure 5.3a shows the optical micrograph of a graphene film deposited over two gold pads 50 nm thick at about 20 µm distance. The 300 nm wide and 150 nm thick aluminium nanorod is deposited precisely across the two electrodes, electrically connecting them with a total resistance of about R_{Al} = 700 Ω, yielding a resistivity ρ_{Al} = 6x10^{-6} Ωm. This value matches the resistivity of aluminium, around 2x10^{-8} Ωm, taken in

consideration the high contact resistance at the interface between the gold, the graphene and the aluminium.
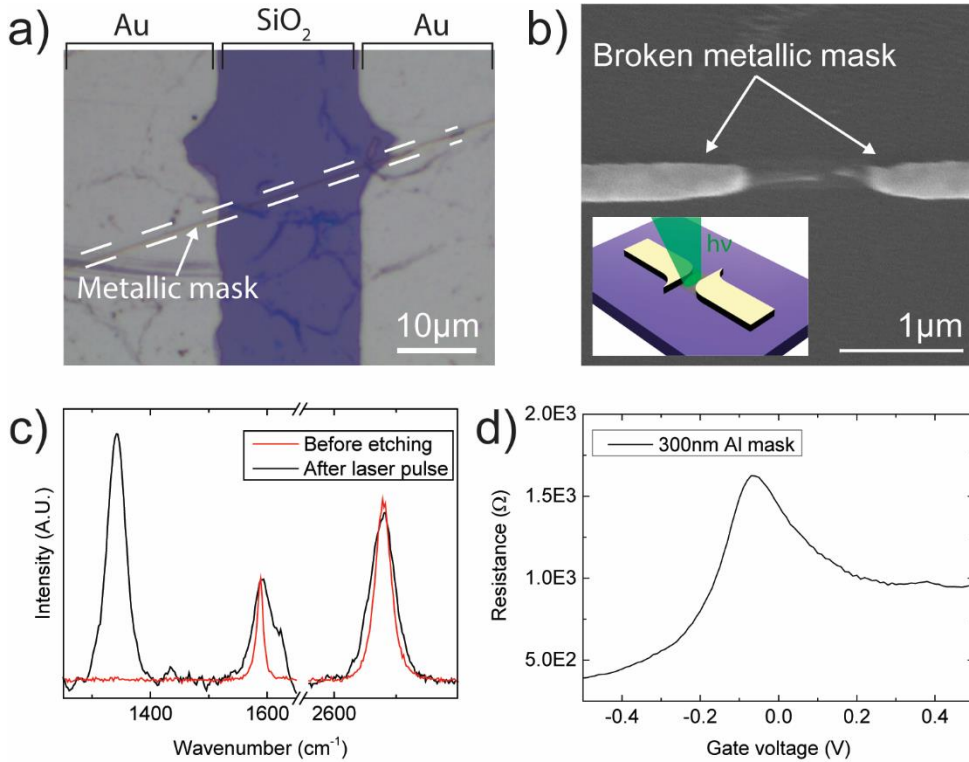

Figure 5.3. Laser induced formation of metallic electrodes. a) Optical micrograph of a graphene nanoribbon covered by a 300 nm wide aluminium nanorod connecting two gold contact pads. b) Rupture of the nanorod due to thermal shock after exposure to a 532 nm laser beam at 58mW for 2 s. Inset: schematization of the rupture process induced by the laser. c) Raman spectra of the graphene before fabricating the nanoribbon and after the opening of the electrodes by a 5s laser irradiation. d) IV characteristic of the 80 nm wide nanoribbon patterned under a 300 nm wide aluminium mask.

Subsequently, reactive ion etching removes the polymer and sculpts a graphene nanoribbon underneath the metallic mask. The nanorod remains over the surface of graphene protecting the basal plane from etching and physically contacting the nanoribbon. Thus, the local rupture of the metallic mask yields a set of independent metallic electrodes already aligned over the graphene nanoribbon, Figure 5.3b. This step, importantly, avoids the demand for further lithographic processing otherwise required to design electrodes for the electrical

characterization of the graphene nanoribbons. Particularly, the lithography of the electrodes would involve polymeric masks, leading to contaminations, beyond the intrinsic difficulties of designing nanometric aligned electrodes (see Figure 5.1 of Appendix III). Thus, in order to form the electrodes, the nanorod is broken locally by shining a 532 nm, 58 mW laser through a 100X objective and using a mechanical shutter to limit the exposure time. The irradiation energy of the laser beam is converted into thermal energy absorbed by the metallic nanorod[26]. The high density of power causes an abrupt expansion of the metallic nanorod, a thermal shock, causing the rupture. The mechanical shutter avoids prolonged exposure times. In fact, the prolonged irradiation of such a high intensity laser might compromise the graphene nanoribbon. An exposure time of 2 s over a 300nm wide aluminium nanorod yields a rupture in the nanorod tens of nanometres long, forming independent electrodes. Notably, for the Raman investigation the laser was shone for 5s over the nanorod, in order to open a gap wide enough to allow the characterization of the graphene nanoribbon by Raman spectroscopy, Figure 5.3c. In this case, the I(D)/I(G) ratio is above one, highlighting the presence of damages induced by the rupture of the nanorod, probably due to the prolonged exposure of the graphene to the laser beam. Nonetheless, the Raman signature indicates the presence of the graphene nanostructure yielding a conductive nanoribbon. For 2s exposure (thus limited exposure), the resistivity of the graphene is around R = 1.5 KΩ for a square resistance $R_{sq.}$[27] above 1 KΩ, considering an average electrode spacing in the order of few hundreds of nanometres over an 80 nm wide ribbon, Figure 5.3d. The electrical characteristic is measured against a gating potential applied from a 1 M solution of KCl in ultra pure water and against an Ag/AgCl electrode. The plot shows the rise in resistivity typical of the cone band structure of graphene, shifting from around 500 Ω up to about 1.75 kΩ and reaching its apex at the Dirac point[28], at slightly negative gating potential.

Metallic masks offer inert interfaces for the sculpting of graphene, drastically limiting the source of contaminations at least compared to conventional lithography[29]. Furthermore, the physical mask protects the surface of graphene forcing the sculpting of the nanoribbons via the edges, also regulating the chemistry at the edges. Thus, the geometry of the mask and the etching environment actively modify the physical and chemical properties of graphene. For instance, the reduction of the mask width directly reflects a narrowing of the graphene nanoribbon sculpted underneath. Raman spectroscopy in Figure 5.4a

shows an increase of I(D)/I(G) ratio with decreasing ribbons width. In fact, the edges activate a defect related Raman mode referred to as D at 1340 cm^{-1}. Its intensity is measured with respect to the G band at 1590 cm^{-1} and increases with the amount of edges[30], thus inversely proportional to the width of the nanoribbons (see Figure 5.2 of Appendix III), Figure 5.4b.
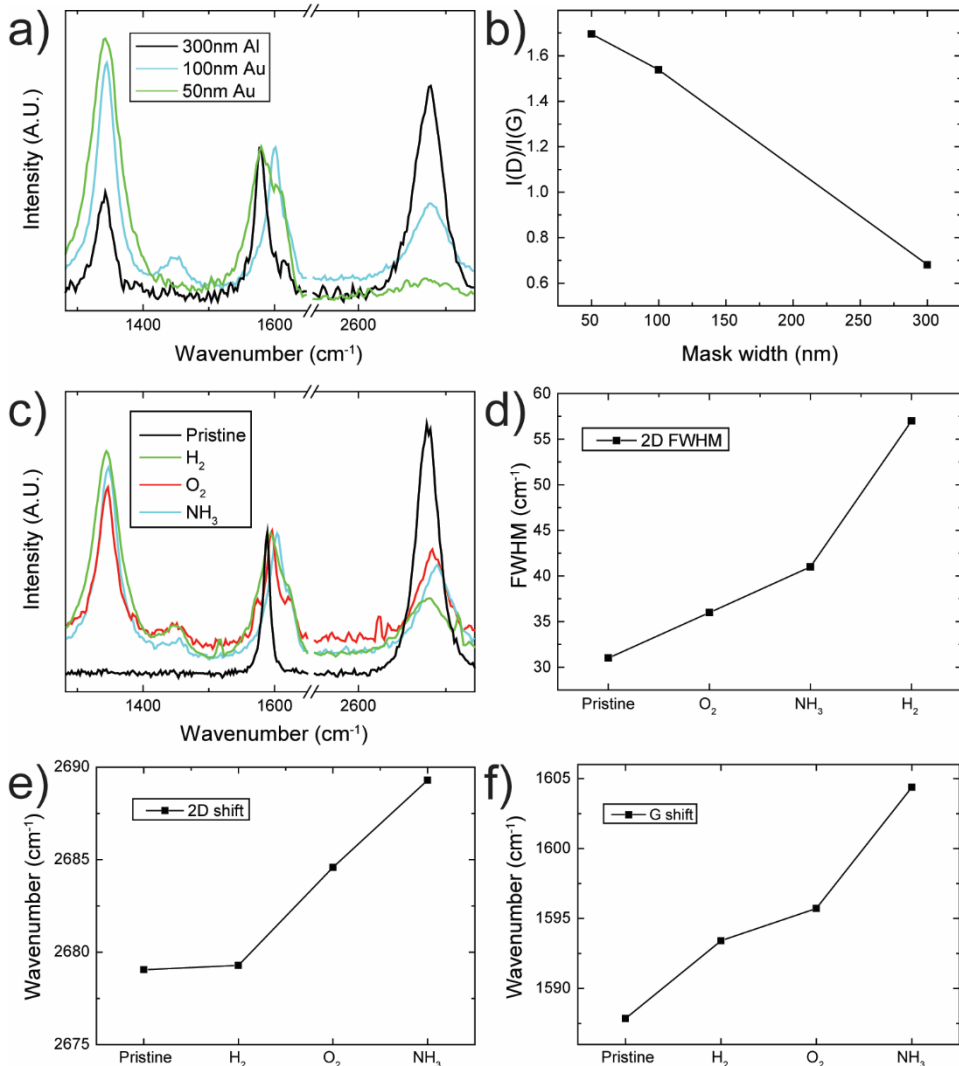

Figure 5.4. Raman characterization of graphene nanoribbons produced under metallic masks. a) Raman spectra of graphene nanoribbons patterned underneath metallic masks respectively of 50nm gold, 100 nm gold and 300 nm Al. b) I(D)/I(G) ratio for the different mask sizes. c) Raman spectra of graphene nanoribbons formed under 100 nm wide metallic

masks in H_2, O_2 and NH_3 plasma. d) G-peaks position of the nanoribbons illustrated in panel c). e) and f) 2D peak position shift and full width half maximum, FWHM, for graphene nanoribbons etched respectively in H_2, O_2 and NH_3 plasma.

Similarly, varying the etching environment impacts on the chemistry of the edges of graphene, thus on its properties such as the electronic structure. Accordingly, Raman spectroscopy highlights differences in the graphene structures for nanoribbons designed under 100 nm wide nanorods respectively in H_2, O_2 and NH_3 plasma, all at 0.3 mbar 60 W, Figure 5.4c. The I(D)/I(G) intensity is constant among the three different structures, as expected for masks of the same size. Nonetheless, the different etching gases affect differently the chemistry of the edges. The results can be monitored in terms of shifts in the 2D and G Raman peaks of the graphene nanoribbons[32–39] and in the full-width half maximum, FWHM, intensity of the 2D peaks. Accordingly, at fixed D band position, the G and 2D bands shift differently for different etching environments, Figure 5.4c, along with a widening of the 2D peaks, as confirmed in Figures 5.4d. Such variations in terms of 2D peaks are in line with the nanostructuring of the graphene sample and the increased amount of edge carbons atoms composing the nanostructure[30,35,40]. G and 2D bands are particularly sensitive to the edge chemistry, and the electrical properties of narrow graphene nanostructures (with high amount of edges) are more influenced by the chemical functionalization of the edge atoms. Heteroatoms linked to the lattice of graphene are characterized by different electro-negativities and electronic energy levels, yielding different charge doping levels via holes and electrons injections. Particularly, electronegative atoms like oxygen and nitrogen are expected to induce p-doping in the structure of graphene, donating holes and withdrawing electrons. This, supposedly, induces a red-shift in the G and 2D band of graphene[31,41]. Accordingly, comparing Figure 5.4e and Figure 5.4f we observe a more prominent red-shift on the G and 2D peaks of nanoribbons etched via O_2 and NH_3, while the red-shift is weaker for elemental hydrogen, the same trend is not observed for the D peak. If we compare the results with respect to the pristine graphene, we can observe a relevant shift for all the three etching gases. This can be the result of a combined effect of the nanostructuring together with elemental doping. We can observe that, especially in the case of NH_3 and O_2, the composition of the gas environment appears to offer a more visible effect on the control of the edge chemistry. In fact, doping varies the amount of electrons and holes density in the band structure of graphene, modifying also the 2D band of graphene during

110

Raman spectroscopy[24]. The result is a shift in the 2D band wavelength together with a widening of its FWHM. Importantly, observing the Raman spectra in Figure 5.4, we might need to consider the presence of residual oxygen traces during all the etching processes, which remains during the low vacuum pumping, and that can strengthen the doping effect, particularly in the case of hydrogen functionalization.

Additionally, metallic masks are chemically resistant to several reactive environments. For instance, metallic masks composed of gold and aluminium are insoluble in organic solvents (as opposed to polymeric masks used in conventional lithography). Thus, the use of metallic masks opens possibilities to address selectively the edge chemistry of graphene nanoribbons in organic solvents. For instance, graphene nanoribbons were functionalized using ferrocyanol azide under UV irradiation. More precisely, a graphene nanoribbon was first etched under a 300 nm wide mask in H_2 atmosphere and further exposed to ferrocyanol azide in a solution of tetrahydrofuran, THF, under UV irradiation at 365 nm. Ferrocyanol azide releases N_2 under UV irradiation, forming highly reactive radicals proved to be reactive with polyaromatic hydrocarbons, nanographenes and carbon nanotubes[42,43]. During the reaction, the mask protects the surface of graphene, while the ferrocyanol radicals react with the hydrogenated edges of graphene, as proposed in Figure 5.5a. The Raman spectra of the graphene nanoribbon is proposed Figure 5.5b, green line: the reaction with ferrocyanol azide in THF under UV for half an hour, Figure 5.5b blue line, causes a strong increase of the D band of graphene. The D band increase is ascribed to the functionalization of graphene with the iron ligand, in agreement with what is observed for the edge functionalization of graphene with nitro-aryl radicals[29]. Most importantly, we can observe a strong red-shift in the positions of the G and 2D bands, in line with the red shift expected for nitrogenated linkers.
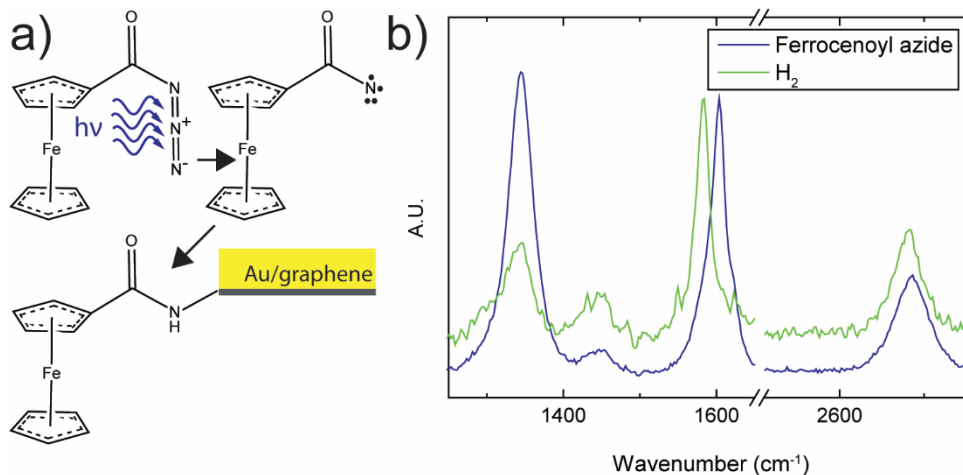
Figure 5.5. Edge functionalization of a graphene nanoribbon using ferrocyanol azide. a) Schematics of the edge functionalization of a graphene nanoribbon formed under a gold mask by exposure to ferrocyanol azide activated by UV irradiation. b) Comparison of the Raman spectra of nanoribbons prepared by H_2 plasma etching under 300 nm wide mask (green) and after reaction with ferrocyanol azide (blue).

Importantly, the metallic mask allows the functionalization of the edges of graphene via the reaction with ferrocyanol azide in organic solvents under UV irradiation, otherwise impossible with conventional lithographic masks such as PMMA. In fact, the combined effect of the organic solvent and the UV irradiation would most likely dissolve PMMA, uncovering the surface of graphene yielding a direct reaction of the ferrocyanol azide with the basal plane of graphene.

5.3   Conclusions

To conclude, we developed a lithographic approach for the scalable synthesis of graphene nanoribbons with controlled edge terminations, where graphene nanoribbons are directly electrically connected with metallic electrodes prepared in-situ. The use of metallic masks introduces enormous advantages over polymeric masks: the chemical inertness of the mask allows for the specific edge functionalization of graphene in organic solvents. The inertness of the metallic masks allows also the prolonged exposure of the graphene to harsh etching environments and reactive compounds. Separately, laser pulse induced thermal shock allows to employ the nanorods as in-situ deposited electrodes, preventing the post-processing of the graphene nanoribbons, and permitting the in-situ and

112

direct measurement of chemically derivatized nanoribbons. These results mark a step forward towards the simple nanofabrication of graphene-based nanoarchitectures with tunable, controllable edge chemistry.

5.4   References

(1)   Zurutuza, A.; Marinelli, C. *Nat. Nanotechnol.* **2014**, *9* (10), 730–734.

(2)   Liu, J. *Nat. Nanotechnol.* **2014**, *9* (10), 739–741.

(3)   Jiang, Y.; Biswas, P.; Fortner, J. D. *Environ. Sci. Water Res. Technol.* **2016**, *2* (6), 915–922.

(4)   Kostarelos, K.; Novoselov, K. S. *Nat. Nanotechnol.* **2014**, *9* (10), 744–745.

(5)   Ahn, J.-H.; Hong, B. H. *Nat. Nanotechnol.* **2014**, *9* (10), 737–738.

(6)   Torrisi, F.; Coleman, J. N. *Nat. Nanotechnol.* **2014**, *9* (10), 738–739.

(7)   Sadeghi, H.; Algaragholy, L.; Pope, T.; Bailey, S.; Visontai, D.; Manrique, D.; Ferrer, J.; Garcia-Suarez, V.; Sangtarash, S.; Lambert, C. J. *J. Phys. Chem. B* **2014**, *118* (24), 6908–6914.

(8)   Saha, K. K.; Drndić, M.; Nikolić, B. K. *Nano Lett.* **2012**, *12* (1), 50–55.

(9)   Puster, M.; Rodrıguez-Manzo, J. A.; Balan, A.; Drndic, M. *ACS Nano* **2013**, *7* (12), 11283–11289.

(10)   Ritter, K. a; Lyding, J. W. *Nat. Mater.* **2009**, *8* (3), 235–242.

(11)   Celis, A.; Nair, M. N.; Taleb-Ibrahimi, A.; Conrad, E. H.; Berger, C.; de Heer, W. A.; Tejeda, A. *J. Phys. D. Appl. Phys.* **2016**, *49* (14), 143001.

(12)   Schwierz, F. *Nat. Nanotechnol.* **2010**, *5* (7), 487-496.

(13)   Zhan, B.; Li, C.; Yang, J.; Jenkins, G.; Huang, W.; Dong, X. *Small* **2014**, *10* (20), 1-24.

(14)   Yavari, F.; Koratkar, N. *J. Phys. Chem. Lett. **2012**, 3 (13), 1746–1753*.

(15)   Davaji, B.; Cho, H. D.; Malakoutian, M.; Lee, J. K.; Panin, G.; Kang, T. W.; Lee, C. H. *Sci. Rep.* **2017**, *7* (1), 8811.

(16)   Zomer, P.; Guimarães, M. *Appl. Phys. Lett.* **2014**, 105, 013101.

(17)   Xu, Q.; Rioux, R. M.; Dickey, M. D.; Whitesides, G. M. *Acc. Chem. Res.* **2008**, *41* (12), 1566–1577.

(18)   Fischbein, M. D.; Drndic, M., *Appl. Phys. Lett.* **2018**, 93, 113107.

(19)   Gass, M. H.; Bangert, U.; Bleloch, A. L.; Wang, P.; Nair, R. R.; Geim, A. K. *Nat. Nanotechnol.* **2008**, *3* (11), 676–681.

(20)   Ishigami, M.; Chen, J. H.; Cullen, W. G.; Fuhrer, M. S.; Williams, E. D. *Nano Lett.* **2007**, *7* (6), 1643–1648.

(21)   Arjmandi-Tash, H.; Bellunato, A.; Wen, C.; Olsthoorn, R. C.; Scheicher, R. H.; Zhang, S.-L.; Schneider, G. F. *Adv. Mater.* **2017**, 1703602.

(22)   Wiley, B. J.; Lipomi, D. J.; Bao, J.; Capasso, F.; Whitesides, G. M. *Nano Lett.* **2008**, *8* (9), 3023–3028.

(23)   Ferrari, A. C.; Basko, D. M. *Nat. Nanotechnol.* **2013**, *8* (4), 235–246.

(24)   Ferrari, A. C. *Solid State Commun.* **2007**, *143* (1–2), 47–57.

(25)   Ferrari, A. C.; Robertson, J. *Phys. Rev. B* **2000**, *61* (20), 14095–14107.

(26)   Zhou, L.; Lu, J.; Yang, H.; Luo, S.; Wang, W.; Lv, J.; Qiu, M.; Li, Q. *Appl. Phys. Lett.* **2017**, *110* (8), 081101.

(27)   Peng, S.; Jin, Z.; Ma, P.; Zhang, D.; Shi, J.; Niu, J.; Wang, X.; Wang, S.; Li, M.; Liu, X.; Ye, T.; Zhang, Y.; Chen, Z.; Yu, G. *Carbon* **2015**, *82*, 500–505.

(28)   Castro Neto, a. H.; Peres, N. M. R.; Novoselov, K. S.; Geim, A. K. *Rev. Mod. Phys.* **2009**, *81* (1), 109–162.

(29)   Choi, W.; Shehzad, M. A.; Park, S.; Seo, Y. *RSC Adv.* **2017**, *7* (12), 6943–6949.

(30)   Casiraghi, C.; Hartschuh, A.; Qian, H.; Piscanec, S.; Georgi, C.; Fasoli, A.; Novoselov, K. S.; Basko, D. M.; Ferrari, A. C. *Nano Lett.* **2009**, *9* (4), 1433–1441.

(31)   Ferrari, A. C.; Meyer, J. C.; Scardaci, V.; Casiraghi, C.; Lazzeri, M.; Mauri, F.; Piscanec, S.; Jiang, D.; Novoselov, K. S.; Roth, S.; Geim, A. K. *Phys. Rev. Lett.* **2006**, *97* (18), 187401.

(32)   Wang, X.; Li, X.; Zhang, L.; Yoon, Y.; Weber, P. K.; Wang, H.; Guo, J.; Dai, H. *Science.* **2009**, *324* (5928).

(33)   Rybin, M.; Pereyaslavtsev, A.; Vasilieva, T.; Myasnikov, V.; Sokolov, I.; Pavlova, A.; Obraztsova, E.; Khomich, A.; Ralchenko, V.; Obraztsova, E. *Carbon* **2016**, *96*, 196–202.

(34) Piazza, A.; Giannazzo, F.; Buscarino, G.; Fisichella, G.; La Magna, A.; Roccaforte, F.; Cannas, M.; Gelardi, F. M.; Agnello, S. *Phys. status solidi* **2016**, *213* (9), 2341–2344.

(35) Iqbal, M. W.; Iqbal, M. Z.; Jin, X.; Hwang, C.; Eom, J. *ACS Appl. Mater. Interfaces* **2014**, *6*, 4207.

(36) Xie, W.-G. W.; Lai, X.; Wang, X.-M. X.; Wan, X.; Yan, M.-L.; Mai, W.-J.; Liu, P.-Y.; Chen, J.; Xu, J. *Spectrosc. Lett.* **2014**, *47* (6), 465–470.

(37) Xie, L.; Jiao, L.; Dai, H. *J. Am. Chem. Soc.* **2010**, *132* (42), 14751–14753.

(38) Stampfer, C.; Wirtz, L.; Jungen, A.; Graf, D.; Molitor, F.; Hierold, C.; Ensslin, K. *Appl. Phys. Lett.* **2007**, *91* (24), 241907.

(39) Stampfer, C.; Molitor, F.; Graf, D.; Ensslin, K.; Jungen, A.; Hierold, C.; Wirtz, L. *Appl. Phys. Lett.* **2007**, *91* (24), 241907.

(40) Eckmann, A.; Felten, A.; Mishchenko, A.; Britnell, L.; Krupke, R.; Novoselov, K. S.; Casiraghi, C. *Nano Lett.* **2012**, *12* (8), 3925–3930.

(41) Zhang, C.; Fu, L.; Liu, N.; Liu, M.; Wang, Y.; Liu, Z. *Adv. Mater.* **2011**, *23* (8), 1020–1024.

(42) Rabti, A.; Raouafi, N.; Merkoçi, A. *Carbon* **2016**, *108*, 481–514.

(43) Takahashi, S.; Anzai, J., *Materials* **2013**, *6* (12), 5742–5762.

CHAPTER 6

Transverse nanogaps from the layered assembly of polyelectrolytes

Molecular transistors, electromagnetic waveguides and quantum tunnelling junctions comprise precisely separated nanogaps of nanometric and subnanometric spacing. Nonetheless, fabricating a nanogap remains a technological challenge, particularly using approaches such as breakdown electromigration and lithography. Hereby, nanogaps are templated via microtomy of metallic thin films embedded in a polymer matrix and precisely separated by a nanometric, sacrificial layer of polyelectrolytes grown via Layer-by-Layer (LbL) deposition. The versatility of the LbL technique, both in terms of number of layers and composition of polyelectrolytes, allows to finely tune the spacing across the gap. Further, microtomy converts such films into nanogaps transferrable on arbitrary substrates. Ultimately, reactive plasma etches the sacrificial layers of polyelectrolytes, effectively opening the gap. These findings pave the path towards molecularly defined nanogaps of high precision and stability, modular into complex architectures for the next generation of devices integrating nanogap components.

6.1   Introduction

Solid state nanogaps interface bulky electrodes at nanometric distance either as in plane nanogaps or in the form of molecular break junctions. The precise control of the spacing across a nanogap is critical for the design of such architectures and their application into tunnelling junctions[1–4], molecular transistors[3,5–8] and waveguides[9–13]. For instance, the characteristics of devices such as molecular transistors rely on the specific molecular structure of the bridging element, and most importantly require electrodes separated by a gap having a width comparable to the one of a single molecule[14], i.e. a few nanometres. Similarly, tunnelling junctions are based on electrodes separated by a few nanometres, across which the tunnelling current flowing between the electrodes has been used to detect[15] or study electronic transport through single molecules[16–19]. Nonetheless, the precise, controllable fabrication of nanogaps still challenges the limits of conventional lithography. While innovative strategies have been developed to achieve precisely aligned electrodes[20,21], several drawbacks remain, mainly the stability of the gap with temperature[22,23] and the presence of particles detrimental for the performances of the gap[24]. Alternatively, sacrificial layers have been used to separate the metallic electrodes using organic or inorganic frameworks which are – in a later step – selectively etched yielding an empty gap spacing[25–27].

In this chapter, the Layer-by-Layer deposition[28], LbL, is used to grow multilayered films of polyelectrolytes of discrete thicknesses between large area metallic thin films, subsequently embedded into a polymeric matrix and converted by microtomy into molecular nanogaps spaced by a sacrificial film of polyelectrolytes. Microtomy was first introduced by Whitesides and co-workers as an unconventional approach towards the reliable and serial production of metallic nanostructures and nanoelectrodes[29–31]. Here, a diamond knife transversally slices the polymer matrix and the metallic thin films, yielding thin slabs of polymer surrounding a gold-polyelectrolytes-gold nanogap. Next, the molecular nanogap opens using plasma reactive etching of the sacrificial polyelectrolytes, emptying the spacing across the gap. The polymeric support allows the manipulation of such nanostructures, their precise alignment and the assembly into complex architectures. For instance, by precisely transferring two consecutive slabs on

porous substrates, we could assemble nanopores devices, impossible otherwise, by overlapping two twisted nanogaps[32,33].

The multilayered film is grown by simple alternate dipping of the substrate into aqueous solutions of oppositely charged polyelectrolytes. The growth is self-limited and governed by electrostatic interactions between the polyelectrolyte layers. The effective charge of the polyelectrolytes in solution can be controlled by modulating the ionic strength of the solvent, namely the concentration of the salt in solution during deposition, through counter ion screening[34]. Particularly, with polyelectrolytes such as poly (allylamine hydrochloride) (PAH) and poly (sodium 4-styrenesulfonate) (PSS), each layers within the stratified film can have a thickness varying between 0.25-2.2 nm in aqueous solutions of NaCl with concentration varying from 0.015 M[35] to 2M[34]. The temperature and the humidity during the deposition can also modulate the compactness of the layers composing the films, resulting in thinner polyelectrolytes films at higher temperatures (and lower humidity), due to a lower water content within the multilayered film[36]. Thus, multilayered films of polyelectrolytes yield nanometric thin films with possibility to control the film thickness down to a nanometer, allowing to design polyelectrolyte-nanogap architectures with tunable gap size in the nanometer range.

6.2   Results and discussion

The multilayered spacers are grown via Layer-by-Layer deposition (LbL) of alternatively charged polyelectrolytes between large area metallic thin films. Next, microtomy slices nanometric thin sections of the metallic thin films by means of an ultra-sharp diamond knife. The diamond knife cuts the metallic films into parallel pairs of nanorods forming a nanogap, which gap is filled with multilayered polyelectrolytes. Reactive ion etching removes the polyelectrolytes, emptying the space across the gap, and yielding nanogaps composed of precisely separated metallic nanorods.

The mechanical cut performed during microtomy requires a strong adhesion of the multilayered polyelectrolytes to the metallic thin films, in order to preserve the architecture of the nanogap between nanorods. While the multilayered polyelectrolytes are bound together via electrostatic interactions between the individual polyelectrolytes layers, the first metallic film must be functionalized in order to attract and bind the first layer of polyelectrolytes. Therefore, a gold thin

film was deposited over a supporting substrate (i.e. SiO_2) and functionalized with a mixed self-assembled-monolayer (SAM) of amino and alkyl-thiols assembled from a solution of 5 mM 1-dodecanethiol and 5 mM 1-amino 11-undecanethiol in ethanol[37] (respectively what we refer to as alkyl thiols and aminothiols), Figure 6.1a.
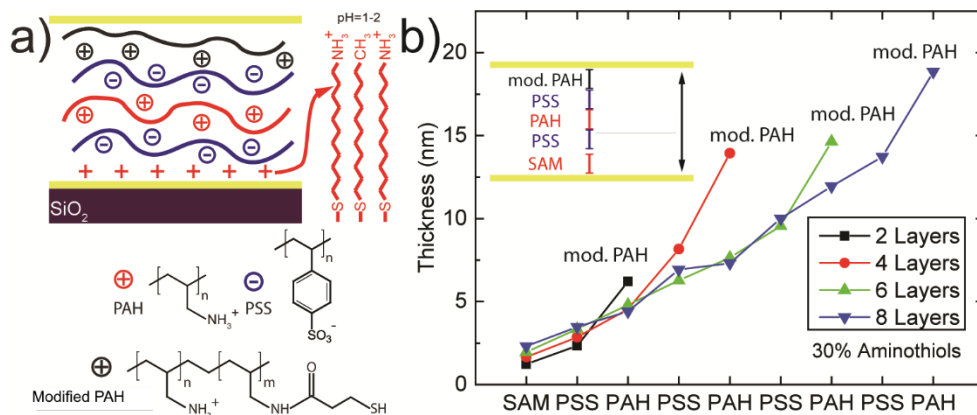

Figure 6.1. Multilayered polyelectrolytes-nanogap. a) Alternated Layer-by-Layer deposition of poly (sodium 4-styrenesulfonate) and poly (allylamine hydrochloride) in between two large area (1 X 1 cm²) gold layers to form a multilayered nanogap. The first gold layer is functionalized with a mixed self-assembled monolayer of amino-thiols and alkyl-thiols formed from a solution of 5 mM 1-dodecanethiol and 5 mM 1-amino 11-undecanethiol in ethanol at a 7:3 volume ratio. The top layer of polyelectrolytes is a poly (allylamine hydrochloride) layer derivatized with thiols (see Figure IV.2 appendix IV). b) Characterization of the growth of the multilayered polyelectrolytes by ellipsometry.

Next, the thiolated gold film was immersed into an acidic solution of PSS at pH= 1-2. The amines of the aminothiol are protonated favouring the adsorption of a layer of negatively charged PSS[28], Figure 6.1a. Then, the multilayered spacer is grown via alternated dipping of the substrate in an aqueous solution of PSS and PAH in 1M KCl. Finally, the multilayered polyelectrolytes are coated with a second gold film deposited via thermal resistance evaporation. In order to promote the adhesion between the multilayered polyelectrolytes and the top gold film, the outmost layer of polyelectrolytes is chemically functionalized. To do so, the amines of the outmost PAH layer are partially converted into thiol groups which seal to the gold through thiols bonds (see Figure 6.2 appendix IV). When immersed in KCl solution, the residual amines of the thiolated PAH (i.e. modified PAH in Figure 6.1a) drive

the deposition over the multilayered film of polyelectrolytes, while the thiols bind the gold film, Figure 6.1a.

The thickness of the multilayered film grows linearly, around 1.5 +/- 0.1 nm per layer. The last partially thiolated PAH layer is around 5 +/- 0.3 nm thick, due to the lower content of amines on its backbone, Figure 6.1b. In fact, the adsorption of polyelectrolytes depends on electrostatic interactions and charge screening. As a result, each layer adsorbs until the charge of the previous layer is compensated, with polyelectrolyte residual groups providing a charge overcompensation. Since the last thiolated PAH possesses a lower amines content compared to the pristine PAH, a thicker film was obtained: a higher amount of polyelectrolyte chain is required to screen effectively the negative charge in the previous PSS layer.

In order to process the multilayered nanogap by microtomy, the gold films are embedded within a polymer scaffold (Figure 6.2a) composed of a mixture of pentaerythritoltetrakis mercaptopropionate (PEMPT), and triallyl triazinetrione (TATATO) with a 3:4 molar proportion and cured under UV irradiation at 532 nm for half an hour (see materials and methods in Appendix IV). Next, a diamond knife slices the polymer scaffold via microtomy, forming nanometric polymeric slabs 150 nm thick embedding a nanogap comprising two gold nanorods spaced by a multilayered polyelectrolyte film (Figure 6.2b). The polymer frame mechanically supports the nanogap and allows the facile transfer of the slices from the diamond knife to a support substrate. Finally, reactive O_2 plasma etching removes the sacrificial film of polyelectrolytes and (for longer exposures) the supporting polymer, yielding a planar nanogap across metallic nanorods (Figure 6.2c).
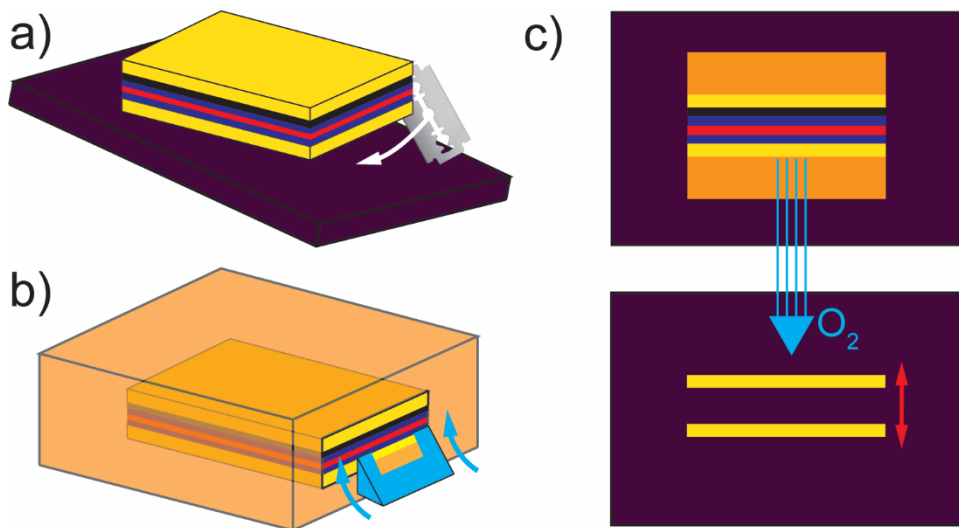
Figure 6.2. Illustration of the transverse microtomy of the multilayered nanogap and subsequent formation of an empty nanogap between two gold electrodes. a) The multilayered film of polyelectrolytes is coated with a second layer of gold. The stack is lifted from the substrate by intercalating a razor blade between the gold film and the substrate. The stack is then embedded inside a polymer matrix composed of pentaerythritoltetrakis mercaptopropionate (PEMPT), and triallyl triazinetrione (TATATO) in molar ratio 3 : 4. b) Microtomy of the polymer matrix yielding a nanogap supported by a polymer slab. c) The slab is deposited on a substrate (Si/SiO₂, transmission electron microscope grid, glass) and oxidized using an O₂ plasma to etch both the PEMPT/TATATO polymer and the sacrificial layer of polyelectrolytes, yielding the formation of the nanogap.

The presence of the supporting polymer matrix and the multilayered film of polyelectrolytes prevents the nanogap to shrink during microtomy, therefore permitting the subsequent transfer of the multilayered nanogap to an arbitrary substrate, such as Si/SiO₂ wafers, transmission electron microscope (TEM) grids or SiN membranes (Figure 6.3a and Figure 6.3b). In fact, after microtomy, the slabs slide from the diamond knife to an air-water meniscus placed behind the blade. Next, a perfect loop (i.e. a titanium ring of 1 mm in diameter) is positioned on the water surface surrounding the polymeric slabs. The ring exploits the surface tension of the water to withdraw a droplet of water containing the floating polymeric slabs. The perfect loop allows the transfer of the droplet onto any target substrate, while the water slowly evaporates landing the nanogap over a surface. The slow evaporation of the water gives time to precisely align the slab

over the substrate, using a needle connected to a micro-step manipulator pinning the polymer slab and controlling its position.
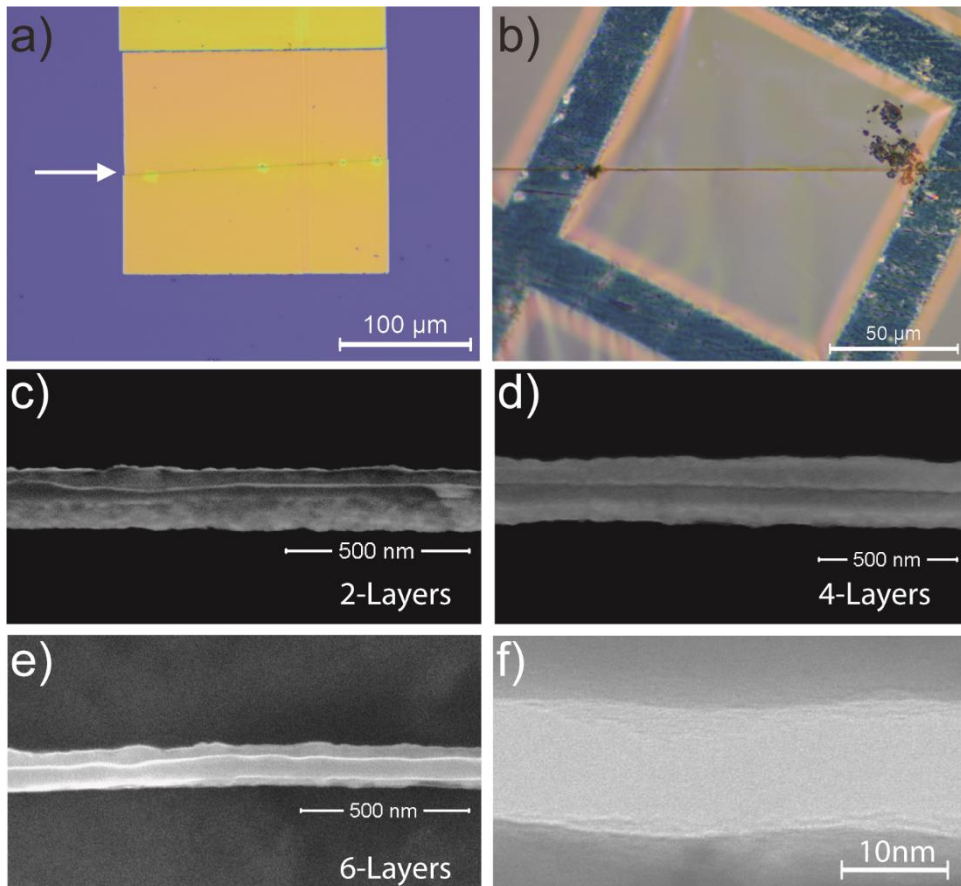

Figure 6.3. Optical and electron microscopy characterization of supported metallic nanogaps. a) Optical micrograph of a PEMPT/TATATO slab (yellow) on a Si/SiO$_2$ wafer (purple). The position of the gold/polyelectrolytes/gold stack is pointed by the white arrow. b) Optical micrograph of a polymer slab and gold/polyelectrolytes/gold stack supported by a holey TEM grid. c), d) and e) SEM micrographs of molecular nanogaps of two, four and six layers of polyelectrolytes transferred on a Si/SiO$_2$. f) TEM micrograph of a nanogap formed by four layers of polyelectrolytes.

Figure 6.3c to Figure 6.3e show the scanning electron microscope, SEM, micrographs of a multilayered nanogap on SiO$_2$ composed respectively of two (Figure 6.3c), four (Figure 6.3d) and six (Figure 6.3e) layers of polyelectrolytes, with thicknesses varying from 5 nm to 15 nm (thicknesses determined by ellipsometry).

Figure 6.3f shows the transmission electron micrograph of a multilayered nanogap composed of four polyelectrolytes layers film of polyelectrolytes. The multilayered film was etched via O_2 plasma prior to imaging, yielding a high contrast in the transmission electron microscopy micrograph (Figure 6.3f) between the empty space of the gap (white area) and the gold nanorods (darker regions at the upper and lower boundaries of the image). TEM allows the high-resolution imaging across the gap, which size, in the order of 10 nm, matches the measurements performed by ellipsometry (Figure 6.1b).

6.3   Conclusions

To conclude, multilayered polyelectrolytes adsorb via Layer-by-Layer deposition between large area gold films further converted into multilayered nanogaps using microtomy. Advantageously, multilayered polyelectrolytes assemble by simple immersion of a substrate in aqueous solutions of polyelectrolytes, forming organic thin films which thickness can be readily monitored by optical methods such as ellipsometry. The chemical functionalization of the gold substrate with self-assembled monolayers and the chemical synthesis of a thiolated PAH ensure the strong adhesion of the multilayered polyelectrolytes to the gold films during microtomy. The mechanical sectioning via microtomy yields multilayered nanogaps embedded within nanometric polymeric supports, allowing the facile handling of the nanogap samples, which are precisely transferrable on discrete target substrates. Specifically, the transfer using a perfect loop and the further alignment allow for the precise control of the position of the nanogap over the substrate, with the possibility of assembling larger (and more complex) architectures by stacking layers of transverse nanogaps on top of each other. For instance, nanopores with sub 10 nm pores can be assembled at the crossing interface of two twisted nanogaps, where the long range nanorods would directly function as nanofluidic injection channels towards the rim of the pore, as we show in Chapter 7[32]. Furthermore, metallic nanorods can be employed as in-situ electrodes for the electrical characterization of the nanogaps, either in the form of tunnelling junctions or molecular transistors.

6.4   References

(1)   Reed, M. A. *Science* **1997**, *278* (5336), 252–254.

(2)   Huang, S.; He, J.; Chang, S.; Zhang, P.; Liang, F.; Li, S.; Tuchband, M.; Fuhrmann, A.; Ros, R.; Lindsay, S. *Nat. Nanotechnol.* **2010**, *5* (12), 868–873.

(3)   Liang, X.; Chou, S. Y. *Nano Lett.* **2008**, *8* (5), 1472–1476.

(4)   Fanget, A.; Traversi, F.; Khlybov, S.; Granjon, P.; Magrez, A.; Forró, L.; Radenovic, A. *Nano Lett.* **2014**, *14* (1), 244–249.

(5)   Li, T.; Hu, W.; Zhu, D. *Adv. Mat.* **2010**, 22(2), 286–300.

(6)   Hwang, J. S.; Kong, K. J.; Ahn, D.; Lee, G. S.; Ahn, D. J.; Hwang, S. W. *Appl. Phys. Lett.* **2002**, *81* (6), 1134–1136.

(7)   Kyu Kim, S.; Cho, H.; Park, H.-J.; Kwon, D.; Min Lee, J.; Hyun Chung, B. *Nanotechnology* **2009**, *20* (45), 455502.

(8)   Porath, D.; Bezryadin, A.; de Vries, S.; Dekker, C. *Nature* **2000**, *403* (6770), 635–638.

(9)   Ward, D. R.; Hüser, F.; Pauly, F.; Cuevas, J. C.; Natelson, D. *Nat. Nanotechnol.* **2010**, *5* (10), 732–736.

(10)   Wu, H.-Y.; Choi, C. J.; Cunningham, B. T. *Small* **2012**, *8* (18), 2878–2885.

(11)   Chen, X.; Ciracì, C.; Smith, D. R.; Oh, S.-H. *Nano Lett.* **2015**, *15* (1), 107–113.

(12)   Marqués-González, S.; Matsushita, R.; Kiguchi, M. *J. Opt.* **2015**, *17* (11), 114001.

(13)   Siegfried, T.; Ekinci, Y.; Martin, O. J. F.; Sigg, H. *Nano Lett.* **2013**, *13* (11), 5449–5453.

(14)   Perrin, M. L.; Burzurí, E.; Van Der Zant, H. S. J. *Chem. Soc. Rev* **2015**, *44* (44), 835–1030.

(15)   Tsutsui, M.; Taniguchi, M.; Yokota, K.; Kawai, T. *Nat. Nanotechnol.* **2010**, *5* (4), 286–290.

(16)   Perrin, M. L.; Verzijl, C. J. O.; Martin, C. A.; Shaikh, A. J.; Eelkema, R.; Van Esch, J. H.; Van Ruitenbeek, J. M.; Thijssen, J. M.; Van Der Zant, H. S. J.; Dulić,

D. *Nat. Nanotechnol.* **2013**, *8* (4), 282–287.

(17)   Martin, C. A.; Smit, R. H. M.; van der Zant, H. S. J.; van Ruitenbeek, J. M. *Nano Lett.* **2009**, *9* (8), 2940–2945.

(18)   Martin, C. A.; Ding, D.; Van Der Zant, H. S. J.; Van Ruitenbeek, J. M. *New J. Phys.* **2008**, *10* (6), 065008.

(19)   Martin, C. A.; Ding, D.; Sørensen, J. K.; Bjørnholm, T.; van Ruitenbeek, J. M.; van der Zant, H. S. J. *J. Am. Chem. Soc.* **2008**, *130* (40), 13198–13199.

(20)   Park, H.; Lim, A. K. L.; Alivisatos, A. P.; Park, J.; McEuen, P. L. *Appl. Phys. Lett.* **1999**, *75* (1999), 301–303.

(21)   Lambert, M. F.; Goffman, M. F.; Bourgoin, J. P.; Hesto, P. *Nanotechnology* **2003**, *14* (7), 772–777.

(22)   Danvers E. Johnston; Douglas R. Strachan; A. T. Charlie Johnson, Nano Lett., **2007**, 7 (9), 2774–2777.

(23)   Esen, G.; Fuhrer, M. S. *Appl. Phys. Lett.* **2005**, *87* (26), 263101.

(24)   Thiti Taychatanapat; Kirill I. Bolotin; Ferdinand Kuemmeth; Ralph, D. C. *Nano Lett.*, **2007**, 7 (3), 652–656.

(25)   Zaretski, A.; Marin, B. C.; Moetazedi, H.; Dill, T. J.; Jibril, L.; Kong, C.; Tao, A. R.; Lipomi, D. J. *Nano Lett.* **2015**, *15* (1), 635–640.

(26)   Fursina, A.; Lee, S.; Sofin, R. G. S.; Shvets, I. V.; Natelson, D. *Appl. Phys. Lett.* **2008**, *92* (11), 113102.

(27)   Zhou, Z.; Zhao, Z.; Yu, Y.; Ai, B.; Mohwald, H.; Chiechi, R. C.; Yang, J. K. W.; Zhang, G. *Adv. Mater.* **2016**, *28* (15), 2956–2963.

(28)   Decher, G. *Science.* **1997**, *277* (5330), 1232–1237.

(29)   Lipomi, D. J.; Martinez, R. V; Whitesides, G. M. *Angew. Chem. Int. Ed. Engl.* **2011**, *50* (37), 8566–8583.

(30)   Storm, a J.; Chen, J. H.; Ling, X. S.; Zandbergen, H. W.; Dekker, C. *Nat. Mater.* **2003**, *2* (8), 537–540.

(31)   Carlotti, M.; Degen, M.; Zhang, Y.; Chiechi, R. C. *J. Phys. Chem. C* **2016**, *120* (36), 20437–20445.

(32)   Arjmandi-Tash, H.; Bellunato, A.; Wen, C.; Olsthoorn, R. C.; Scheicher, R. H.; Zhang, S.-L.; Schneider, G. F. *Adv. Mater.* **2018**, 1703602.

(33)   Bellunato, A.; Vrbica, S. D.; Sabater, C.; de Vos, E. W.; Fermin, R.; Kanneworff, K. N.; Galli, F.; van Ruitenbeek, J. M.; Schneider, G. F. *Nano Lett.* **2018**, *18* (4), 2505–2510.

(34)   Decher, G.; Schmitt, J. In *Trends in Colloid and Interface Science VI*, **1992**, 160–164.

(35)   Elżbieciak-Wodka, M.; Warszyński, P. *Electrochim. Acta* **2013**, *104*, 348–357.

(36)   Decher, G.; Schlenoff, J. *Multilayer Thin Films: Sequential Assembly of Nanocomposite Materials, 2nd Edition*; Wiley-VCH, **2012**; Vol. 1.

(37)   Love, J. C.; Estroff, L. A.; Kriebel, J. K.; Nuzzo, R. G.; Whitesides, G. M. *Chem. Rev.* **2005**, *105* (4), 1103–1169.

CHAPTER 7

Zero-depth interfacial nanopore capillaries

High-fidelity analysis of translocating biomolecules through nanopores demands shortening the nanocapillary length to a minimal value. Existing nanopores and capillaries, however, inherit a finite length from the parent membranes. Here, nanocapillaries of zero depth are formed by dissolving two superimposed and crossing metallic nanorods, moulded in polymeric slabs. In an electrolyte, the interface shared by the crossing fluidic channels is mathematically of zero thickness and defines the narrowest constriction in the stream of ions through the nanopore device. This novel architecture provides the possibility to design nanopore fluidic channels, particularly with a robust 3D architecture maintaining the ultimate zero thickness geometry independently of the thickness of the fluidic channels. With orders of magnitude reduced biomolecule translocation speed, and lowered electronic and ionic noise compared to nanopores in 2D materials, the findings establish interfacial nanopores as a scalable platform for realizing nanofluidic systems, capable of single-molecule detection.

7.1   Introduction

Conventional nanopores are nano-sized fluidic channels drilled across a solid-state membrane[1–6] or moulded in polymeric structures[7,8] and mounted in a flow cell. The flow cell is equally filled with an ionic solution on both sides of the membrane, while a potential difference is applied across the cell serving as the driving force for the ionic transport. Thereby, a flux of ions is established through the nanopore.

Charged molecules can translocate through the nanopore. The instant passage of the molecule momentarily impacts the conductance by locally reducing the aperture size of the channel. The resulting variations of the ionic conductance depends on the local topology of the translocating molecule; particularly, portions of long chain molecules such as polymers, proteins or DNA mark the electronic read-out with specific conductance blockade fingerprints; and ultimately allow for reconstructing the sequence of monomers composing the translocating strands[9].

Consequently, thinner pores, i.e. capillaries with shorter channels, are capable of resolving shorter portions of molecules, leading for instance towards high resolution sequencing devices[1]. Thus, the challenge towards high-resolution sequencing has driven the development of ultra-short channel nanopores. Historically, two major classes of nanopores, i.e. biological and solid state nanopores, have been considered. The thickness of these nanopores varies from a few nanometres, as for α-hemolysin biological nanopores[10,11], up to tens of nanometres for solid-state nanopores[12]. A revolutionary breakthrough aiming at reducing the capillary length of nanopores was achieved by the introduction of two-dimensional (2D) materials such as graphene[13–15], hexagonal boron nitride [16] and molybdenum disulfide[17–20]. Indeed, the monoatomic capillary length of 2D nanopores is expected to offer sequencing capabilities[2], but has not been realized yet. Inferior mechanical stability is one of the downside of thin membranes inherently limiting the sustainability of 2D nanopores. Moreover, the complex fabrication process, involving cleanroom facilities and electron beam lithography[21–23], can be demanding to scale up to industrial production. The noise levels in such devices are also orders of magnitude higher than those for long capillary-based nanopores, thus hindering their application for sequencing[24].

7.2   Results and discussion

To address these issues, we introduce the concept of interfacial nanopores, generated at the crossing of two trenches, as illustrated in Figure 7.1. Fundamentally, the cross-section of two one-dimensional straight lines is a zero-dimensional entity defined as a point (Figure 7.1a). The addition of a second dimensionality implies the overlap of two components to become a surface (Figure 7.1b). Similarly, in a three-dimensional space, the interface shared between two tangent rectangular parallelepipeds is a surface, hence mathematically two-dimensional (Figure 7.1c). Unlike nanopores commonly fabricated in two-dimensional materials – which notwithstanding still possess a finite thickness – the surface defined by the crossing parallelepipeds is strictly two-dimensional and thus does not exhibit any thickness. A negative mould of this structure therefore yields a nanopore with a capillary of length zero (Figure 7.1f).
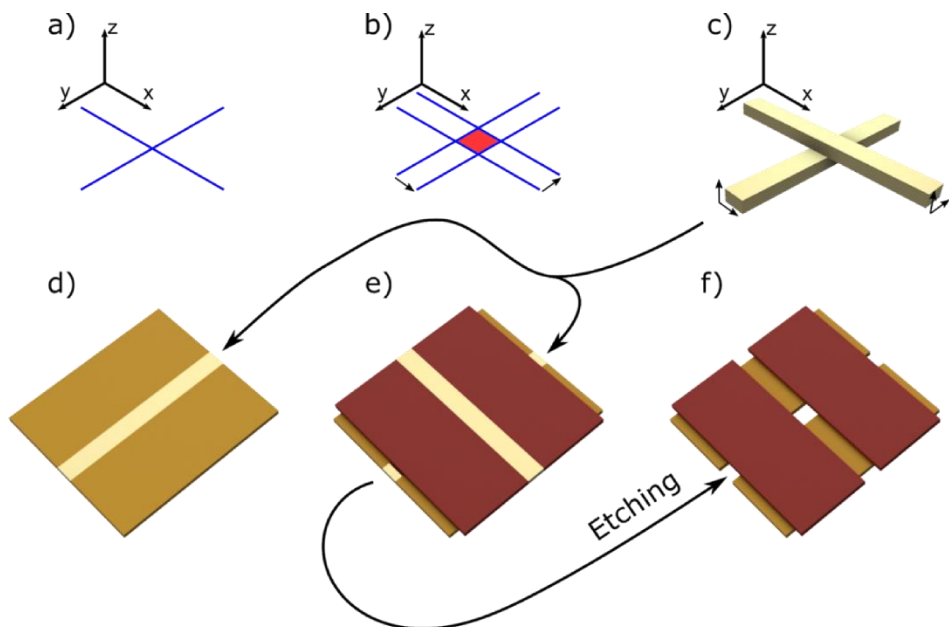

Figure 7.1. Interfacial nanopores: from geometrical concepts to fabrication. a) Zero-dimensional point at the cross-section of two crossing lines. b) 2D lozenge formed at the intersection of two crossing rectangles. c) The lozenge surface is preserved at the interface of two crossing rectangular parallelepipeds. d) A polymeric slab containing a parallelepipedal gold nanorod. e) Stack of two tangent slabs, in a twisted configuration, each containing a rectangular gold parallelepiped nanorod. f) Selective etching of the gold

nanorods with potassium cyanide yielding an interfacial nanopore at the lozenges' interface between the slabs.

In practice, the rectangular parallelepipeds are fabricated by cutting thin (tens of nanometres in thickness) polymeric slabs containing a gold film (Figure 7.1d)[25]. Positioning two of those slabs on top of each other (Figure 7.1e) and selectively etching gold yields the interfacial nanopore (Figure 7.1f). In a typical application, the narrowest constraint in the passage of the buffer solution and ions from one side to the other side of the membrane (two slabs) is of zero thickness.

Atomic force micrographs of the fabricated devices bearing the interfacial nanopore in the middle are shown in Figure 7.2a and 7.2b, respectively before and after dissolving the gold structures. A glass substrate with a microscale opening at the centre was used to provide a mechanical support for the stack of slabs (Figure 7.2c).
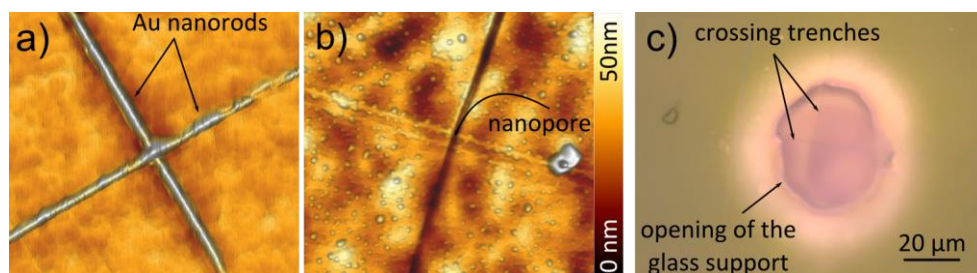

Figure 7.2. AFM characterization. a) Atomic force microscopy image of a two slab stack showing the two tangent-crossing nanorods embedded in the polymeric matrix. b) Atomic force microscopy image of the two slab stack after the etching of the gold using potassium cyanide. The black arrow points toward the nanopore created after the selective etching of the gold nanorods. Both the mappings in (a) and (b) are of 3 μm x 3 μm in size. c) Optical microscopy image of the final structure of a nanopore composed of two slabs, freely standing at the opening of a glass substrate (purple area). The dotted arrows show the lines of the two crossing parallelepipedal trenches.

Figure 7.3a illustrates the I-V characteristic of a nanopore achieved by etching two gold nanorods of 50 nm width and 200 nm height (respectively referred to as a and h throughout the chapter, see the inset in Figure 7.3b), leading to a pore area of 50×50 nm^2 (see Appendix V for the experimental details). The transmembrane potential sweeps from -200 mV to +200 mV and the salt concentration ranges between 1 mM and 1 M. The linear I-V behaviour confirms the ionic conduction of a nanopore filled with electrolytic solution and allows to exclude the establishment

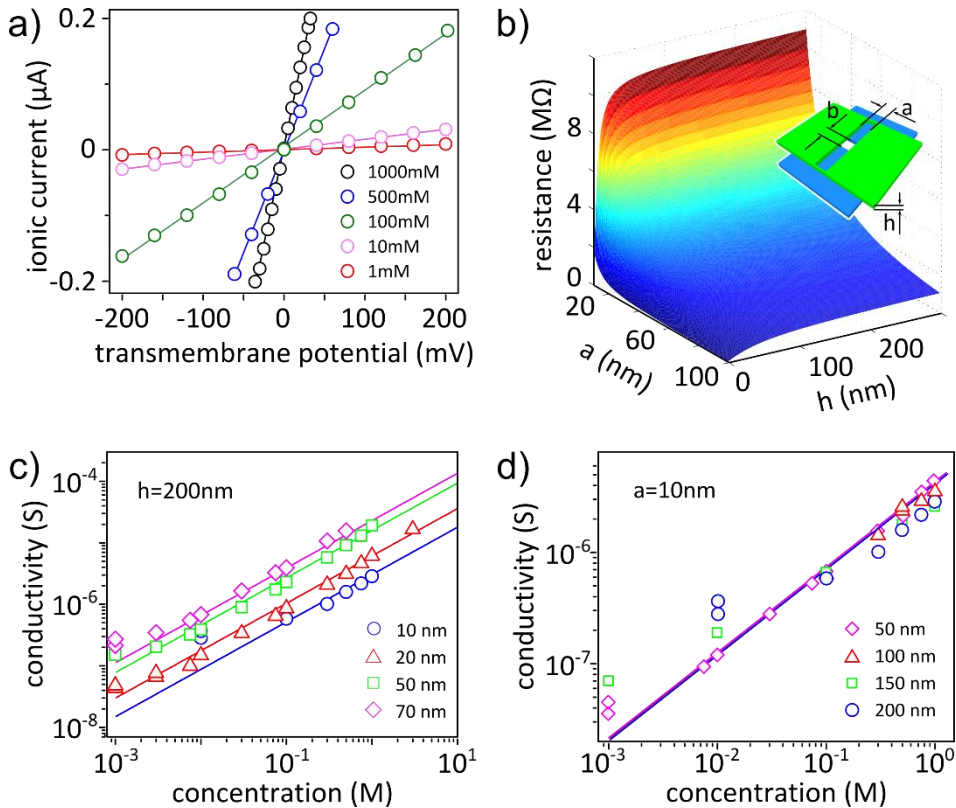of any electrochemical reaction within the flow-cell, especially in the proximity of the pore[13–15].

Figure 7.3. Ionic transport through interfacial nanopores. a) Ionic conduction through an interfacial nanopore (h=200 nm, a=50 nm) upon applying transmembrane potentials in KCl containing buffer solutions of different concentrations. b) Theoretically predicted resistance of interfacial nanopores as a function of the trench widths (a=b) and the equal thickness of the slabs (h). The inset depicts the three-dimensional architecture of the interfacial nanopore slab stack. The misorientation angle in between the trenches and the KCl concentration respectively were set to 90° and 1 M in this mapping. c) Conductivity of nanopores of different trench widths (a) as a function of the KCl concentration; Slabs of h = 200 nm thickness were used to fabricate these nanopores. The continuous lines show the best fittings with equation 1. d) Conductivity of nanopores of different thicknesses of the slabs (h) as a function of the KCl concentration; All the samples were of the same trench width of a = 10 nm. The continuous lines show the prediction of our model for the conduction and overlap each other.

The ionic flow through conventional nanopores experiences a total resistance due to i) the friction with the channel inside the pore region (pore resistance), and ii)

the convergence of the electric field lines at the 'mouth' of the nanopore (access resistance). Interestingly, the 2D nature of the interfacial nanopore eliminates the pore resistance term. Still, the access resistance of an interfacial nanopore is composed of two terms: i) the access resistance between the reservoir and the channels in the polymeric slabs, and ii) the resistance inside the channel towards the pore, on both sides. Analytically, the overall access resistance (R_t) of an interfacial nanopore is expressed as (see Appendix V):

$$R_t = \gamma \, \frac{F(a,b,h)}{\pi a b q c^n (\mu_+ + \mu_-)} \tag{1}$$

where c is the salt concentration in the electrolyte, $q = 1.6 \times 10^{-19}\,\text{C}$ is the elementary charge, μ_+ and μ_- are the mobility of cations and anions, a and b are the width of the upper and lower channels and h is the equal thickness of the slabs (inset in Figure 7.3b). F is a function of the geometrical parameters explained in Appendix V. The fitting parameters γ and n are introduced to take into account the surface conductivity of the pore upon the formation of an electrical double layer, which may impact on the linearity of the I-V curves.

Based on the model in Equation 1, Figure 7.3b provides a mapping for the expected resistance of the nanopore upon changing the geometrical parameters a and h (here $a = b$). The dependency of the resistance on the trench width is normally stronger than on the slab thickness; particularly for $h > 80\,nm$, the resistance is almost independent of h.

We experimentally measured the conductance of interfacial nanopores with different trench widths ranging from 10 nm up to 70 nm (Figure 7.3c). As expected, increasing a lowers the resistance due to the diffusion of ions leading to increased conductances in widened trenches. In Figure 7.3c, the continuous lines representing the prediction of the model in Equation 1 match with the experimental results for KCl concentrations above 1 mM. As expected, at lower KCl concentrations – and similarly to conventional solid-state nanopores – surface charges on the channel walls yield higher conductances than the one predicted by our model[26,27]. Remarkably and as predicted (Figure 7.3b), the effect of the slab thickness on the measured ionic resistance is negligible, most particularly for slabs thicker than tens of nanometres for ionic strengths above 10 mM (Figure 7.3d).

134

Again, at lower salt concentrations surface charges add-up to the total conductance of the nanopore architecture.

Figure 7.4a shows a typical time trace of the ionic current through an interfacial nanopore (a = 70 nm, h = 50 nm) immersed in a 5 mM LiCl buffer solution. Upon addition of 48.5 kbp λ-DNA molecules, a series of drops in the conductance of the nanopore appears, depicting the translocation of DNA molecules through the nanopore. Translocation was verified by a polymerase chain reaction (PCR) experiment (See Appendix V).
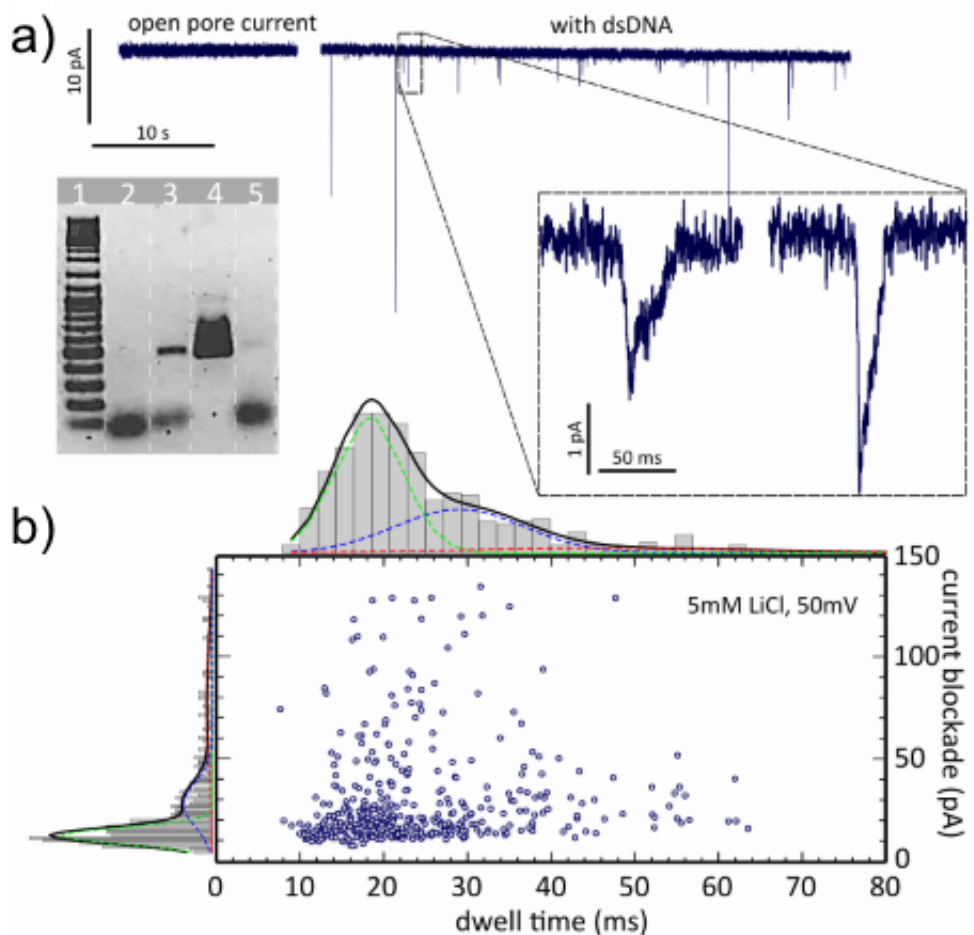

Figure 7.4. Interfacial nanopore as a single molecule sensor. a) Time-trace of the ionic current before and after the injection of λ-DNA (48.5 kbp) to the *cis* chamber of an interfacial nanopore (*a*=50nm, *h*=50nm). The measurement was performed in 5mM LiCl

buffer solution under the application of 30 mV transmembrane potential. The base line current approaches 1.23 nA and the trace is plotted after applying a low-pass filter ($f_{th} = 1\ kHz$). The right inset zooms on two translocation events. The left inset shows the result of the polymerase chain reaction (PCR) experiment where lanes 1, 2, 3, 4, and 5 respectively refer to the DNA marker, lambda DNA present in trans chamber before the translocation, lambda DNA present in trans chamber after translocation, 3 pg λ-DNA and water used as positive and negative controls for PCR (see Appendix V for the experimental details). b) Scatter plot of the amplitude of the current blockade versus translocation time for DNA translocation events through the same nanopore as in (a). The plot features ~400 translocation events, recorded during 10 min of experiments with λ-DNA at a concentration of 10 ng/µl. The distributions of the dwell time and current blockade are separately plotted in left and top inset panels. The dashed lines represent the fits of the events to Gaussian functions.

The duration and blockade current of the translocation events (~400 events) are plotted in Figure 7.4b. Two highly-populated events with Gaussian distributions are identified in both histograms (green and blue dashed curves) that can be attributed to the translocation of DNA molecules with different foldings. The more populated component exhibits an average translocation duration of ~22 ms which corresponds to ~450 ns/bp. Interestingly the measured dwell time is 1.5 to ~100 times longer than the reports for two-dimensional (5 ns/bp[14] - 56 ns/bp [2]), biological (30 ns/bp[28]) and solid-state (40 ns/bp - 300 ns/bp) nanopores[29].

Several observations suggest the presence of a strong interaction between DNA and the walls of the trench, which eventually slows down the translocation of molecules. First, the majority of the translocation events in interfacial nanopores starts sharply but ends smoothly (Figure 7.4a). This observation can be well explained considering a binding mechanism between DNA and the walls of the trench; in fact, the binding requires time and energy to break, in order to let the DNA exit the nanopore (Appendix V). Second, increasing the salt concentration lowers the dwell time through interfacial nanopores (Appendix V). This observation is in striking contrast to the reported behaviour of DNA in SiNx nanopores[29] in which the strong binding between Li$^+$ to DNA suppresses the translocation speed in high salt concentrations and can be well explained by considering the DNA-nanopore interaction. Third, the widely spread event duration, ranging from less than ~14 ms to over 80 ms (Figure 7.4b), is another signature of the DNA-nanopore interaction: in the absence of such interaction, DNA molecules are expected to exhibit uniform translocations[30]. Hydrophobic interaction between DNA and the

trench walls or cross-over from base-base pi-stacking to base-polymer pi-stacking[31] may govern the DNA-wall interaction.

The ionic resistance of nanopores, generally, is intuitively dominated by that of the most restrictive point (e.g. the interface region for interfacial nanopores) where the electric field is the strongest. Thus, the effective thickness of the nanopore can be defined by referring to the profile of the electric field along the central axis perpendicular to the nanopore area (Appendix V). Specifically, the effective thickness is twice the distance from the nanopore centre to the point where the electric field intensity drops to 1/e of its peak value. According to this definition, the effective thickness of interfacial nanopores with varied slab thicknesses is compared with that of conventional nanopores in Figure 7.5a. We recall the discussion from an earlier section where while ionic resistance in conventional nanopores consists of two components (pore and access resistances), the zero-geometrical thickness (as opposed to the effective thickness) of interfacial nanopores suppresses any contribution of the pore resistance. Indeed, interfacial nanopores show obvious advantages (lower effective nanopore thickness) over conventional nanopores with the channel thicknesses larger than the nanopore size ($h > a$). Our simulations show that the channel length (the thickness of the membrane) governs the effective thickness of conventional nanopores (Appendix V).
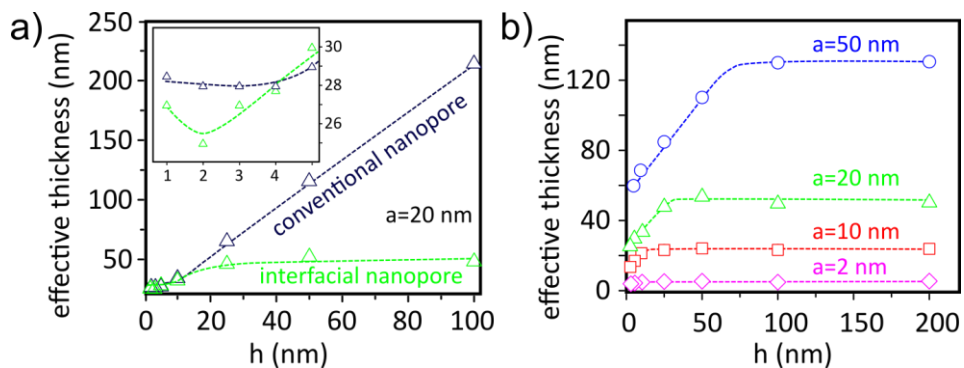

Figure 7.5. Effective thickness of the interfacial nanopores. a) Comparison of the calculated effective thickness of interfacial and conventional nanopores at different thicknesses: The membrane thickness of the conventional nanopore is *2h* to be comparable with interfacial nanopore formed by stacking two membranes, each having the thickness *h*. Both the nanopores are of squared shape openings of $20\ nm \times 20\ nm$. The inset focuses on a small window at very low *h*. The vertical and horizontal axis of the inset figure have the same

unit of the main panel. b) Evolution of the effective thickness of interfacial nanopores calculated for different slab thicknesses h and nanopore diameters a.

In the other extreme ($h < a$, comparable to the typical geometry of 2D nanopores) the effective thickness on each side of the interfacial nanopores can be estimated as half the width of the trench, $a/2$. This estimation resembles the conventional picture of the access resistance in single circular nanopores as two hemispheres with radius $r = d/2$ (where d is the diameter of the nanopore) at each side of the membrane[32,33]. Here, the interfacial nanopores are clearly advantageous since due to the lack of any pore resistance, its effective thickness always falls below that of the conventional nanopores (sum of the access and pore region, inset 7.5a).

As is demonstrated by our simulations (inset and main panel in Figure 7.5a), a conventional nanopore of h = 4 nm is preferred over the one of h = 100 nm as the former provides an effective thickness of ~8 times smaller (higher resolution); but at the same time, such a thin membrane is of poor stability. Hence, a thickness of few tens of nanometres provides a compromise between resolution and stability; this may partially explain why most of the conventional nanopores in solid state materials[34–37] have been sculpted in membranes with a thicknesses of ~ 20 nm. The introduction of interfacial nanopores dramatically shifts this compromise: here the effective thickness of a nanopore with h = 100 nm is just ~1.7 times higher than that of h = 4 nm; hence much thicker nanopores can be chosen without losing the resolution considerably. This is an intriguing property of the interfacial nanopores as the thickness of the membrane and the effective thickness (resolution) are now disentangled. The design of interfacial nanopores is unique as it eliminates the pore thickness; the remaining access resistance term can be minimized by optimizing the geometrical parameters (lowering the area of the pore, Figure 7.5b). Then the design allows to reach an ultimate resolution which is not reachable with conventional designs, always having a finite pore thickness. We note that the experimental evidences for an ultimate resolution can be achieved only when biomolecule sequencing is performed; this is not the case so far as prominent experimental challenges including high translocation speed of molecules do not allow single base reading[2].

Figure 7.6a compares the noise power spectral densities (PSD, denoted by S_I) of three types of nanopores, including a nanopore in graphene, a nanopore in SiNx and an interfacial nanopore, all of similar ionic conductances and comparable

nanopore areas. We used here 1 M KCl to be able to compare the noise of interfacial nanopores with previous reports[14,24]. The parasitic capacitive coupling of the fluidic chambers highly depends on the dielectric constant of the buffer and of the thickness of membrane separating the *cis* and *trans* fluidic reservoirs. The use of a borosilicate-glass support with millimetre thickness lowers the capacitance across the sample: the high frequency noise of the interfacial nanopores is at least one order of magnitude lower compared to conventional nanopores. Yet similar to that of the long channel SiNx nanopores, the maximum low frequency noise of interfacial nanopores is considerably lower than the one in 2D nanopores: the normalized PSD measured at 1 Hz with the current squared $\left(C_{1Hz} = \frac{S_{I,1Hz}}{I^2}\right)$ for twelve different interfacial nanopores at 100 mV transmembrane potential shows a normal distribution centered at $C_{1Hz} = 1.7 \times 10^{-7}$, well comparable to (~4 times higher than) in SiNx nanopores (4.4×10^{-8}) and almost 40 times lower than in 2D nanopores (6.3×10^{-6}) if measured under similar conditions[24] (Figure 7.6b). In fact, evaluating C_{1Hz} is a common approach to compare the noise among different nanopore devices[24].
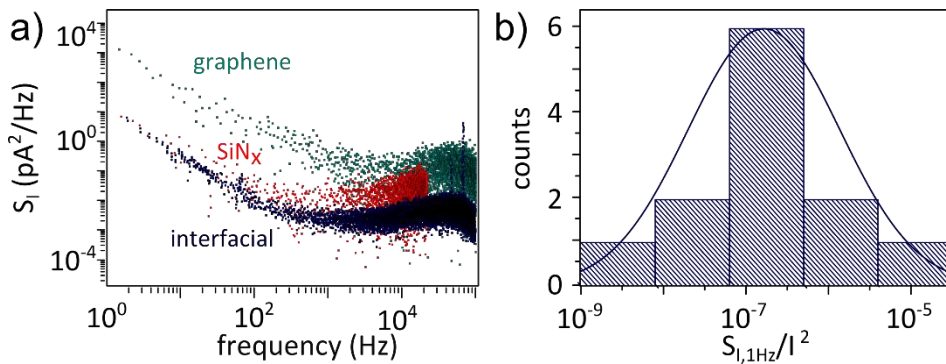

Figure 7.6. Characterization of the noise in interfacial nanopores. a) Comparison of the noise power spectral densities (PSD) of nanopores in graphene ($d = 14.2\ nm$, $R = 9.1\ M\Omega$), in SiNx membrane ($d = 20\ nm, t = 30\ nm, R = 7.5\ M\Omega$), and in an interfacial nanopore (a: $20\ nm, h$: $300\ nm, R = 9.9\ M\Omega$): All the measurements were performed in a 1M KCl buffer solution and under a 100 mV transmembrane potential. b) Distribution of the noise power (at $f = 1Hz$) of interfacial nanopores: measurements performed with 1M KCl buffer solution and under a 100 mV transmembrane potential. Data from 12 different samples with diverse geometries ($100\ nm \leq h \leq 300\ nm$ and $10\ nm \leq a \leq 70\ nm$) were used. Solid line is the Gaussian fit for the distribution.

At frequencies below 1 kHz, a wide variety of nanoscale devices exhibit flicker noise[38], characterized by PSDs exponentially decaying with the frequency: $S_I \propto \frac{1}{f^\alpha}$. For the majority of the nanopores studied so far[24,35,38], $\alpha = 1$, hence the low frequency noise is dubbed as $1/f$ noise. At commonly used transmembrane potentials (≤200 mV), however, the PSD in the interfacial nanopores, surprisingly exhibits a stronger dependency on frequency as $1/f2$ (i.e. $\alpha = 2$). Considerably increasing the potential, however, invokes the $1/f$ noise characteristics in the interfacial nanopores (Figure 7.7a). As the origin of the $1/f$ noise in conventional nanopores is yet unclear[2,24], understanding the factors altering the noise-frequency dependency in interfacial nanopores are complex, a fortiori (See Appendix V).
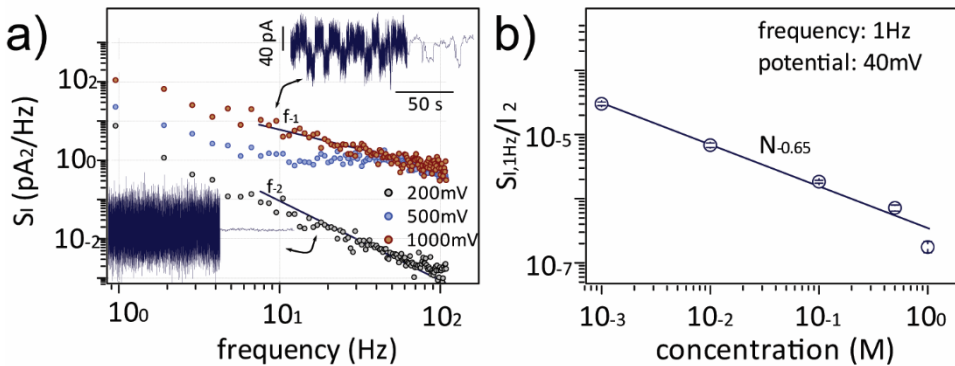

Figure 7.7. Low frequency noise of interfacial nanopores. a) Low frequency noise in an interfacial nanopore ($h = 250\,nm$, $a = 50\,nm$) at three different transmembrane potentials: Lines with f^{-1} and f^{-2} dependencies are superimposed to the data. Top and bottom insets show the corresponding signals in time-domain (right side low-pass filtered at 1 kHz), respectively measured at 1V and 200mV. The same horizontal and vertical scale bars apply for both of the traces. b) Noise power at $f = 1\,Hz$ as the function of KCl concentration: The data were extracted from 19 different samples with diverse geometries ($50\,nm \le h \le 300\,nm$ and $10\,nm \le a \le 70\,nm$) under 40mV transmembrane potential. The dotted line shows the best fitting of the data with $C^{-0.65}$.

The low frequency noise in solid-state and biological nanopores obeys Hooge's empirical relation[24,35,36,39] in which the normalized PSD is inversely proportional to the number of charge carriers, $C_{1Hz} \propto N^{-1}$. The model, however, ceases to explain the low frequency noise in graphene [24] and in interfacial nanopores (See Appendix V). We collected $S_I(f = 1\,Hz)$ for 19 different samples (with diverse a and h

values) at various KCl concentrations and plotted against the corresponding squared currents upon applying a constant 40 mV transmembrane potential, Figure 7.7b (see Appendix V). Interestingly, the data corresponding to each concentration level (regardless of the geometry) follows the lines of certain slopes that can be best fitted by $\frac{S_{I,1Hz}}{I^2} \propto N^{-0.65\pm0.05}$. The measured dependency is weaker than the Hoog's prediction, yet stronger than what was observed for graphene nanopores ($\propto N^{-0.27}$)[24].

7.3   Conclusions

In summary, nanopore sensors lacking a capillary depth showed the successful detection of translocating DNA molecules. Compared to the different nanopores studied so far, interfacial nanopores combine an absolute minimal channel length with outstanding mechanical stability, minimum noise level, and reduced translocation rates. The fabrication of interfacial nanopores is scalable and does not require high-level precision. Furthermore, taking advantage of the two nanogaps as potential masks directly aligned with a nanopore, the sandwiching of 2D materials in between the slabs will allow the realization of – for example – graphene nanogap[40] electrodes in a straightforward manner. Future improvements focusing on reducing even further the nanogap widths with alternative parallelepipedal templates will provide insights into sequencing applications with tunnelling currents, an application never achieved hitherto, primarily because of the challenging nanofabrication considerations.

7.4   References

(1)   Schneider, G. F.; Dekker, C. *Nat. Biotechnol.* **2012**, *30* (4), 326–328.

(2)   Arjmandi-Tash, H.; Belyaeva, L. A.; Schneider, G. F. *Chem. Soc. Rev.* **2016**, *45* (3), 476–493.

(3)   Venkatesan, B. M.; Bashir, R. *Nat. Nanotechnol.* **2011**, *6* (10), 615–624.

(4)   Kowalczyk, S. W.; Blosser, T. R.; Dekker, C. *Trends Biotechnol.* **2011**, *29* (12), 607–614.

(5)   Dekker, C. *Nat. Nanotechnol.* **2007**, *2*, 209–215.

(6)   Kim, M. J.; Wanunu, M.; Bell, D. C.; Meller, A. *Adv. Mater.* **2006**, *18* (23), 3149–3153.

(7)   Sen, Y. H.; Karnik, R. *Anal. Bioanal. Chem.* **2009**, *394* (2), 437–446.

(8)   Jain, T.; Guerrero, R. J. S.; Aguilar, C. A.; Karnik, R. *Anal. Chem.* **2013**, *85* (8), 3871–3878.

(9)   Sathe, C.; Zou, X.; Leburton, J.-P.; Schulten, K. *ACS Nano* **2011**, *5* (11), 8842–8851.

(10)   Cherf, G. M.; Lieberman, K. R.; Rashid, H.; Lam, C. E.; Karplus, K.; Akeson, M. *Nat. Biotechnol.* **2012**, *30* (4), 344–348.

(11)   Song, L.; Hobaugh, M. R.; Shustak, C.; Cheley, S.; Bayley, H.; Gouaux, J. E. *Science.* **1996**, *274* (5294), 1859–1865.

(12)   Venkatesan, B. M.; Dorvel, B.; Yemenicioglu, S.; Watkins, N.; Petrov, I.; Bashir, R. *Adv. Mater.* **2009**, *21* (27), 2771–2776.

(13)   Schneider, G. F.; Kowalczyk, S. W.; Calado, V. E.; Pandraud, G.; Zandbergen, H. W.; Vandersypen, L. M. K.; Dekker, C. *Nano Lett.* **2010**, *10* (8), 3163–3167.

(14)   Merchant, C. A.; Healy, K.; Wanunu, M.; Ray, V.; Peterman, N.; Bartel, J.; Fischbein, M. D.; Venta, K.; Luo, Z.; Johnson, A. T. C.; Drndić, M.; et al. *Nano Lett.* **2010**, *10* (8), 2915–2921.

(15)   Garaj, S.; Hubbard, W.; Reina, A.; Kong, J.; Branton, D.; Golovchenko, J. a. *Nature* **2010**, *467* (7312), 190–193.

(16) Zhou, Z.; Hu, Y.; Wang, H.; Xu, Z.; Wang, W.; Bai, X.; Shan, X.; Lu, X. *Sci. Rep.* **2013**, *3*, 3287.

(17) Barati Farimani, A.; Min, K.; Aluru, N. R. *ACS Nano* **2014**, *8* (8), 7914–7922.

(18) Waduge, P. *ACS Nano* **2015**, *9* (7), 7352–7359.

(19) Liu, K.; Feng, J.; Kis, A.; Radenovic, A. *ACS Nano* **2014**, *8* (3), 2504–2511.

(20) Feng, J.; Liu, K.; Bulushev, R. D.; Khlybov, S.; Dumcenco, D.; Kis, A.; Radenovic, A. *Nat. Nanotechnol. **2015**, 10, 1070–1076*.

(21) Traversi, F.; Raillon, C.; Benameur, S. M.; Liu, K.; Khlybov, S.; Tosun, M.; Krasnozhon, D.; Kis, A.; Radenovic, A. *Nat. Nanotechnol.* **2013**, *8* (12), 939–945.

(22) Fischbein, M. D.; Drndi, M., Appl. Phys. Lett. **2008**, 93, 113107.

(23) Liu, S.; Lu, B.; Zhao, Q.; Li, J.; Gao, T.; Chen, Y.; Zhang, Y.; Liu, Z.; Fan, Z.; Yang, F.; You, L.; Yu, D. *Adv. Mater.* **2013**, *25*, 4549–4554.

(24) Heerema, S. J.; Schneider, G. F.; Rozemuller, M.; Vicarelli, L.; Zandbergen, H. W. *Nanotechn.* **2014**, 1–18.

(25) Lipomi, D. J.; Martinez, R. V; Whitesides, G. M. *Angew. Chem. Int. Ed. Engl.* **2011**, *50* (37), 8566–8583.

(26) Stein, D.; Kruithof, M.; Dekker, C. *Phys. Rev. Lett.* **2004**, *93* (3), 035901.

(27) Smeets, R. M. M. R. M. M.; Keyser, U. F. U. F.; Krapf, D.; Wu, M. Y. M. Y.; Nynke, H.; Dekker, C.; Dekker, N. H.; Dekker, C. *Nano Lett.* **2006**, *6* (1), 89–95.

(28) Wanunu, M.; Sutin, J.; McNally, B.; Chow, A.; Meller, A. *Biophys. J.* **2008**, *95* (10), 4716–4725.

(29) Kowalczyk, S. W.; Wells, D. B.; Aksimentiev, A.; Dekker, C. *Nano Lett.* **2012**, *12* (2), 1038–1044.

(30) Garaj, S.; Liu, S.; Golovchenko, J. A.; Branton, D. *Proc. Natl. Acad. Sci.* **2013**, *110* (30), 12192–12196.

(31) Akca, S.; Foroughi, A.; Frochtzwajg, D.; Postma, H. W. C. *PLoS One* **2011**, *6* (4), e18442.

(32)   Hall, J. R. *J. Gen. Physiol.* **1975**, *66* (2), 531–532.

(33)   Levadny, V.; Aguilella, V. M.; Belaya, M. *Biochim. Biophys. Acta - Biomembr.* **1998**, *1368*, 338–342.

(34)   Smeets, R. M. M.; Keyser, U. F.; Wu, M. Y.; Dekker, N. H.; Dekker, C. *Phys. Rev. Lett.* **2006**, *97* (8), 088101.

(35)   Smeets, R. M. M.; Dekker, N. H.; Dekker, C. *Nanotechnology* **2009**, *20* (9), 095501.

(36)   Smeets, R. M. M.; Keyser, U. F.; Dekker, N. H.; Dekker, C. *Proc. Natl. Acad. Sci. U. S. A.* **2008**, *105* (2), 417–421.

(37)   Kowalczyk, S. W.; Hall, A. R.; Dekker, C. *Nano Lett.* **2010**, *10* (1), 324–328.

(38)   Balandin, A. *Nat. Nanotechnol.* **2013**, *8* (8), 549–555.

(39)   Bezrukov, S. M.; Vodyanoy, I.; *Biomembrane Electrochemistry*; **1994**; 375–399.

(40)   Postma, H. W. C. *Nano Lett.* **2010**, *10* (2), 420–425.

CHAPTER 8

Summary, Conclusions & Outlook

8.1   Summary and general conclusions

Despite a series of promising first and conceptual results, the widespread use of graphene encountered a series of bottlenecks. Beyond the difficulties concerning the agile handling and cheap synthesis of this material, also the nanofabrication and the limited control over its chemistry represent serious limitations. The most promising devices still rely on extremely complicated production processes, which can hardly meet the standardization requirements of large scalability. Furthermore, chemical functionalization is often referred to as the most powerful tool towards the next generation of sensing devices, entitled of advanced molecular selectivity. Still, little or few is achieved concerning the selective functionalization of graphene films, particularly at the edges. Edge functionalities can finely tune the chemical-physical properties of graphene, particularly of nanostructures, where the amount of edges becomes significant over the amount of carbon atoms composing the lattice of graphene. At the state of the art, only chemical synthesis yields highly controlled chemically designed graphene nanostructures, still facing the impossibility of their integration into sensing devices. On the other hand, top down approaches demonstrated the possibility to chemically functionalize graphene, however with limited selectivity between the basal plane and the edges.

This thesis focuses on the unconventional nanofabrication of graphene based nanostructures, while maintaining a strong control on the edge chemistry of graphene. By means of mechanical approaches such as microtomy, in combination with bulk methods such as reactive ion etching or cyclic voltammetry, we fabricated nanopores, nanogaps and nanoribbons architectures, avoiding conventional lithographic procedures. The presented nanofabrication strategies, also, are implemented towards an improved control over the chemistry of the edges of graphene. Accordingly, the thesis is divided in two main parts, first the edges of graphene, their chemistry and application in Chapter 2, Chapter 3, and Chapter 4. Second, we focused on the unconventional fabrication of graphene nanostructures in Chapter 5, and 2D nanoarchitectures in polymeric and metallic supports, in Chapter 6 and Chapter 7. The results demonstrated a first step towards the achievement of scalable, unconventional nanofabrication processes capable of fabricating graphene nanostructures while maintaining and controlling the edge chemistry. We believe that the implementation of these technologies, singularly,

and their integration into a unique device is paramount for the next-generation sensing platforms based on graphene. In the near future, for instance, nanogaps and nanopores will merge into a sole nanofluidic system equipped of tunnelling electrodes, where the chemistry at the edges of graphene will be tailored for specific sensing applications.

In Chapter 2, we begin providing an extensive literature review about the chemistry at the edges of graphene. This chapter aims to highlight the state of the art in the field, referring to the most recent literature. The chapter illustrates the importance of the chemistry at the edges of graphene to fine tune the electrical properties of graphene.

Inspired by the outcome of this literature research, in Chapter 3 we investigate the chemical functionalization of the edges of a chemically vapour deposited, CVD, graphene monolayer. The selective functionalization of CVD graphene remains hardly achievable because of the competitive reaction sites provided by the basal plane, primarily at defects and grain boundaries. In order to achieve selective reactions on the edges, we encapsulated graphene within a polymer matrix that was subsequently sectioned via microtomy. Microtomy opens an edge exposed through the sliced interface of the polymeric embodiment. We then built an electrochemical cell for the wet functionalization of this edge. In fact, the edge of graphene is addressed by cyclic voltammetry, where graphene works as the working electrode against an Ag/AgCl reference electrode. Interestingly, we demonstrated the possibility of addressing the chemistry at the edges of graphene without any conventional nanofabrication nor atomic characterization, introducing an innovative approach to the current literature.

The controlled formation of edges in graphene using bulk methods was further explored employing reactive ion etching. Starting from the etching of a suspended CVD film of graphene, in Chapter 4, we successfully built a tunnelling junction between the edges of two graphene electrodes precisely interfaced at sub nanometric distances. This approach yielded the first dynamic tunnelling junction across two single carbon atoms at the edges of two supported graphene monolayers. Our architecture comprises a nanogap composed of two independently supported graphene films interfaced by means of piezoelectric actuators. The edges are interfaced with a twisted configuration crossing in a single

point and forming a tunnelling junction across two single carbon atoms. Our adjustable junction allowed also to explore the dynamics of what we speculate being the electrical fingerprint of carbon-carbon bonds forming across the two extremities of the junction upon contact.

Employing a similar approach, in Chapter 5 we used reactive ion etching to address the edge chemistry of another class of graphene nanostructures: graphene nanoribbons. First, we used microtomy to slice metallic nanorods employed as inert masks for the lithography of graphene nanoribbons. Precisely aligned nanorods avoid the application of polymeric resists common in conventional lithography. This, in first instance, prevents polymeric contaminations on the surface of the graphene. Secondly, metallic masks withstand within harsh chemical conditions, for instance during prolonged etching times or, as we attempted, during solution functionalization in organic solvents, incompatible with polymeric resists. Additionally, we employed different etching atmospheres in order to control the edge chemistry of graphene. Despite a poor of control on the crystal structure of the edges of the graphene nanoribbons, we still could observe a modification of the Raman fingerprint, characteristic of doping induced by the chemical functionalization of the edges.

The microtomy of nanorods from metallic thin films is a powerful nanotechnology tool. Beyond the lithography of graphene nanoribbons, microtomy can produce series of metallic nanorods aligned in a parallel fashion and regularly spaced. The coupling of pairs of nanorods at nanometric distance directly yields nanogaps between two metallic electrodes, namely the pair of nanorods. In Chapter 6, multilayered films of polyelectrolytes were grown via Layer-by-Layer deposition and were used as polymeric spacers between gold thin films further converted into nanogaps via microtomy. Microtomy slices the gold films separated at nanometric distance, yielding a nanogap between two nanorods. The flexibility of the Layer-by-Layer deposition and ease of preparation yield a versatile method to assemble thin layers of polyelectrolytes between electrodes with controllable interlayer distance down to 1.5 nm.

In the previous chapters, we extensively worked on the nanostructuring of graphene and its chemical functionalization. The previous work has been performed aiming to fabricate a graphene device integrated into fluidic system

able to deliver analytes to the graphene sensing element. Therefore, in Chapter 7, we proposed an innovative nanopore/nanocapillary fluidic system, composed of layered polymeric slabs, which would allow in the future to integrate a nanopore device with a pair of tunnelling electrodes. Similarly to inert mask lithography, we slice metallic thin films embedded in polymeric matrices via microtomy, yielding metallic nanorods supported by polymer slabs. Two nanorods are deposited on top of each other in a crossed configuration. Subsequently, we etch the metallic rods opening two crossing slits through the polymeric supports. The trenches form two nanofluidic channels sharing an aperture: a nanopore. Notably, the overlapping of the two slits forms a nanopore of zero-depth. This capillary, in principle, has the geometrical advantages of atomically thin materials such as graphene, without demanding for extremely complicated fabrications.

Briefly, the present thesis focuses on the unconventional design of nanostructures and the chemical functionalization of graphene edges. This work is the outcome of the attentive analysis of the factors representing a bottleneck in the state of the art in the nanofabrication and chemical functionalization of graphene, which often cannot proceed further than the prototyping phase. Our findings propose a new approach to the field, attempting in a simplification of the current standards of both fabrication, functionalization, and characterization.

We successfully demonstrated the innovative and unconventional achievement of some of the most common nanostructures such as nanopores, nanoribbons and nanogaps, while first proposing a simple, yet effective, way to address the chemistry of the edges of a graphene CVD film. These results, we believe, are of primarily importance to push forward the advancement of the nanotechnology community, particularly for the exploration of non-standard solutions to shape graphene in devices while controlling the chemistry of this material to a larger extent.

8.2 Outlook

Our work explored the fabrication and the chemical functionalization of graphene nanostructures composing sensing devices, and comprising nanopores, nanoribbons and nanogaps.

We already begun exploring the behaviour of tunnelling junctions in water and in presence of buffer solutions and biomolecules. Similarly, lithographic steps were attempted to deliver molecular junctions through gold nanorods separated by multilayered films of polyelectrolytes.

More interestingly, we would like to offer an overview on the shared horizon of these starting results. In fact, in the introduction we highlighted how nanopores, nanoribbons and nanogaps are reunited into sensing devices, even though often only in theoretical simulations. The results and the nanostructures we achieved, instead, can be assembled into real devices. For instance, the multilayered polymeric slabs composing the zero-depth nanopores can host graphene layers in between the two polymer slabs. Etching first the rods and then graphene through the resulting slits, can deliver what is the first graphene nanogap embedded in a nanopore, first joining the electrical device to the fluidic system, Figure 8.1.
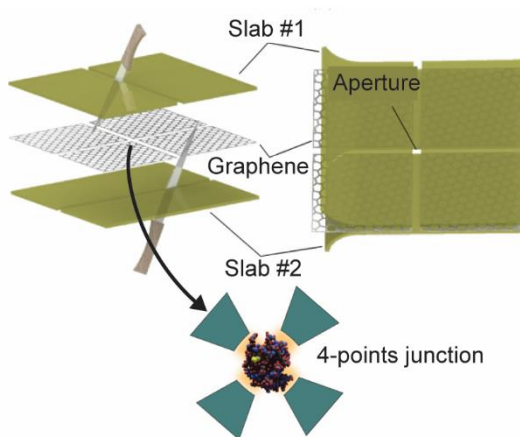

Figure 8.1. Embedding of a nanogap into a nanopore. A four point nanogap is opened in a graphene layer via reactive etching through the slits composing the zero-depth nanopore.

Interestingly, our experiments on reactive etching are the starting point to determine the chemistry of the graphene electrodes, which once immersed into the nanofluidic systems can be addressed for instance via electrochemical approaches, as demonstrated by the electrografting experiments presented in Chapter 3.

In this direction, it is of particular interest to know the characteristic of a tunnelling junction in graphene, and its behaviour when immersed into a liquid environment, similarly to what performed and illustrated in a system such as the twisted nanogaps in Chapter 4.

Thus, we believe that the integration of these nanopore and nanogap components is possible, and we already begun its development. We assembled the very first zero-depth nanopores embedding graphene films and attempted to open a nanometric gaps across the pore, Figure 8.2.
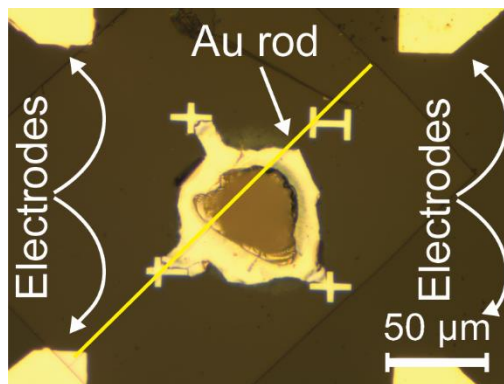

Figure 8.2. Zero depth-nanopore/nanogap. A supported gold nanorod is deposited on a micrometer window as first layer of a zero-depth nanopore embedding a graphene nanogap.

We believe that our work is an important starting point towards the fabrication of graphene based tunnelling junctions and that further investigation can lead to the assembly of real sensing devices operating in water with graphene and other two dimensional materials as the main sensing element.

8.3   General perspectives

Since its discovery, graphene promised to revolutionize many aspects of technology, varying from electronics, to composites and building materials. Particularly, the 2D nature of graphene and its outstanding thermal, mechanical, and electronic properties pointed straight to its application at the nanometre scale, reaching atomistic control over the topology and chemical structure of the carbon atoms composing its lattice. Eventually, graphene could be tailored in size and properties for almost any imaginable application.

Through this work, graphene demonstrated itself as a flexible and powerful platform, which can be adapted to an extended variety of processing techniques, fulfilling the long-told promise of applicability that too often fatigues to be translated into actual technology (especially out of the lab). In fact, the promise of a flexible material, easily tailored in various architectures at the nanoscale and chemically defined, inspired the different chapters composing this thesis. Indeed, graphene demonstrated a great degree of flexibility, that successfully applied to different architectures such as nanoribbons, embedded transistors and nanogaps. Outstandingly, the high workability of such a simple layer of carbon atoms allowed the investigation of extremely complex problems with fairly easy approaches, designed to adapt to graphene at the nanoscale, while being simple and innovative. Whereas graphene appears as the only common element connecting the dots through this work, it actually demonstrates its ability to adapt and to be incorporated in completely different systems expected to compose extremely different devices addressing problems that range from highly scientific platforms for the study of tunnelling currents across nanogaps and molecules, to small transistors which might one day compose any electronic device. Based on the major research interest of our working group, a great focus was pointed to the potential of these graphene architectures into biomolecular sequencing devices, as suggested also by the innovative work performed on layered nanopores architectures, meant to integrate graphene nanogaps and nanopores.

In our perspective, graphene maintained its promise of being a robust and flexible material, with outstanding properties and the potential of interesting many aspects of science and technology. Huge efforts were spent in the attempts of modulating also the chemistry at the edge of graphene. This subject is of rising interest in the scientific community as it represents a valuable tool in order to specifically address the properties of graphene both in terms of its physical properties and chemical interactions. Graphene, thanks to the extended aromaticity, is often imaged as an inert material. Edges, nonetheless, offer excellent reactivity and ideal reaction sites for the chemical functionalization of graphene. The edge functionalization of graphene is too often explored from the perspective of chemically synthetized graphene, or exfoliated graphene, where the process solution also addresses the chemistry of this material. Nonetheless, most of the technological application of graphene in the near future are expected to interest CVD graphene in the form of top-down processed graphene, starting from

large graphene films which original edge chemistry is uncontrollable. Is this a limit of graphene? Do its flexibility and ability of being widely processed and structured encounter a bottle neck when dealing with its chemistry? Is its edge chemistry controllable also in top down approaches and on large area CVD films? We demonstrated at least two different transistor architectures, on completely different substrates and prepared accordingly to two completely different protocols which answer these questions. Yes, the chemistry at the edge of graphene can be controlled and can be addressed even when not processed through organic synthesis nor solution-based exfoliation. The chemistry of the edges of graphene becomes accessible at large, thin film scale, with immediate repercussion on its properties, and for the first time studied with bulk characterization methods, rather than hardly accessible atomistic approaches such as scanning probe microscopy. We functionalized CVD graphene films that can be transferred, isolated, and processed out of synthesis solutions and CVD exfoliation media. In this research, the chemistry at the edges of graphene at last encounters graphene samples which can be translated into actual devices and practical technologies.

Appendix I

Supporting Information to Chapter 3

I.I   Materials and Methods

I.I.I   The embedding polymer

The graphene edge electrode was embedded in a polymer scaffold made of pentaerythritol tetrakis (3-mercaptopropionate) (PEMPT; i.e., component A), and 1,3,5-Triallyl-1,3,5-triazine-2,4,6(1H,3H,5H)-trione (TATATO; i.e., component B) mixed in molar proportion 3 : 4 = A : B. The mixture was degassed under vacuum for about one hour. Next, 1%$_{WT}$ of dimethoxy-phenylacetophenone was added to the A : B mixture as photo-initiator[1,2]. Last, the polymer was hardened in air under the irradiation of a 365 nm ultraviolet lamp for 30 minutes, 7000 µW/cm^2 at 38,2 cm of distance.

I.I.II   Preparation of the graphene layer

A drop of polymer was casted and cured onto a Si/SiO$_2$ wafer (purchased from University Wafer) patterned with a thermally evaporated gold electrode (5 X 5 mm^2, homemade thermal resistance evaporator operating below 1x10^{-6} bar). The embedding polymer contains thiol functionalities, promoting a strong adhesion to the gold. Next, to lift the gold electrode from the SiO$_2$ surface, a razor blade is intercalated between the polymer and the surface of the wafer. The lift-off process yields an ultra-flat polymeric substrate embedding a gold contact pad used for the electrical connection of the graphene sample. The cured polymer embedding the gold electrode was then exposed to an oxygen plasma (Diener Plasma Etcher at 0.3mbar O$_2$, 60W for 30s) in order to convert its surface to hydrophilic. Afterwards, the polymeric substrate was immersed in a petri-dish containing ultra pure water with the gold electrode facing the water surface. Subsequently, a graphene layer coated with poly (methyl methacrylate), PMMA, was transferred floating over the water surface. The transfer proceeds via the removal of the water and the gentle deposition of the graphene over the surface of the polymer across the gold electrode. The alignment of the PMMA coated graphene with the gold electrode was performed using a needle and a micro-manipulator. Graphene was purchased from Graphenea®, grown via chemical vapor deposition on top of a Cu substrate. The graphene layer was spin-coated with PMMA and back-etched using an oxygen plasma at 0.3 mbar O$_2$, 60 W for 45 s, in order to remove any trace of carbon from the uncoated (back) side of the Cu substrate. Afterwards the Cu was etched in a

156

0.5 M solution of $(NH_4)_2S_2O_8$. Following the etching of the copper, the PMMA coated graphene was rinsed through three petri-dishes filled with ultra pure water, in order to remove any trace of etchant from the surface of the graphene. All the chemicals were purchased from Sigma-Aldrich®.

I.II   Microtomy

The edge electrode was exposed through the polymer scaffold by microtomy sectioning (see Figure 3.1 of Chapter 3). The polymeric matrix embedding the edge of graphene was first cut in two parts with a razor blade in order to expose the graphene. Next, the surface of the polymer scaffold exposing the graphene edge was flattened by trimming via microtomy employing a Leica® EM UC 6 mounting a Diatome® trim tool 20®. Last, the polymer scaffold was finely sectioned by microtomy using an Ultra Diamond Knife 35®. The microtomy process yields an ultra-flat polymeric surface exposing the edge of a PMMA-coated graphene film, namely the graphene edge electrode (see Figure 3.1 of Chapter 3).

I.III   Cyclic voltammetry

The graphene edge acts as a working electrode in a two electrodes system against an Ag/AgCl reference/counter electrode. Cyclic voltammetry characterizations were performed using an Autolab® potentiostat. The characterization of the edge was performed initially in 0.1 M KCl at 0.1 Vs^{-1}, 0.05 Vs^{-1} and 0.01 Vs^{-1}. The cyclic voltammetry in presence of a redox probe was performed at 0.05 Vs^{-1} with a 5 mM solution of $K_3Fe(CN)_6$ in 0.1 M KCl. The functionalization with a nitrobenzene tetrafluoroborate diazonium salt, $BF_4N_2C_6H_4NO_2$, was carried in a solution of 1 mM $BF_4N_2C_6H_4NO_2$ in 0.1 M $HClO_4$ in ultra pure water. All the chemicals were purchased from Sigma-Aldrich®.

I.IV   Raman characterization

The graphene was first characterized by Raman spectroscopy on top of a Si/SiO_2 wafer (inset Figure 3.2a of Chapter 3). A sample of PMMA coated graphene was transferred over a SiO_2 substrate. Next, the PMMA was removed with acetone and the sample was rinsed with isopropanol and ethanol.

Additionally, the variation of the Raman signature of the embedding polymer was monitored to exclude the adsorption of nitrobenzene on the polymeric surface. The edge electrode and the surrounding polymer were rinsed with ultra pure water after electrografting. Figure I.1 shows the Raman spectroscopy of the embedding polymer before (black curve) and after (red curve) functionalization of the edge electrode. No significant changes in the Raman spectra occurred after the electrografting reaction (particularly observing the peaks at 1425 cm^{-1} and 1650 cm^{-1}), indicating that the electrografting did not involve the polymer embedding (only the edge electrode as discussed in Chapter 3).

All the Raman spectra were acquired using a WITec Raman Alpha 3000® instrument equipped with a 532nm laser source.
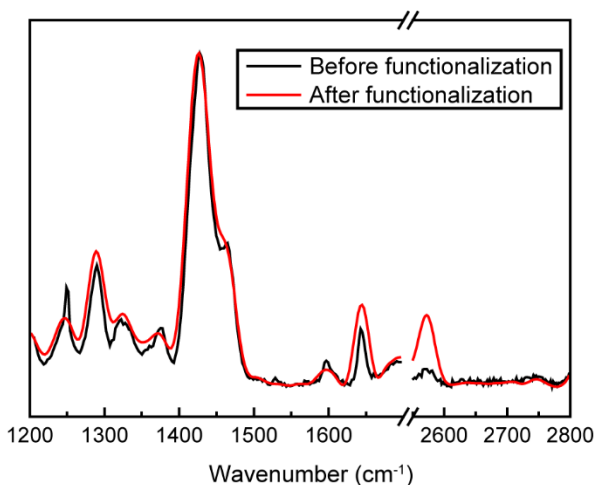

Figure I.1. Raman spectra of the embedding polymer. Black curve: Raman spectrum obtained with a 532 nm laser before the electrografting reaction. Red curve: Raman spectrum obtained with a 532 nm laser after the electrografting reaction. The spectra are normalized over the peak at 1425 cm^{-1}.

I.V   Electrical characterization

The gating experiments were performed using a lock-in amplifier from Stanford Research System (SR830). The electrical characterization of the graphene transistor was performed in a liquid gating configuration (see Figure 3.5 of Chapter 3 and Figure I.2a). The graphene edge electrode was loaded at the gate voltage through a 1 M KCl solution and an Ag/AgCl electrode connected to the direct

coupling (DC) source of the amplifier, sweeping the gating potential between -0.5 V and 0.2 V.

The output voltage of the lock-in was set at 1 V and 77.77 Hz and connected to a 1 MΩ resistor used to impose a 1 µA current through the source and drain of the transistor, while the drain was grounded (Figure 3.5 of Chapter 3 and black line connecting the gold electrodes in the schematics of Figure I.2a).

The edge selectivity of the electrografting was confirmed with a control experiment forming an edge on SiO_2 via oxygen plasma etching. Figure I.2a shows the preparation of the sample: a CVD film of graphene was deposited on a SiO_2 substrate and partially covered with the PEMPT-TATATO polymer. The excess of graphene was etched using an oxygen plasma. The remaining graphene was covered by the polymer. The role of the polymer is to protect the graphene, forming an edge at its extremity. Next, the graphene was probed electrically using a liquid gating configuration as shown in Figure I.2a (right side) using a 1 M KCl electrolytic solution.

Afterwards, the edge was first functionalized by electrografting nitrobenzene diazonium via cyclic voltammetry with voltages ranging from 0.05 Vs^{-1} to -0.5 V and 0.1 V in a 1 mM solution of 4-nitrobenzene diazonium tetrafluoroborate (NBD; $BF_4N_2C_6H_4NO_2$) dissolved in an acidic solution of 0.1 M perchloric acid ($HClO_4$), and then probed electrically.
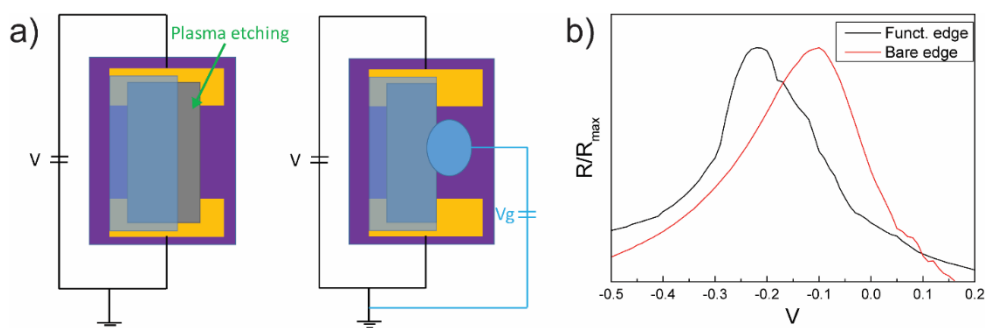

Figure I.2. Graphene edge electrode fabricated on a Si/SiO_2 wafer. a) A graphene field effect transistor, GFET, with an exposed edge electrode was formed by partially coating a graphene film with the PEMPT/TATATO polymer. An oxygen plasma etches the unprotected graphene, forming an edge at the interface with the protecting polymer. The edge electrode was in contact with an electrolyte solution of 1 M KCl and a gate potential

V$_g$ was applied to the edge through the solution. b) Conductivity measurements of the GFET before functionalization (red curve) and after functionalization (black curve).

Figure I.2b compares the gating curves of the graphene film before functionalization (red curve) and after functionalization (black curve). The results of the control experiment in Figure I.2b suggest a behaviour comparable to what was observed with the polymer-embedded graphene edge electrode in Figure 3.3d in Chapter 3. As shown in Figure I.2b, the conductivity of the graphene sample was negligibly affected by the electrografting at the edge, indicating the protection of the basal plane towards electrografting. The shift in resistivity at the charge neutrality point was around three times the minimum in resistivity at negative gating potential, as observed also for the edge electrode in Chapter 3.

I.VI   References

(1)   Lu, H.; Carioscia, J. A.; Stansbury, J. W.; Bowman, C. N. *Dent. Mater.* **2005**, *21* (12), 1129–1136.

(2)   Mays, R. L.; Pourhossein, P.; Savithri, D.; Genzer, J.; Chiechi, R. C.; Dickey, M. D. *J. Mater. Chem. C* **2013**, *1* (1), 121–130.

Appendix II

Supporting Information to Chapter 4

II.I   Materials and Methods

II.I.I   Graphene

Graphene nanogaps were formed using chemically vapor deposited graphene, CVD, on Cu purchased from Graphenea®. Before the deposition on the supports, the copper substrate of the CVD graphene was removed via wet etching in a 0.5 M aqueous solution of ammonium persulfate $(NH_4)_2S_2O_8$ purchased from Sigma-Aldrich®.

II.I.II   The protecting polymer

Graphene was first coated with a protecting film of poly (bisphenol A carbonate), PCA (M_W 45000 gmol^{-1}), prepared in a chloroform solution (1.5% wt). The film was spin-coated at 4000 rpm for 60 s over the graphene film on copper. After the deposition on the Si/SiO$_2$ substrates, the suspended graphene was etched via reactive ion etching. Afterwards, the protecting PCA film was dissolved in chloroform overnight and rinsed in methanol and isopropanol (all the chemicals were purchased from Sigma-Aldrich®).

II.I.III   Preparation of the supports

The graphene edge electrodes were prepared by etching of a suspended graphene film transferred over two independent Si/SiO$_2$ supports.

We employed undoped Si/SiO$_2$ supports from Sieger Wafers® with a polished oxide surface 285 nm thick. The supports were prepared by notching a Si/SiO$_2$ wafer using a diamond scribe. The notch indents the oxide initiating a crack in the Si crystal. Upon applying strain to the wafer, the crack propagates along the crystallographic orientation of the wafer yielding two supports with extremely sharp edges. Sharp edges were a prerequisite to have uniform edge electrodes and facilitate the approach of the tunnelling junction.

Before the deposition, the supports were cleaned by organic solvents (acetone, isopropanol, ethanol) and further cleaned in a piranha solution (1:3=hydrogen peroxide : sulphuric acid) and afterwards exposed to O$_2$ plasma at 0.3 mbar 60 W for several minutes. The piranha solution and the plasma clean the surface of the

Si/SiO$_2$ wafers from any organic residuals, increasing the hydrophilicity of the surface to facilitate the deposition of the graphene.

II.I.IV   Plasma etching

The etching of the suspended graphene and the formation of the independent edge electrodes employed to form the tunnelling junction was performed using a Diener GmbH plasma etcher.

II.I.V   Sheet resistance and point contact resistance

In contrast to 3D metallic systems, the point contact resistance measured here was dominated by a large contribution from the sheet resistance of the graphene electrodes that cannot be separated from the measurements. The total measured resistance was the quantum point contact resistance in series with the classical resistance of the sheets. The classical resistance R_G of the sheets on either side of the contact can be estimated as (1):

$$R_G = \frac{1}{\pi\sigma} \int_{l_0}^{L} \frac{1}{r} \, dr \quad (1)$$

where σ is the sheet conductance, L is the size of the sample (2mm), and l_0 is the electrons mean free path. Using the semi-classical expression for the sheet conductance (2):

$$\sigma = \frac{e^2}{h} 2E_F \tau / \hbar \quad (2)$$

and the linear dispersion of the Fermi energy $E_F = \hbar v_F k_F$, and $k_F = \sqrt{\pi n}$, we can express the mean free path in terms of the conductivity and the electron density (3):

$$l_0 = \frac{\sigma}{e^2/h} \frac{1}{2\sqrt{\pi n}} \quad (3)$$

Using the conductance of $\sigma = (11 \pm 2)\ e^2/h$ found for our samples, and the typical dependence between charge density and conductance in this regime[1,2] we obtained an estimate of $l_0 = 27$ nm. With this, an estimated resistance for the sum of the two graphene electrodes of 17 ± 3 kΩ was obtained. Subtracting twice this value from the measured point contact resistance of 28 kΩ, we found an estimate for the quantum point contact resistance of 11±3 kΩ.

II.I.VI Simmons model for symmetric barrier

Considering tunnelling through a symmetric barrier, the work function ϕ can be approximately the same for both electrodes. The current density in a symmetric tunnel junction with a barrier along the z-axis (Figure II.1) is described with a Simmons model[3] (4):

$$J \sim \frac{e}{2\pi h d^2} \left[(\phi - \mu_L)e^{-\frac{2d\sqrt{2m(\phi-\mu_L)}}{\hbar}} - (\phi - \mu_R)e^{-\frac{2d\sqrt{2m(\phi-\mu_R)}}{\hbar}} \right] (4)$$

where $d = z_1 - z_2$, and μ_L and μ_R are the chemical potentials of the left and the right electrode, respectively.
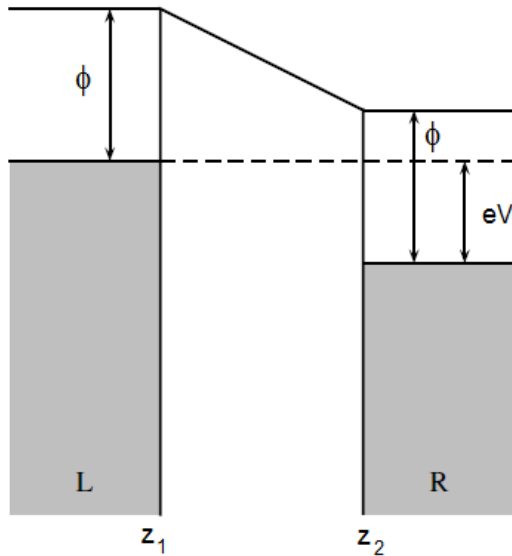

Figure II.1. Symmetric tunnel junction with barrier height ϕ and barrier width $d = z_1 - z_2$

Parameters fitted to the Simmons model are the pre-factor A (which contains a cross-section of the junction), the barrier height φ and the gap size d. The parameters A and φ cannot be fitted completely independently, but with a suitable choice for the pre-factor the barrier height obtained agrees with the range of results found in the literature, see the main text. The gap distance d is more robust and it is estimated with approximately 5% accuracy.

II.II   Graphene-gold tunnelling junction

In order to identify the edge electrodes that extend to the end of their supports, we formed a tunnelling junction against a gold sample. This, in first instance allowed the facile electrical characterization of the edge electrode and secondly demonstrated the flexibility of our system, capable of employing independent edge electrodes in multiple systems, either symmetric or asymmetric junctions.

Figure II.2a illustrates the schematics of the set-up. The graphene edge electrode was mounted on a holder over a piezoelectric actuator (thick grey block on the left) which approaches a thick sample of pure gold. Figure II.2b shows the I(V) characteristic of the tunnel junction at a fixed distance, sweeping the bias voltage V between -1.5 V and + 1.5 V. The shape of the sigmoidal IV curve is characteristic of an asymmetric tunnel barrier. This is a result of the different work function across the two terminals of the junction. Figure II.2c shows the tunnelling current as a function of distance (black curve, $I(z)$) between the graphene and the gold sample at V = 0.48 V bias voltage. A clear exponential increase (exponential fit red curve) of the current with decreased distance was observed, characteristic of a tunnelling regime.
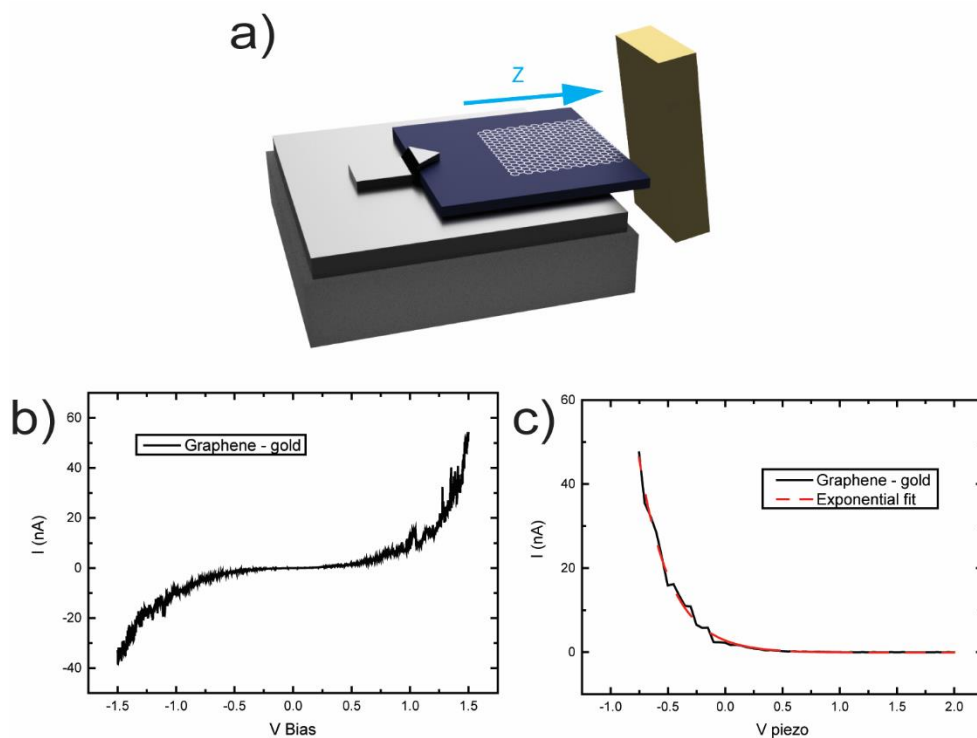
Figure II.2. a) Schematics of the gold – graphene tunnel junction etched in H_2 plasma. The graphene electrode was mounted on a piezoelectric actuator which moves the sample along the Z axis to approach a gold macro electrode. b) IV characteristic of the graphene-gold junction. c) Representative I(z) characteristic of graphene-gold tunnel junction (black line) fitted to exponential function (red line).

II.III Oxygen and nitrogen etching

Reactive ions etch the suspended graphene until the edge of the SiO_2 supports. The etching atmosphere, consequently, affects the chemistry of the graphene edge electrodes. In order to study the effect of different chemistries on the characteristics of the edge electrodes, we performed etching in various plasma atmospheres, namely: H_2, O_2 and NH_3.

The results concerning etching in hydrogen plasma are reported in the main text of Chapter 4, illustrating the successful formation of independent supported graphene edge electrodes. The same etching conditions (0.3mbar at 60W, 30s) were applied for O_2 and NH_3, etching the suspended graphene. While these

conditions worked for a hydrogen atmosphere, we did not manage to build stable tunnelling junctions between two graphene edge electrodes using O_2 and NH_3 plasmas. Particularly, no tunnelling devices were obtained with NH_3 etching, while stable asymmetric junctions were achieved using graphene edge electrodes prepared in O_2 plasma when measured in tunnelling junctions against gold counter-electrode, Figure II.3. The asymmetric IV characteristic confirmed the tunnelling between carbon and gold electrodes, but it was not possible to extrapolate the correct value of the work function and thus the tunnelling gap size, primarily because of the impossibility of fitting the results with the Simmon's model, Figure II.3a. The current-distance, I(z), characteristic was noisier and appeared less stable than the ones obtained with hydrogen. Once more, the lack of information about the work-function did not allow to calibrate the distance between the edge electrode and the gold counter electrode. Nonetheless, an exponential increase of the current was still observed at tunnelling current, Figure II.3b.
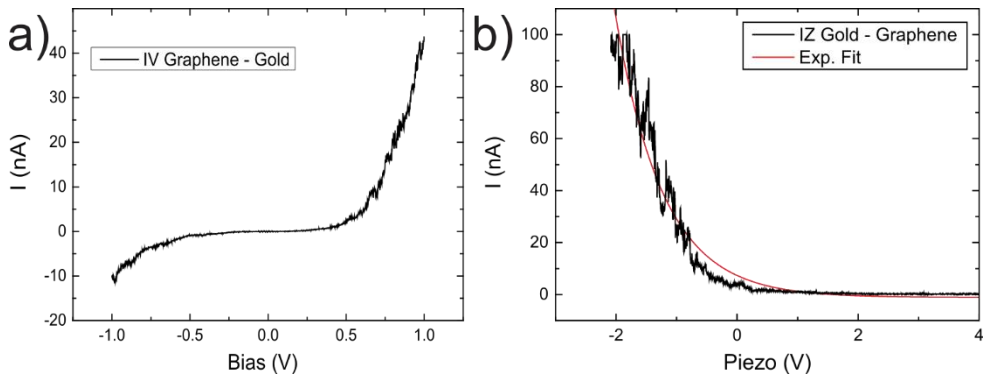

Figure II.3. Graphene – gold tunnelling junctions etched in an oxygen plasma. a) I(V) characteristic of the junction. b) I(z) characteristic of the tunnelling junction showing current exponential growth while approaching the gold counter electrode.

Comparing Figure II.2b and Figure II.3a a slight delay on the inset of the tunnelling currents for hydrogenated edges (Figure II.2b) can be observed with respect to the bias voltage for oxygen etched edge electrodes (Figure II.3a). Nonetheless, the lack of information due to the impossibility of fitting the Simmon's model, did not allow the proper calibration of the piezo stage. However, the qualitative differences

acting on different edge chemistries can be explained. We observed a strong asymmetricity in the case of oxygen etched electrodes. Particularly, for the same bias voltage in the IV curve of Figure II.3a compared to Figure II.2b, we can observe a higher tunnelling current at positive bias potentials, and lower at negative. If the difference at positive potentials could be ascribed to a closer distance of the gap in the case of oxygenated edges with respect to hydrogenated edges, this does not justify the lower current intensity at negative potentials. A possible explanation is the differences in the work functions between oxygenated and hydrogenated edges. The work function works as a barrier for tunnelling electrons. Smaller work functions are expected for hydrogenated edges, which at negative bias voltages might represent a smaller tunnelling barrier with respect to oxygenated edges, thus increasing the transmission intensity from graphene to gold electrodes. Accordingly, the tunnelling intensity at negative bias potentials was lower for oxygenated edges (higher barrier) than for hydrogenated edges (lower barrier), possibly showcasing the effect of the edge chemistry on the electron transmission through the tunnelling junction.

II.IV   References

(1)   Hwang, E. H.; Adam, S.; Sarma, S. Das. *Phys. Rev. Lett.* **2007**, *98* (18), 186806.

(2)   Novoselov, K. S.; Geim, A. K.; Morozov, S. V.; Jiang, D.; Katsnelson, M. I.; Grigorieva, I. V.; Dubonos, S. V.; Firsov, A. A. *Nature* **2005**, *438* (7065), 197–200.

(3)   Simmons, J. G. *J. Appl. Phys.* **1963**, *34* (6), 1793–1803.

Appendix III

Supporting Information to Chapter 5

III.I   Materials and methods

III.I.I   Graphene

Graphene nanoribbons were formed using chemically vapor deposited, CVD, on Cu purchased from Graphenea®. Graphene sheets were deposited on Si/SiO$_2$ wafers (285 nm thick SiO$_2$ purchased from University Wafer) and on gold coated mica substrates purchased from Ted-Pella®. The copper substrate of the CVD graphene was previously etched using a 0.5 M aqueous solution of ammonium persulfate (NH$_4$)$_2$S$_2$O$_8$ purchased from Sigma-Aldrich®.

III.I.II   The metallic mask

Graphene nanoribbons were fabricated underneath metallic masks prepared via microtomy of metallic thin films embedded in a polymer scaffold. The metallic thin films were first thermally evaporated (Leiden University home built thermal resistance evaporator operating below 1x10^{-6} bar) on a Si/SiO$_2$ wafer (purchased from University Wafer), then coated with a drop of photocurable polymer (see Appendix I.I.I) and cured. The metallic films were lifted from the SiO$_2$ substrate using a razor blade intercalated between the metallic film and the surface of the wafer. Next, the metallic film coated with a polymer drop was immersed in a mould filled with photocurable polymer and cured, yielding a metallic thin film embedded in a polymer scaffold (Figure 5.1 of Chapter 5). The polymer scaffold is sectioned using a Leica® EM UC 6 microtome equipped with a Diatome® trim tool 20® and an Ultra Diamond Knife 35®, yielding polymeric slabs embedding metallic nanorods and with a surface ranging from 50 X 50 μm^2 to 150 X 150 μm^2 and from 50 nm to 150 nm thick, using a cutting speed varying between 1,0 mms^{-1} and 2,5 mms^{-1}.

III.I.III   Plasma etching

The polymer slab and the excess of graphene were etched in O$_2$, H$_2$ and NH$_3$ using a Diener Electronic GmbH plasma etcher according to the experimental conditions reported in Chapter 5.

III.II   Square resistance of graphene

Square resistance, or sheet resistance, is a unit of resistance employed in thin films of known uniform thickness, such as monoatomic graphene. Starting from the conventional definition of resistance R (1):

$$R = \rho \frac{L}{A} = \rho \frac{L}{WT} \,(1)$$

The square resistance was derived applying the know thickness, T, of the film as a constant, thus in the case of graphene T=0.34 nm and (1) became (2):

$$R = \rho' \frac{L}{W} \,(2)$$

Both sheet length, L, and width, W, were expressed in m, thus R returned a value in Ohm. The special case where R = ρ' represents the case where W = L, thus a square. Practically, the resistivity of the graphene film could be measured where W = L taking the name of square resistance R=(ohm/sq.).

In the case of graphene, the square resistance varies greatly according to experimental conditions, particularly the temperature, the nature of the electrical contacts and the substrate roughness. Nonetheless, the literature reported graphene square resistances in the order of hundreds of Ohm/sq[1,2], with an average around 600 Ohm/sq. Graphene purchased from Graphenea®, as the one employed in the experiments, reports an average of 450 Ohm/sq. on SiO_2. (https://www.graphenea.com/products/monolayer-graphene-on-sio2-si-4-wafer) in line with the values obtained for our measurements, i.e. R =1.65 kΩ for a device 80nm wide and in the order of 1 µm long.

III.III   Electron beam lithography of metallic electrodes

In order to characterize electrically the graphene nanoribbons formed underneath the metallic mask, electrodes were deposited also via electron beam lithography (Raith® eLine electron beam pattern generator, EBPG). Nonetheless, by means of EBPG lithography we could not properly form electrodes. A first major issue was the difficult alignment between the nanometre wide graphene nanoribbons and the electron beam of the EBPG, yielding misplaced electrodes with respect to the nanostructures, Figure III.1a.
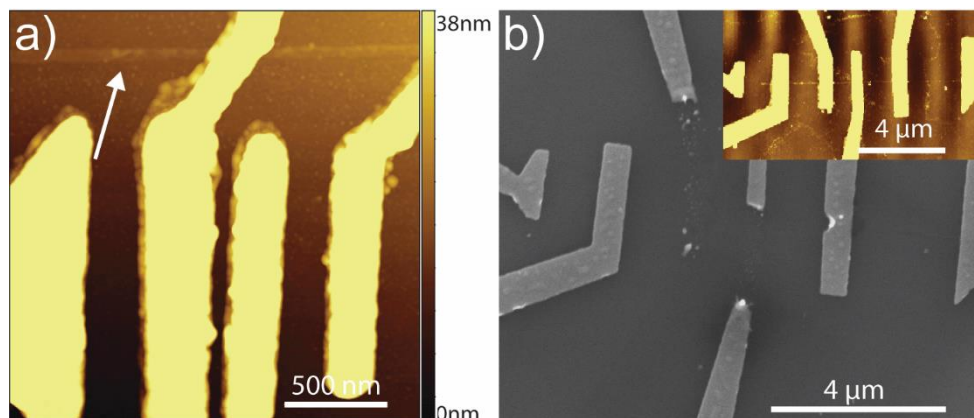
Figure III.1 AFM and SEM micrographs of gold electrodes prepared by electron beam lithography. a) AFM micrograph of gold electrodes misaligned with respect to a graphene nanoribbon. Bright yellow: gold electrodes designed via EBPG. The graphene nanoribbon, bright line on top highlighted by the white arrow, does not cross all the electrodes due to misalignment issues. b) SEM micrograph of electrodes broken during electrical characterization by means of electrons discharge. Inset: AFM micrograph of the graphene nanoribbon and the correctly aligned electrodes before electrical characterization.

Second, electrodes designed via electron beam lithography EBPG (even if correctly aligned over the graphene nanoribbon) showed severe discharging issues during the electrical characterization of the graphene nanoribbons leading to their rupture, Figure III.1b. More in detail, the inset of Figure III.1b shows the atomic force microscope AFM image of gold electrodes (bright yellow lines) crossing a graphene nanoribbon before the electrical characterization. Upon electrical characterization, an electronic discharge caused the rupture of the electrodes, as illustrated by the scanning electron microscope, SEM, micrograph in Figure III.1b. Because charges accumulate on the sample during EBPG, the electrical characterization forms a closed circuit with the sample, allowing the sudden flow of these accumulated charges, enabling a current flows which intensity is high enough to damage the electrodes.

III.IV   Scalability

Metallic masks were prepared via microtomy of metallic thin films. Microtomy finely fabricated masks of different widths. The top panels of Figure III.2a to III.2c show metallic nanorods of different widths prepared via microtomy and used to form graphene nanoribbons, bottom panels of Figure III.2a to III.2c.

Importantly, the graphene nanoribbons were all prepared under the same etching conditions in H_2 plasma at 0.3 mbar 60 W for 2.5 minutes in order to remove the polymer slabs supporting the nanorods and the excess of graphene. The partial diffusion of reactive ions underneath the metallic masks yielded nanoribbons thinner than the mask and scaling with the mask width, Figure III.2d and III.2e.
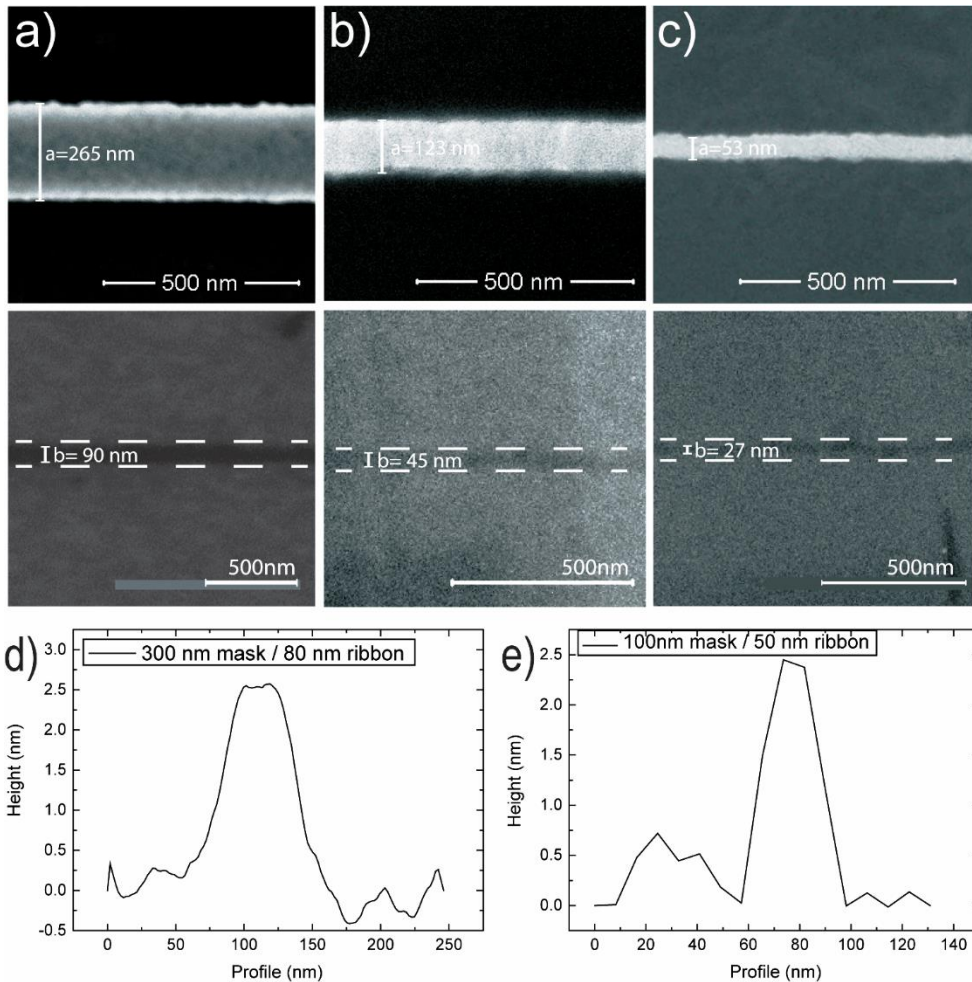

Figure III.2. Narrowing-down of graphene nanoribbons. From a) to c) SEM micrograph of metallic nanorods (top) of thicknesses respectively of 300 nm (aluminium), 100 nm (gold) and 50 nm (gold), and the graphene nanoribbons sculpted underneath in H_2 plasma (bottom). d) and e) AFM cross sections of graphene nanoribbons sculpted in H_2 plasma under metallic masks of respectively 300 nm aluminium and 100 nm gold.

III.V   References

(1)   Zhang, Z.; Du, J.; Zhang, D.; Sun, H.; Yin, L.; Ma, L.; Chen, J.; Ma, D.; Cheng, H.-M.; Ren, W. *Nat. Commun.* **2017**, *8*, 14560.

(2)   Lee, J.-K.; Park, C.-S.; Kim, H. *RSC Adv.* **2014**, *4* (107), 62453–62456.

Appendix IV

Supporting Information to Chapter 6

IV.I   Materials and Methods

IV.I.I   Self-Assembled-Monolayer, SAM

A gold film was deposited on a Si/SiO$_2$ wafer (University wafer) via thermal resistance evaporation at P < 1*10^{-6} mbar.

Next, a mixed self-assembled monolayer was formed on the gold film from a mixed solution of 1,11-amino undecanethiol (at) and 1-dodecanethiol (dt) in ethanol. Namely, a solution of 1,11-amino undecanethiol (at) 5mM in ethanol was mixed in a petri dish with a solution of 1-dodecanethiol (dt) 5mM in ethanol with volume ratios varying from 0 % to 100 %. The self-assembled monolayer formed by immersing the substrate into the petri-dish filled with the mixed solution of at and dt at room temperature, under argon atmosphere for approximatively 12 hours[1].

The at and dt solutions were prepared in bottom round flasks in ethanol and sonicated 10 minutes before being mixed in a petri-dish. All the wares were cleaned using a piranha solution (3:1 sulfuric acid and hydrogen peroxide). All the chemicals were purchased from Sigma-Aldrich®. The gold substrate was cleaned in O$_2$ plasma at 100 W, 0.5 mbar for 30 s (Diener plasma etcher).

The thickness of the SAM was determined by ellipsometry, Figure IV.1a. For ratios of at : dt above 40 : 60 the thickness of the SAM exceeded the thickness of a monolayer, in the order of 1 nm, indicating the formation of multilayers (disordered layers[1]). Next, the SAM formed from a mixed solution 30 : 70 = dt : at was characterized by X-ray photoelectron spectroscopy, Figure IV.1b. The NS1 and NS1a peaks respectively at 399 eV and 407 eV rise from the asymmetric bonds of N in the amine of the aminothiols that forms both N-C and N-H bonds, indicating the presence of aminothiols in the mixed SAM. The weak intensity of the N1S and N1Sa peaks is ascribed to the low content of nitrogen atoms in the SAM. In fact, each aminothiol contains one nitrogen atoms every eleven carbon atoms. Thus, statistically, one every ten molecules in each aminothiol contributes with a Nitrogen emission derived by a single nitrogen atom.
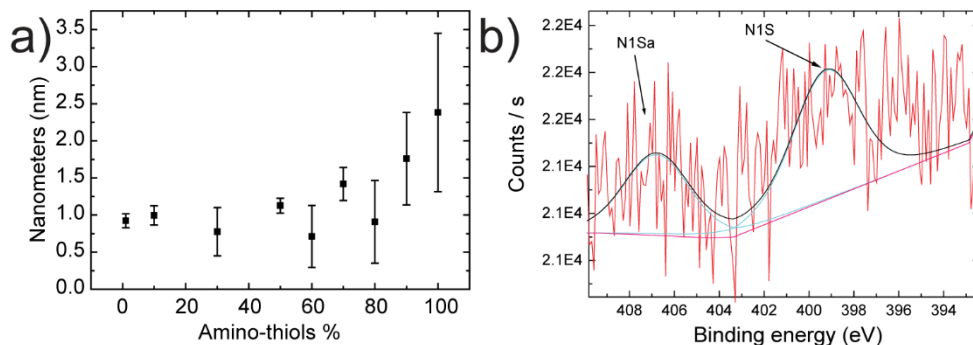
Figure IV.1. SAM characterization. a) Ellipsometry measurements of a SAM with various at/dt ratios. b) XPS analysis of the N1S and N1Sa peaks obtained from a SAM formed from a mixed solution of 30 : 70 = at : dt assembled on a gold substrate. The spectrum was acquired over 10 spots at a 0.01 eV excitation energy with an acquisition time of 9 s over a line sample of 400 μm using a K-Alpha XPS by Thermo Scientific (property of the technical university of Eindhoven).

IV.I.II   Layer-by-Layer deposition

The multilayered film of polyelectrolytes was grown via Layer-by-Layer deposition, LbL, using poly (allylamine hydrochloride), PAH, (M_w = 17500 gmol^{-1}) and poly (sodium 4-styrenesulfonate), PSS, (M_w = 70000 gmol^{-1}) purchased from Sigma-Aldrich®. The film was grown on a Si/SiO$_2$ substrate coated with a gold film functionalized with a mixed SAM 30 : 70 = at : dt ratio.

To grow the multilayered film of polyelectrolytes, the substrate was alternatively dipped into a solution of PSS (3 mM in repetitive units) in 1:1 EtOH and 0.5 M NaCl in H$_2$O and a solution of PAH (3 mM in repetitive units) in 1:1 EtOH and 0.5 M NaCl in H$_2$O, at room temperature each time for 20 minutes. Between each layer, the substrate was rinsed with EtOH/H$_2$O (1:1), and then dried under argon stream[2]. In order to promote the adhesion between the multilayered film of polyelectrolytes and the substrate, the first layer of PSS was deposited from an acidic solution of PSS in 0.5 M NaCl in 1:1 EtOH/H$_2$O, with H$_2$O previously adjusted at pH=2 by adding 40 μL of HCl (37% HCl in aqueous solution from Sigma-Aldrich) to 50 mL of ultra pure water. In fact, the acidic solution protonates the amines of the mixed SAM attracting the first, negatively charged PSS layer.

IV.I.III Microtomy of the metallic nanogaps

The gold layer comprising the multilayered film of polyelectrolytes was embedded within a photocurable polymer in order to be sectioned later via microtomy, forming nanogaps between metallic nanorods (where the gap spacing has the thickness of the LbL multilayer). First, a drop of photocurable polymer was casted over the gold/polyelectrolytes/gold stack on Si/SiO_2 and cured (see Appendix I.I.I). Next, the stack is lifted from the Si/SiO_2 substrate by intercalating a razor blade between the first gold layer and the SiO_2 substrate (see Figure 6.2a). Last, the stack is immersed into a PDMS mould filled with photocurable polymer and cured, yielding a polymer scaffold embedding the gold/polyelectrolytes/gold stack (see Figure 6.2b).

The transverse nanogaps were prepared by microtomy sectioning of the polymer scaffold embedding the gold/polyelectrolytes/gold stack. We employed a Leica® EM UC 6 microtome first trimming the polymer with a trimmer Diatome® trimtool 20®, then sectioning the polymer scaffold with an Ultra Diamond Knife 35®. The cutting proceeds with the blade parallel to the gold films (Figure 6.3 of Chapter 6), sectioning polymeric slabs 50 X 50 μm^2, 150 nm thick at a cutting speed of 1,6 mm/s.

IV.I.IV Thiolation of poly (allylamine hydrochloride) polyelectrolyte

A solution of 3,3'-dithiopropionic acid (DTPA) (55.9 mg, 0.266 mmol, 1.0eq), N-(3-dimethylaminopropyl)-N'-ethylcarbodiimide hydrochloride (EDC·HCl) (968.2 mg, 6.23 mmol, 23.4eq) and N-hydroxysyccinimide (NHS) (659.7 mg, 5.73 mmol, 21.5 eq.) in DMF (60 ml) was dissolved by sonication, Figure IV.2 a-i. The solution was stirred at room temperature under an argon atmosphere for 2.5 hrs and then evaporated via rotary evaporation[3]. The product was added to a solution of PAH (M_W 17500 gmol^{-1}; 99.4 mg, 5.68 µmol, 0.5 eq.) in H_2O/DMF (1 : 1, 40 mL), followed by the addition of dithioltheritol (DTT) (39mg, 0.256 mmol, 0.96 eq.), Figure IV.2 a-ii. The solution was stirred at room temperature under an argon atmosphere for 4 hrs and rotary evaporated. The product was added to a solution of 40 ml of trifluoroacetic acid (TFA) (1% in H_2O) with 2g of zinc and stirred at room temperature for 2 hrs, Figure IV.2 a-iii. Then, the solution was centrifuged for 10 min at 4000 rpm prior to dialysis using a 30kDa membrane. The dialysis was performed at room temperature to a total of 72hrs. The dialysis water was

replaced every 12hrs. The solvent was removed by rotary evaporation and freeze-dried.

Solid-state ^{13}C NMR of the resultant product, Figure IV.2b, shows two ill-resolved signals at 44.15 ppm and 36.78 ppm, which were assigned to the methylene moieties of the polymer backbone and attached thiopropionate, by comparison with unreacted PAH. Importantly, a signal at 172.98 ppm indicated the successful incorporation of the thiopropionate into the polymer. The solid-state ^{13}C NMR measurements were measured using a Bruker AV-I 750MHz spectrometer with 17.6 Tesla magnetic field. The ^{13}C were irradiated with 40.32 kHz radio frequency pulses with a contact time of 2 ms, and 10000 scans were acquired. All the ^{13}C spectra were externally referenced to methyl signal of TMS and were processed in Topspin 3.2 and MestReNova software.

To further prove the presence of thiol groups in the polymer, an Ellman's test was performed[4]. A sample of the product (0.5 mg) was dissolved in ultra pure water (3 mL) and diluted 1:100 into a solution of 0.1 M Na_3PO_4 and 1 mM ethylenediamine tetraacetic acid (EDTA). To the solution was then added 10 µL of Ellman's reagent, to generate 2-nitro-5-thiobenzoic acid (NTB). The concentration was determined using Beer-Lambert law, using an extinction coefficient of $\varepsilon = 14150$ M^{-1}cm^{-1}. A total of 6.4 nmol was found.

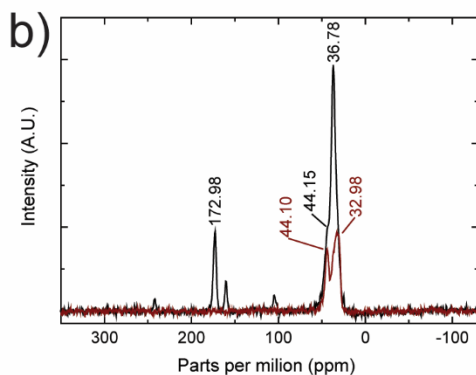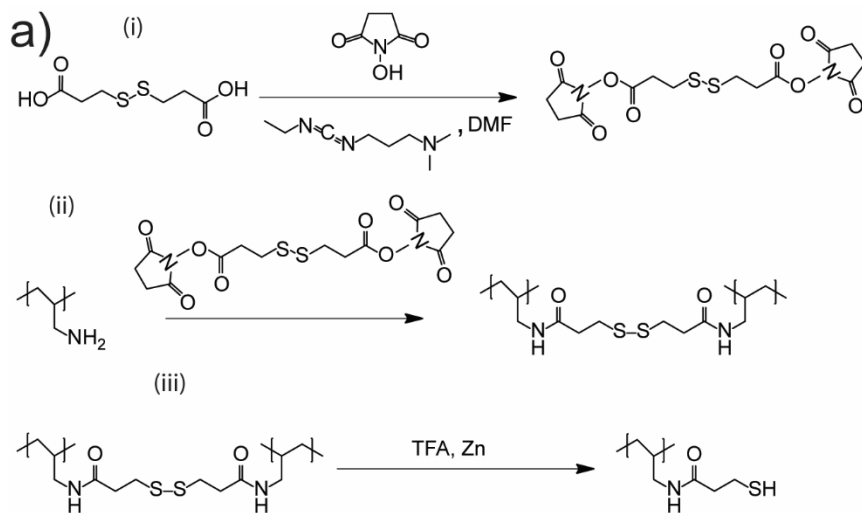All chemicals were purchased from Sigma-Aldrich and used without further purification.

Figure IV.2. a) Thiolation of the PAH polyelectrolyte. b) ^{13}C solid state NMR of the pristine PAH (red curve) and the thiolated PAH (black curve). The peaks at 44.10 ppm and 32.98 ppm on the red curve were attributed to the methylene bridge respectively on the backbone of the pristine PAH polyelectrolyte and the amine. The peaks at 44.15 ppm and 36.76 ppm in the black curve result from the methylene bridges on the backbone of the polyelectrolyte and attached to the thiopropionate. The peaks at 110 ppm and 160 ppm represent contaminations.

IV.II   References

(1)   Graham, D.; Dingman, S. A Step-by-Step Guide for Solution Based Self-Assembly, Sigma-Aldrich https://www.sigmaaldrich.com/technical-documents/articles/material-matters/a-step-by-step-guide0.html.

(2)   Lvov, Y.; Decher, G.; Sukhorukov, G. *Macromolecules* **1993**, *26* (20), 5396–5399.

(3)   Sam, S.; Touahir, L.; Salvador Andresa, J.; Allongue, P.; Chazalviel, J.-N.; Gouget-Laemmel, A. C.; Henry de Villeneuve, C.; Moraillon, A.; Ozanam, F.; Gabouze, N.; Djebbar, S. *Langmuir* **2010**, *26* (2), 809–814.

(4)   Ellman, G. L. *Arch. Biochem. Biophys.* **1958**, *74* (2), 443–450.

Appendix V

Supporting Information to Chapter 7

V.I   Materials and methods

V.I.I   Formation of the polymer matrix used for the embedding of the gold films

A gold film few tens of nanometres thick was deposited by resistance evaporation on top of a Si/SiO$_2$ wafer (purchased from University Wafers). Gold was thermally evaporated inside a high vacuum chamber at P<10^{-6} mbar and its thickness monitored by a quartz crystal microbalance (Leiden University home built thermal resistance evaporator operating below 1x10^{-6} bar). After the evaporation, a polymeric mixture of pentaerythritol tetrakis (3-mercaptopropionate) (Sigma-Aldrich), PETMP, and 1,3,5-triallyl-1,3,5-triazine-2,4,6(1H,3H,5H)-trione (Sigma-Aldrich), TATAO, (with proven competence for microtomy process[1]) was drop-casted over the gold film. The mixture was stirred for 2 minutes and set to rest in the desiccator to remove any air bubble. Lastly, 1% in weight ratio of 2,2-dimethoxy-2-phenylacetophenone, DMPA, was added to the mixture as photo-initiator. The polymer was hardened in air under the irradiation of a 365 nm UV lamp for 30 minutes, 7000 μW/cm^3 at 38,2 cm of distance. After the curing, the gold with the polymer on top was carefully stripped-off from the Si wafer and re-embedded inside a PDMS mould filled with uncured polymer mixture and once again UV cured.

V.I.II   Preparing the slabs

A gold film with a thickness of a few tens of nanometres was embedded inside a polymeric support and sectioned by ultramicrotomy[1]. The microtome was a Leica UC6 equipped with a DiATOME diamond trim of 20° for the sample preparation, and 45° for the sectioning of the polymer matrix into slabs, each including a gold nanorod. The thickness of the slabs ranges from 50 nm to 500 nm, finely tuned by motor-actuators of the microtome.

Upon cutting, the ultrathin slabs shifted towards the boat of the knife, which was filled with ultra pure water. The slabs floated on the boat exploiting the surface tension of the water. Then, a circular tungsten wire, around 0.5 mm radius (the perfect loop), was placed on the surface of the water surrounding the slabs. The surface tension between the wire and the water displaces a drop of liquid that

remains constrained inside the loop, enabling the transfer of the polymer slabs floating on surface of the trapped drop.

Subsequently, the perfect loop was positioned carefully close to the opening (d=30 µm to 50 µm) drilled in a glass substrate acting as the support for the slabs (NPC chips purchased from NanIon). The substrate was previously oxidized inside an environmental plasma at 7×10^{-2} mbar for 15 s, promoting the hydrophilicity of the glass. While the surface of the glass was still wet, we used a microstep manipulator (Thor-Labs) to gently move the slabs over the glass substrate in order to align the gold nanorod across the glass opening.

The position of the slab was adjusted during the slow evaporation of the water in order to maintain in place the gold nanorod across the window of the membrane. Additionally, the plasma oxidation of the membrane allowed the uniform evaporation of the water from the surface, avoiding the misalignment of the slabs induced by sudden water displacements. Finally, the water completely evaporated and the slab fully adhered on the surface of the membrane.

Subsequently, the membrane was placed inside a 40°C oven to completely evaporate the water residuals trapped between the surface and the polymer slab. Afterwards, the protocol was accurately repeated in order to deposit a second slab. The orientation of the slabs was in a way that the embedded gold nanorods form a misalignment angle of ~90°.

Further then, both sides of the membrane were exposed to a 0.5 M solution of KCN in ultra pure water, which etches the gold nanorods and forms a nanopore. The sample was then rinsed three times in ultra pure water to remove any etchant residuals and, then, dried under vacuum.

V.I.III Nanopore experiments

Samples prepared with the precise alignment of the slabs, after etching away the gold lines, were mounted in a custom-made flow cell out of PEEK (Figure V.1). The design of the flow cell provides sufficient sealing on either side of the glass support. The measurements were performed by injecting buffer solutions (both KCl and LiCl) with different concentrations ranging from 1 mM to 1 M containing 10 mM Tris-HCl and 1 mM EDTA. To drive the electrophoretic flow of ions, transmembrane

potentials were applied to Ag/AgCl electrodes, pre-mounted on the flow cell. A resistive feedback amplifier (Axopatch 200B, Axon Instruments) and digitized at 500 kHz measured the corresponding current traces.

For translocation detection experiments, 48.5 kbp unmethylated λ-DNA (10 ng/ μL, reference no. D152A, lot no. 27420803, Promega, Madison, WI) was used. The event detection and sorting were performed by the Matlab based Transalyzer package[2].

V.I.IV   The nanopore set-up

Ionic conduction was measured in a custom-design flow-cell made out of PEEK. Figure V.1a and V.1b illustrate the design: two main reservoirs (cis and trans) were linked through a nanopore deposited on a glass support, namely an NPC-Chip (Nanion Technologies, NPC®-Chips). Each chamber was equipped of three inlets, two for the flow of the ionic solution and one for the electrodes.
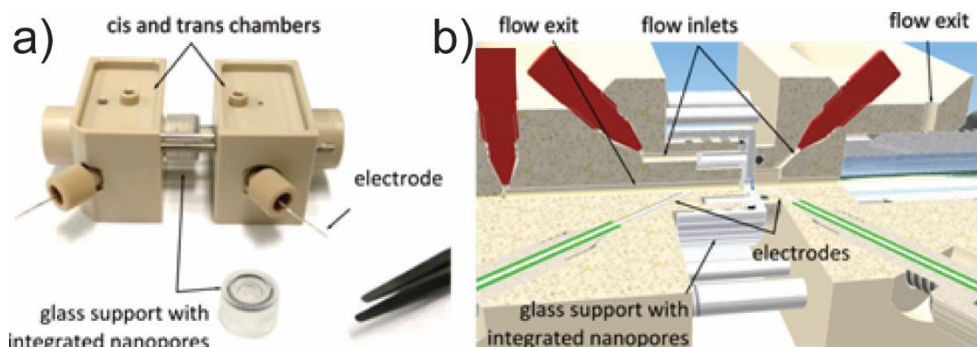

Figure V.1. Experimental set up. Optical micrograph (a) and schematics (b) of the home-made experimental setup: different components are marked on the images.

V.II   Access resistance of a rectangular area: theoretical model

An interfacial nanopore is defined by two crossing nano-slits that are carved through their respective nano-membranes stacked together. The top-view of the nanopore usually assumes a parallelogram with its angles determined by the membrane stacking and its side lengths determined jointly by the membrane stacking as well as by the original widths of the slits. Two different types of access resistances prevail for ions that will eventually pass through the nanopore. The ions diffuse from the bulk electrolyte to the slit on the *cis* side as well as from the

190

slit to the bulk electrolyte on the *trans* side. They are subsequently pulled into/out the nano-trenches (defined by sealing one side of the nano-slides by the other membrane) by the electric field. The sum of those resistances accounts for the trench access resistance $R_{a,t}$. Then, the ions in the trenches diffuse and drift to the nanopore and finally pass through. This process generates another access resistance named pore access resistance $R_{a,p}$. The path of the ions is symmetric on both sides of the pore. Thus, the total pore resistance, R_t, is (1):

$$R_t = 2R_{a,t} + 2R_{a,p} \qquad (1)$$

In order to calculate the access resistance, we first calculate the corresponding capacitance, C, for an equivalent electrode with the same shape of the access area. It is a rectangular strip for $R_{a,t}$ and a parallelogram for $R_{a,p}$. The resistance can then be derived via[3] (2):

$$R = \frac{\varepsilon_0 \rho}{C} \qquad (2)$$

where, ε_0 is the permittivity of vacuum and ρ is the resistivity of the electrolyte. The electric field lines in the capacitor are analogues to the current lines in the resistor.

For C corresponding to $R_{a,t}$, the opposite electrode has an infinite area placed infinitely away from the equivalent electrode with the rectangular strip trench area (see above). For C corresponding to $R_{a,p}$, the opposite electrode has an area equal to that above the pore with a distance equal to the slab thickness, h. The rectangle and parallelogram electrodes are assumed to carry positive charge with a uniform charge density. The electric field strength along the central axis can be obtained by integrating the charge on the electrodes. By integrating the electric field strength along the central axis, the electric potential is found. This leads to the calculation of C as the following (3):

$$C = \frac{Q}{\Delta U} = \frac{\sigma A}{\Delta U} \qquad (3)$$

where, Q is the total charge on the electrode, ΔU is the potential drop between two electrodes, σ is the charge density, and A is the area of the

rectangular/parallelogram electrode. Equation (2) should be multiplied with a factor of 2 when calculating R in order to count for the fact that C is calculated for the whole space while the ions only enter the pore from one side of the membrane stack.
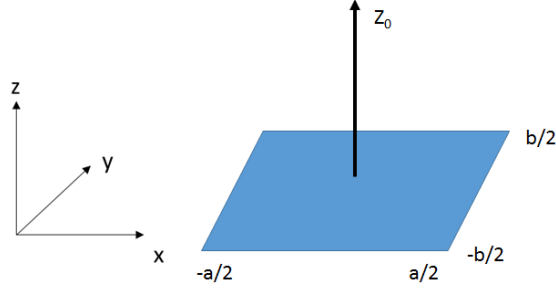

Figure V.2. Geometry of interfacial nanopore, used for simulation.

If the two slits are placed orthogonal to each other so that the top-view of the pore is a rectangle, an analytical solution to R exists. As illustrated in Figure V.2, the electrode carries charge with a uniform density, σ. The width of electrode is a and length is b. The electric field strength at height z along the central axis can be obtained by (4):

$$E(Z) = \frac{\sigma}{4\pi\varepsilon_0} \iint_{area} \frac{dxdy}{x^2 + y^2 + z^2} \frac{z}{\sqrt{x^2 + y^2 + z^2}} = \frac{\sigma z}{4\pi\varepsilon_0} \int_{-a/2}^{a/2} \int_{-b/2}^{b/2} \frac{dxdy}{(x^2 + y^2 + z^2)^{3/2}}$$

$$= \frac{\sigma z}{4\pi\varepsilon_0} \int_{-b/2}^{b/2} \frac{ady}{\sqrt{a^2 + y^2 + z^2}(y^2 + z^2)}$$

$$(4)$$

Equivalent to (5):

$$E(z) = \frac{\sigma}{4\pi\varepsilon_0} arctan\left(\frac{ay}{z\sqrt{a^2 + z^2 + y^2}}\right)\Big|_{b/2}^{-b/2} = \frac{\sigma}{4\pi\varepsilon_0} arctan\frac{ab}{z\sqrt{a^2 + z^2 + b^2}} \quad (5)$$

By integrating the electric filed strength along the z direction, we can get the potential as follows (6):

$$U(z_0) = \int_0^{z_0} E(z)dz \text{ (6)}$$

Equivalent to (7):

$$U(z_0) = \frac{\sigma}{4\pi\varepsilon_0}(z_0 \arctan \frac{ab}{z_0\sqrt{a^2 + b^2 + z_0^2}} - a \arctan h \frac{\sqrt{a^2 + b^2 + z_0^2}}{b} - b \arctan h \frac{\sqrt{a^2 + b^2 + z_0^2}}{a})$$

$$= \frac{\sigma}{4\pi\varepsilon_0} L(a,b,z_0)$$

(7)

i.e. L(a,b,z₀) is introduced to denote the calculation in the parentheses. Hence, the capacitance, *C*, of this rectangular electrode with an opposite electrode with an equal potential surface placed at distance *s* is (8):

$$C = \frac{Q}{U} = \frac{ab\sigma}{U(s) - U(10^{-10})} = \frac{4\pi\varepsilon_0 ab}{L(a,b,s) - L(a,b,10^{-10})} = \frac{4\pi\varepsilon_0 ab}{F(a,b,s)} \text{ (8)}$$

Since the potential at zero distance from the electrode is infinite, the potential at 1 Å is assigned as the reference and $F(a,b,s)=L(a,b,s)-L(a,b,10^{-10})$ is introduced. If *s* tends to infinity, *C* asymptotically approaches a constant value; it is the capacitance of two rectangular electrodes separated by an infinite distance. Finally, the access resistance, R_a, is (9):

$$R_a = \frac{2\varepsilon_0\rho}{C} = \frac{\rho}{2\pi ab} F(a,b,s) \text{ (9)}$$

However, for pores with a general parallelogram-shape, the integration of electric field strength can be done only in a numerical way. In what follows, modelling results are shown for a pore formed with two identical membranes of thickness *h* and slit (trench) width *a*. The angle between the crossing slits is ϑ. The slit/trench length *L* = 1 mm is very large compared with *a*. For a 1 M KCl solution, ρ = 0.1 Ω·m. The modelling results are summarized in the table below.

a (nm)	h (nm)	ϑ (°)	$R_{a,t}$ (Ω)	$R_{a,p}$ (kΩ)
20	100	90	382	2,620
20	10	90	382	1,518

200	100	90	310	154
200	100	30	310	82

Obviously, For the dimensions typical in this work, $R_{a,p}$ is fund to be larger than $R_{a,t}$ by at least two orders of magnitude. Therefore, $R_{a,t}$ can be neglected.

This model is approximate because C is calculated in free space around the pore area, a simplification of the situation with the ion paths being confined by the sidewalls of the trenches on both sides of the membrane stack. This model does not consider possible contributions of surface conductivity from the electrical double layer on the pore surface, which may influence the linear relationship between conductance and salt concentration. To compensate for such deficiencies, two coefficients γ and n are introduced as fitting parameters in R_t (10):

$$R_t = 2\gamma \frac{2\varepsilon_0 \rho \Delta U}{\sigma A} = \gamma \frac{F(a,b,h)}{\pi a b q c^n (\mu_+ + \mu_-)} \text{ (10)}$$

where, a and b are the side lengths of the pore area, c is the salt concentration in the electrolyte, q is elementary charge ($1.6 \cdot 10^{-19}$ C), μ_+ and μ_- are mobility of cation and anion, respectively, h is the thickness of membrane (i.e. depth of the trenches) and F is a function of a, b and h as described in Supporting Information.

V.III COMSOL simulation

We simulated the ionic current of the interfacial nanopore using COMSOL Multiphysics. The motion of ions in electrolyte is described by the Nernst-Planck equation (NPE), while the electric potential distribution is described by the Poisson equation (PE). In simulation, the "transport of diluted species" module (NPE) and the "electrostatics" module (PE) were fully coupled to govern the system of a three-dimension model. For KCl solution, the mobility of K^+ and Cl^- are 6.95×10^{-8} m^2/Vs and 7.23×10^{-8} m^2/Vs, respectively[4]. The diffusion coefficients were determined by referring to the Einstein relationship. All the interfaces in the system were neutral and the voltage bias was set at 0.2 V. The total current was a numerical integration of the ion flux density in the pore area. Figure V.3 shows the distribution of current density and electrical potential in nanopore structure from the COMSOL simulation.
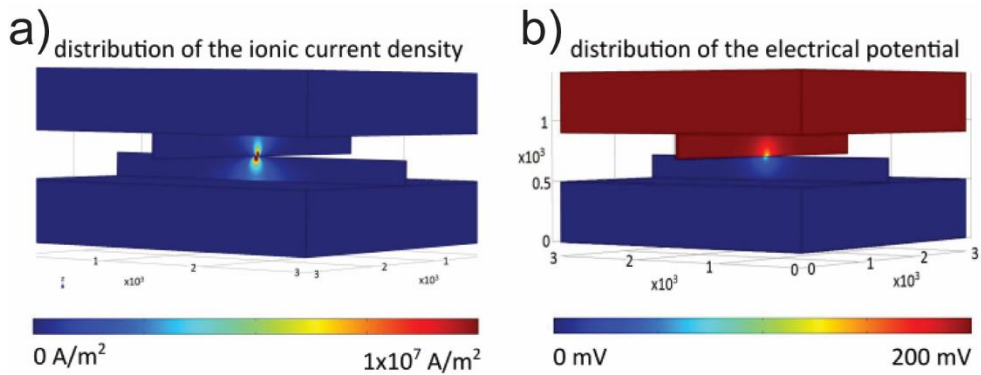
Figure V.3. COMSOL simulation of the ionic current density (a) and electrical potential (b) distribution of an interfacial nanopore with h = 200 nm and a = 10 nm. The simulations consider buffer solution of 1 M KCl and under the applied transmembrane potential of 200 nm.

V.IV   Detection of translocated DNA by PCR

To verify that Lambda DNA was translocated to the trans chamber during the experiment, we used polymerase chain reaction (PCR). PCR is a very sensitive assay that is capable of detecting minute amounts of DNA. We chose to amplify a region of 449 bp corresponding to nts 24201-24649 of lambda DNA (48502 bp) using the forward primer Lamfor (5'-ggtgaacttccgatagtgcggg-3') and reverse primer Lamrev (5'-gcaacgtttcagcagctacagtcag-3'). Conditions for PCR were as follows: total volume 12.5 µl, 1 unit of Pfu Polymerase (Thermo Fischer Scientific), Pfu buffer plus $MgSO_4$, primers 200 nM, dNTPs 200 µM , 0.5 µl chamber sample. Program: 3 min 94 ºC, 35 cycli of 1 min 94 ºC, 1 min 57 ºC , 1 min 72 ºC.

PCR products were electrophoresed on a 1.5% (w/v) agarose gel in TAE buffer (40 mM Tris, 20 mM acetic acid, and 1 mM EDTA). Inset Figure 7.3a (Chapter 7) shows the result of PCR after 35 cycles. Lane 2 showed that before the translocation reaction no Lambda DNA could be detected in the bottom compartment (the band that is visible corresponds to the input primers that migrate near the 100 bp DNA fragment from the DNA ladder (lane 1). Lane 3 showed that after translocation, a PCR fragment of the correct size could be obtained. This product had the same size as that of lane 4 which was obtained by PCR using 3 pg of pure lambda DNA (i.e. the positive control). In lane 5 instead of lambda DNA, water was added to the PCR

(negative control). From these data we could conclude that lambda DNA was indeed translocated to the trans chamber.

V.V   Characterization of DNA translocation

We probed the translocation of the dsDNA through the same interfacial nanopore shown in Figure 7.4a of the main text by varying the transmembrane potential and the LiCl buffer concentration. The data are plotted in Figure V.4. Note that the data in blue and green colours corresponded to the populations shown in Figure 7.4b (Chapter 7) with the same colour.
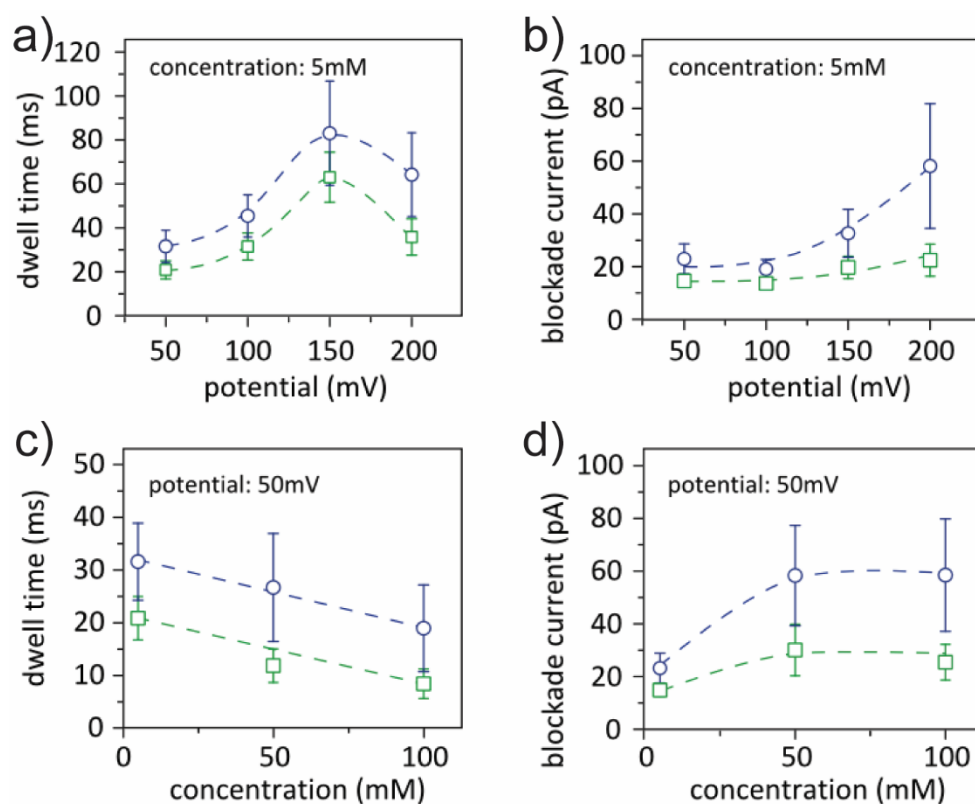

Figure V.4. Characterization of the DNA translocation through an interfacial nanopore. a) and b) translocation with different potentials. c) and d) translocation at different LiCl concentrations. The data in blue and green colours correspond to the evolution of the two major populations of the data shown with the same colours in the Figure 7.4b (Chapter 7).

The dwell time in conventional nanopore systems is largely dependent on the applied transmembrane potential (for a constant ionic strength). Lowering the potential weakens the electrostatic force acting on the DNA molecule and reduces the translocation speed (i.e. increases the dwell time). One could observe this behaviour in our system upon lowering the potential from 200 mV to 150 mV (Figure V.4a). The dwell time of the DNA, however, decreased at < 150 mV. With the low transmembrane potential and ionic strength used in our measurement, effects related to surface charges[5] and DNA/nanopore interaction played complex roles. Understanding the interplay between those forces within our novel architecture involving polymeric materials (rarely used and studied compared to solid state materials) invoked substantial further theoretical and experimental investigations.

Varying the concentration of the DNA in the buffer solution provided more insights into the translocation mechanism. We studied DNA translocation at two concentrations, 10 ng/µl and 20 ng/µl (Figure 7.3b Chapter 7 and Figure V.**5**) through the same nanopore. Doubling the DNA concentration only slightly increased the capture rate – the rate at which DNA molecules were captured by and subsequently translocated through the nanopore – from 400 up to 430 events in 10 minutes of experiment. Obviously, the capture rate in interfacial nanopores failed to scale proportionally with DNA concentration, unlike what has been reported for conventional nanopores[6]; This observation could imply the presence of a strong drag force, e.g. the DNA/nanopore interaction with a more dominant role than the accessibility of the DNA for the translocation. This conclusion was further backed-up by considering that our measured capture rates were few orders of magnitudes lower than those reported for conventional nanopores[7-9].
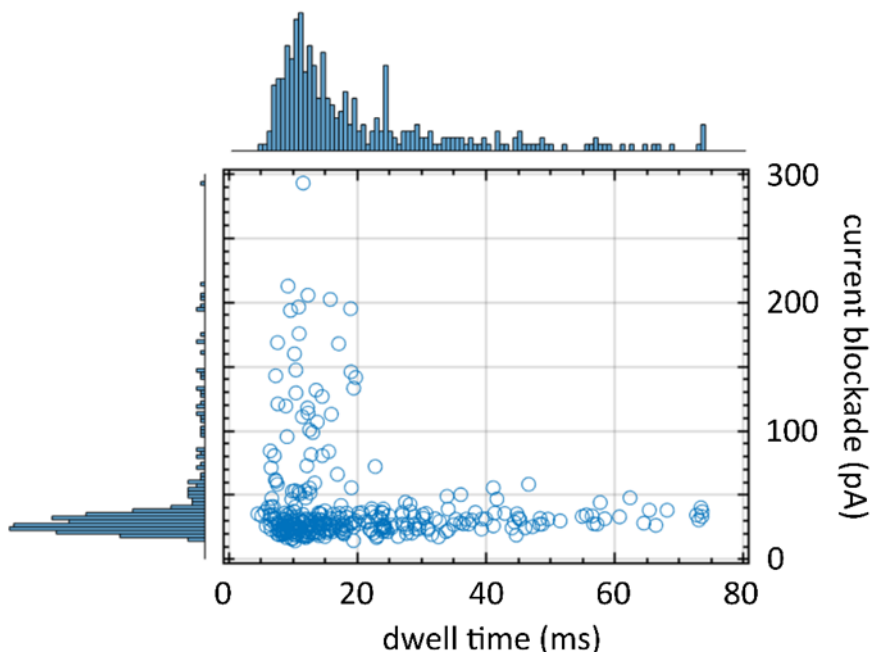
Figure V.5. Scatter plot of the amplitude of the current blockade versus translocation time for DNA translocation events through the same nanopore as in Figure 7.4a of Chapter 7. The measurement was performed under the same conditions as in Figure 7.4a except that the DNA concentration was doubled (to 20 ng/µl). The plot features ~430 translocation events, recorded during 10 min of experiments. The distributions of the dwell time and current blockade were separately plotted in left and top inset panels.

V.VI   Simulation of the DNA translocation in an interfacial nanopore

Figure V.6 shows the ionic waveform of translocation event simulated by COMSOL. Parameters a and h were both set at 50 nm and the radius of DNA is set at 5 nm. Using the actual radius of dsDNA (r = 1 nm) gave rise to a very high mesh density with unacceptable simulation time. So, we used r = 5 nm instead for illustration. This modification might have only influenced the blockage level (the change of current) and would have not impacted the shape of the waveform. We used the salt concentration and the bias voltage of 100 mM and 200 mV, respectively. Since the position of DNA was manually set step by step, the translocation speed was not affected by the bias voltage. Any possible DNA-nanopore interaction was omitted in this modelling attempt. The simulation returned with a sharp

translocation waveform both at the start and the end of the event, in the absence of any interaction between DNA and interfacial nanopores.
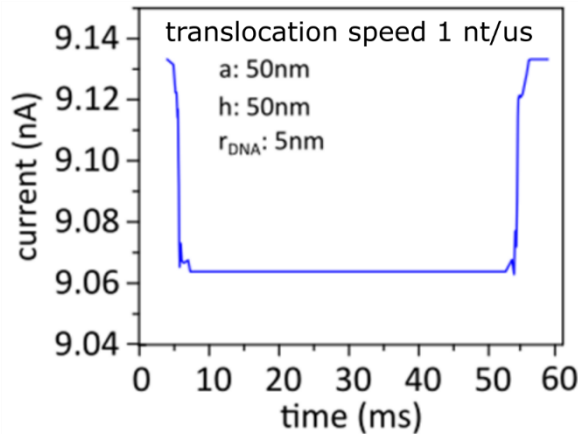

Figure V.6. COMSOL simulation result of a DNA translocation through an interfacial nanopores with the same geometry as in Figure 7.4a of Chapter 7.

V.VII Effective thickness of nanopore

The electrical resistance of a nanopore intuitively was dominated by that of the most restrictive region, i.e. the pore itself where the electric field was the strongest. Thus, the effective thickness of nanopore could be defined by referring to the profile of the electric field along the central axis perpendicular to the nanopore area. Specifically, the effective thickness was twice the distance from the pore centre to the point where the electric field intensity dropped to e^{-1} of its peak value for the symmetric system we were considering with regard to geometry and properties of membrane material and electrolytes.

We simulated the electric field distribution of interfacial and conventional nanopores of varied thicknesses using the COMSOL Multiphysics software package (Figure V.7a to V.7d). The centre of the nanopore was set at the origin of the coordinate system. The membrane thickness of the conventional nanopore was $2h$, in order to compare with its counterpart interfacial nanopore that was formed by stacking two membranes, each with thickness h. The two slits of the interfacial nanopores were assumed to be perpendicular to each other. The conventional nanopore was further assumed to take a square shape instead of the commonly encountered circular one. With the definition above, the effective thickness of the

ordinary nanopore could be approximately viewed as the sum of its membrane thickness ($2h$) and twice the thickness of the access region commensurate with half the side length of the pore, a.

Although the interfacial nanopore exhibited obvious advantages (measured by effective nanopore thickness) over conventional nanopore for large h as seen in Figure V.7e and Figure 7.5 (Chapter 7), it was of general interest to minimize h for sequencing purposes. Figure V.7f separately compares the thicknesses of access and pore regions of conventional nanopores with the effective thickness of interfacial nanopores for very thin ($h \leq 5$ nm) nanopores. Obviously, in this regime the effective thickness of interfacial nanopores converged towards that of the access region of the conventional nanopores. Here, interfacial nanopores were clearly advantageous since they had no pore region. Indeed, the zero pore thickness of interfacial nanopores was always smaller than the finite pore thickness in conventional nanopores. However, the benefit of interfacial nanopores could only be fully exercised if the effective thickness of the access region was reduced e.g. by lowering a.
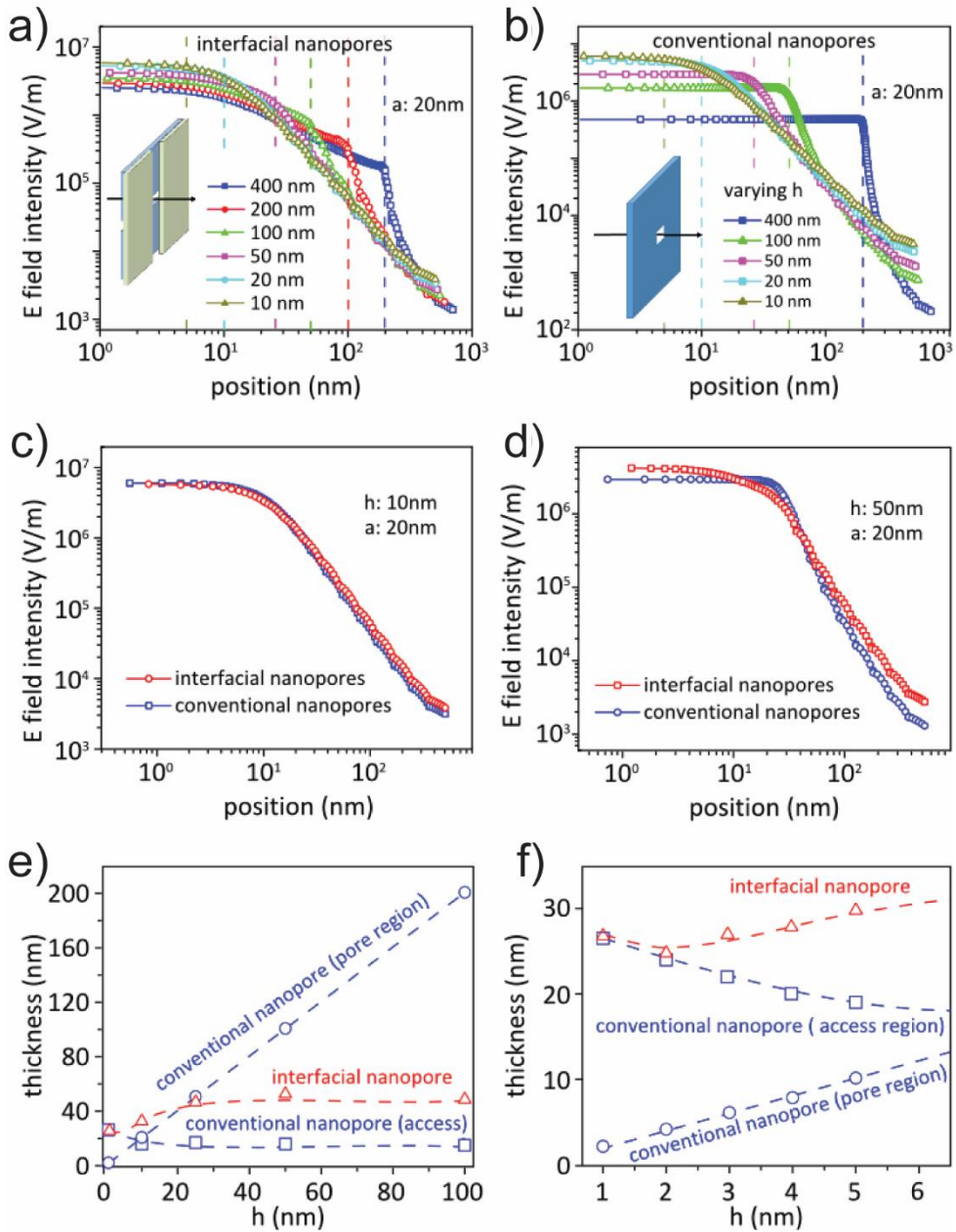
Figure V.7. Gradient of the electrical field profile near the conventional and interfacial nanopores. a and b) Electric field profiles for (a) interfacial and (b) conventional nanopores with different membrane thickness *h* but fixed pore size *a* = 20 nm. Conventional nanopores of squared shapes were considered to match the geometry of interfacial nanopores. c) and d) Comparison of the electric field profiles of conventional (blue lines)

and interfacial (red lines) nanopores with a = 20 nm for (c) h = 10 nm, and (d) h = 50 nm. e) and f) Simulation of the characteristic thicknesses of conventional (two-component) and interfacial (single-component) nanopores, plotted in different ranges.

V.VIII   Sensitivity of interfacial nanopores

Resolution and sensitivity are the parameters quantifying the ability of a nanopore to resolve an analyte. Resolution represents the capability of the nanopore in resolving short (in length) objects and patterns present in the analyte (e.g. nucleotides on a DNA strand) and depends on the length of the narrowest area of restriction in the flow of ions (normally equivalent to the thickness of the membrane in conventional nanopores)[10]. In the main text, we mathematically illustrated that the resolution of interfacial nanopores – having zero physical length, even shorter than the monoatomic thickness of 2D nanopores – outperforms all existing nanopores.

Sensitivity, on the other hand, defines the capability of the nanopore in detecting small changes in the outer diameter of the analyte and depends on how tightly the nanopore "hugs" the translocating molecule[10]. Here, the sensitivity could be roughly expressed as the arithmetic sum of two components one from the pore region and one from the access region (11):

$$S = R_{pore}\left(\frac{v_{pore}}{V_{pore}}\right) + R_{acc}\left(\frac{v_{mouth}}{V_{mouth}}\right) (11)$$

Here, R_{pore} was the pore resistance, R_{acc} was the access resistance, V_{pore} was the volume of the pore, V_{mouth} was the volume of the mouth of the pore (corresponding to the access resistance), v_{pore} was the volume of the external molecule inside the pore and v_{mouth} was the volume of the external molecule inside the mouth of the pore. Note that except for ultra-thin membranes, a DNA nucleotide (or small DNA gyration) that was enclosed entirely inside the pore region of a conventional nanopore did not occupy any volume corresponding to the access resistance. Hence, the first term was dominant for conventional nanopores while the second term (in the absence of any pore volume) was relevant for interfacial nanopores. Furthermore, as illustrated in Figure 7.2 (Chapter 7), the resistance of interfacial nanopores approached many of the other conventional nanopore systems; hence we excluded R_{pore} and R_{acc} in our discussions below.

We considered two nanopore systems: i) an interfacial nanopore of slab thicknesses h and trench width a and ii) a square shape conventional nanopore of lateral size a and total thickness $2h$. The parameters were illustrated in the schematics of Figure V.8. V_{mouth} in the conventional nanopore system could be approximated by a hemisphere of radius r ($r = a/2$) on each side of the membrane; the hemisphere approximation became better for circular nanopores. Similarly, V_{mouth} in the interfacial nanopore scaled with $a/2$ (a: width of the trench) and was independent of h (inset in Figure V.8b). In contrast, the pore volume in the conventional nanopore scaled with h (inset in Figure V.8a). Hence, the comparison of the sensitivity of interfacial and conventional nanopores corresponded to the comparison of parameters h and a.

Accordingly, keeping the trench size (a) smaller than the total thickness of the membrane ($2h$) was an important consideration in order to maximize the sensitivity of interfacial nanopores. Note that for ultrathin membranes (h is comparable to the size of a nucleotide e.g. in graphene nanopores), both the volume of the pore and that of the pore mouth were in play in conventional nanopores; hence the sensitivity of interfacial nanopores was slightly superior, even for large a.
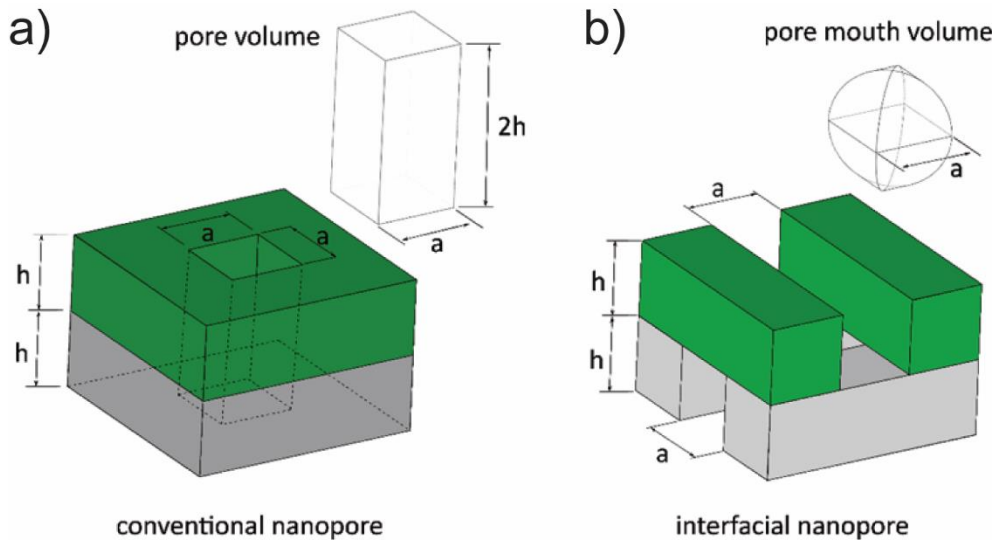

Figure V.8. Schematic representation of the geometry of (a) conventional and (b) interfacial nanopores used for our simulations.

Similarly to the study reported in ref [9], we have simulated and compared the distribution of the electric field in interfacial and conventional nanopore systems of Figure V.**8** for two different regimes: i) $h \geq a$ and ii) $a > h$.

For $h \geq a$ (Figure V.9a, and V.9b), the electric field of interfacial nanopore (b) was concentrated around the pore opening. The high-field region (*i.e.* the effective thickness) was much shorter than that in conventional pore (a) with the same size and membrane thickness. When $a > h$ (Figure V.9c and V.9d), the interfacial nanopore (d) exhibited a similar electric field distribution as in the conventional nanopore (c), which indicated a similar sensitivity. Note that the electric field distribution governed the "effective thickness" of a nanopore (the distance over which the field fell to 1/e of its maximum value).
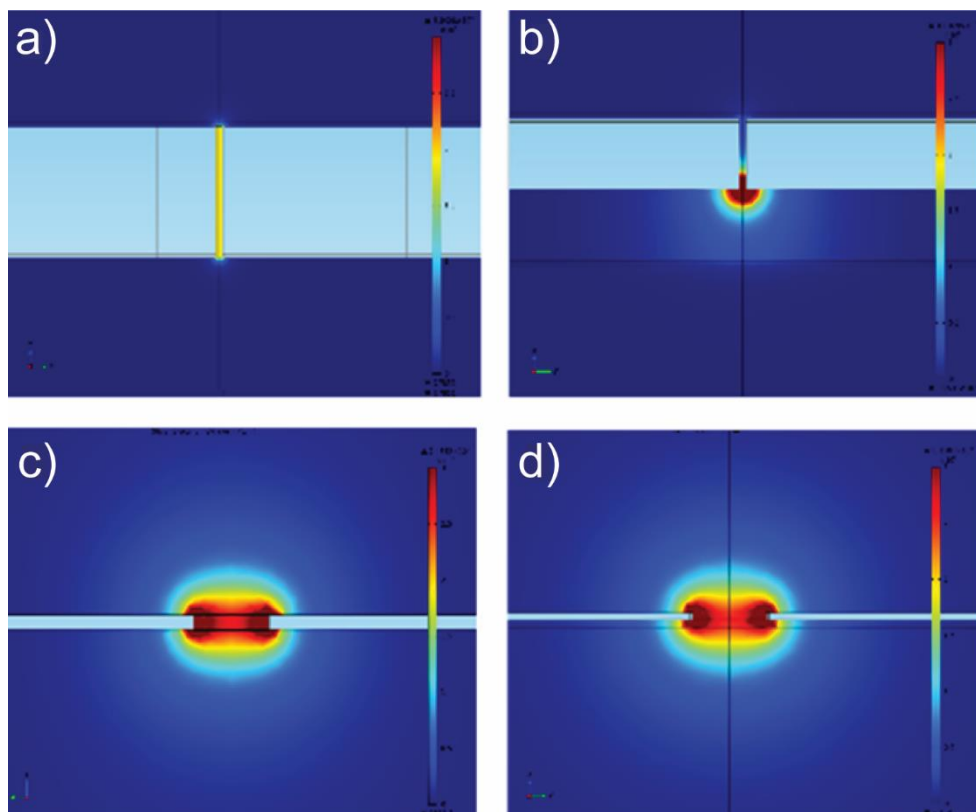

Figure V.9. Distribution of the electric field in different nanopore systems. a) Conventional nanopore with a = 5 nm and $2h$ = 100 nm. b) Interfacial nanopore with a = 5 nm and h = 50 nm. c) Conventional nanopore with a = 50 nm and $2h$ = 10 nm. d) Interfacial nanopore with

a = 50 nm and h = 5 nm. The simulation was done with 1 M KCl under 0.2 V bias voltage and the panels show the side view representations. The colour bar range is 0 to 3×10^6 V/m.

As a complementary study, we also simulated the waveform associated with the translocation of a nanoparticle through conventional and interfacial nanopores of a = 50 nm, h = 50 nm in Figure V.10. The radius of the nanoparticles was set as 5 nm which approaches the gyration radius of a short DNA/RNA strand and some large proteins.
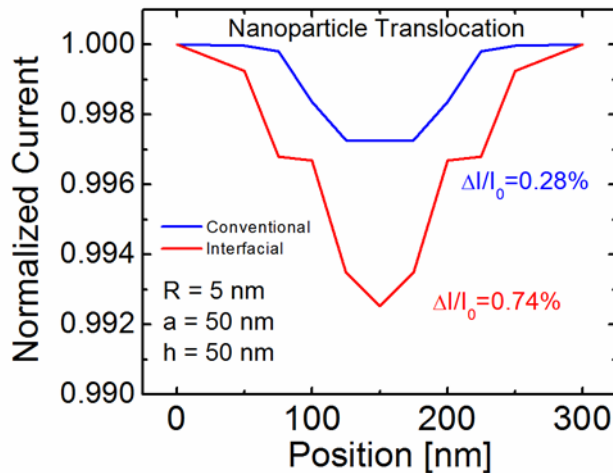

Figure V.10. Translocation waveform of a nanoparticle through conventional and interfacial nanopores. The current was normalised to its open pore state current.

The amplitude of the signal in the interfacial nanopore was significantly larger than that of the conventional nanopore which is due to the smaller volume of the mouth of the nanopore with respect to the total volume of the pore. Indeed, the electric field in the interfacial nanopore was confined in a smaller space compared with the conventional one with the same size, hence the translocation waveform showed a sharper peak when the particle passes through the nanopore centre, where the electric field reached its maximum value.

V.IX   Noise analysis

Interfacial nanopores showed the characteristic $1/f^2$ noise. To the best of our knowledge, only two studies have reported $1/f^2$ noise in conventional nanopores [11,12] which may help to elucidate the background phenomenon in our nanopores as well. In nanopores drilled in some polymeric materials, the momentary opening-closing the channel by cleaved polymer strands (dangling ends) present at the pore rim was postulated as the origin of $1/f$ noise [11]. In the time domain, such noise was characterized by sudden transitions of the conductance between multiple (usually two) levels. The fluctuations were missing in nanopores in polymers with more stable subunits constituting the channel walls, leading to the $1/f^2$ noise dependency. As the interfacial nanopores exhibited the same characteristics both at time and frequency domains (at typically used transmembrane potentials) we considered the absence of the dangling ends as the origin of the observations. Indeed, in the interfacial nanopores the area close to the pore were fabricated upon moulding (curing) the polymer; hence, in contrast to the techniques based on drilling (breaking) the membrane, no dangling ends were anticipated. The presence of the nanosized air bubbles in the buffer solution also was capable of distorting the noise characteristics of a nanopore towards $1/f^2$ [12]. Such bubbles might be even large enough to trigger solitary jumps (as oppose to multiple transitions observed in the $1/f$ noise) in the conductance upon passage through the pore area. We have observed similar jumps in the conductance of some of the samples; hence the presence of nanobubbles in nanopore might have been also postulated as the origin of the observed $1/f^2$ behavior in interfacial nanopores. Indeed, the trapped air in between the two polymeric slabs upon fabrication could serve as a continuous source of injecting such bubbles. On the basis of the discussion here, a systematic study was demanded to understand the observed $1/f^2$ noise in the interfacial nanopores. We noted that, at first glance, no direct link between either of the discussed scenarios and the observed turn-over between the $1/f^2$ to $1/f$ noise upon increasing the transmembrane potential (Figure V.11a and V.11b) could be considered.
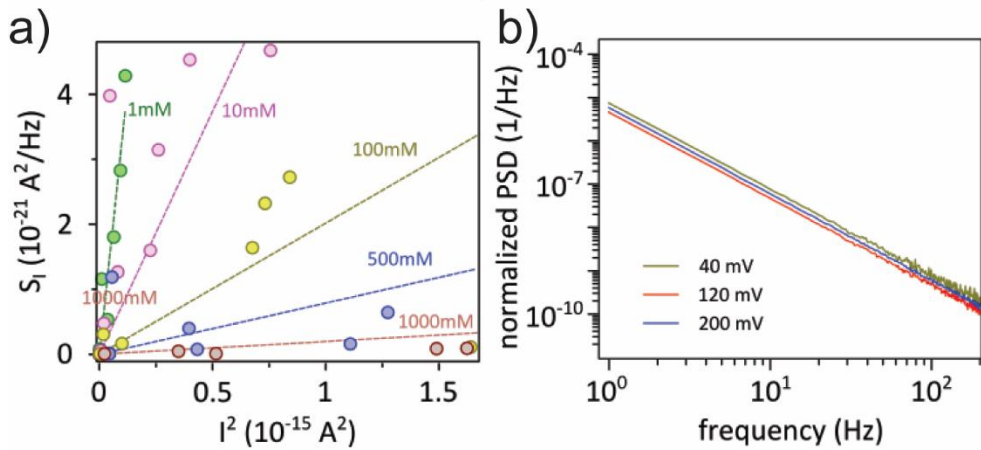
Figure V.11. Noise characterization in interfacial nanopores. a) The distribution of the PSDs of 19 different samples as a function of squared current I^2: Samples with diverse geometries ($50\ nm \leq h \leq 300\ nm$ and $10\ nm \leq a \leq 70\ nm$) were measured at fixed transmembrane potential (40 mV), but with different KCl concentrations. Dashed lines show the best linear fit for the data of each concentration. b) Normalized power spectral density of an interfacial nanopore ($h = 200\ nm,\ a = 50\ nm$), in low frequency regime and under different transmembrane potentials; the measurements performed with 100 mM KCl. Clearly, the noise in our nanopores did not follow the Hoog's model as if so, one would have expect overlapping of the curves.

V.X   References

(1)   Lipomi, D. J.; Martinez, R. V; Whitesides, G. M. *Angew. Chem. Int. Ed. Engl.* **2011**, *50* (37), 8566–8583.

(2)   Plesa, C.; Dekker, C *Nanotechnol.* **2015**, 26(8), 084003.

(3)   Hall, J. R. *J. Gen. Physiol.* **1975**, *66* (2), 531–532.

(4)   Wanunu, M.; Dadosh, T.; Ray, V.; Jin, J.; McReynolds, L.; Drndić, M. *Nat. Nanotechnol.* **2010**, *5* (11), 807–814.

(5)   Smeets, R. M. M. R. M. M.; Keyser, U. F. U. F.; Krapf, D.; Wu, M. Y. M. Y.; Nynke, H.; Dekker, C.; Dekker, N. H.; Dekker, C. *Nano Lett.* **2006**, *6* (1), 89–95.

(6)   He, Y.; Tsutsui, M.; Taniguchi, M.; Kawai, T. *J. Mater. Chem.* **2012**, *22* (27), 13423.

(7)   Schneider, G. F.; Kowalczyk, S. W.; Calado, V. E.; Pandraud, G.; Zandbergen, H. W.; Vandersypen, L. M. K.; Dekker, C. *Nano Lett.* **2010**, *10* (8), 3163–3167.

(8)   Singer, A.; Rapireddy, S.; Ly, D. H.; Meller, A. *Nano Lett.* **2012**, *12* (3), 1722–1728.

(9)   Merchant, C. A.; Healy, K.; Wanunu, M.; Ray, V.; Peterman, N.; Bartel, J.; Fischbein, M. D.; Venta, K.; Luo, Z.; Johnson, A. T. C.; Drndić, M.; et al. *Nano Lett.* **2010**, *10* (8), 2915–2921.

(10)   Garaj, S.; Liu, S.; Golovchenko, J. A.; Branton, D. *Proc. Natl. Acad. Sci.* **2013**, *110* (30), 12192–12196.

(11)   Siwy, Z.; Fuliński, A. *Phys. Rev. Lett.* **2002**, *89* (15), 158101.

(12)   Smeets, R. M. M.; Keyser, U. F.; Wu, M. Y.; Dekker, N. H.; Dekker, C. *Phys. Rev. Lett.* **2006**, *97* (8), 88101.

Samenvatting

Ondanks een veelbelovende reeks eerste resultaten, zijn er een aantal punten die het wijdverbreid gebruik van grafeen belemmeren. Naast de problemen wat betreft de handelbaarheid en chemische synthese van dit materiaal, zorgen de nanofabricatie en beperkte controle over de chemie van het materiaal ook voor grote belemmeringen. De meest veelbelovende apparaten zijn afhankelijk van een extreem gecompliceerd productieproces, wat maakt dat productie op grote schaal moeilijk haalbaar is. Verder wordt de chemische functionalisering gezien als een belangrijke stap richting een nieuwe generatie sensoren en meetapparaten die zijn uitgerust met geavanceerde moleculaire selectiviteit. Desondanks is er nog maar weinig bereikt wat betreft de selectieve functionalisering van grafeenfilmen, vooral rondom de randen. Randfunctionaliteit zou de chemische eigenschappen van grafeen kunnen verbeteren, met name van nanostructuren, waarvan de hoeveelheid randen significant is ten opzichte van de koolstofatomen waaruit het raster van grafeen is opgemaakt. Momenteel leveren chemisch ontworpen grafeen-nanostructuren alleen door middel van chemische synthese wat op, en dat staat integratie in meetapparatuur in de weg. Desondanks heeft een top-down aanpak laten zien dat grafeen chemisch te functionaliseren is, al is er weinig selectiviteit tussen het basaal vlak en de randen.

Dit onderzoek houdt zich bezig met de onconventionele nanofabricatie van nanostructuren die hun basis vinden in grafeen, en de chemie van de randen van grafeen. Door middel van microtomen in combinatie met reactief ionenetsen of cyclovoltammetrie hebben wij nanopores, nanogaps en nanoribbons gemaakt, en daarmee hebben wij conventionele lithografische procedures vermeden. Deze methodes zijn gebruikt vanwege een verbeterde controle over de chemie van de randen van grafeen. Daarom is deze scriptie in tweeën gedeeld. Eerst komen de grafeenranden samen met hun chemie en toepassingen aan bod in hoofdstukken 2, 3 en 4. Vervolgens komt de onconventionele vervaardiging van grafeen nanostructuren aan bod in hoofdstuk 5, en de 2D nanoarchitecturen in polymeer en metalen structuren in hoofdstukken 6 en 7. De resultaten laten zien dat de eerste stap richting het behalen van de schaalbare, onconventionele vervaardiging van grafeen nanostructuren en het vasthouden en controleren van randchemie, hiermee gemaakt is. Wij zijn van mening dat de realisatie van deze technologieën en hun integratie in meetapparatuur van groot belang zijn in de stap richting de

volgende generatie sensoren met grafeen als basis. In de toekomst zullen bijvoorbeeld nanogaps en nanopores samenkomen in een nanofluidisch systeem uitgerust met tunnelling elektroden, waar de chemie van de grafeenranden op maat gemaakt kunnen worden voor specifieke meetapparaten.

Hoofdstuk 2 vormt een literatuuroverzicht van de chemie van grafeenranden. Dit hoofdstuk laat aan de hand van de meest recente literatuur zien hoe het staat met onze kennis over grafeen. Daarnaast illustreert dit hoofdstuk het belang van de chemie van grafeenranden voor het nauwkeurig afstellen van elektrische eigenschappen van grafeen.

Aan de hand van dit literatuuronderzoek bekijken wij in hoofdstuk 3 de chemische functionalisering van de randen van een chemische dampdepositie, CVD, grafeen monolaag. De selectieve functionalisering van CVD grafeen blijft moeilijk haalbaar door de concurrerende reactieplaatsen van het basaal vlak, vooral op defecten en grain boundaries. Om specifieke reacties op de randen te krijgen, hebben wij grafeen omhuld in een polymeer matrix, die vervolgens door middel van microtomie is gesplitst waardoor de randen zichtbaar worden. Vervolgens hebben wij een elektrochemische cel gebouwd voor de natte functionalisering van de rand. De grafeenrand is bewerkt met cyclovoltammetrie, waarbij grafeen werkt als de elektrode tegen een Ag/AgCI referentie-elektrode. Dit onderzoek laat zien dat het mogelijk is om te werken met de chemie van de grafeenranden zonder conventionele nanofabricatie of atomaire karakterisatie. Iets wat een significante innovatie is ten opzichte van de huidige literatuur.

De gecontroleerde vervaardiging van grafeenranden door middel van bulk methoden is verder onderzocht met gebruik van reactief ionenetsen. In hoofdstuk 4 komt het etsen van een opgeschorte CVD-film van grafeen aan bod. wij hebben met succes een tunnelling junction gebouwd tussen de randen van twee grafeen elektroden met een precieze interface op sub-nanometrische afstand. Deze aanpak leverde de eerste dynamische tunnelling junction tussen twee enkele koolstofatomen aan de randen van ondersteunde grafeenmonolagen. Onze architectuur bestaat uit een nanogap van twee onafhankelijk ondersteunde grafeenfilms die gekoppeld zijn door middel van piezoelectric actuators. De randen zijn gekoppeld aan een gedraaide configuratie die samenkomt en een tunnelling junction over twee enkele koolstofatomen vormt. Middels deze verstelbare

tunnelling junction kunnen wij de dynamieken bekijken van wat vermoedelijk een elektrische vingerafdruk is van koolstof-koolstofbindingen die vormen over twee uiteinden van de tunnelling junction bij contact.

Met een vergelijkbare aanpak hebben wij in hoofdstuk 5 reactief ionenetsen gebruikt om de randchemie van een andere klasse van grafeen nanostructuren te bekijken, namelijke grafeen nanoribbons. Allereerst hebben wij met microtomie metalen nanostaafjes gemaakt om als inerte maskers voor de lithografie van grafeen nanoribbons te gebruiken. Door de nauwkeurig opgestelde nanostaafjes is een polymeer afdeklaag niet nodig, iets wat bij conventionele lithografie wel het geval is. In eerste instantie voorkomt dit dat er polymeercontaminatie plaatsvindt op de oppervlakte van het grafeen. Daarnaast zijn deze metalen maskers, in tegenstelliing tot polymeer afdeklagen, bestand tegen agressieve chemicaliën. Iets wat een significante verbetering is voor processen zoals graveren of chemische functionalisatie in organische oplosmiddelen. Ook hebben wij verschillende graveeromstandigheden geprobeerd om de randchemie van grafeen te kunnen reguleren. Ondanks dat wij weinig controle hadden over de kristalstructuur van de randen van de grafeen nanoribbons, hebben wij de modificatie van de Raman fingerprintvingerafdruk kunnen zien, wat een kenmerk is van doping, geïnduceerd door de chemische funtionalisering van de randen.

De microtomie van nanostaafjes van metalen films is een belangrijk hulpmiddel voor nanotechnologie. Naast de lithografie van grafeen nanoribbons, kan microtomie een reeks metalen nanostaafjes produceren die parallel en regelmatig gespreid zijn. Het koppelen van paren nanostaafjes op nanometrische afstand geeft nanogaps tussen twee metalen elektroden, namelijk de tweetal nanostaafjes. Hoofdstuk 6 betreft meerlagige films van polyelektrolyten, gemaakt door middel van Layer-by-Layer depositie, en gebruikt polymeer afstandhouders tussen gouden films die verder omgezet zijn in nanogaps met microtomie. Met microtomie zijn de gouden films op nanometrische afstand van elkaar gescheiden, wat een nanogap gaf tussen nanostaafjes. De elasticiteit van de Layer-by-Layer depositie en het gemak van de bereiding geeft dunne lagen polyelektrolyten, met een regelbare tussenlaagafstand tot en met 1.5 nm, tussen elektroden samen te stellen.

In de voorgaande hoofdstukken hebben wij uitvoerig gewerkt aan de nanostructurering van grafeen en de chemische functionalisering daarvan. Eerder onderzoek heeft gewerkt aan het vervaardigen van een grafeen-apparaat wat geïntegreerd is in een fluidisch system dat in staat is analyses in staat is om analyses aan het sensing element van grafeen toe te voegen. Daarom stellen wij in hoofdstuk 7 een innovatieve nanopore/nanocapillary fluidisch system voor, samengesteld uit gelaagde polymere platen, wat het in de toekomst mogelijk zou maken om een nanopore apparaat en een tweetal tunnelling electroden te integreren. Vergelijkbaar met inerte maskers voor lithografie hebben wij dunne metalen films ingesloten in polymeer matrices met microtomie, wat metalen nanostaafjes ondersteund door polymeerplaten opleverde. Twee nanostaafjes zijn gekruist bovenop elkaar gezet, waarna wij ze kruislings graveren door middel van een insnijding van de polymeer ondersteuning. De ontstane gleuven vormen twee nanofluidische kanalen die een opening delen: een nanoporie. Noemenswaardig is dat de twee insnijdingen een zero-depth nanopore vormen. Deze capillair heeft de geometrische voordelen van atomisch dunne materialen zoals grafeen, maar zonder een gecompliceerd productieproces.

In het kort: dit onderzoek richt zich op het onconventioneel ontwerpen van nanostructuren en de chemische functionalisering van grafeenranden. Dit onderzoek komt voort uit een analyse van de factoren die knelpunten vormen in de huidige nanofabricatie en chemische functionalisering van grafeen, wat vooralsnog vaak niet verder komt dan de prototypefase. Aan de hand van onze bevindingen kunnen wij een nieuwe aanpak aanbieden op dit gebied, en trachten wij de huidige standaarden van vervaardiging, functionalisering en characterisering te simplificeren.

Wij hebben aangetoond dat innovatieve en onconventionele processen om de meest gangbare nanostructuren te ontwikkelen, zoals nanopores, nanoribbons en nanogaps, succesvol zijn. Daarnaast hebben wij een simpele, maar effectieve, manier aangetoond om de chemie van de randen van een grafeen CVD-film te controleren. Wij zijn van mening dat deze resultaten van belang zijn voor de vooruitgang van de nanotechnologie, en voornamelijk de ontdekking van niet-standaard oplossingen voor het gebruik van grafeen in apparaten en de regelbaarheid van de chemie van dit materiaal op grote schaal.

List of publications

1. **Dynamic Tunnelling Junctions at the Atomic Intersection of Two Twisted Graphene Edges.**
Amedeo Bellunato, Sasha D. Vrbica, Carlos Sabater, Erik W. de Vos, Remko Fermin, Kirsten N. Kanneworff, Federica Galli, Jan M. van Ruitenbeek and Grégory F. Schneider. Nano Letters, 2018, 18(4), 2505-2510.

2. **Zero-Depth Interfacial Nanopore Capillaries.**
Hadi Arjmandi-Tash, **Amedeo Bellunato**, Chenyu Wen, René C. Olsthoorn, Ralph H. Scheicher, Shi-Li Zhang, and Grégory F. Schneider. Advanced Materials, 2018, 30, 1703602.

3. **Chemistry at the Edge of Graphene.**
Amedeo Bellunato, Hadi Arjmandi Tash, Yanina Cesa and Grégory F. Schneider. Chem. Phys. Chem. 2015, 17(6).

4. **Electrophilic Radical Coupling at the Edge of Graphene.**
Amedeo Bellunato and Grégory F. Schneider, Nanoscale 2018, 10, 12011-12017.

5. **Inert Mask Lithography of Edge Narrowed Graphene Nanoribbons with In-situ Metallic Electrodes.**
Amedeo Bellunato, Alex van der Ham, Pauline van Deursen and Grégory F. Schneider. In preparation.

6. **Multilayered Polymeric Nanogaps Between Metallic Electrodes.**
Amedeo Bellunato, Clarisse de Sere, Zhanna Overchenko, Bram Koster, Sai Sankar Gupta, Pauline van Deursen and Grégory F. Schneider. In preparation.

7. **Implementation of Carbon Thin Film Coatings in the Super Proton Synchrotron (SPS) for Electron Cloud Mitigation.**
Pedro Costa Pinto, **Amedeo Bellunato**, Tessa Basso, Paul Edwards, Mounir Mensi, Alban Sublet and Mauro Taborelli. Proceedings of IPAC 2014, 07, T14, 2574-2576.

Curriculum Vitae

Amedeo Bellunato was born in Turin, Italy on November 30th 1987.

He attended high-schools in Monza, Italy at Liceo Scientifico Paolo Frisi, where he graduated in 2007. In that year, he enrolled to the bachelor degree in Physics Engineering at Politecnico di Milano. He graduated in 2011 after a research internship on Scanning Probe Microscopy, focusing on Magnetic Force Microscopy.

Afterwards, he received a master degree in Materials Engineering and Nanotechnology at Politecnico di Milano in 2014 after a year spent as a technical student at CERN, the European Research Centre for Nuclear Research.

At CERN, he designed and implemented an innovative carbon coating system for the stainless-steel dipoles chambers of the Super Proton Synchrotron. This work was summarized in his master thesis: "Experimental Investigation on the Electron Multipacting and the Surface Conditioning", and his first publication was published in IPAC2014 in 2014 "Implementation of Carbon Thin Film Coatings in the Super Proton Synchrotron (SPS) for Electron Cloud Mitigation".

In June 2014 he started as a PhD student in the group of dr. Grégory Schneider at the Leiden Institute of Chemistry within the Supramolecular and Biomaterials Chemistry department of Professor dr. Alexander Kros. His work focused on the unconventional nanofabrication of graphene devices for biosensing applications, such as nanopores, nanogaps and nanoribbons. His research interest focused also on the functionalization of graphene edges, aiming to tune the physical-chemical properties of graphene.

During his PhD he extensively collaborated with the Leiden Institute of Physics, particularly with the group of Prof. dr. Jan M. van Ruitenbeek, and with the Leiden University Medical center, particularly with Pr. Dr. Ir. Bram Koster. He also supervised two international bachelor students, respectively from France and Ukraine, and a master student from Leiden University.

He lectured Dutch high-school teachers about quantum mechanics in real world applications at the "quantum wereld" day organized by Leiden University. He has

been an invited speaker at the open day of Leiden Science for International students in 2016, 2017 and 2018.

Parts of the results reported in this dissertation were presented at the following meetings and conferences:

- 24-04-2018, This week discovery at Leiden University, Leiden, The Netherlands.
  Zero-depth nanopores and twisted graphene nanogaps: perspectives on the future of biosensing, talk.

- 06-12-2017, Chains 2017, Veldhoven, The Netherlands.
  The unconventional design of nanopore, nanogap, nanowire 2D sensors, invited talk.
  Multilayered molecular nanogaps, poster.

- 23-08-2017, Chem2Dmat, Strasbourg, France.
  Dynamic single carbon tunnelling nanogaps for biomolecular detection, poster.

- 28-09-2017, Graphene Week 2017, Athens, Greece.
  Chemical tools for graphene nanotechnology, talk.
  Dynamic single carbon-carbon tunnelling nanogaps for biomolecular detection, poster.

- 28-06-2017, NanotechFrance 2017, Paris, France.
  Tunable Au nanogaps via Layer-by-Layer deposition of organic fillers and thiolated polyelectrolytes, talk.

- 06-12-2016, Chains 2016, Veldhoven, The Netherlands.
  Stabilized aminothiols self-assembled monolayers for Layer-by-Layer deposition on gold thin films, poster.